

**Seismic Performance of Steel Buildings with Braced Dual Configuration and  
Traditional Frame Systems through Nonlinear Collapse Simulations**

Yudong Wang

A Thesis

in

The Department

of

Building, Civil and Environmental Engineering

Presented in Partial Fulfillment of the Requirements

for the Degree of Master of Applied Science (Civil Engineering) at

Concordia University

Montreal, Quebec, Canada

August 2018

© Yudong Wang, 2018

CONCORDIA UNIVERSITY  
School of Graduate Studies

This is to certify that the thesis prepared

By: Yudong Wang

Entitled: Seismic Performance of Steel Buildings with Braced Dual Configuration and  
Traditional Frame Systems through Nonlinear Collapse Simulations

and submitted in partial fulfillment of the requirements for the degree of

**Master of Applied Science (Civil Engineering)**

complies with the regulations of the University and meets the accepted standards with  
respect to originality and quality.

Signed by the final Examining Committee:

\_\_\_\_\_ Dr. K. Galal \_\_\_\_\_ Chair

*Chair's name*

\_\_\_\_\_ Dr. R. Sedaghati \_\_\_\_\_ Examiner

*Examiner's name*

\_\_\_\_\_ Dr. A. Bagchi \_\_\_\_\_ Examiner

*Examiner's name*

\_\_\_\_\_ Dr. L. Tirca \_\_\_\_\_ Supervisor

*Supervisor's name*

Approved by \_\_\_\_\_

Chair of Department or Graduate Program Director

\_\_\_\_\_ 2018 \_\_\_\_\_

\_\_\_\_\_  
Dean of Faculty

**ABSTRACT****Seismic Performance of Steel Buildings with Braced Dual Configuration and  
Traditional Frame Systems through Nonlinear Collapse Simulations**

Yudong Wang

Traditional concentrically braced frames, CBF, are stiff and provide limited to moderate ductility, while moment resisting frames, MRF, are able to dissipate seismic energy when undergoing large lateral displacements. However, these traditional earthquake resistant systems do not show uniformly distributed damage along the building height. Changes in structural properties during nonlinear hysteresis behaviour may lead to drift concentration and weak-storey response. Moreover, both traditional systems are susceptible to long-duration subduction earthquakes.

The pursuit of these issues led to the concept of utilizing multiple-resisting structural systems that act progressively so that the overall seismic resistance is not significantly reduced during long-duration earthquakes. The structural system consisting of a rigid braced frame that provides primary stable cyclic behavior and a moment frame acting as a backup system with good flexural behavior is the steel Braced Dual System studied herein.

The objectives of this study are: a) to investigate the seismic response of steel Braced Dual building from yielding to failure, as well as, to identify the types of failure mechanism; b) to assess the seismic response of Braced Dual System against the traditional MRFs and CBFs with moderate ductility through incremental dynamic analysis; c) to evaluate the effect of long duration subduction earthquakes versus crustal type earthquakes on these

building systems through collapse safety criteria using FEMA P695 procedure and to assess the probability of exceeding defined performance levels using fragility analysis.

To carry out these objectives, detail numerical models were developed using the OpenSees framework. The prototype 8-storey office building is located on firm soil in Vancouver, B.C. and is subjected to two sets of crustal and subduction ground motions. Two traditional earthquake resistant systems (MD-CBF, MD-MRF) and the Braced Dual System are considered. Design is conducted according to NBCC2015 and CSA/S16-14.

From nonlinear time history analysis, the following results are reported: for the Braced Dual System, two types of failure mechanism involving either one floor or two adjacent floors (in general the bottom floors) were identified which also involve flexural yielding of MRF beam of critical floors; the Braced Dual System provides larger ductility than the MD-CBF, shows significant increase of seismic resistant capacity for similar seismic demands, provides the largest collapse margin ratio and collapse safety capacity under both earthquake types. In addition, the building with Braced Dual System shows a progressive seismic behavior and a more uniform damage distribution along the building height. From fragility analysis resulted that at Collapse Prevention (CP) limit state, the Braced Dual System experiences 100% probability of exceedance after it was subjected to two times larger seismic demand than the MD-CBF or MD-MRF systems. All studied structural systems are sensitive to long duration subduction earthquake.

## ACKNOWLEDGEMENTS

First and foremost, I would like to express my most sincere gratitude to my supervisor, Dr. Lucia Tirca, who has supported me throughout the entire research project with her patience, enthusiasm, and expert guidance. I couldn't remember how many late nights and weekends Dr. Tirca spent to help me accomplish this thesis. One simply could not wish for a better supervisor.

Besides my supervisor, I would like to thank the rest of my committee members: Dr. Ashutosh Bagchi, Dr. Khaled Galal, and Dr. Ramin Sedaghati for their insightful comments and questions. Special thanks to Dr. Melina Bosco.

I would also like to thank Concordia University for providing such an extraordinary academic environment, and its fabulous team of professors for their enlightening lectures.

Also, I would like to thank my friends: Anastasia Athanasiou, Liang Chen, Laura Manolache, Masaaki Ohira, Siamak Pejmanfar, Fangping Qiu, Ovidiu Serban, and all the people from the office: Hamid A., Mohammed A., Armin F., Shadman H., Omer Yagob. It is my pleasure to meet all of you guys and I wish all the best of you.

I would also like to express my gratitude to Concordia University for providing such an extraordinary academic environment, and its fabulous team of professors for their enlightening lectures.

Funding from IC-IMPACTS is gratefully acknowledged.

Last but not least, I would like to thank my parents for their endless love and support, I love you!

## Table of Contents

CHAPTER 1. INTRODUCTION .....	1
1.1 General .....	1
1.2 Objective and Scope .....	3
1.3 Description of Methodology .....	3
1.4 Thesis Organization .....	4
CHAPTER 2. LITERATURE REVIEW .....	7
2.1 Past Studies on Dual Systems .....	7
2.2 The Open System for Earthquake Engineering Simulation .....	12
2.3 Modeling of Concentrically Braced Frame using OpenSees .....	13
2.4 Modeling of Moment Resisting Frame using OpenSees .....	17
2.5 Incremental Dynamic Analysis .....	24
2.6 Fragility Analysis .....	28
CHAPTER 3. SEISMIC DESIGN OF BRACED DUAL SYSTEM VS. TRADITIONAL SYSTEMS USING NONLINEAR ANALYSIS .....	31
3.1 Introduction .....	31
3.2 Building Design Criteria According to NBCC 2015 & CSA/S16 2014 .....	32
3.2.1 Gravity loads .....	32
3.2.2 Seismic load .....	33
3.3 System Ductility Classes and Restrictions .....	35
3.4 Design Criteria for MD-CBFs According to CSA/S16 2014 Requirements .....	37
3.4.1 Design of tension-compression bracing members .....	37
3.4.2 Design of brace-to-frame gusset plate connections .....	40
3.5 Design Criteria for MRFs According to CSA/S16 2014 Requirements .....	44
3.5.1 Design of MRF beams .....	45
3.5.2 Design of MRF columns .....	45
3.5.3 Design of beam-to-column joints and connections .....	47
3.6 Building Description .....	47
3.6.1 Design of MD-CBF office building using equivalent static force procedure ..	48
3.6.2 Design of MD-MRF office building using equivalent static force procedure .	52

3.6.3 Design of office building with Braced Dual System using equivalent static force procedure.....	55
3.7 Seismic Response of MD-CBF Building Based on Nonlinear Time-History Analysis .....	58
3.7.1 Modeling of MD-CBF building using OpenSees .....	58
3.7.2 Selection of ground motions .....	62
3.7.3 Seismic response of MD-CBF building subjected to crustal GMs from time history analysis.....	66
3.7.4 Seismic response of MD-CBF building subjected to subduction GMs from time history analysis.....	69
3.8 Seismic Response of MD-MRF Building Based on Nonlinear Time-History Analysis .....	71
3.8.1 Modeling of MD-MRF building using OpenSees .....	71
3.8.2 Selection of ground motions .....	74
3.8.3 Seismic response of MD-MRF building under crustal GMs from time history analysis.....	75
3.8.4 Seismic response of MD-MRF building under subduction GMs from time history analysis.....	77
3.9 Seismic Assessment of Braced Dual System 8-storey Office Building Based on Nonlinear Time-History Analysis.....	79
3.9.1 Modeling of Braced Dual System.....	80
3.9.2 Selection of ground motions .....	82
3.9.3 Seismic response of Braced Dual System building under crustal GMs from time history analysis.....	83
3.9.4 Seismic response of Braced Dual System building under subduction GMs from time history analysis .....	86
CHAPTER 4. SEISMIC RESPONSE OF STEEL BUILDINGS USING INCREMENTAL DYNAMIC ANALYSIS.....	89
4.1 Incremental Dynamic Analysis of the 8-storey MD-CBF Building.....	89
4.1.1 The IDA response of 8-st. MD-CBF Building under crustal GMs.....	90
4.1.2 The IDA response of 8-st. MD-CBF building under subduction GMs.....	94
4.2 Incremental Dynamic Analysis of the 8-storey MD-MRF Building .....	98
4.2.1 The IDA response of 8-st. MD-MRF building under crustal GMs.....	101

4.2.2 The IDA response of 8-st. MD-MRF building under subduction GMs.....	106
4.3 Incremental Dynamic Analysis of the 8-storey Building with Braced Dual System .....	113
4.3.1 The IDA Response of 8-st. building with Braced Dual System under crustal GMs .....	113
4.3.2 The IDA response of 8-st. building with Braced Dual System under subduction GMs.....	128
4.4 Discussion.....	148
4.4.1 Comparison of seismic responses between the MD-CBF and Braced Dual System.....	148
4.4.2 Issues on reaching convergence during nonlinear time history analysis .....	153
CHAPTER 5. COLLAPSE ASSESSMENT AND FRAGILITY ANALYSIS .....	155
5.1 Collapse Margin Ratio .....	155
5.2 Fragility Analysis.....	158
5.2.1 Performance limit states and damage levels .....	158
5.2.2 Calculation of fragility.....	160
5.2.3 Fragility of 8-storey MD-CBF building.....	161
5.2.4 Fragility of 8-storey MD-MRF building.....	163
5.2.5 Fragility of 8-storey building with Braced Dual System.....	165
5.3 Comparison of Fragility Curves.....	167
CHAPTER 6. CONCLUSIONS AND FUTURE WORK.....	169
6.1 Conclusions.....	169
6.2 Future Work .....	172
<i>REFERENCES</i> .....	174

## Table of Figures

Fig. 2.1 Evolution of seismic force resisting systems (FEMA 454, 2006).....	9
Fig. 2.2 San Jose federal building (FEMA 454, 2006).....	10
Fig. 2.3 Interstorey drift and residual interstorey drift ratio profiles along buildings height (Kiggins and Uang, 2006).....	11
Fig. 2.4 Median and 84th percentile of maximum story drift angle (Xie, 2008).....	11
Fig. 2.5 Model of HSS brace with end-connections: (a) Opensees model; (b) geometry of gusset plate (Tirca and Chen, 2014) .....	15
Fig. 2.6 The effect of out-of-straightness on the buckling strength of S1B specimen (Tirca and Chen, 2014).....	16
Fig. 2.7 The effect of modeling parameters on the hysteresis response of S1B specimen (a) types of fiber discretization technique; (b) number of elements, (c) fiber discretization cross-section (Tirca and Chen, 2014) .....	17
Fig. 2.8 Beam with hinges element with modified Gauss-Radau plastic hinge integration method (Bosco and Tirca, 2017 according to Scott and Fenves, 2006) .....	19
Fig. 2.9 Fiber-based cross-section and distribution of fatigue ductility coefficients (Bosco and Tirca, 2017).....	20
Fig. 2.10 Comparison between the experimental and numerical response with fatigue material (Bosco and Tirca, 2017).....	21
Fig. 2.11 Sensitivity analysis: (a) variation of number of segments within the flange, (b) variation of number of layers within the web, (c) variation of number of layers within the flange (Bosco and Tirca, 2017).....	23
Fig. 2.12 IDA curves of a $T_1=1.8$ s, 5-storey steel braced frame subjected to four different records (Vamvatsikos and Cornell, 2002) .....	26
Fig. 2.13 The 30 individual IDA curves of a 5-storey steel braced frame with $T_1 = 1.8$ s (Vamvatsikos and Cornell, 2002) .....	27
Fig. 2.14 IDA curves: (a) twenty IDA curves and the associated limit-state capacities, (b) the summary of the IDA curves and corresponding limit-state capacities into their 16%, 50%, and 84% fractiles (Vamvatsikos and Cornell, 2004).....	28
Fig. 3.1 Brace -to-frame connection and parameters considered.....	42
Fig. 3.2 Shear lag effects on slotted HSS brace ends (CSA/S16-14, 2014) .....	44
Fig. 3.3 Plan and elevation view of MD-CBF building.....	49

Fig. 3.4 Normalized base shear distribution of MD-CBF building from equivalent static method and response spectrum method .....	51
Fig. 3.5 Plan view of MD-MRF building .....	52
Fig. 3.6 Elevation view of MD-MRFs .....	52
Fig. 3.7 Normalized base shear distribution of MD-MRF building from equivalent static method and response spectrum method .....	54
Fig. 3.8 Plan view of building with Braced Dual System.....	55
Fig. 3.9 Normalized base shear distribution of Braced Dual System building from equivalent static method and response spectrum method .....	57
Fig. 3.10 Opensees model of the MD-CBF building: (a) model of $\frac{1}{4}$ building; (b) elevation of model studied when MD-CBF acts in N-S direction.....	59
Fig. 3.11 HSS cross section fiber discretization .....	60
Fig. 3.12 The HSS brace to frame connection model: (a) geometry, (b) nonlinear rotational spring model in the brace buckling plan .....	60
Fig. 3.13 W-shape cross section fiber discretization .....	61
Fig. 3.14 Response spectrum of scaled crustal GMs for 8-storey MD-CBF building.....	64
Fig. 3.15 Response spectrum of scaled subduction GMs for 8-storey MD-CBF building.....	64
Fig. 3.16 Nonlinear response of 8-storey MD-CBF building subjected to crustal GMs ..	66
Fig. 3.17 Hysteretic response of 6th floor HSS braces under GM #C8: (a) interstorey drift time history and accelerogram, (b) hysteresis loops of left and right HSS brace .....	67
Fig. 3.18 Hysteretic response of 8th floor braces under GM #C11: (a) interstorey drift time history and accelerogram, (b) hysteresis loops of left and right HSS brace .....	68
Fig. 3.19 Nonlinear seismic response of MD-CBF building subjected to subduction GMs .....	69
Fig. 3.20 Hysteretic response of 7th floor braces under GM #S4: (a) interstorey drift time history and accelerogram, (b) hysteresis loops of left and right HSS brace .....	70
Fig. 3.21 Opensees model of the MD-MRF building: (a) model plan; (b) model Elevation in N-S direction.....	72
Fig. 3.22 Fiber discretization of MRF beam cross section .....	73
Fig. 3.23 Response spectrum of scaled crustal GMs for 8-storey MD-MRF building.....	74
Fig. 3.24 Response spectrum of scaled subduction GMs for MD-MRF building .....	75
Fig. 3.25 Nonlinear response of 8-storey MD-MRF building subjected to crustal GMs ..	76

Fig. 3.26 Hysteretic behavior and DI of MD-MRF beam at 7th floor under GM #C8: (a) 7 <sup>th</sup> floor drift time history and accelerogram, (b) beam hysteresis loop and damage index ..	77
Fig. 3.27 Nonlinear response of MD-MRF building subjected to subduction GMs.....	78
Fig. 3.28 Hysteretic behavior and DI of MD-MRF beam at 8th floor under GM #S4: (a) 8 <sup>th</sup> floor drift time history and accelerogram, (b) beam hysteresis loop and damage index ..	79
Fig. 3.29 Opensees model of the Braced Dual System building: (a) model plan; (b) model elevation (N-S direction).....	81
Fig. 3.30 Response spectrum of scaled crustal GMs for 8-storey building with Braced Dual System.....	82
Fig. 3.31 Response spectrum of scaled subduction GMs for 8-storey building with Braced Dual System .....	83
Fig. 3.32 Nonlinear response of 8-st. building with Braced Dual System subjected to crustal GMs.....	83
Fig. 3.33 Hysteresis loops of HSS braces of the 8 <sup>th</sup> floor of Braced Dual System subjected to #C8.....	85
Fig. 3.34 Hysteresis loops of MRF beams of the 8 <sup>th</sup> floor of Braced Dual System subjected to #C8.....	85
Fig. 3.35 Nonlinear response of building with Braced Dual System subjected to subduction GMs.....	86
Fig. 3.36 Braced Dual System 7th floor HSS brace hysteretic behavior under MYG001	87
Fig. 3.37 Braced Dual System 8th floor MRF beam hysteretic behavior under #MYG001 .....	88
Fig. 4.1 The IDA curves of studied MD-CBF 8-storey building under crustal GMs.....	90
Fig. 4.2 The interstorey drift, residual interstorey drift and floor acceleration associated to the near-collapse limit state of 8-storey MD-CBF building under crustal ground motions .....	91
Fig. 4.3 Hysteretic response of 8 <sup>th</sup> floor HSS braces of MD-CBF building and their DI of critical fiber of HSS brace cross section under #1083-170 scaled to near-collapse limit state .....	92
Fig. 4.4 Outermost fibers of HSS brace cross section .....	93
Fig. 4.5 Seismic response of MD-CBF system under #1083-170 scaled to near-collapse limit state.....	93
Fig. 4.6 The 1 <sup>st</sup> floor axial force-bending moment interaction diagram under #1083-170 scaled to near-collapse limit state .....	94

Fig. 4.7 The IDA curves of 8-storey MD-CBF building under subduction GMs.....	95
Fig. 4.8 The interstorey drift, residual interstorey drift and floor acceleration associated to the near-collapse limit state of 8-storey MD-CBF building under subduction GMs.....	96
Fig. 4.9 Hysteretic response of 7th floor HSS braces of MD-CBF building under #TCG009 record scaled to near-collapse limit state and the damage index of critical fiber of HSS cross-section.....	97
Fig. 4.10 IDA curve of MD-MRF building under #1052-090.....	100
Fig. 4.11 Truncated IDA curves of 8-storey MD-MRF building under crustal GMs.....	101
Fig. 4.12 Interstorey drift, residual interstorey drift and floor acceleration of 8-storey MD-MRF building associated to $DI_{80\%}$ damage limit state under crustal ground motions....	102
Fig. 4.13 Hysteretic response of 4 <sup>th</sup> floor beam of 8-storey MD-MRF building under #1086-090 scaled to reach $DI_{80\%}$ .....	103
Fig. 4.14 Deflected shape of MD-MRF building under #1086-090 scaled to reach $DI_{80\%}$ damage state and the maximum damage index at each floor.....	103
Fig. 4.15 The moment-rotation hysteresis loops of beam's plastic hinge at each floor corresponding to $DI_{80\%}$ damage state.....	104
Fig. 4.16 The axial compression force vs. bending moment interaction diagram recorded at the bottom cross section of MD-MRF columns of 1 <sup>st</sup> and 4 <sup>th</sup> storey under #1086-090 scaled to $DI_{80\%}$ damage state.....	105
Fig. 4.17 Truncated IDA curves of 8-storey MD-MRF building under subduction GMs.....	106
Fig. 4.18 Deflected shape of MD-MRF building under # MYG001 scaled to reach $DI_{80\%}$ damage state and the maximum damage index at each floor.....	107
Fig. 4.19 Hysteretic response of 8 <sup>th</sup> floor side beam of 8-storey MD-MRF building under #MYG001 scaled to $DI_{80\%}$ damage state .....	107
Fig. 4.20 Interstorey drift, residual interstorey drift and floor acceleration of 8-storey MD-MRF building associated to $DI_{80\%}$ damage state under subduction GMs.....	108
Fig. 4.21 IDA curve of MD-MRF building under GMs: (a) #MYG001 and (b) #FKS005.....	109
Fig. 4.22 Seismic response of MD-MRF building under #FKS005 scaled to reach $DI_{80\%}$ damage state.....	110
Fig. 4.23 Hysteretic response of 8th floor beam of MD-MRF building under #FKS005 scaled to $DI_{80\%}$ damage state.....	110

Fig. 4.24 The moment-rotation hysteresis loops of beam's plastic hinges at each floor under #FKS005 corresponding to $DI_{80\%}$ damage state .....	111
Fig. 4.25 The axial compression force vs. bending moment interaction diagram recorded at bottom column cross section of 1 <sup>st</sup> and 8 <sup>th</sup> floor under #FKS005 scaled to $DI_{80\%}$ damage state .....	112
Fig. 4.26 IDA curves of Braced Dual System building vs. CBF building under crustal GMs: (a) #802-90, (b) #983-022.....	113
Fig. 4.27 Comparison of seismic response between MD-CBF system and Braced Dual System under #802-90 scaled to $ST1 = 0.8g$ : a) MD-CBF; b) Braced Dual System....	114
Fig. 4.28 Seismic response of Braced Dual System under #802-90 scaled to $S(T_1) = 1.0g$ .....	115
Fig. 4.29 Hysteretic behavior of critical HSS braces, the associated MRF beam and the strain time history and damage of the outermost fibers of HSS brace cross sections of Dual system under #802-90 scaled to $S(T_1) = 1.0g$ : (a) hysteretic response of HSS brace and MRF beam; (b) strain history and damage of outermost fibers of HSS braces .....	116
Fig. 4.30 Seismic response of Braced Dual System under #802-90 scaled to near-collapse limit state ( $S(T_1) = 1.1g$ ) .....	117
Fig. 4.31 Hysteretic behavior of critical HSS braces, the associated MRF beam and the strain time history and damage of the outermost fibers of HSS brace cross sections of Dual system under #802-90 scaled to $S(T_1) = 1.1g$ : (a) hysteretic response of HSS brace and MRF beam; (b) strain history and damage of outermost fibers of HSS braces .....	118
Fig. 4.32 The 1 <sup>st</sup> floor axial compression force-bending moment interaction diagram under #802-90 scaled to 1.1g (near-collapse limit state) .....	119
Fig. 4.33 Time-history response of Braced Dual System members under #802-90 scaled to 1.1g (near-collapse limit state).....	120
Fig. 4.34 IDA curve of Braced Dual System vs. MD-CBF system of 8-storey building under #787-270 .....	121
Fig. 4.35 Comparison of seismic response between MD-CBF system and Braced Dual System under #787-270 scaled to $ST1 = 1.1g$ : (a) MD-CBF; (b) Braced Dual System	122
Fig. 4.36 Seismic response of Braced Dual System under #787-270 scaled to 1.7g.....	122
Fig. 4.37 Hysteretic behavior of critical HSS braces, the associated MRF beam and the strain time history and damage of the outermost fibers of HSS brace cross sections of Dual system under #787-270 scaled to $S(T_1) = 1.7g$ : (a) hysteretic response of HSS brace and MRF beam; (b) strain history and damage of outermost fibers of HSS braces .....	123

Fig. 4.38 Seismic response of Braced Dual System under #787-270 scaled to 1.8g (near-collapse limit state) .....	124
Fig. 4.39 Hysteretic behavior of critical HSS braces, the associated MRF beam and the strain time history and damage of the outermost fibers of HSS brace cross sections of Dual system under #787-270 scaled to $S(T_1) = 1.8g$ : (a) hysteretic response of HSS brace and MRF beam; (b) strain history and damage of outermost fibers of HSS braces .....	125
Fig. 4.40 The 1 <sup>st</sup> floor axial force-bending moment interaction diagram under #787-270 scaled to 1.8g (near-collapse limit state).....	126
Fig. 4.41 IDA curves of studied 8-storey building with Braced Dual System under 11 crustal GMs.....	127
Fig. 4.42 Near collapse response of building with Braced Dual System under crustal GMs .....	128
Fig. 4.43 IDA curve of 8-storey building with Braced Dual System vs. MD-CBF system under #IBR006.....	129
Fig. 4.44 Comparison of seismic response between MD-CBF system and Braced Dual System under #IBR006 scaled to $ST1 = 0.7g$ : (a) MD-CBF; (b) Braced Dual System	130
Fig. 4.45 Seismic response of 8-st. Braced Dual System under #IBR006 scaled to 1.1g .....	130
Fig. 4.46 Hysteretic behavior of critical HSS braces, the associated MRF beam and the time history of strain and damage of the outermost fibers of HSS brace cross sections of Braced Dual System under #IBR006 scaled to $S(T_1) = 1.1g$ : (a) hysteretic response of HSS brace and MRF beam; (b) strain history and damage of outermost fibers of HSS braces .....	131
Fig. 4.47 Seismic response of Braced Dual System under #IBR006 scaled to near-collapse limit state.....	132
Fig. 4.48 Hysteretic behavior of critical HSS braces, the associated MRF beam and the strain time history and damage of the outermost fibers of HSS brace cross sections of Braced Dual System under #IBR006 scaled to $S(T_1) = 1.2g$ : (a) hysteretic response of HSS brace and MRF beam; (b) strain history and damage of outermost fibers of HSS braces .....	133
Fig. 4.49 The 1 <sup>st</sup> floor axial force-bending moment interaction diagram under #IBR006 scaled to 1.2g (near-collapse limit state).....	134
Fig. 4.50 The 7 <sup>th</sup> floor axial force-bending moment interaction diagram under #IBR006 scaled to 1.2g (near-collapse limit state).....	134
Fig. 4.51 IDA curve of 8-storey building with Braced Dual System vs. MD-CBF system under #MYG004 .....	135

Fig. 4.52 Comparison of seismic response between MD-CBF system and Braced Dual System under #MYG004 scaled to $ST1 = 0.5g$ : (a) MD-CBF; (b) Braced Dual System .....	136
Fig. 4.53 Seismic response of 8-st. Braced Dual System under #MYG004 scaled to $0.7g$ .....	136
Fig. 4.54 Hysteretic behavior of critical HSS braces, the associated MRF beam and the strain time history and damage of the outermost fibers of HSS brace cross sections of Braced Dual System under #MYG004 scaled to $S(T_1) = 0.7g$ : (a) hysteretic response of HSS brace and MRF beam; (b) strain history and damage of outermost fibers of HSS braces .....	137
Fig. 4.55 Seismic response of 8-storey Dual system under #MYG004 scaled to $0.8g$ (near-collapse limit state) .....	138
Fig. 4.56 Hysteretic behavior of critical HSS braces, the associated MRF beam and the strain time history and damage of the outermost fibers of brace cross sections of Braced Dual System under #MYG004 scaled to $S(T_1) = 0.8g$ : (a) hysteretic response of HSS brace and MRF beam; (b) strain history and damage of outermost fibers of HSS braces .....	139
Fig. 4.57 The 1 <sup>st</sup> floor axial load-bending moment interaction diagram under #MYG004 scaled to $0.8g$ (near-collapse limit state).....	140
Fig. 4.58 IDA curve of 8-storey building with Braced Dual System vs. MD-CBF system under #IBR004.....	141
Fig. 4.59 Comparison of seismic response between MD-CBF system and Dual system under #IBR004 scaled to $STa = 0.6g$ : (a) MD-CBF; (b) Braced Dual System .....	141
Fig. 4.60 Seismic response of 8-st. Braced Dual System under #IBR004 scaled to $0.7g$ .....	142
Fig. 4.61 Hysteretic behavior of critical HSS braces, the associated MRF beam and the strain time history and damage of the outermost fibers of brace cross sections of Braced Dual System under #IBR004 scaled to $S(T_1) = 0.7g$ : (a) hysteretic response of HSS brace and MRF beam; (b) strain history and damage of outermost fibers of HSS braces .....	143
Fig. 4.62 Seismic response of 8-storey Braced Dual System under #IBR004 scaled to $0.8g$ (near-collapse limit state).....	143
Fig. 4.63 Hysteretic behavior of critical HSS braces, the associated MRF beam and the strain time history and damage of the outermost fibers of brace cross sections of Braced Dual System under #IBR004 scaled to $S(T_1) = 0.8g$ : (a) hysteretic response of HSS brace and MRF beam; (b) strain history and damage of outermost fibers of HSS braces .....	145
Fig. 4.64 The 1 <sup>st</sup> floor axial force-bending moment interaction diagram under #IBR004 scaled to $0.8g$ (near-collapse limit state).....	146

Fig. 4.65 IDA curves of 8-storey Braced Dual System building under subduction GMs .....	146
Fig. 4.66 Seismic response of 8-storey building with Braced Dual System under subduction GMs at near-collapse limit state .....	147
Fig. 4.67 Comparison of seismic responses of 8-storey MD-CBF vs. 8-storey Braced Dual System under 11 crustal GMs scaled to near-collapse limit state: (a) MD-CBF building; (b) Braced Dual System building .....	150
Fig. 4.68 Comparison of seismic responses of 8-storey MD-CBF vs. 8-storey Braced Dual System under 11 subduction GMs scaled to near-collapse limit state: (a) MD-CBF building; (b) Braced Dual System building.....	151
Fig. 4.69 Comparison of 50 <sup>th</sup> percentile IDA curve among studied buildings subjected to: (a) crustal ground motions, (b) subduction ground motions.....	152
Fig. 5.1 Mapping damage control against building performance levels according to ASCE/SEI 41 (Tirca et al., 2014) .....	159
Fig. 5.2 Structural performance levels and damage for steel MRF as per ASCE/SEI 41 .....	160
Fig. 5.3 Seismic demand for selected damage levels and fragility curves of 8-Storey MD-CBF building under Crustal GMs .....	162
Fig. 5.4 Seismic demand for selected damage levels and fragility curves of 8-Storey MD-CBF building under subduction GMs .....	163
Fig. 5.5 Seismic demand for selected damage levels and fragility curves of 8-Storey MD-MRF building under crustal GMs .....	164
Fig. 5.6 Seismic demand for selected damage levels and fragility curves of 8-Storey MD-CBF building under subduction GMs.....	165
Fig. 5.7 Seismic demand for selected damage levels and fragility curves of 8-Storey building with Braced Dual System under crustal GMs .....	166
Fig. 5.8 Seismic demand for selected damage levels and fragility curves of 8-Storey building with Braced Dual System under subduction GMs.....	167
Fig. 5.9 Comparison of fragility curves of 8-storey building with different SFRSs at SD state under: (a) crustal GMs; (b) subduction GMs.....	167

## List of Tables

Table 2.1 Drift angle, $DI(80\%)$ , plastic rotations and $\epsilon/\epsilon_y$ Ratio associated to $DI(80\%)_{prop}$ , margin safety and plastic rotation associated to beam failure (Bosco and Tirca, 2017).....	24
Table 3.1 Acceleration response spectra ordinates for site Class C in Vancouver.....	33
Table 3.2 Design of gravity frames.....	48
Table 3.3 Design summary of MD-CBF located on N-S direction .....	50
Table 3.4 Characteristics of MD-CBF building from equivalent static method and response spectrum method.....	50
Table 3.5 Design summary of HSS brace to frame gusset plate connections.....	51
Table 3.6 Characteristics of MD-MRF building from equivalent static method and response spectrum method.....	53
Table 3.7 Design summary of MD-MRFs in N-S and E-W direction .....	54
Table 3.8 Design MRF cross sections of building as a backup frame of the dual system	56
Table 3.9 Characteristics of MD-MRF building from equivalent static method and response spectrum method.....	57
Table 3.10 Vibration periods of MD-CBF building in ETABS and OpenSees (N-S).....	62
Table 3.11 Seismic characteristics of crustal ground motions selected.....	63
Table 3.12 Seismic characteristics of selected subduction GM records.....	65
Table 3.13 Vibration periods of MD-MRF 8-st. building in ETABS and OpenSees (N-S) .....	74
Table 3.14 Vibration periods of building with Braced Dual System (N-S).....	82
Table 5.1 Collapse margin ratio (CMR) derived from IDA curves.....	155
Table 5.2 Selection of SSF according to FEMA P695 .....	156
Table 5.3 Spectral shape factor (SSF) for studied buildings .....	156
Table 5.4 Evaluation of collapse safety according to FEMA P695 methodology.....	158

## List of Symbols

$A$	gross area
$A_f$	area of flange
$A_m$	shear area of effective fusion face
$A_w$	area of effective weld throat
$ACMR$	adjusted collapse margin ratio
$C_f$	compressive force in a member or component under factored load
$C_r$	factored compressive resistance of a member or component
$C_u$	probable compressive resistance of a member
$C'_u$	post-buckling probable compressive resistance of bracing members
$C_w$	warping torsional constant
$CMR$	collapse margin ratio
$CP$	collapse prevention performance level
$D_w$	fillet weld size
$DI$	damage index
$DM$	damage measure
$E$	modulus of elasticity
$EDP$	engineering demand parameters
$F_u$	ultimate stress of steel material
$F_y$	yield stress
$G$	shear modulus of steel material
$GM$	ground motion
$I_E$	earthquake importance factor of the structure
$IM$	intensity measure
IO	immediate occupancy performance level
$I_x, I_y$	moment of inertia about x-x, y-y
$J$	torsion constant
$K$	effective length factor

$K_{gusset}$	out-of-plane flexural stiffness of the gusset plate
$KL$	effective length
$L_p$	length of plastic hinge
$L_v$	shear length
$LS$	life safety performance level
$M_{pb}$	reduced plastic moment of the brace
$M'_{rc}$	nominal flexural resistance of MRF columns
$M_u$	critical elastic moment of the unbraced segment
$M_v$	higher mode factor
$N_f(\varepsilon_i)$	number of cycles the material can sustain at strain level $\varepsilon_i$
$P_b$	compression force
$PGA$	peak ground acceleration
$PGV$	peak ground velocity
$R$	a parameter that defines the shape of the unload curve
$R_d$	ductility related factor
$R_o$	over strength related factor
$S_a$	pseudo acceleration
$SSF$	spectral shape factor
$T_a$	fundamental period of structure
$T_u$	probable tensile resistance of a member
$U$	factor account for shear lag effect
$V$	design base shear
$W$	building weight
$W_w$	Whitmore width
$X_u$	electrode ultimate tensile strength
$Z$	section modulus
$m_R$	median capacity
$t_g$	thickness of the gusset plate
$\beta$	standard deviation of $\ln(IM)$

$\beta_C$	uncertainty in capacity
$\beta_{D S_a}$	seismic demand uncertainty
$\beta_R$	logarithmic standard deviation
$\beta_{RR}$	aleatoric uncertainty
$\beta_{RU}$	epistemic uncertainty
$\beta_{RTR}$	record-to-record uncertainty
$\beta_{DR}$	design requirements uncertainty
$\beta_{TR}$	test data uncertainty
$\beta_{MDL}$	modeling uncertainty
$\beta_{TOT}$	total uncertainty
$\varepsilon^*$	effective strain depending on the unload/reload interval
$\varepsilon_0$	fatigue ductility coefficient
$\varepsilon_i$	number of cycles when strain $\varepsilon_i$ is reached
$\theta$	median of the fragility function
$\theta_{max}$	maximum drift angle
$\lambda_f$	slenderness ratio of flange
$\lambda_w$	slenderness of the beam web
$\sigma^*$	effective stress depending on the unload/reload interval
$\Phi()$	standard normal cumulative distribution function
$\Phi[]$	standard normal probability integral
$b$	ratio of the final to initial tangent stiffness
$l, L$	length
$m$	fatigue ductility exponent
$r$	radius of gyration
$t$	thickness
$w$	width; web thickness
$\xi$	damping ratio
$\phi$	resistance factor for steel
$\phi M_{pc}$	nominal plastic moment resistance

# CHAPTER 1. INTRODUCTION

## 1.1 General

The traditional Concentrically Braced Frame (CBF) and Steel Moment Resisting Frame (MRF) are widely used as lateral force resisting systems. The CBF possesses high lateral stiffness, while the MRF is featured with high ductility. However, both systems have their drawbacks. In general, the CBF is governed by low plastic redistribution capacity after a brace is in the verge of fracture failure, which leads to concentration of plastic deformation within a few storeys. Conversely, the MRF is believed to be the most ductile system being able to dissipate large amounts of energy by flexural yielding of beams ends, however, the MRF usually could not provide sufficient lateral stiffness to fulfill the serviceability requirements.

Analysing the effect of earthquakes on buildings, it was found that the traditional seismic force resisting systems are prone to weak-storey mechanism and susceptible to long-duration earthquakes. To overpass this drawback, the concept proposed utilizing multiple-resisting structural systems that act progressively so that the overall seismic resistance is not significantly reduced during the earthquake (FEMA454, 2006).

To mitigate the weak-storey mechanism, several significant solutions have been developed. Among them, there is the dual-system concept which is able to provide stable hysteresis behavior, typical for rigid braced frame, while the moment frame acts as a backup system to maintain good flexural behavior. Dual structural systems provide structural redundancy required to resist large earthquakes and to assure a secure load path.

On the other hand, the west coast of Canada exhibits three types of seismic hazards that cause significant seismic activity. The Cascadia subduction zone, formed due to the Juan de Fuca plate converging with and subducting (sliding) beneath the North American plate, can produce powerful mega-thrust earthquakes that could affect a wide geographic area and could generate tsunamis (IBC, 2013). Thus, the building stock in Vancouver, B.C. is susceptible to crustal, subduction intra-slab, and the mega-thrust subduction inter-slab earthquakes.

In the past, a few researchers (Jain et al., 1993; Khatib et al., 1988) demonstrated that the interaction between CBF and MRF is beneficial to seismic response of structure. In the ASCE/SEI 7-10 standard, it is recommended to consider the MRF of the dual system as a backup system, designed to resist 25% of the design base shear of the CBF.

In the current NBCC code provision, no guideline is provided for dual system. However, in the CSA/S16 provisions, it is noticed that for type D steel plate walls, the infill plate shall be designed to resist 100% of the applied factored storey shear force, and “beams at every storey shall have sufficient flexural resistance such that at least 25% of the applied factored storey shear force is resisted by beams and columns forming a moment-resisting frame”. This idea complies with the design concept of dual systems described in ASCE code provision.

Even though these code provisions have similar specifications for designing the Dual Systems, no detailed research was done to study the nonlinear seismic response and failure modes investigation of such system (e.g. moderately ductile CBF+MRF). Also, the contribution of the backup MRF to the seismic resistance of the entire system is unclear.

## 1.2 Objective and Scope

The objectives of this research are:

- To develop a numerical model of steel Braced Dual Frame able to show accurate nonlinear behavior from yielding to failure including the low-cycle fatigue fracture of braces and flexural yielding of MRF's beams.
- To assess the seismic performance of Braces Dual System versus the traditional MD-CBF and MD-MRF system when subjected to crustal and subduction ground motions using nonlinear time history analysis and incremental dynamic analysis.
- To identify the failure mechanisms of Braces Dual System versus the MD-CBF system employed in middle-rise building applications when subjected to crustal and subduction ground motions.
- To assess the probability of exceedance of different damage states by fragility analysis and the collapse safety of these three seismic force resisting systems, as well as the effect of long-duration subduction earthquakes on these buildings.

## 1.3 Description of Methodology

To achieve the above objectives, the study contains the following parts:

- Three prototype buildings with Braces Dual System, traditional MD-CBF system, and traditional MD-MRF system were designed according to NBCC 2015 code provisions and CSA/S16 (2014) standard. Numerical nonlinear models were developed in the OpenSees framework using similar computation algorithm as used by Uriz (2005).

- To account for seismic actions on middle-rise steel buildings located on firm soil in Vancouver, B.C., two suites of ground motions compatible with seismic intensity and source distance were selected and scaled according to the NBCC 2015 requirements. Thus, 11 crustal ground motions were selected from California earthquake records and 11 subduction ground motions were mostly selected from the mega-thrust magnitude 9 Tohoku earthquake in Japan (March 11, 2011) which is the proxy event.
- The nonlinear seismic response of these three prototype 8-storey office buildings is obtained from nonlinear time history analysis considering the 22 selected ground motions. To analyse the seismic response at the code demand level, the investigated parameters are: the interstorey drift, residual interstorey drift and floor acceleration.
- To identify the failure mechanism of these structural systems, the incremental dynamic analysis was performed, and the IDA curves were computed from yielding to failure for each individual ground motions.
- Seismic performance through nonlinear collapse simulations of all three prototype buildings was assessed according to FEMA P695 (2009) procedure. Fragility analysis was performed to assess the probability of these prototype buildings to exceed the defined limit states specified in ASCE/SEI 41 (2013).

## **1.4 Thesis Organization**

This thesis contains six chapters:

- Chapter 1 includes the introduction, objectives, and methodology.

- Chapter 2 contains the literature review conducted on steel dual systems, and numerical modeling techniques applied to simulate the seismic response of MD-CBF and MD-MRF structural systems using the finite element software OpenSees. The detailed procedure of Incremental dynamic analysis is presented and a methodology for deriving fragility curves based on results from Incremental dynamic analysis considering uncertainties is introduced.

Chapter 3 describes the design requirements specified in NBCC 2015 and CSA/S16 (2014) standard for traditional earthquake resistant systems. Based on these requirements the 8-storey MD-CBF system, 8-storey MD-MRF system and the 8-storey Braces Dual System were designed to resist seismic loads and were checked to respond in elastic range under wind loads. The selection and scaling methodology applied to ground motions is illustrated. Detailed numerical models for these structural systems were developed in OpenSees. Seismic performance of these three prototype buildings is assessed by nonlinear time history analysis conducted at the design level with a 2% probability of exceedance in 50 years.

- Chapter 4 presents the results from incremental dynamic analysis conducted on these prototype buildings, as well as, illustrates the types of failure mechanisms identified for each system under the selected accelerograms.
- Chapter 5 covers the Fragility analysis of these three structural systems by using data collected from IDA curves. Both epistemic and aleatoric uncertainties were considered. In addition, the collapse margin safety was computed for these three prototype buildings using the FEMA P695 (2009) procedure, as well as, the effect

of long-duration subduction earthquake on the response of these building structures is discussed.

- Chapter 6 concludes the research. Proposals for future work are made.

## CHAPTER 2. LITERATURE REVIEW

This Chapter reports on the literature review of previous studies on the seismic behaviour of dual systems versus the seismic behaviour of steel Concentrically Braced Frames (CBF) and steel Moment Resisting Frames (MRF). Detailed modeling concepts of these steel frames using the OpenSees framework are discussed. In addition, some guidelines regarding seismic performance assessment including fragility assessment are also reviewed.

### 2.1 Past Studies on Dual Systems

Steel Concentrically Braced Frames (CBF) are characterised by high lateral stiffness and low-to-medium ductility. However, due to their reduced plastic redistribution capacity, the plastic deformation always concentrates within one or a few stories leading to weak-storey mechanism. Among steel frames, the MRFs are characterised by high ductility and low lateral stiffness. It was found that these traditional systems employed in multi-storey buildings taller than 10 storeys are susceptible to damage when subjected to long-duration subduction earthquakes as those expected across the Cascadia subduction fault (Tirca et al., 2015, Bosco and Tirca, 2018). To mitigate the weak-storey seismic response of CBF systems, researchers proposed the Braced Dual structural system that account on the elastic frame action of MRFs.

The *Dual system of ductile moment-resisting space frame and ductile flexural walls* dated since 1970 (NBCC, 1970). The ductile flexural wall was defined as a ductile flexural member cantilevering from the foundation consisting of a ductile reinforced concrete wall and the ductile moment-resisting frame was designed to resist at least 25% of total base shear. In the 1975 edition of NBCC it was introduced the *Dual system* consisting of a

ductile moment-resisting space frame and ductile flexural walls or steel bracing designed as follows: moment-resisting frame must be designed to resist at least 25% of total base shear and walls or bracing must be designed to resist 100% of base shear. The same recommendations for Dual structural system is provided in the 1980 and 1985 edition of NBCC. However, in the 1985 edition it is noted that the ductile moment-resisting frame shall have the capacity to resist not less than 25% of base shear but in no case shall the ductile moment-resisting frame have a lower capacity than that required in accordance with the relative rigidities. Since the ductility related force modification factor,  $R$ , was introduced in the 1990 edition of NBCC, each lateral force resisting system is individually characterised and the Dual structural system is no longer defined or mentioned until recently. In the Clause 4.1.8.9(3) of NBCC 2015, it is noted that for a Dual structural system comprising a moment-resisting frame and a shear wall or braced frame, the lowest value of the product  $R_d R_o$  be used, where  $R_d$  and  $R_o$  are the ductility related-force modification factor and the overstrength related-force modification factor, respectively. The purpose of this Clause is to ensure that the lateral earthquake design force,  $V$ , is based on the seismic force resisting system with the lower value of  $R_d R_o$  which results in a higher value of  $V$ . Thus, the response of the Dual system is governed by its part which has the lower ductility capacity and overstrength.

In the same Clause of NBCC 2015, it is also noted that the Dual structural system should be designed so that 100% of the seismic load is carried by the system having the higher value of  $R_d R_o$ . If this design approach is followed, the other system, which is now not considered to be part of the seismic force resisting system (SFRS), must be designed to

retain its own functionality meaning it should support its gravity loads while undergoing earthquake-induced deformations.

In the case that both SFRSs of Dual structural system participate to share the seismic force, both SFRSs must be proportioned in accordance with their relative stiffnesses using the principles of structural mechanics. For Dual system consisting of SFRSs with different values of  $R_d$ , it is important to ensure that the less ductile SFRS can sustain displacements associated with the more ductile SFRS without losing its strength. In the case that structural elements are common to both SFRSs, the detailing of these elements must meet the requirements for the more ductile of the two systems.

The evolution of seismic force resisting systems is presented in FEMA 454 (2006) and illustrated in Fig. 2.1. It is noted that Dual systems were applied in many practical cases

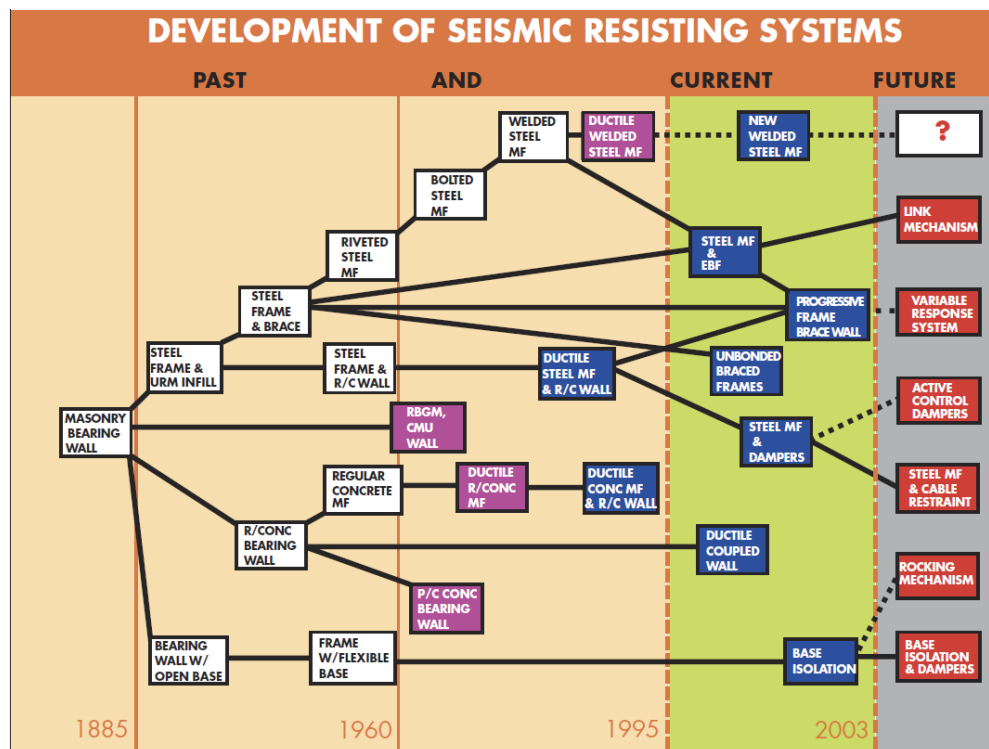


Fig. 2.1 Evolution of seismic force resisting systems (FEMA 454, 2006)

and buildings designed with Dual systems showed good seismic performance. For example, the San Jose Federal Building shown in Fig. 2.2, was built in 1983 using steel eccentrically braced frames (EBF) with backup moment-resisting frames to achieve economy and reliable seismic performance. As indicated in FEMA 454 (2006), this building has experience three moderate to strong earthquakes without exhibited structural damage.

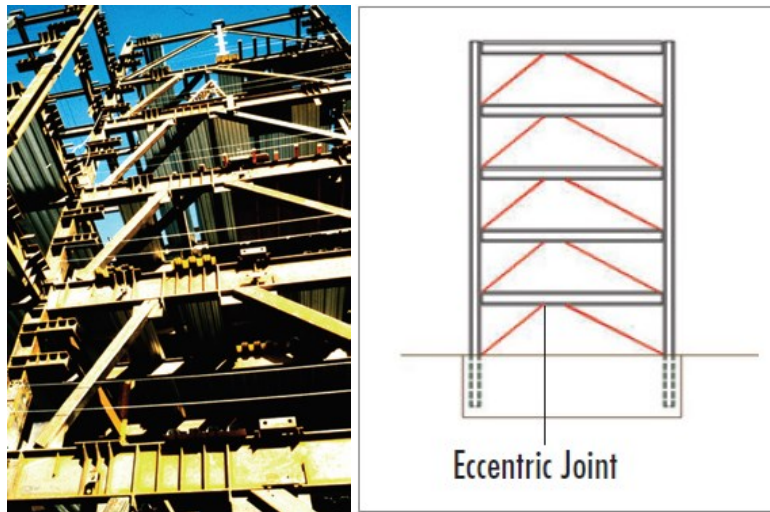


Fig. 2.2 San Jose federal building (FEMA 454, 2006)

In the last decade, researchers studied the effects of the backup moment resisting frame added in parallel to a steel braced frame system. Thus, Kiggins and Uang (2006) conducted a comparative study between the seismic behavior of a bare buckling-restrained braced frame (BRB) and a Dual system composed of a BRB frame and a backup MRF frame using a 3-story and a 6-story building. Employing nonlinear dynamic time history analysis using 6 ground motions, they concluded that the Dual system shows a reduced maximum interstorey drift and a significantly lower residual interstorey drift as shown in Fig. 2.3.

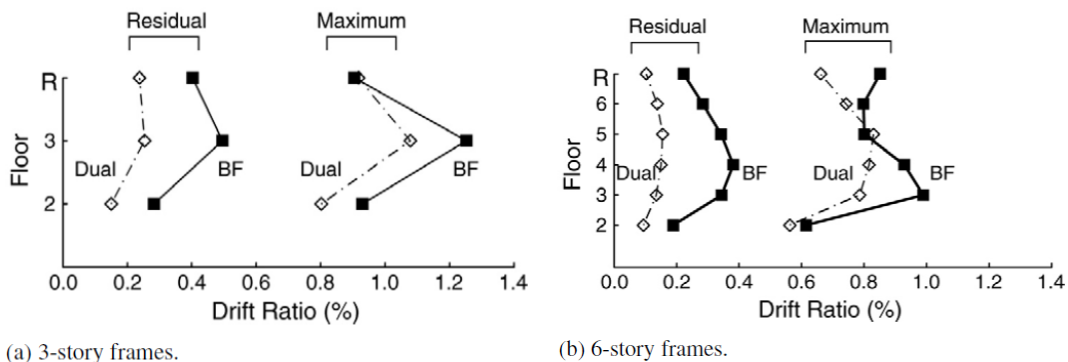


Fig. 2.3 Interstorey drift and residual interstorey drift ratio profiles along buildings height (Kiggins and Uang, 2006)

Xie (2008) studied the seismic response of BRB-MRF system with various stiffness ratios assigned to the backup MRF. Nonlinear time history analysis was performed on two 4-storey and 12-storey prototype buildings using 6 ground motions. It was concluded that using 20% stiffness ratios for the backup moment resisting frame it can reduce the maximum interstorey drift. The results are illustrated in Fig. 2.4.

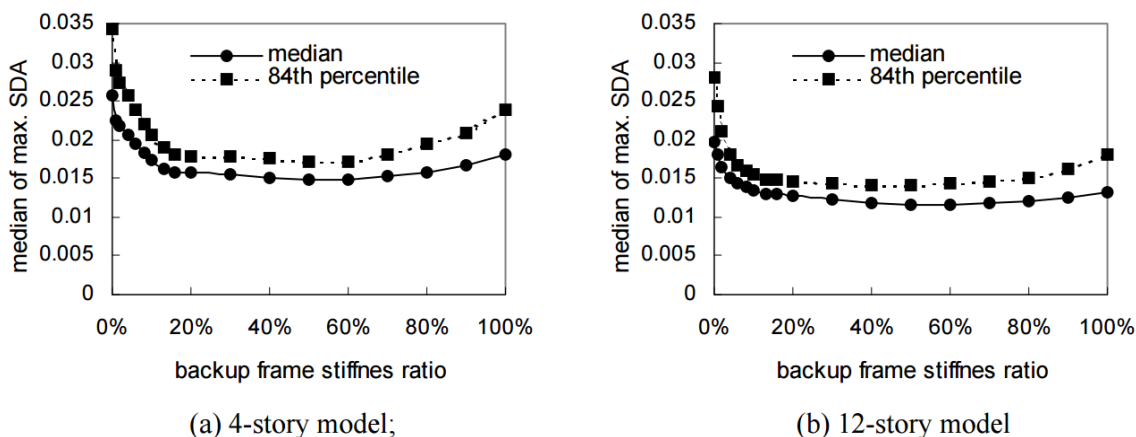


Fig. 2.4 Median and 84th percentile of maximum story drift angle (Xie, 2008)

Moreover, several researchers from Europe studied the seismic response of Braced Dual System (Bosco et al., 2012; Giugliano et al., 2010; Longo et al., 2014, 2016; etc.) and Dual EBF-MRF system (Nastri et al., 2015; Montuori et al., 2016; etc.). Design requirements

for Dual systems are also covered in ASCE/SEI 7-10. The MRFs belonging to the Dual system were conceived as backup frames to the braced frames and thus were intended to provide strength and stiffness to prevent the collapse of the structure in the occurrence of an intense and rare ground motion (AISC, 2005). To this belief, in the ASCE/SEI 7-10 code, it is specified in section 12.2.5.1 that “For a dual system, the moment frames shall be capable of resisting at least 25% of the design seismic forces”.

As aforementioned there are not detailed studied on the seismic response of Dual Steel Frame systems and no studies were conducted to analyse the seismic response of this structural system to long-duration subduction ground motions.

## **2.2 The Open System for Earthquake Engineering Simulation**

To investigate the seismic performance of structures, accurate numerical models are essentially required. The Open System for Earthquake Engineering Simulation, known as OpenSees, is an open source software framework developed at University of California at Berkeley (2004). OpenSees is primarily written in C++ with several Fortran numerical libraries and it allows users creating programs/applications with scripts in Tcl language. It is widely used by researchers to simulate the seismic response of multi-storey structures and geotechnical system, while being more computationally efficient than other finite element computer programs when performing time-history dynamic analysis.

The detailed modeling concepts for simulating the seismic response of CBFs and MRFs structural systems using OpenSees are discussed below.

### 2.3 Modeling of Concentrically Braced Frame using OpenSees

The CBF systems dissipate energy through buckling and yielding of brace members while keeping the remaining of the structural members in the elastic range.

Uriz (2005) proposed the first brace fracture model in OpenSees framework. A simplified rainflow cyclic counting algorithm was employed to account for the accumulated damage. The model considers constant plastic strain amplitude of low-cycle fatigue and damage is considered based on the accumulative strain using Miner's rule:

$$DI = \sum_{j=1}^n \left( \frac{n(\varepsilon_i)}{N_f(\varepsilon_i)} \right)^j \quad (2.1)$$

where  $n(\varepsilon_i)$  is the number of cycles when strain  $\varepsilon_i$  is reached and the  $N_f(\varepsilon_i)$  is the number of cycles the material can sustain at strain level  $\varepsilon_i$ .

The plastic strain amplitude  $\varepsilon_i$  and the number of cycles to failure  $N_f(\varepsilon_i)$  follows the equation below which is in accordance with a low-cycle fatigue relationship proposed by Mason (1965) and Coffin (1954) independently:

$$\varepsilon_i = \varepsilon_0 (N_f)^m \quad (2.2)$$

where  $\varepsilon_0$  is the fatigue ductility coefficient and  $m$  is the fatigue ductility exponent. The stress and stiffness of a fiber becomes zero, when its fatigue life is reached ( $DI > 1$ ).

Considering the experimental test performed by Yang (2005), for all brace sizes, Uriz (2005) proposed constant values for parameters:  $\varepsilon_0 = 0.095$  and  $m = -0.5$ . Later on, Santagati et al. (2012) and Salawdeh and Goggins (2013) conducted research using 32 hollow structural section (HSS) specimens and 28 HSS specimens, respectively. The following sets of parameter values were recommended:  $\varepsilon_0 = 0.07$  and  $m = -0.45$

(Santagati et al., 2012) and  $\varepsilon_0 = 0.19$  and  $m = -0.5$  (Salawdeh and Goggins, 2013). As resulted, the larger recommended  $\varepsilon_0$  value of 0.19 is more than twice of the smaller one (0.07). Moreover, it was found that the number of life cycles experienced by the model is different from the physical brace test when different low-cycle fatigue parameters are used. In order to overpass this deficiency, Lignos and Karamanci (2013) proposed an empirical regression equation to predict the  $\varepsilon_0$  value for HSS braces at the onset of fracture:

$$\varepsilon_{0,pred} = 0.291 \left(\frac{kL}{r}\right)^{-0.484} \left(\frac{w}{t}\right)^{-0.613} \left(\frac{E}{F_y}\right)^{0.3} \quad (2.3)$$

The equation was validated for HSS braces with slenderness ratio between 27 and 85. By using  $m = -0.3$  and  $\varepsilon_{0,pred}$ , the predicted and calibrated  $\varepsilon_0$  match very well, while the value of  $\varepsilon_0$  varies between 0.05 and 0.10 with an average of 0.064.

Tirca and Chen (2014) proposed the following equation for predicting the failure strain of square HSS braces for a single reversal  $\varepsilon_{0,pred}$  considering slenderness ratio between 50 and 150:

$$\varepsilon_{0,pred} = 0.006 \left(\frac{kL}{r}\right)^{0.859} \left(\frac{w}{t}\right)^{-0.6} \left(\frac{E}{F_y}\right)^{0.1} \quad (2.4)$$

Tirca and Chen (2014) validated the numerical model of HSS brace developed in OpenSees framework using 14 HSS brace specimens with slenderness ratio between 52.4 and 143.5 found in the literature. In selected experimental tests, braces buckled out-of-plane and reached fracture failure.

The effect of parameters required for modeling the HSS brace response was also discussed by Tirca and Chen (2014). The fiber-based brace model consisting of non-linear beam column elements with distributed plasticity was employed. The nonlinearity is accounted

in the assigned Giuffre-Menegotto-Pinto material (known as Steel 02 material in OpenSees) with isotropic strain hardening.

$$\sigma^* = b\varepsilon^* + \frac{(1-b)\varepsilon^*}{(1+\varepsilon^*R)^{\frac{1}{R}}} \quad (2.5)$$

In Eq. 2.5,  $\sigma^*$  and  $\varepsilon^*$  are the effective stress and strain depending on the unload/reload interval,  $b$  is the ratio of the final to initial tangent stiffness,  $R$  is a parameter that defines the shape of the unload curve. The Giuffre-Menegotto-Pinto steel material are defined as considered by Aguero et al. (2006).

To simulate the brace to frame gusset plate connection, a torsional spring and two rotational springs are defined in the *Zerolength* element. These springs connect the HSS brace to rigid links as shown in Fig. 2.5.

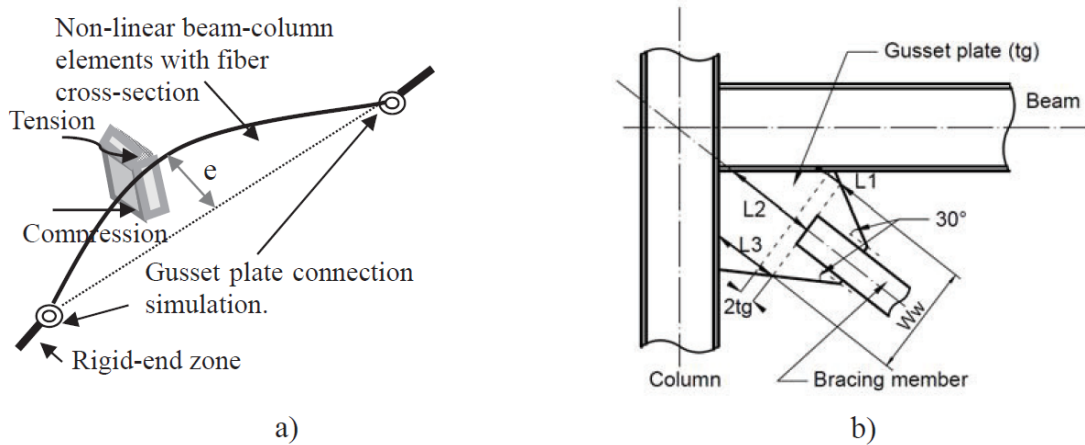


Fig. 2.5 Model of HSS brace with end-connections: (a) Opensees model; (b) geometry of gusset plate (Tirca and Chen, 2014)

The out-of-plane flexural stiffness of the gusset plate,  $K_{gusset}$ , is calculated according to the following equation recommended by Hsiao et al. (2012):

$$K_{gusset} = \left(\frac{E}{L_{ave}}\right)\left(\frac{W_w t_g^3}{12}\right) \quad (2.6)$$

where  $E$  is the Young's modulus of steel,  $W_w$  is the Whitmore width defined by a  $30^\circ$  projection angle,  $L_{ave}$  is the average of  $L_1$ ,  $L_2$ ,  $L_3$  as shown in Fig. 2.5b, and  $t_g$  is the thickness of the gusset plate.

The torsional stiffness is calculated using the following equation:

$$K_{tor} = \frac{GJ}{L_{ave}} \quad (2.7)$$

where  $G$  is the shear modulus of steel material,  $J$  is the torsional constant of the Whitmore cross-section.

Tirca and Chen (2014) also discussed the effect of initial out-of-straightness on the response of braces. The S1B specimen (HSS 76x127x4.8) tested by Archambault (1995) was investigated as shown in Fig. 2.6.

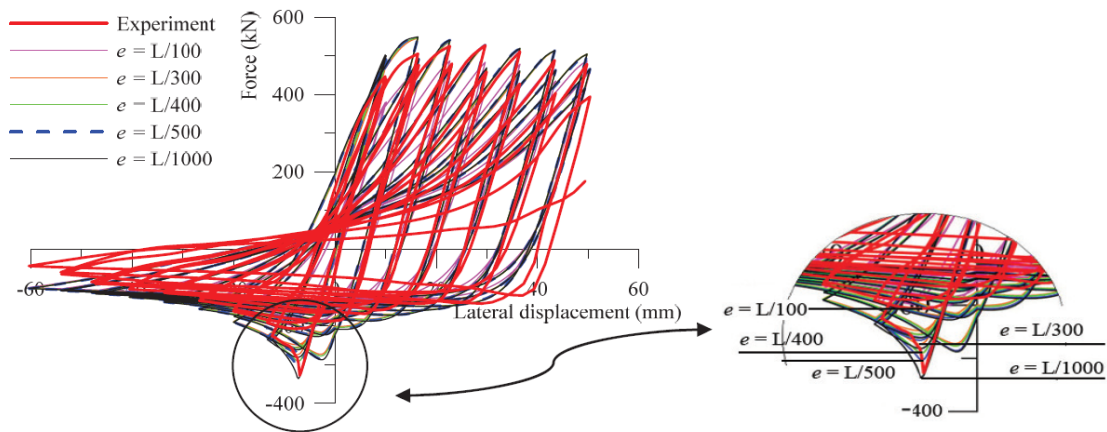


Fig. 2.6 The effect of out-of-straightness on the buckling strength of S1B specimen (Tirca and Chen, 2014)

It was found that when the initial out-of-straightness,  $e$ , varied between  $0.2\%L_b$  and  $0.33\%L_b$ , the simulated buckling force resulted in a small difference. They concluded that

the value  $e = \frac{1}{500}l_b$  proposed by Ziemian (2010) fits well the response.

Sensitivity analysis was performed to find the optimum number of elements, integration points, and fiber discretization as shown in Fig. 2.7. It was concluded that mesh refinement “is not important for the global response of the brace but plays a significant role in the determination of the inelastic deformations at the critical brace sections” (Uriz and Mahin, 2008).

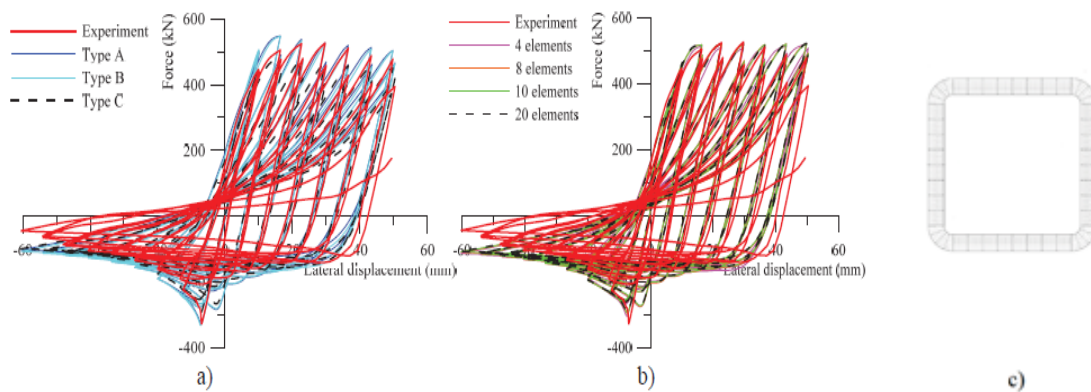


Fig. 2.7 The effect of modeling parameters on the hysteresis response of S1B specimen (a) types of fiber discretization technique; (b) number of elements, (c) fiber discretization cross-section (Tirca and Chen, 2014)

In order to capture the brace fracture caused by low-cycle fatigue, a minimum of 16 elements are required for modeling the response of HSS brace (Hsiao et al., 2013). It was reported that the response is not sensitive to the change in number of integration points per element, however, a minimum of three integration points per element are recommended (Uriz and Mahin, 2005; Tremblay, 2008; Uriz et al., 2008).

## 2.4 Modeling of Moment Resisting Frame using OpenSees

Modeling the steel moment resisting frame requires a reliable, robust, and computational efficient model (Ribeiro et al., 2015). When subjected to cyclic loading, for beams and columns plastic deformations repeatedly occurs, damage would accumulate and lead to failure of beam members.

In general, there are three modeling schemes widely accepted to simulate the seismic response of moment resisting frames using OpenSees: a) The concentrated plasticity model, in which the frame is modeled with elastic beam and column elements, and nonlinear springs account for plasticity developed at the ends of these elements; b) The distributed plasticity model, in which the frame is modeled with *nonlinear beam column elements* with distributed plasticity; c) The model where beams and columns are simulated with *beam with hinges elements* where the nonlinear hinge segments discretized in fibers account for plasticity (Bosco and Tirca, 2017).

In case a), the beams and columns are made of elastic elements, while the behavior of plastic hinges is accounted by nonlinear rotational springs installed at the ends of beam elements. The nonlinear springs are usually modeled with the modified Ibarra-Krawinkler material, known as *Billin* material developed in OpenSees. The model takes several modes of degradation into account complying with Option (1) of ATC 72 -10 and the hysteretic response is calibrated against experimental test. However, in order to conserve elastic stiffness of beams and columns, rotational springs are often assigned with high stiffness, which often causes numerical convergence problems. Moreover, Chopra and McKenna (2016) pointed out that the initial stiffness assumed for plastic hinges could have significant influences on the dynamic response of structure.

In case b), the MRF members are simulated using force-based nonlinear elements with distributed plasticity along the length of the member. Thus, plastic hinges always form at the location where the maximum bending moment occurs. However, as pointed out by Scott and Fenves (2006), this type of element does not have a unique solution for strain softening behavior.

In case c), the *Beam With Hinges* element in OpenSees is used to model the MRF beam. This beam model is composed of an elastic element in the middle and plastic hinge elements at its ends. Assigning a moment-curvature relationship to the plastic hinges, the numerical convergence problem under dynamic loading could be minimized (Ribeiro et al., 2015). However, this model requires accurate prediction of plastic hinge location.

In this study, the refined cyclic deterioration beam model proposed by Bosco and Tirca (2017) is adopted. This model is able to take into account the strength and stiffness deterioration of I-shaped flanges caused by local buckling, as well as the fracture mechanism caused by low-cycle fatigue (Bosco and Tirca, 2017). The proposed model uses the beam with hinges element, where fiber discretized cross sections are used in the plastic hinge segments. The beam with hinges element with modified Gauss-Radau integration method is employed and shown in Fig. 2.8. The Modified Gauss-Radau integration method developed by Scott and Fenves (2006) is applied to each MRF beam and the plasticity is confined to a single integration point at each end of the element. In this case, it is ensured that localized deformation is integrated over the specified plastic hinge length,  $L_p$ . The interior integration points are considered to have elastic properties.

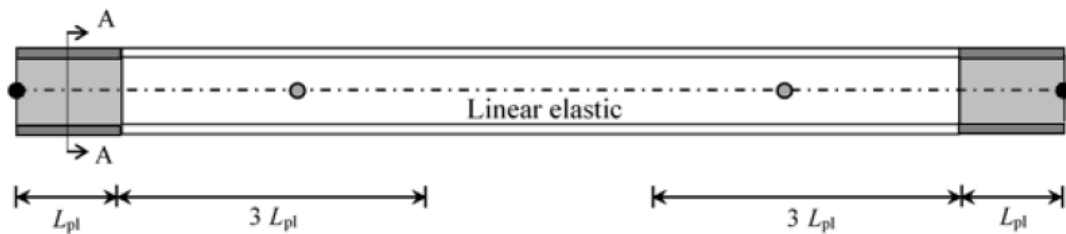


Fig. 2.8 Beam with hinges element with modified Gauss-Radau plastic hinge integration method (Bosco and Tirca, 2017 according to Scott and Fenves, 2006)

As illustrated in Fig. 2.9, in this beam model, each flange of I-shaped cross-section is divided into  $n_{f,s}$  segments and  $n_{f,l}$  layers, while the web is discretized into  $n_{w,l}$  layers. The

Giuffrè-Menegotto-Pinto steel material known as *Steel02* in OpenSees was assigned to fibers and is able to account for accumulated plastic deformation at each point of load reversal (Bosco and Tirca, 2017).

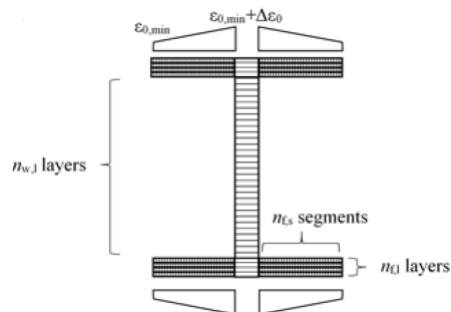


Fig. 2.9 Fiber-based cross-section and distribution of fatigue ductility coefficients (Bosco and Tirca, 2017)

In addition to the *Steel02* material, each fiber is wrapped by a fatigue material that considers damage based on accumulative strain as described in Section 2.1 with Eq. 2.1 and Eq. 2.2.

According to Bosco and Tirca (2017), the proposed numerical model was calibrated against 18 experimental tests from five different studies found in the literature.

The plastic hinge length is usually defined correlating to the wave length of beam flange during local buckling, the depth of cross-section, and the shear length. According to Lay (1965), the buckling wave length of beam flange for a beam under moment gradient could be calculated as:

$$L_m = 2\beta c \quad \text{with } c = 0.5b_f \text{ and } \beta = 0.6 \left(\frac{t_f}{t_w}\right)^{\frac{3}{4}} \left(\frac{d}{c}\right)^{\frac{1}{4}} \quad (2.9)$$

However, it is reported by D'Aniello et al. (2012) that it is more accurate to calculate parameter  $c$  using the following equation:

$$c = 0.5 (b_f - t_w) \quad (2.10)$$

It is concluded that the plastic hinge length can be expressed as a function of the shear length,  $\alpha L_v$ , where the coefficient  $\alpha$  is equal to 0.22.

For the low-cycle fatigue, the value of  $m$  is set to be equal to -0.5, and the value of  $\varepsilon_0$  was calibrated so that the hysteresis loops of numerical model could overlap the hysteresis loops resulting from experimental test as shown in Fig. 2.10.

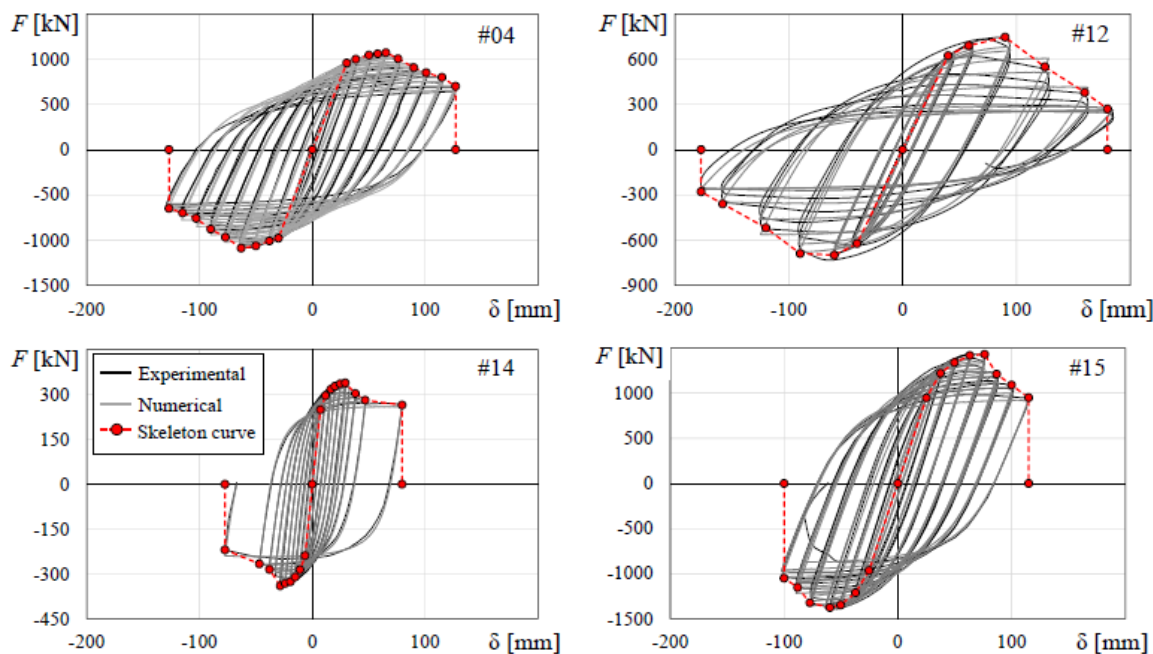


Fig. 2.10 Comparison between the experimental and numerical response with fatigue material (Bosco and Tirca, 2017)

From Fig. 2.9, it shows that there are two fatigue coefficients,  $\varepsilon_{0,min}$  and  $\Delta\varepsilon_0$ , where  $\varepsilon_{0,min}$  varies from 0.025 to 0.035 as observed from experiments. Thus, for the  $\varepsilon_{0,min}$ , the average value of 0.029 is adopted. Theoretical and experimental studies showed that I-shaped beams with smaller width to thickness ratio of flanges could reach the maximum strength at a larger end rotation and show slower strength degradation after the maximum strength is reached (Bosco and Tirca, 2017). The coefficient  $\Delta\varepsilon_0$  is strongly related to the slenderness of the beam flange. In addition to the flange slenderness ratio, the dependence

of  $\Delta\varepsilon_0$  on the ratio  $L_m/L_V$  was also investigated to account for the effect of moment gradient. Moreover, other parameters presented in the literatures (Lignos and Krawinkler, 2011; D’Aniello et al., 2012), are also considered:  $b_f/L_v$ ,  $b_f t_f/dL_v$ ,  $b_f d/L_v^2$ ,  $L_v/\rho_y$ ,  $A_f/A$ , and  $\lambda_w$  in the study of Bosco and Tirca (2017). Herein,  $A_f/A$  is the ratio of the flange area to the cross section gross area,  $L_v/\rho_y$  is sensitive to lateral-torsional buckling, and  $\lambda_w$  is the slenderness of the beam web, calculated as:

$$\lambda_w = \frac{h}{t_w} \sqrt{\frac{F_{yw}}{E}} \quad (2.11)$$

Based on regression analysis, the value of  $\Delta\varepsilon_0$  could be predicted using the following equation:

$$\Delta\varepsilon_{0,pred} = 0.217 - 0.770\lambda_f + 0.452 \frac{b_f t_f}{dL_v} + 0.902 \frac{L_m}{L_V} \geq 0 \quad (2.12)$$

where  $\lambda_f$  is the slenderness ratio of flange, which can be calculated as following equation:

$$\lambda_f = \frac{b_f}{2t_f} \sqrt{\frac{F_{yw}}{E}} \quad (2.13)$$

In order to develop a computational efficient model, a sensitivity analysis was performed to optimize the number of cross section meshes (Bosco and Tirca, 2017). As shown in Fig. 2.11, it was found that when flanges are discretized into 20 or more segments ( $n_{f,s} = 20$ ), there is no difference in the response, however, when fewer segments were considered (e.g.  $n_{f,s} = 5$  or  $n_{f,s} = 10$ ), the strength deterioration slightly increases. When the number of web layers ( $n_{w,l}$ ) is in the range of 10 to 30, the results show no difference, and there is no difference in the response when the flange layers increase from 4 to 7.

Thus, it is recommended to use at least 20 segments, 4 layers of fibers for each flange and at least 10 layers of fibers for the web.

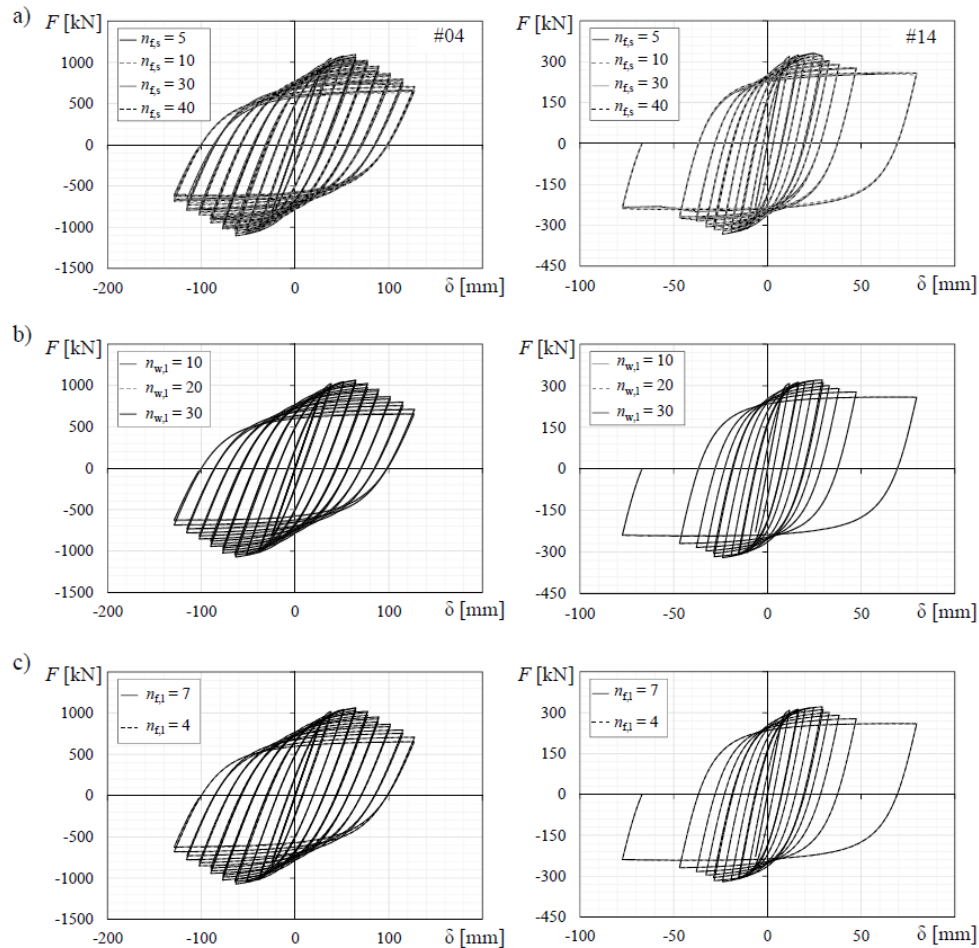


Fig. 2.11 Sensitivity analysis: (a) variation of number of segments within the flange, (b) variation of number of layers within the web, (c) variation of number of layers within the flange (Bosco and Tirca, 2017)

From experimental test results, it was found that the failure of an MRF beam could be defined when the beam loses 20% of its maximum moment resistance. A global damage index ( $DI_{(80\%)}$ ) was proposed based on 16 numerical models of the aforementioned test specimen to determine the occurrence of beam failure.

The drift angle, global damage index, plastic rotations associated to beam failure are shown in Table 2.1.

Table 2.1 Drift angle,  $DI_{(80\%)}$ , plastic rotations and  $\varepsilon/\varepsilon_y$  Ratio associated to  $DI_{(80\%)prop}$ , margin safety and plastic rotation associated to beam failure (Bosco and Tirca, 2017)

ID	Cross-section	$\Delta/L_{V(80\%)}$	DIs(80%)	$DI_{(80\%)prop}=0.375$		No. cycles to collapse	Collapse $\theta_{pl}(rad)$
				$\theta_{pl}(rad)$	$\varepsilon/\varepsilon_y$		
#1	W36x150	0.032	0.359	0.0250	14.0	4	0.0387
#2	W36x150	0.031	0.349	0.0262	14.4	4	0.0321
#3	W36x150	0.031	0.383	0.0391	17.9	6	0.0392
#4	W36x150	0.034	0.440	0.0210	11.3	5	0.0370
#5	W36x150	0.034	0.451	0.0235	12.5	6	0.0402
#6	W36x150	0.030	0.282	0.0233	12.7	6	0.0397
#7	W36x150	0.030	0.295	0.0236	12.9	6	0.0407
#8	W30x99	0.040	0.355	0.0289	10.5	3	0.0454
#9	W30x99	0.042	0.326	0.0300	11.3	2	0.0437
#10	W30x99	0.044	0.388	0.0303	10.9	3	0.0488
#11	W30x99	0.042	0.359	0.0298	10.8	4	0.0525
#12	W30x99	0.042	0.366	0.0302	10.9	5	0.0539
#13	W18x40	0.058	0.525	0.0400	18.4	1	0.0511
#14	W21x44	0.050	0.533	0.0281	15.0	1	0.0446
#15	W36x150	0.036	0.274	0.0223	13.1	3	0.0354
#16	W36x150	0.036	0.275	0.0225	13.2	5	0.0423
<b>Average</b>		<b>0.038</b>	<b>0.373</b>	<b>0.028</b>	<b>13.1</b>		<b>0.043</b>
<b>Standard dev.</b>		<b>0.008</b>	<b>0.080</b>	<b>0.006</b>	<b>2.39</b>		<b>0.006</b>

As illustrated, MRF beam fails at an average global damage index of 0.373. However, since in the model the four flanges of I-shaped contain 480 fibers in total, it is suggested to consider  $DI_{(80\%)prop} = 0.375$  as collapse indicator (Bosco and Tirca, 2017). In this case, it means that collapse should be considered when 180 out of 480 flange fibers fail.

## 2.5 Incremental Dynamic Analysis

The concept of Incremental Dynamic Analysis (IDA) has been first mentioned by Bertero (1977). After the 1994 Northridge earthquake, the method was named Dynamic Pushover

and was used to subject a structure to ground motions with a wider range of scaling. This method was believed to be a tool used to check multiple limit-states of structures. The idea for Incremental Dynamic Analysis was born from the Dynamic Pushover analysis. Since then, it was adopted by several researchers from the John A. Blume Earthquake Research Center of Stanford University. Moreover, Federal Emergency Management Agency (FEMA) of the U.S. also recommended using the IDA method to evaluate the global collapse capacity of steel moment resisting frames (FEMA 350, 2000).

In 2002, Vamvatsikos and Cornell proposed a detailed methodology for performing IDA, which is widely employed in this study. Based on the proposed methodology, the IDA curve can be constructed by joining points defined by two measurements namely Intensity Measure (IM) and Damage Measure (DM). One single IDA curve could be derived by analyzing a structure using one ground motion that is scaled to multiple intensity levels. Commonly, a Monotonic Scalable Ground Motion Intensity Measure should be selected, which can be one of the following: Peak Ground Acceleration (PGA), Peak Ground Velocity (PGV), the  $\xi = 5\%$  damped Spectral Acceleration at the Structure's first-mode period ( $S_a(T_1, 5\%)$ ), etc. The Damage Measure (DM) is also known as Structural State Variable, which characterizes the response of the structure under prescribed earthquake loading. In general, the possible DM can be: maximum base shear, node rotations, peak storey ductility, floor peak interstorey drift, etc. The IM is usually plotted on the vertical axis.

As pointed out by Vamvatsikos and Cornell (2002), a single IDA curve can show different behavior such “softening”, “hardening”, and “weaving” under different ground motion records as showed in Fig. 2.12.

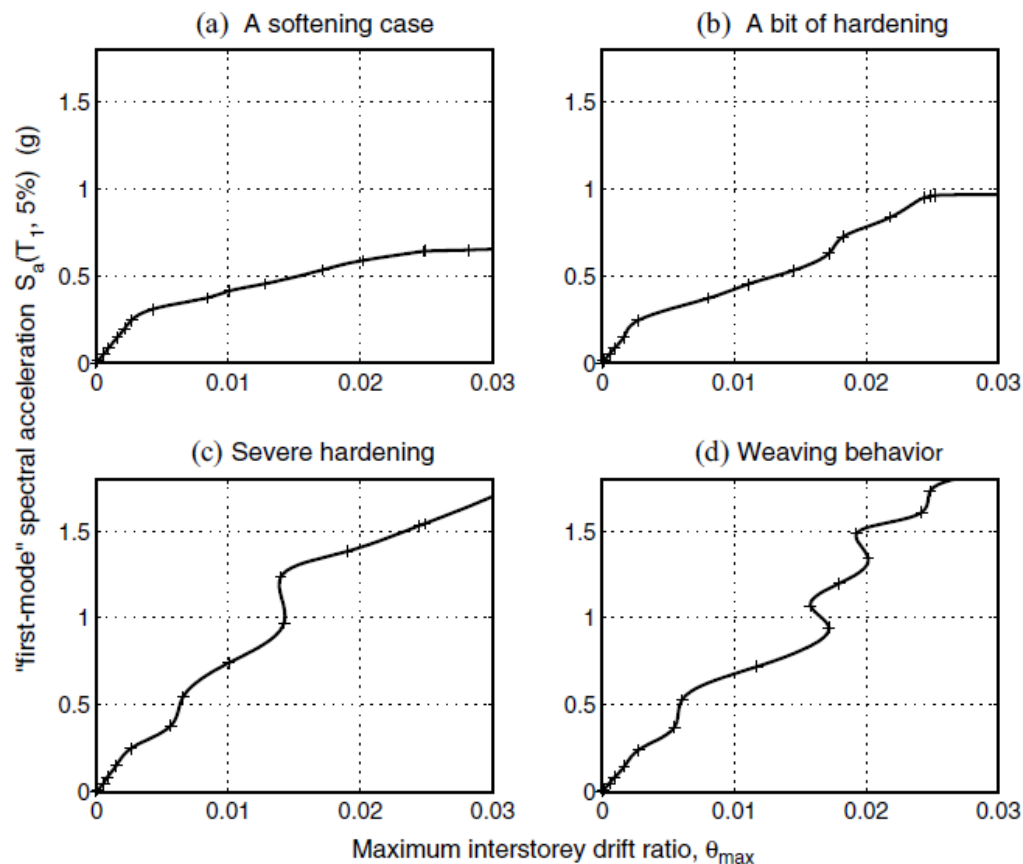


Fig. 2.12 IDA curves of a  $T_1=1.8$  s, 5-storey steel braced frame subjected to four different records (Vamvatsikos and Cornell, 2002)

Curves (c) and (d) show a combination of “hardening” and “softening” segments of IDA curves, where “hardening” means the slope of the curve increases with increase of IM, and “softening” means the reverse. In case of structure analysis, if the failure mechanism can be tracked by the DM that one chose, a final softening of IDA curve would be observed when the IM is increased to a certain intensity (Vamvatsikos and Cornell, 2002). For example, in Fig. 2.12b, when IM increases to 1.0, the curve becomes flat, the DM becomes infinite, which means dynamic instability of the structure occurs.

As stated by Vamvatsikos and Cornell (2002), the IDA study is unique for each different accelerogram and numerical model. When different ground motions are employed, a model

will often show quite disparate responses. Thus, the shapes of IDA curves are difficult to predict. However, as shown in Fig. 2.13, the structural model with initial linearly elastic elements exhibits first a distinct elastic linear region, then, the linearity terminates when the first element performs into non-linear range.

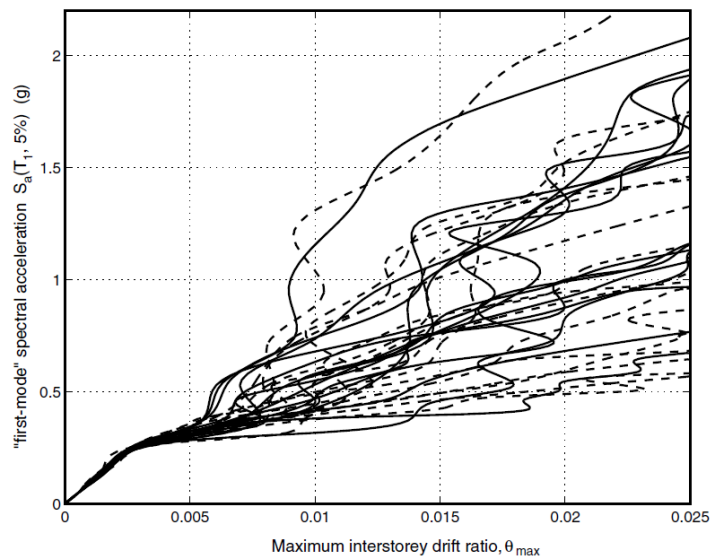


Fig. 2.13 The 30 individual IDA curves of a 5-storey steel braced frame with  $T_1 = 1.8$  s (Vamvatsikos and Cornell, 2002)

To perform analysis/calculations for Performance Based Earthquake Engineering, defining limit-states is a need and the IDA curves are used for it. The limit states can be defined by exploring structural response from each analysis. The immediate occupancy (IO) for CBFs can be define when the first buckling of brace occurs and for MRFs when the first beam end experiences flexural yielding.

According to Vamvatsikos and Cornell (2004), due to large amount of data gathered from IDA and the wide range of IDA curves behaviour, it is essential to summarize such data and quantify the randomness introduced by the records (Vamvatsikos and Cornell, 2004). As shown in Fig. 2.14, each IDA curve is unique. In order to get robust results from IDA,

usually several ground motion records should be used, and the 16<sup>th</sup>, 50<sup>th</sup>, and 84<sup>th</sup> percentile IDA curves should be summarized.

In general, the instability of structure occurs as the IDA curve goes flattening. FEMA 350 (FEMA, 2000) proposes a 20% tangent slope approach against a horizontal line for defining the collapse of structure. The capacity point is defined as the last point on the curve with a tangent slope equal to 20% of the elastic slope.

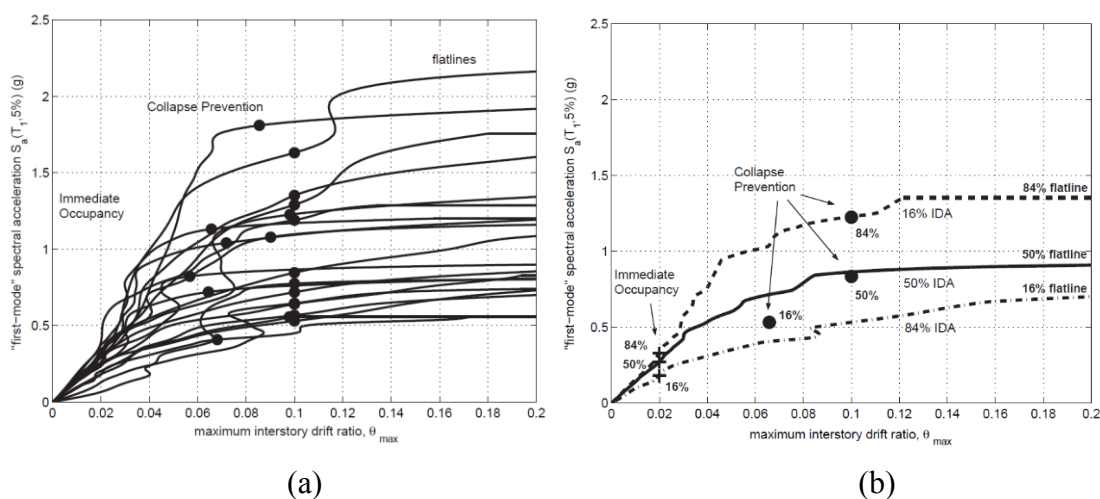


Fig. 2.14 IDA curves: (a) twenty IDA curves and the associated limit-state capacities, (b) the summary of the IDA curves and corresponding limit-state capacities into their 16%, 50%, and 84% fractiles (Vamvatsikos and Cornell, 2004)

## 2.6 Fragility Analysis

Fragility analysis is one of the probabilistic approaches of seismic assessment, in which a probabilistic characterization is established between demands and capacity. In general, a fragility function describes the probability of collapse or the probability of exceeding a target limit state of a structure as a function of an intensity measure, IM. There are various ways of performing nonlinear structural analysis and to collect data for fragility analysis. Among them, the incremental dynamic analysis (IDA) is the one selected in this study. The

fragility function usually follows a lognormal cumulative distribution expressed by the equation below (Ibarra et al., 2002; Baker and Cornell, 2005; Ellingwood et al., 2007).

$$P(C|IM = x) = \Phi\left(\frac{\ln(x/\theta)}{\beta}\right) \quad (2.14)$$

where  $P(C|IM = x)$  is the probability that a ground motion with  $IM = x$  will cause the structure to collapse,  $\Phi(\cdot)$  is the standard normal cumulative distribution function (CDF),  $\theta$  is the median of the fragility function and  $\beta$  is the standard deviation of  $\ln(IM)$ .

However, uncertainty in response of buildings under earthquake ground motions rises due to the inherent randomness (aleatoric uncertainty) in ground motions, local design and construction practices. Moreover, additional uncertainty in estimating the capacity is induced from assumptions made in the analysis and from limitation of database, those epistemic uncertainty can be reduced through more comprehensive analysis.

Ellingwood et al. (2007) proposed the same equation as Eq. 2.14 where aleatoric and epistemic uncertainty were included. The function is described as below:

$$F_R(x) = \Phi[\ln(x/m_R)/\beta_R] \quad (2.15)$$

where  $m_R$  is the median capacity,  $\beta_R$  is the logarithmic standard deviation, and  $\Phi[\cdot]$  is the standard normal probability integral. By replacing  $\beta_R$  with Eq. 2.16, the aleatoric and epistemic uncertainty can be taken into consideration:

$$\beta_R = \sqrt{\beta_{RR}^2 + \beta_{RU}^2} \quad (2.16)$$

Herein,  $\beta_{RR}$  stands for the aleatoric uncertainty and  $\beta_{RU}$  is the epistemic uncertainty.

The  $\beta_{RR}$  is calculated using following equation:

$$\beta_{RR} = \sqrt{\beta_{D|S_a}^2 + \beta_C^2} \quad (2.17)$$

where  $\beta_C$  is the uncertainty in capacity, which is dependent on the performance level.  $\beta_{D|S_a}$  is the seismic demand uncertainty. A nonlinear regression analysis of power-law form was used to assess  $\beta_{D|S_a}$  as shown in the following equation:

$$\theta_{max} = a * S_a^b * \varepsilon \quad (2.18)$$

In the above equation,  $a$  and  $b$  are constants,  $\varepsilon$  is a lognormal random variable with median value of 1.0,  $\theta_{max}$  is the maximum drift angle, which could be replaced by other engineering demand parameters (EDP) obtained from the IDA curve. By performing a logarithmic transform, Eq. 2.18 could be transformed to a linear form as shown in Eq. 2.19.

$$\ln(EDP) = \ln a + b \ln S_a \quad (2.19)$$

The constants  $a$  and  $b$  could be determined by a simple linear regression analysis. The “best” fitted linear regression line is the one that passes through the data points with the least total error which can be obtained by minimizing the sum of the squared errors,  $s^2$ . The expression of seismic demand uncertainty can be calculated using following equation provided by Wen et al. (2004):

$$\beta_{D|S_a} = \sqrt{\ln(1 + s^2)} \quad (2.20)$$

This methodology for calculating the fragility curves was adopted by Tirca et al. (2016).

# CHAPTER 3. SEISMIC DESIGN OF BRACED DUAL SYSTEM VS. TRADITIONAL SYSTEMS USING NONLINEAR ANALYSIS

## 3.1 Introduction

To emphasize the seismic response of Braced Dual System, a comparative study is presented hereafter. The dual system is proposed to overpass the drawbacks of traditional CBF and MRF systems that are prone to weak-storey response under earthquake loading. Herein, the seismic response of Braced Dual System is compared with that of a bare moderately ductile concentrically braced frame (MD-CBF) system, as well as, a bare moderately ductile moment resisting frame (MD-MRF) system. An 8-storey prototype office building was selected and three seismic force resistant systems such as: a) MD-CBF, b) MD-MRF, and c) Braced Dual System were designed and analyzed according to NBCC 2015 and CSA S16-14. It is noted that Braced Dual System is designed such that the MD-CBF is proportioned to resist 100% of base shear force and the MRF is designed as a backup system proportioned to carry additional 25% of seismic force. Furthermore, in the User's Guide of NBCC 2015 it is noted that when designing dual systems, the same ductility related force modification factor  $R_d$  and overstrength related force modification factor  $R_o$  should be used. To examine the seismic response of the three- aforementioned seismic force resisting systems the nonlinear time history analysis is employed using two suites of ground motions for each prototype building located on Site Class C, in Vancouver, B.C.

## 3.2 Building Design Criteria According to NBCC 2015 & CSA/S16 2014

Building structure is composed of a gravity system including gravity columns and floor beams, as well as lateral force resisting system (LFRS). Both systems are designed to resist vertical loads such as: dead load (D), live load (L), and snow load (S). In addition to this, the LFRS is also proportioned to carry lateral loads like wind load (W), and earthquake load (E).

The NBCC 2015 requires design verifications for two limit states: the *ultimate limit state* (USL) concerning safety and the *serviceability limit state* (SLS) dealing with deflection criteria by restricting the intended use and occupancy of building. The former verifies if the system has sufficient strength such that factored resistance is greater than the effect of factored loads, while the later verifies if deflection/ permanent deformation resulted under service load is within the code limits. In the process of designing the seismic force resisting system the capacity design method is applied.

### 3.2.1 Gravity loads

The gravity system is designed to withstand the maximum of factored loads resulted from the following load combinations:

$$\text{a) } 1.4D \quad (3.1)$$

$$\text{b) } 1.25D + 1.5L + 1.0 S \quad (3.2)$$

$$\text{c) } 1.25D + 1.5S + 1.0 L \quad (3.3)$$

The dead load includes the building self-weight; live loads are specified in NBCC 2015 for different building occupancies and a live load reduction factor is considered; snow load is calculated based on the following equation given by NBCC 2015:

$$S = I_s[S_s(C_b C_w C_s C_a) + S_r] \quad (3.4)$$

In Eq. (3.4)  $I_s$  is importance factor,  $S_s$  is 1-in-50-year ground snow load,  $C_b$  is basic roof snow load factor,  $C_w$  is wind exposure factor,  $C_a$  is accumulation factor,  $S_r$  is 1-in-50-year associated rain load.

The lateral force resisting system should be designed considering following load combinations:

$$d) 1.25D + 1.4W + 0.5L \text{ or } 0.5S \quad (3.5)$$

$$e) 1.0D + 1.0E + 0.5L + 0.25S \quad (3.6)$$

For an office building,  $L = 2.4$  kPa, and for the building in Vancouver,  $S_s = 1.8$  kPa,  $S_r = 0.2$  kPa,  $S = 1.64$  kPa.

### 3.2.2 Seismic load

As per NBCC 2015, earthquake load is calculated based on the 5% - damped horizontal spectral acceleration for 0.2, 0.5, 1.0, 2.0, 5.0, and 10.0 second periods, and the acceleration response spectra ordinates corresponding to a 2% probability of exceedance in 50 years (2475-year return period) are given for site Class C in Vancouver in Table 3.1.

Table 3.1 Acceleration response spectra ordinates for site Class C in Vancouver

T (s)	T=0-0.2	T = 0.5	T = 1.0	T = 2.0	T = 5.0
$S_a(T)$ , g	0.794	0.699	0.399	0.243	0.125

For steel braced frames, the fundamental period ( $T_a$ ) of a building is estimated using following equation:

$$T_a = 0.025h_n \quad (3.7)$$

For steel moment frames structures, the fundamental period ( $T_a$ ) of a building is estimated based on an empirical equation, which is given as the following:

$$T_a = 0.085(h_n)^{3/4} \quad (3.8)$$

In Eq. (3.7) and Eq. (3.8)  $h_n$  is the total height of the building in meters.

It is noted that the fundamental period could be taken up to 2 times of  $T_a$  for CBF buildings and 1.5 times of  $T_a$  for MRF buildings if a dynamic analysis is performed.

The lateral static force (base shear) due to earthquake load is calculated using the equivalent static force method according to Eq. (3.9).

$$V = S(T_a)M_v I_E W / (R_d R_o) \quad (3.9)$$

Herein,  $S(T_a)$  is the 5%-damped spectral acceleration,  $M_v$  is the higher mode factor,  $I_E$  is the importance factor,  $W$  is the building seismic weight computed by considering additional 25% of snow load,  $R_d$  is the ductility related-force modification factor, and  $R_o$  is the over strength related-force modification factor.

The total seismic force,  $V$ , is distributed along the building height using the following equation:

$$F_x = (V - F_t)W_x h_x / (\sum_{i=1}^n W_i h_i) \quad (3.10)$$

where  $F_t$  is a portion of  $V$  assumed to be concentrated at the top storey. For buildings with fundamental period greater than 0.7s,  $F_t$  is equal to  $0.07T_a V$  but not greater than  $0.25V$  while for buildings with  $T_a < 0.7$  s no concentrated force is applied ( $F_t = 0$ ).

Torsional effects should be also considered in design. However, in this study, the torsional effect caused by accidental eccentricity is neglected and is not presented hereafter.

According to NBCC, the P- $\delta$  effects are considered, and the storey shear force resulted from calculation is amplified with the amplification factor  $U_2$ , which is calculated using the following equation:

$$U_2 = 1 + \theta_x \quad (3.11)$$

where  $\theta_x$  is the stability factor, it should be calculated according to the following equation:

$$\theta_x = \frac{\sum C_f}{\sum V_f} \frac{R_d \Delta_f}{h_s} \quad (3.12)$$

Herein,  $\sum C_f$  is the factored axial force computed according to Eq. (3.6) at the calculation level,  $\sum V_f$  is the design storey shear force at the level under consideration,  $\Delta_f$  is the interstorey drift at the same floor level,  $R_d$  is the ductility-related factor and  $h_s$  is the storey height at the calculation level.

### 3.3 System Ductility Classes and Restrictions

Based on ductility criteria, there are two CBF categories defined in NBCC: i) Moderately Ductile Concentrically Braced Frames (MD-CBF) and ii) Limited Ductile Concentrically Braced Frames (LD-CBF). Both CBF types can be designed either with tension-compression braces or tension only braces. The MD-CBF is characterized by a ductility-related force modification factor  $R_d = 3.0$  and an overstrength-related force modification factor  $R_o = 1.3$ , while the product  $R_d R_o$  is 3.9. The LD-CBF has  $R_d$  reduced to 2.0, while  $R_o$  remains unchanged and  $R_d R_o = 2.6$ . The  $R_o$  parameter includes the overstrength caused by the resistance factors used in design, the strain hardening developed in steel material upon yielding, the difference between the actual and nominal yield strength, etc.

For steel MRF, there are three ductility classes defined in NBCC: i) Ductile Moment-Resisting Frame (Ductile MRF); ii) Moderately Ductile Moment-Resisting Frame (MD-MRF); and iii) Limited Ductility Moment-Resisting Frame (LD-MRF). The  $R_d$  factor for the ductility classes are 5.0, 3.5, 2.0 respectively. An  $R_o$  factor equals to 1.5 is used for Ductile MRF and MD-MRF, while for LD-MRF it is diminished to  $R_o = 1.3$ .

According to the Canadian building code, all ductile structural systems are designed according to the capacity design provision.

In NBCC several restrictions are imposed to CBF buildings' height as a function of brace configuration, ductility factor,  $R_d$ , and the level of seismic zone. For example, when the seismic zone is characterized by:  $I_E F_a S_a(0.2) \geq 0.35g$  or  $I_E F_v S_a(1.0) \geq 0.3g$ , the height of building employing type MD-CBF with tension-compression braces is limited to 40 m, while for LD-CBF type is limited to 60 m. These limits are recommended to reduce the probability of damage concentration at a critical floor and to avoid the soft storey response. In the above expression  $I_E$  is the importance factor,  $F_a = F(0.2)$  and  $F_v = F(1.0)$  are computed from tables as a function of site class and the reference PGA, while  $S_a(0.2)$  is the elastic spectral acceleration at a period of 0.2s.

There is no height restriction specified in NBCC for Ductile MRFs and MD-MRFs. However, for LD-MRFs, the building height is limited to 60 m when  $I_E F_a S_a(0.2)$  ranges from 0.35g to 0.75g and the height is restricted to 30 m when the building is located in seismic area with  $I_E F_a S_a(0.2) \geq 0.75g$  or  $I_E F_v S_a(1.0) \geq 0.3g$ .

### 3.4 Design Criteria for MD-CBFs According to CSA/S16 2014 Requirements

#### 3.4.1 Design of tension-compression bracing members

The brace slenderness ratio  $KL/r$  is limited to 200, where  $KL$  is the effective brace length and  $r$  is the radius of gyration in the direction of bending. However, for seismic areas where  $I_E F_a S_a(0.2) \geq 0.75 g$  or  $I_E F_v S_a(1.0) \geq 0.3g$  the slenderness ratio of HSS bracing members shall not be less than 70. The slenderness parameter  $\lambda$  is calculated using the following equation:

$$\lambda = (KL/r) \sqrt{F_y / \pi^2 E} \quad (3.13)$$

where  $F_y$  is the yielding stress of steel and  $E$  is the modulus of elasticity.

In order to delay the occurrence of local buckling, at least Class 1 section is required for braces. However, for HSS braces of CBF buildings located in seismic areas characterized by  $I_E F_a S_a(0.2) \geq 0.35g$  the width-to-thickness ratio should be less than  $330/\sqrt{F_y}$  if their slenderness ratio is less than 100. For HSS braces with slenderness ratio  $\frac{KL}{r} = 200$ , Class 1 sections should be used. For HSS braces with slenderness ratio between 100 and 200, linear interpolation is recommended.

To resist compression forces, the HSS braces are designed such that  $C_f < C_r$  where  $C_f$  is the factored axial compression force in brace and  $C_r$  is the brace compression resistance:

$$C_r = \phi A_g F_y (1 + \lambda^{2n})^{-\frac{1}{n}} \quad (3.14)$$

where  $\phi = 0.9$  for steel members,  $\lambda$  is computed with Eq. (3.13),  $A_g$  is the gross area of brace cross-section and  $n = 1.34$  for the type of braces selected.

The HSS brace is verified to carry factored axial tensile force such that  $T_f < T_r$  where  $T_r = \phi A_g F_y$ .

### **3.4.2 Design of Beam and Column of MD-CBF**

Beams and columns of MD-CBFs are designed according to capacity design principle. Thus, the beam and column members of MD-CBFs are designed to carry the axial forces generated by braces corresponding to the following two loading conditions (CSA/S16-14):

- i) the compression acting braces attaining their probable compressive resistance  $C_u$  in conjunction with the tension acting braces developing their probable tensile resistance  $T_u$  and
- ii) the compression acting braces attaining their probable post-buckling resistance  $C'_u$  in conjunction with the probable tensile resistance  $T_u$  of tension acting braces.

Herein,  $T_u = A_g R_y F_y$ ,  $C_u = 1.2 C_r R_y / \phi$  and  $C'_u = \min(0.2 A_g R_y F_y; C_r R_y / \phi)$ , where  $R_y$  is the factor applied to  $F_y$  for estimating the probable yield stress  $R_y F_y$ . The value of  $R_y$  shall be 1.1 and the product  $R_y F_y$  as not less than 460 MPa for HSS sections or 385 MPa for other sections as W-shapes. The former is due to the higher variability of yield strength observed for HSS sections compared to W-shape sections.

According to CSA/S16, the beams to which chevron braces are attached shall be continuous between columns, have both top and bottom flanges laterally braced at the brace-to-beam connection and resist bending moment due to associated gravity load

component (assuming no vertical support is provided by brace members) in conjunction with bending moments and axial forces induced by braces probable resistance ( $T_u$  developed in the tension brace and  $C'_u$  in the compression brace).

Beams of MD-CBFs should be checked for cross-sectional strength (CSS), overall member strength (OMS), and combined axial force and bending moment (AT&B) based on the following two equations:

$$\frac{C_f}{C_r} + \frac{0.85U_1M_f}{M_r} \leq 1.0 \quad (3.15)$$

$$\frac{T_f}{T_r} + \frac{M_f}{M_r} \leq 1.0 \quad (3.16)$$

For low-rise buildings with less than four storeys, the probable tensile resistance of braces can be taken as  $0.6T_u$ , provided that the beam is Class 1 section.

Chevron CBFs with strong beams allow braces to develop their yield capacity in tension. As aforementioned, beams of MD-CBFs experience bending moments and axial forces due to the associated gravity loading component and brace forces expressed by their probable resistance in tension and compression without the consideration of vertical support. Similar design approach is considered to size beams of CBFs with multi-storey “X” bracing system. Thus, these beams are designed as beam-column elements and should to be Class 1.

The CBF columns shall be continuous over two or more storeys and of constant cross-section over a minimum of two storeys. Columns in braced bays shall meet the requirements of Class 1 or Class 2 and be designed as beam-columns. Columns are designed to resist in compression the effects of gravity loads combined with those resulted from brace effects expressed by  $C_u$  and  $T_u$ . However, in some cases, braces can be

oversized in order to meet other design criteria such as width-to-thickness ratio, slenderness, interstorey drift, etc. For such cases, the forces associated to brace effects need not exceed the forces induced by a storey shear calculated with  $R_d R_o = 1.3$  which corresponds to elastic design. In addition to the axial force, a bending moment equal to 0.2 times the plastic moment ( $M_p$ ) of column cross-section applied in the bending direction is considered. In design, the CBF columns are assumed to be bent in single curvature, while column splices are designed for axial and shear forces only. It is noted that according to CSA/S16 standard the capacity of beam-column members is examined for: i) cross-sectional strength where  $C_r$  is computed with  $\lambda = 0$ , ii) overall member strength with  $C_r$  is computed based on the axis of bending and iii) lateral torsional buckling strength with  $C_r$  is computed based on the weak-axis.

The column members should be checked for overall member strength (OMS), lateral torsional buckling (LTB), and combined tensile axial force and bending moment (AT&B) using Eq. 3.15 and Eq. 3.16.

### ***3.4.2 Design of brace-to-frame gusset plate connections***

The design of brace to frame connections follows the capacity design approach. To design the gusset plate connections the following failure modes are considered:

- i. Shear resistance of fillet welds connecting the HSS brace to the gusset plate,
- ii. Tensile resistance of filler weld
- iii. Tensile yielding of gusset plate
- iv. Buckling of gusset plate
- v. Net fracture of braces

vi. Block shear failure of braces

The shear resistance of fillet welds is taken as the lesser of the following two cases:

i) Fracture of the weld metal through the weld throat:  $V_r = 0.67\phi_w A_w X_u$  (3.17)

ii) Yielding at the weld-to-base metal interface:  $V_r = 0.67\phi_w A_m F_u$  (3.18)

In Eq. 3.18,  $A_w$  is the area of effective fillet weld throat and  $A_w = 0.707D_w L_w$ , where  $D_w$  is the fillet weld size which should not exceed the thickness of the thinner part of the brace and  $L_w$  is the length of the fillet weld. The other terms in the equation are  $\phi_w = 0.67$  where  $\phi_w$  is the resistance factor of weld metal and  $X_u$  is the electrode ultimate tensile strength. For electrode type E49XX, the  $X_u$  is 490 MPa. In Eq. 3.18,  $A_m$  is the shear area of effective fusion face which is  $A_m = D_w L_w$ . The shear resistance of welding should be not less than the probable tensile resistance  $T_u$  of brace.

The tensile resistance of metal base can be calculated as following:

$$T_r = \phi t_g L_w F_y \quad (3.19)$$

where  $t_g$  is the thickness of gusset plate. The tensile resistance of gusset plate should be not less than the probable tensile resistance,  $T_u$ , of brace.

The tensile yielding of gusset plate is calculated using the Whitmore width ( $W_w$ ) which is defined as the length of the line passing through the end of the brace and intercepted by two 30° lines starting from the intersection of the brace and the gusset plate (Whitmore, 1952) as illustrated in Fig. 3.1.

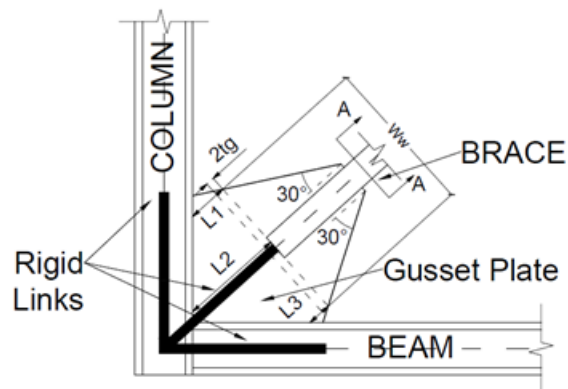


Fig. 3.1 Brace -to-frame connection and parameters considered

The yielding strength of gusset plate is calculated using following equation:

$$T_r = \phi A_g F_y \quad (3.20)$$

where the gross tension area,  $A_g$  is calculated as  $t_g W_w$  and  $t_g$  is the thickness of gusset plate, while  $F_y$  is the yield strength of steel. The gusset plate yielding resistance  $T_r$  should be not less than the probable tensile resistance,  $T_u$ , of brace.

Buckling of gusset plate should be verified such that the compressive resistance of the gusset plate is greater than or equal to the probable compressive resistance of the brace,  $C_u$ .

The compressive resistance of gusset plate is calculated using Eq. 3.14, where  $\lambda$  is :

$$\lambda = (KL_{ave}/r)\sqrt{F_y/\pi^2 E} \quad (3.21)$$

where  $L_{ave}$  is the average of  $L_1$ ,  $L_2$ , and  $L_3$  as shown in Fig. 3.1,  $r$  is the out-of-plane radius of gyration of gusset plate calculated as  $r = \left(\frac{I_g}{A_g}\right)^{0.5}$  and the moment of inertia  $I_g$  is calculated as per Eq. 3.22 for out-of-plane flexural of gusset plate.

$$I_g = W_w t_g^3 / 12 \quad (3.22)$$

To verify the net fracture resistance of HSS brace which is a slotted HSS brace end connection the shear lag effect is considered. Herein, the effective net area  $A_{ne}$  is reduced by the shear lag factor according to Clause 12.3.3.4 of CSA/S16-14 as shown in Fig. 3.2 and  $A_n$  is the net area.

The net fracture resistance of HSS braces is calculated as following:

$$T_r = \phi_u A_{ne} F_u \quad (3.23)$$

where  $\phi_u = 0.75$ ,  $F_u$  is the specified minimum tensile strength and  $A_{ne}$  is calculated according to Eq. 3.24.

- when  $\bar{x}'/L_w > 0.1$ ,  $A_n = A_n \left(1.1 - \frac{\bar{x}'}{L_w}\right) \geq 0.8A_n$  (3.24)
- when  $\bar{x}'/L_w \leq 0.1$ ,  $A_{ne} = A_n$

where  $L_w$  is the length of a single weld segment used to weld the HSS brace to gusset plate (the usual case has the total weld length being  $4L_w$ ) and  $\bar{x}'$  is the distance between the center of gravity of half of the HSS cross section taken from the edge of the connection plate.

The block shear failure of braces should be checked according to CSA/S16 CL 13.11, where  $T_{r-BS}$  should be greater than or equal to the probable tensile resistance,  $T_u$ , of brace.

The following equation is used to calculate the block shear resistance:

$$T_{r-BS} = \phi_u \left[ U_t A_n F_u + 0.6 A_{gv} \frac{F_y + F_u}{2} \right] \quad (3.25)$$

where  $U_t$  is an efficiency factor and  $U_t = 1$  is used for symmetrical blocks or failure patterns and concentric loading,  $A_n$  is the net area in tension and  $A_{gv}$  is the gross area in shear.

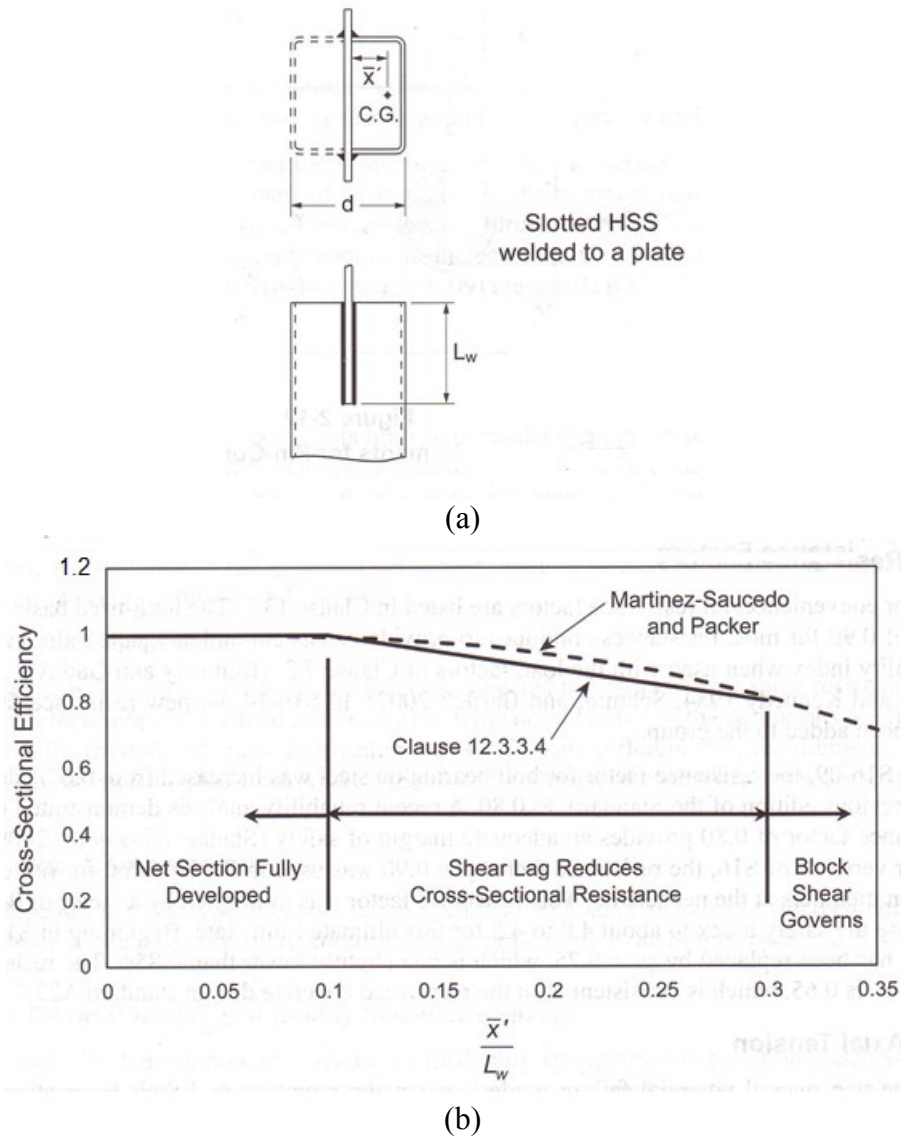


Fig. 3.2 Shear lag effects on slotted HSS brace ends (CSA/S16-14, 2014)

### 3.5 Design Criteria for MRFs According to CSA/S16 2014 Requirements

Moment resisting frame, MRF, is considered as highly ductile system and it consists of beams rigidly connected to columns. The lateral load resistance of MRF is primarily provided by frame action.

The design of MRF follows the capacity design approach which is based on “strong-column weak-beam”. Plastic hinges are allowed to form only in beams rather than in

columns such that the global plastic mechanism could be achieved before failure occurs. According to CSA/S16 CL. 27.2.1, plastic hinges in columns are permitted only at the base of the column, which complies with the “strong-column weak-beam” philosophy.

### ***3.5.1 Design of MRF beams***

According to CSA/S16, the beams of MRF are expected to develop plastic hinges at a short distance from the face of columns. Cross sections used for MRF beams should be Class 1 sections and be laterally braced.

The moment resistance of beams is calculated using the following equation:

$$M_r = \phi Z F_y \quad (3.26)$$

It is assumed that the MRF beams are laterally supported by the composite steel deck in case that the MRF beam carries uniformly distributed load and is laterally supported by secondary beams which provides concentrated loads on the MRF beam. The resistance of cross section used for MRF beam is verified for combined axial force and bending moment using Eq. (3.15) and Eq. (3.16).

The force acting on other members and connections due to plastic hinging shall be calculated using the following equation:

$$M_f = 1.1 R_y Z F_y \quad (3.27)$$

### ***3.5.2 Design of MRF columns***

Columns of MRF should be Class 1 or Class 2 section. As specified in CSA/S16, when a column is expected to develop plastic hinge, it shall be Class 1 section and be laterally braced. The factored axial load shall not exceed  $0.3 A F_y$  if  $I_E F_v S_a(1.0)$  is greater than 0.3.

It is specified that columns of MRF should be designed to resist the gravity loads together with the forces induced by formation of plastic hinges in the beams:

$$\sum M'_{rc} \geq \sum (1.1R_y M_{pb} + V_h(x + \frac{d_c}{2})) \quad (3.28)$$

In the above equation,  $M'_{rc}$  is the nominal flexural resistance of MRF columns,  $M_{pb}$  is the nominal plastic moment resistance of the beam,  $V_h$  is the shear acting at the plastic hinge location,  $x$  is the distance from the centre of a beam plastic hinge to the column face.

The nominal flexural resistance of MRF columns should not exceed the nominal plastic moment resistance and shall be calculated using the following equation:

$$M'_{rc} = 1.18\phi M_{pc} (1 - \frac{C_f}{\phi C_y}) \leq \phi M_{pc} \quad (3.29)$$

In general, the MRF columns are unbraced over their storey height. In this case, the moment resistance of MRF columns should also be taken into consideration, according to CSA/S16.

There are two cases for doubly symmetric Class 1 and Class 2 sections:

i) When  $M_u > 0.67M_p$ :

$$M_r = 1.15\phi M_p (1 - \frac{0.28M_p}{M_u}) \leq \phi M_p \quad (3.30)$$

ii) When  $M_u \leq 0.67M_p$ :

$$M_r = \phi M_u \quad (3.31)$$

The critical elastic moment of the unbraced segment,  $M_u$ , is given by:

$$M_u = \frac{\omega_2 \pi}{L} \sqrt{EI_y GJ + (\frac{\pi E}{L})^2 I_y C_w} \quad (3.32)$$

where  $C_w$  is the warping torsional constant,  $J$  is the St. Venant torsional constant,  $\omega_2$  is the coefficient to account for increased moment resistance of and can be calculated from the following equation:

$$\omega_2 = \frac{4M_{max}}{\sqrt{M_{max}^2 + 4M_a^2 + 7M_b^2 + 4M_c^2}} \leq 2.5 \quad (3.33)$$

### 3.5.3 Design of beam-to-column joints and connections

As per CSA standard, the beam-to-column joint should have a minimum resistance not less than the nominal plastic moment resistance of the beam,  $M_{pb}$ , at the column face. The factored resistance of the beam web-to-column connection shall be greater than the effects of gravity loads combined with shear forces induced by the plastic hinging in the beam.

## 3.6 Building Description

In this study, a fictitious mid-rise (8-storey) office buildings located on Site Class C (very dense soil and soft rock) in Vancouver is designed and analysed. At the roof level, dead load (DL) is 3.5 kPa and at the typical floor level DL = 4.0 kPa. From calculation, the snow load is 1.64 kPa and live load is 2.4 kPa, while 1.0 kPa is considered for claddings. The accidental torsional effects and the notional loads are neglected in design, while the  $P - \Delta$  effect is considered. For this building, three variants of seismic force resisting systems were proposed: a) MD-CBF, b) MD-MRF and c) Braced Dual System. To have a similar  $R_d R_0$  product for MD-CBF building and MD-MRF building the following types of CBF and MRF were selected:

- MD-CBF with  $R_d = 3.0$  and  $R_0 = 1.3$  leading to  $R_d R_0 = 3.9$  and
- MD-MRF with  $R_d = 3.5$  and  $R_0 = 1.5$  leading to  $R_d R_0 = 5.25$

The building plan is showed in Fig. 3.3. As illustrated, in both orthogonal directions, the typical span is 7.5 m, the floor area is  $60.5 \text{ m} \times 38 \text{ m} = 2299 \text{ m}^2$ , the typical storey height is 3.6 m and that of ground floor is 4.0 m. Thus, the building height is 29.2 m. Herein, the live load reduction factor is considered in design as specified in NBCC 2015 and the member sections for the gravity system are summarized in Table 3.2.

Table 3.2 Design of gravity frames

Storey	Sec. Beam	Girder	Int. Column	Ext. Column	Corner Column
8	W360 × 33	W410 × 67	W200 × 42	W200 × 36	W200X27
7	W360 × 33	W410 × 67	W200 × 42	W200 × 36	W200X27
6	W360 × 33	W410 × 67	W250 × 67	W200 × 46	W200X36
5	W360 × 33	W410 × 67	W250 × 67	W200 × 46	W200X36
4	W360 × 33	W410 × 67	W250 × 80	W200 × 59	W200X46
3	W360 × 33	W410 × 67	W250 × 80	W200 × 59	W200X46
2	W360 × 33	W410 × 67	W250 × 115	W200 × 86	W200X59
1	W360 × 33	W410 × 67	W250 × 115	W200 × 86	W200X59

### ***3.6.1 Design of MD-CBF office building using equivalent static force procedure***

As depicted in Fig. 3.3, the building is symmetric in both orthogonal directions and is braced by 4 identical MD-CBFs in each direction. The bracing system is multi-storey X-braces configuration plotted in elevation shown in Fig. 3.3. All columns of braced bays are designed to be continuous over two storeys and to be pinned to the base. The floors are considered as rigid diaphragms. The building seismic weight is  $W = 71768 \text{ KN}$ .

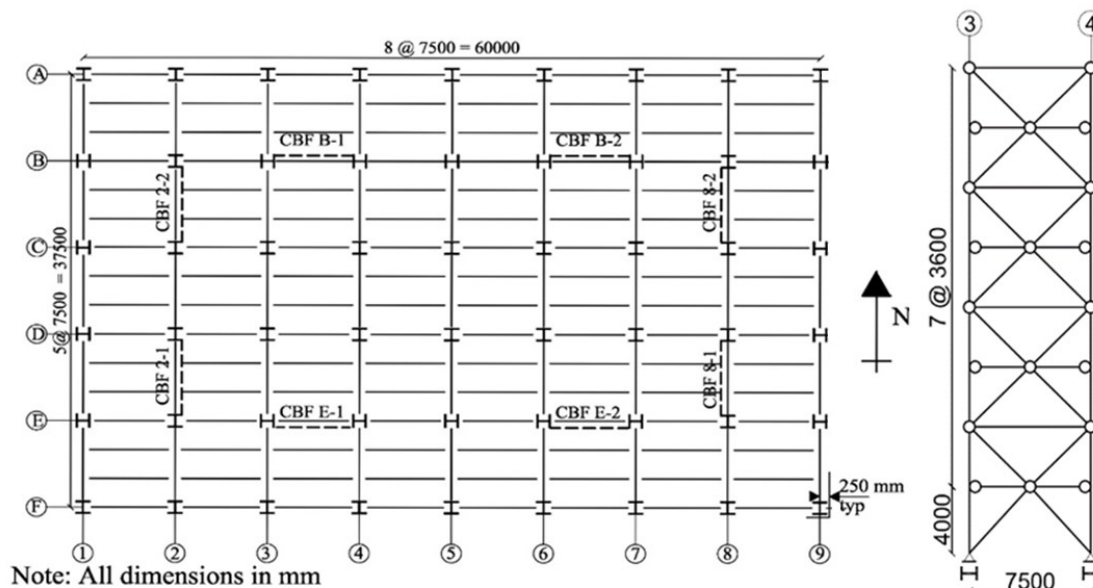


Fig. 3.3 Plan and elevation view of MD-CBF building

Following the Equivalent Static Force Procedure, the design period is calculated as  $2T_a$ , where  $T_a$  is calculated using Eq. 3.7. Thus, the spectrum ordinate is calculated for a fundamental period of building as:  $2T_a = 0.05 \times 29.2 = 1.46$  s. The design spectral ordinates for Site Class C in Vancouver computed for 2% probability of exceedance in 50 years are given in Table 3.1. Using Eq. 3.9 the base shear computed for the entire building is  $V = 6022$  KN.

The design summary of an MD-CBF system displaced in N-S direction is shown in Table 3.3. The P-delta effect was computed using Eq. 3.12 and the amplification factor computed at each floor resulted lower than 1.1 which means that no additional shear is added from the P-delta effect. For both HSS and W-shape members  $F_y = 350$  MPa was considered.

Table 3.3 Design summary of MD-CBF located on N-S direction

Storey	Brace	Beam	Column
8	HSS114 × 8.0	W460 × 106	W310 × 60
7	HSS152 × 8.0	W460 × 144	W310 × 60
6	HSS152 × 8.0	W460 × 144	W310 × 143
5	HSS178 × 9.5	W460 × 158	W310 × 143
4	HSS178 × 9.5	W460 × 177	W310 × 283
3	HSS178 × 9.5	W460 × 89	W310 × 283
2	HSS178 × 9.5	W460 × 177	W310 × 454
1	HSS203 × 9.5	W460 × 106	W310 × 454

The brace connections are designed according to CSA/S16 requirements as explained in previous sections and the design is summarized in Table 3.5. It is noted that the failure mode is net fracture and buckling of gusset plate which are ductile failure modes. The distribution of base shear along the building height normalized to base shear resulted from response spectrum analysis using ETABS software on a 3D model is plotted for one MD-CBF displaced in N-S direction in Fig. 3.4. The 1<sup>st</sup> mode period resulted from ETABS is  $T_1=1.376$  s. The base shear from response spectrum analysis is 6405 kN, which is greater than that from equivalent static method. However, the cross sections from Table 3.3 could still fulfill the seismic demand, thus, no revision is made regarding the design. The building characteristics are summarized in Table 3.4. The calculation was conducted in N-S direction.

Table 3.4 Characteristics of MD-CBF building from equivalent static method and response spectrum method

Building ID	$h_n$ (m)	W (kN)	Equivalent static method			Response spectrum method		
			$2T_a$ (s)	$S_a(T_a)$ (g)	V (kN)	$T_1$ (s)	$S_a(T_1)$ (g)	V (kN)
MD-CBF	29.2	71768	1.46	0.327	6022	1.374	0.343	6405

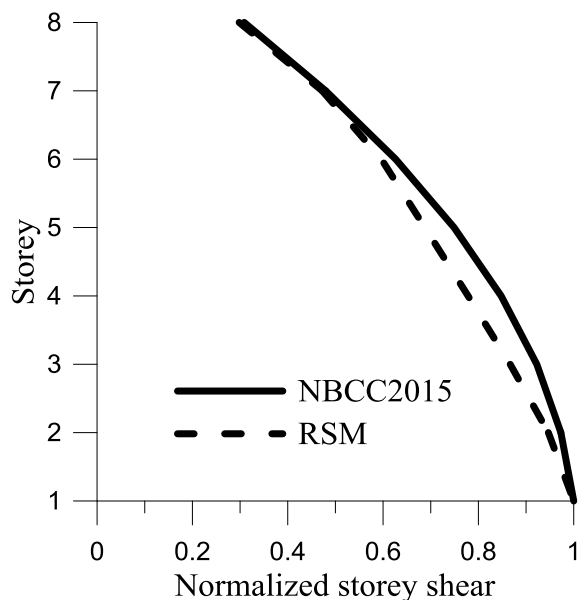


Fig. 3.4 Normalized base shear distribution of MD-CBF building from equivalent static method and response spectrum method

Because the building period is greater than 1.0s, dynamic analysis for wind load calculation according to NBCC 2015 was conducted and resulted that the response of building is in the elastic range under the wind load. The base shear resulted from wind load is 2612 KN for open terrain, thus, the earthquake load governs the design.

Table 3.5 Design summary of HSS brace to frame gusset plate connections

Storey	$L_w$ (mm)	$D_w$ (mm)	$t_g$ (mm)	$L_2$ (mm)	$W_w$ (mm)
8	370.00	6.00	10.00	298.92	564.33
7	500.00	6.00	11.00	397.40	752.44
6	500.00	6.00	10.00	396.90	752.44
5	560.00	7.50	14.00	448.52	847.73
4	560.00	7.50	14.00	448.52	847.73
3	560.00	7.50	14.00	448.52	847.73
2	560.00	7.50	14.00	448.52	847.73
1	610.00	8.00	14.00	443.15	930.46

### 3.6.2 Design of MD-MRF office building using equivalent static force procedure

Similarly, the same 8-storey fictitious office building braced by two MD-MRFs in each orthogonal direction is designed for Site Class C in Vancouver, B.C. All MD-MRFs are displaced on the perimeter. The MD-MRF in N-S direction has 3 adjacent bays of 7.5 m and the MD-MRF in E-W direction has 4 adjacent bays of 7.5 m as depicted in Fig. 3.5. The MD-MRF elevations are depicted in Fig. 3.6. The MRF columns are fixed to the base.

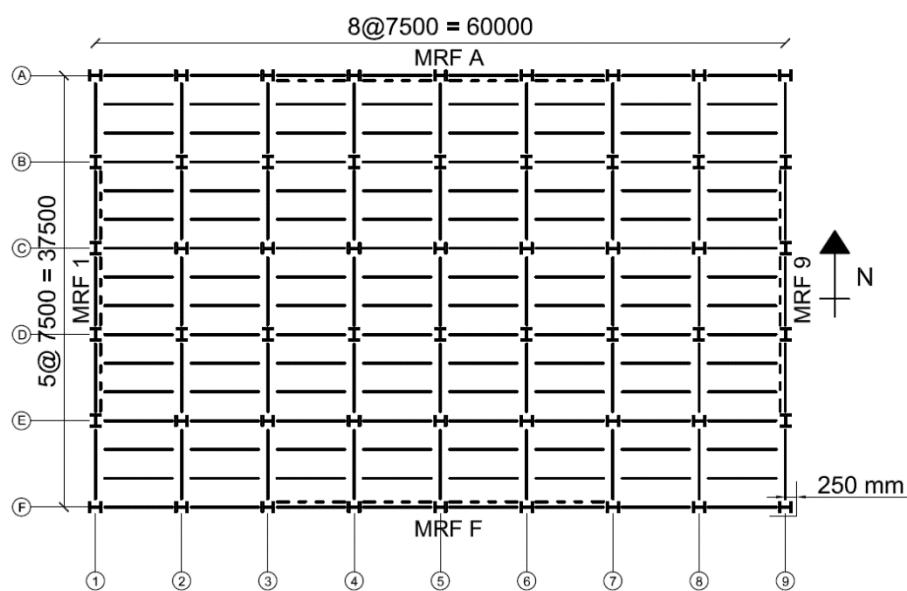


Fig. 3.5 Plan view of MD-MRF building

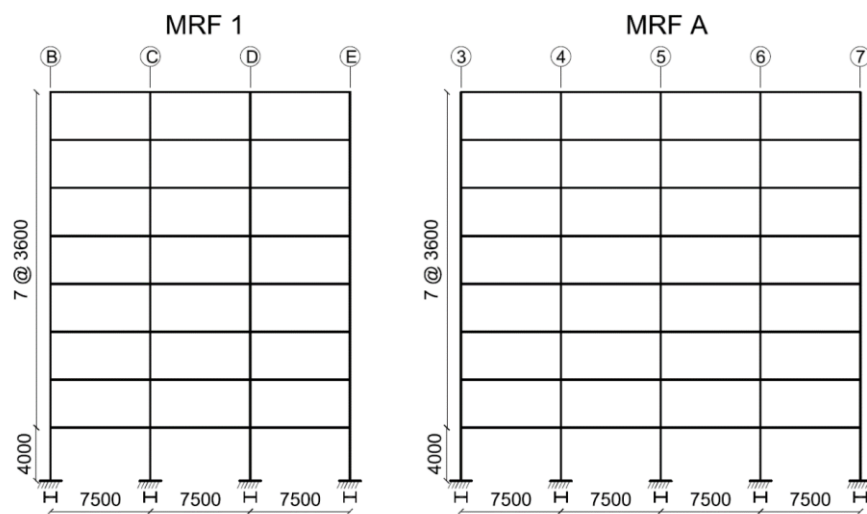


Fig. 3.6 Elevation view of MD-MRFs

The design of MD-MRFs follows the steps mentioned above. The fundamental period of building for preliminary design is taken as  $1.5T_a = 1.60$  s, where  $T_a$  is calculated with Eq. 3.8. The design base shear for the entire building is calculated with Eq. 3.9 and it resulted  $V = 4143$  KN. Performing the spectrum response analysis using ETABS software, the fundamental period resulted in  $T = 2.10$  s, the base shear is 3829 KN. However, it is found that the size of MD-MRF columns resulted from preliminary design should be slightly increase in order to satisfy the serviceability criteria which means a maximum interstorey drift lower than 2.5% as specified in the building code NBCC 2015. After the size of MRF columns was increased, it is found that when the MRF columns reach a demand to capacity ratio of 0.5 specified in Eq. (3.15) the serviceability limit could be met. The P-delta effect was verified for the MD-MRF building with increase column sizes and resulted that the amplification factor is below 1.4 which means that the building stability was achieved. However, for the bottom half floors (1<sup>st</sup> to 5<sup>th</sup> floor) the amplification factor resulted in the ranges 1.2 to 1.3 which means an increase in shear and bending capacity under seismic loads. The design cross sections of the MD-MRF displaced in both N-S and E-W direction are summarized in Table 3.7. In Fig. 3.7 is illustrated the distribution of normalized base shear along the building height as resulted from the static equivalent method and response spectrum method.

Table 3.6 Characteristics of MD-MRF building from equivalent static method and response spectrum method

Building ID	$h_n$ (m)	W (kN)	Equivalent static method			Response spectrum method		
			$1.5T_a$ (s)	$S_a(T_a)$ (g)	V (kN)	$T_1$ (s)	$S_a(T_1)$ (g)	V (kN)
MD-CBF	29.2	71768	1.60	0.305	4143	2.10	0.237	3829

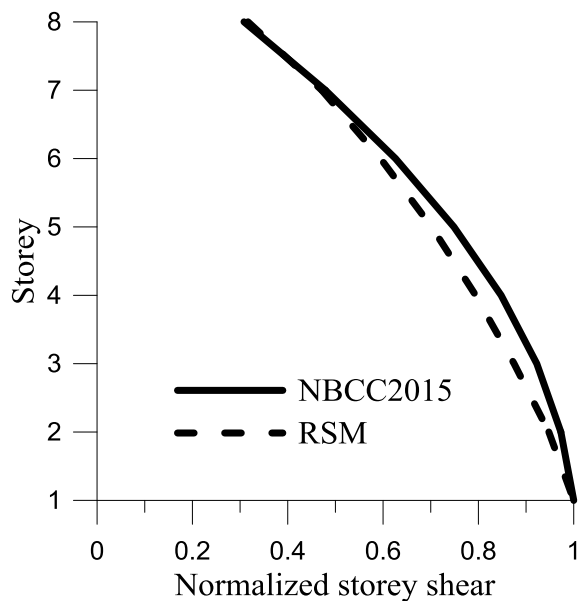


Fig. 3.7 Normalized base shear distribution of MD-MRF building from equivalent static method and response spectrum method

The dynamic procedure for wind load specified in NBCC 2015 is also performed for the MD-MRF building, which results in a total based shear of 2731 KN for open terrain. Thus, the earthquake load governs the design. The characteristic of 8-storey MD-MRF office building are provided in Table 3.6. The calculation was conducted in N-S direction.

Table 3.7 Design summary of MD-MRFs in N-S and E-W direction

Storey	N-S Frame			E-W Frame		
	Beam	Mid Col.	Side Col.	Beam	Mid Col.	Side Col.
8	W530 × 74	W360 × 347	W360 × 196	W460 × 68	W360 × 347	W360 × 196
7	W610 × 92	W360 × 347	W360 × 196	W530 × 101	W360 × 347	W360 × 196
6	W610 × 125	W360 × 634	W360 × 314	W610 × 113	W360 × 509	W360 × 262
5	W690 × 140	W360 × 634	W360 × 314	W690 × 125	W360 × 509	W360 × 262
4	W760 × 147	W360 × 677	W360 × 382	W690 × 140	W360 × 634	W360 × 382
3	W760 × 161	W360 × 677	W360 × 382	W760 × 147	W360 × 634	W360 × 382
2	W760 × 173	W360 × 744	W360 × 509	W760 × 161	W360 × 744	W360 × 421
1	W840 × 176	W360 × 744	W360 × 509	W760 × 173	W360 × 744	W360 × 421

### 3.6.3 Design of office building with Braced Dual System using equivalent static force procedure

The Braced Dual System consists of four MD-CBF frames and two MRFs displaced in each orthogonal direction as shown in Fig. 3.8.

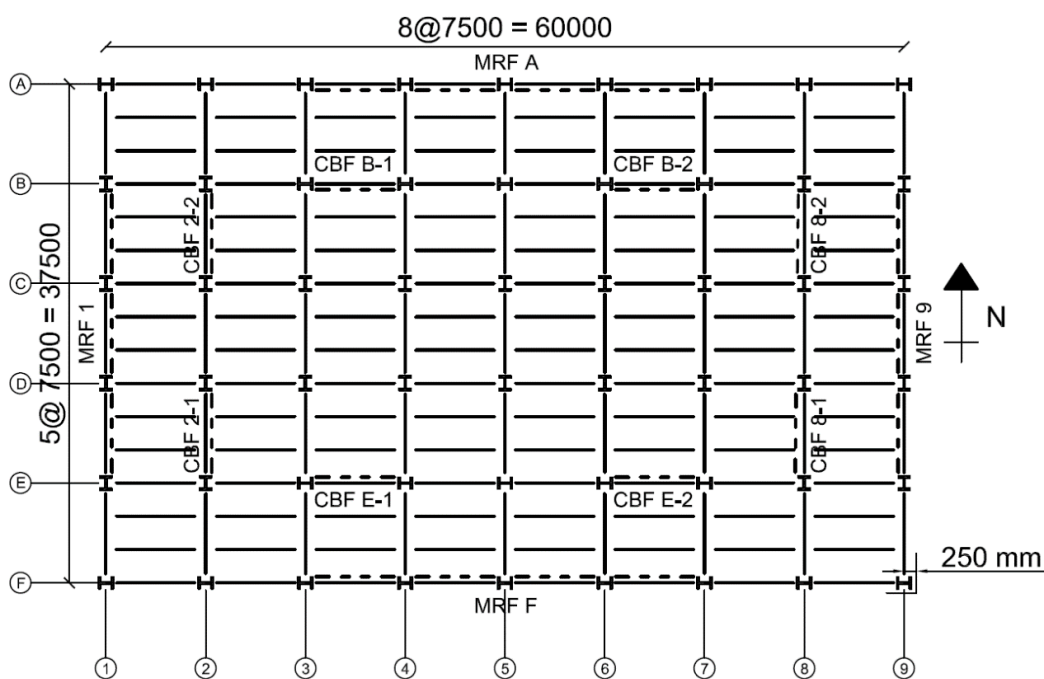


Fig. 3.8 Plan view of building with Braced Dual System

The MD-CBFs are designed to resist 100% of the applied factored storey shear force and the MRF frame is designed to act as a backup frame designed to resist an additional 25% of the design seismic forces. As aforementioned, in User's Guide of NBCC 2015 it is recommended to consider the same  $R_dR_0$  as per the selected concentrically braced frame and to distribute the storey shear to both structural systems proportional to their relative stiffness using the principles of structural mechanics. Furthermore, a similar approach is considered for the design of Ductile Plate Walls that is provided in CSA/S16 Clause 27.9. Thus, for designing Ductile Plate Walls it is required that the infill plate should resist 100% of the applied factored storey shear force and "the beams at every storey shall have

sufficient flexural resistance such that at least 25% of the applied factored storey shear force is resisted by beams and columns forming a moment-resisting frame”. This idea complies with the design concept of dual systems specified in ASCE/SEI 7-10.

Table 3.8 Design MRF cross sections of building as a backup frame of the dual system

Storey	N-S Frame			E-W Frame		
	Beam	Mid Col.	Side Col.	Beam	Mid Col.	Side Col.
8	W310 × 52	W360 × 101	W360 × 79	W360 × 39	W360 × 101	W360 × 79
7	W360 × 57	W360 × 101	W360 × 79	W410 × 46	W360 × 101	W360 × 79
6	W460 × 60	W360 × 122	W360 × 91	W460 × 52	W360 × 122	W360 × 91
5	W460 × 68	W360 × 122	W360 × 91	W460 × 60	W360 × 122	W360 × 91
4	W460 × 74	W360 × 147	W360 × 110	W460 × 68	W360 × 134	W360 × 101
3	W460 × 82	W360 × 147	W360 × 110	W460 × 68	W360 × 134	W360 × 101
2	W460 × 82	W360 × 179	W360 × 122	W460 × 74	W360 × 179	W360 × 122
1	W530 × 85	W360 × 179	W360 × 122	W460 × 82	W360 × 179	W360 × 122

The MD-CBF system is designed as presented in Section 3.6.1. For design, the same period,  $2T_a=1.46$  s, as per the design of the MD-CBF building is considered, and the base shear is 6022 KN. The backup MRF was designed to carry a base shear of  $25\% \times 6022 = 1505$  KN. For the backup MRF system, the capacity to demand ratios for MRF columns are kept close to 1.0, since for dual system there is no concern related to the storey drift due to the high stiffness provided by the MD-CBF frame. Thus, the MD-CBF system has the same cross sections as shown in Table 3.3, while the cross-sections for the MRF are summarized in Table 3.8. Using ETABS software on a 3D model, the 1<sup>st</sup> mode period in N-S direction is  $T_1=1.343$  s, and the base shear resulted from response spectrum analysis is  $V= 6576$  KN. The normalized distribution of base shear along the building height is depicted in Fig. 3.9

Normalized base shear distribution of Braced Dual System building from equivalent static method and response spectrum method.

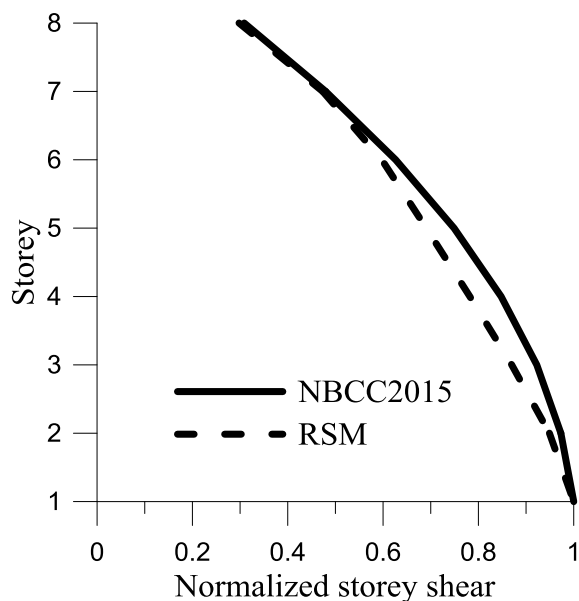


Fig. 3.9 Normalized base shear distribution of Braced Dual System building from equivalent static method and response spectrum method

The characteristics of 8-storey Braced Dual System are given in Fig. 3.9. The calculation is based on N-S direction.

Table 3.9 Characteristics of MD-MRF building from equivalent static method and response spectrum method

Building ID	$h_n$ (m)	W (kN)	Equivalent static method			Response spectrum method		
			$2T_a$ (s)	$S_a(T_a)$ (g)	V (kN)	$T_1$ (s)	$S_a(T_1)$ (g)	V (kN)
MD-CBF	29.2	71768	1.46	0.327	6022	1.343	0.349	6433

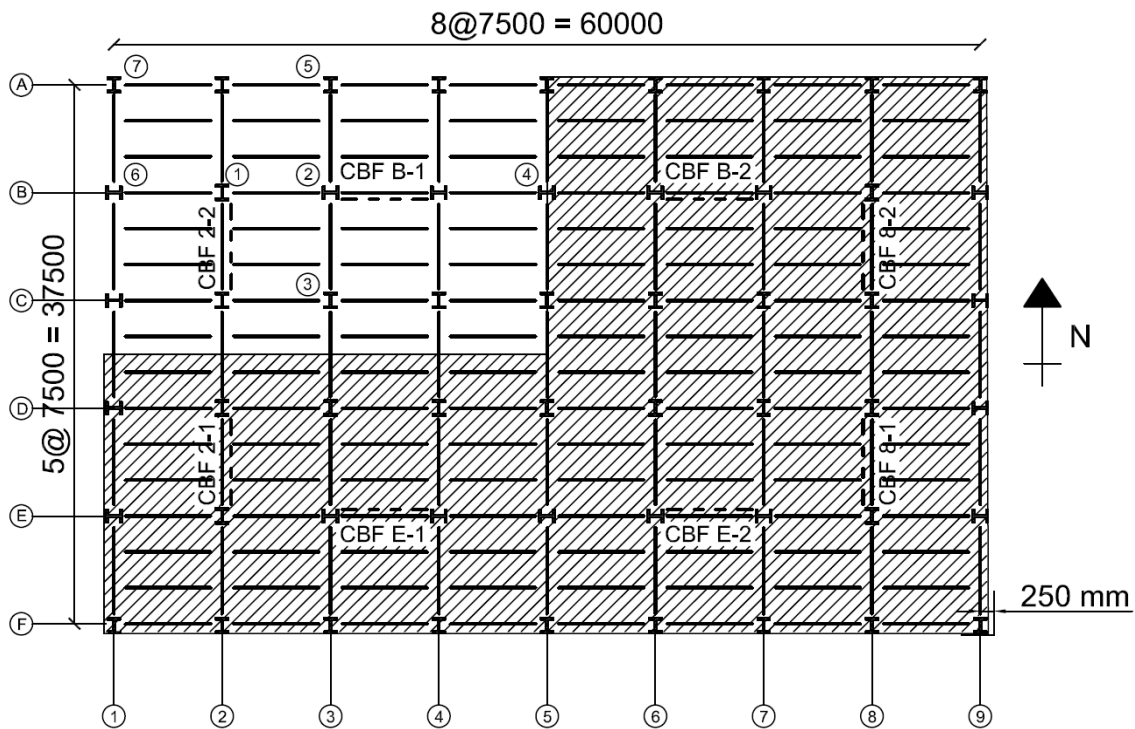
### 3.7 Seismic Response of MD-CBF Building Based on Nonlinear Time-History Analysis

To assess the seismic behavior of the prototype 8-storey MD-CBF office building, a comprehensive nonlinear time history analysis is performed. In order to accurately replicate the nonlinear behavior of the structure, a detailed numerical model is developed using the OpenSees framework.

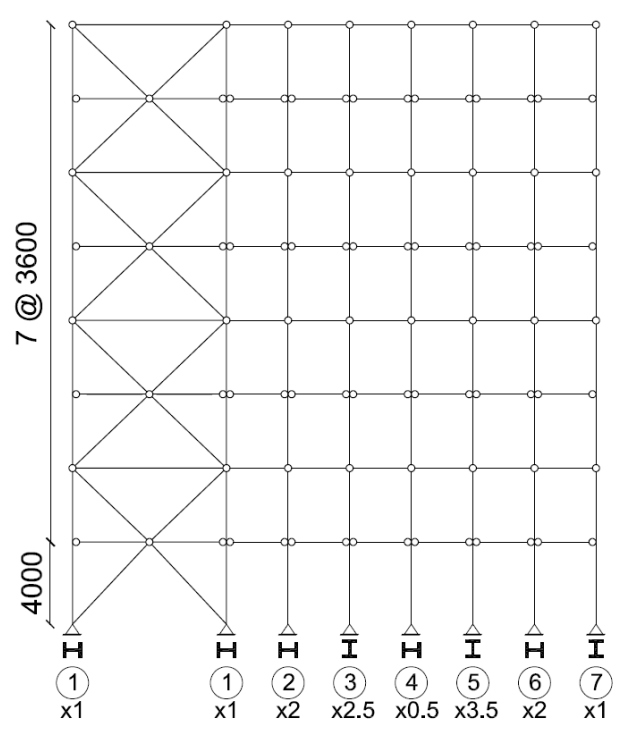
#### 3.7.1 Modeling of MD-CBF building using OpenSees

The geometry of the 8-storey building is symmetrical in both orthogonal directions, as well as the displacement of MD-CBFs. Based on the symmetry feature, only one fourth of the building is simulated using OpenSees as shown in Fig. 3.10. As illustrated, gravity columns are modeled as leaning columns to replicate the stiffness provided by gravity columns as well as to account for P-delta effects.

It is noted that all the columns are continuous over two storeys. All beams are pin connected to column faces. The uniaxial Giuffre-Menegotto-Pinto material, known as *Steel02* material, is used to model the frame elements. According to Lamarche and Tremblay (2008), this material is able to capture the Bauschinger effect and residual stresses accurately. The parameters proposed by Aguero et al. (2006) is adopted in this study for modeling the steel material. In addition, a fatigue material is assigned to the HSS braces to account for the low-cycle fatigue effect, such that the brace fracture could be simulated. The equation proposed by Tirca and Chen (2014) given herein as Eq. (2.4) is used to estimate the parameter,  $\epsilon_{0,pred}$ , required for the definition of fatigue material.



(a)



(b)

Fig. 3.10 Opensees model of the MD-CBF building: (a) model of 1/4 building; (b) elevation of model studied when MD-CBF acts in N-S direction

To accurately replicate the nonlinear response of braces, each brace is model using 16 force based nonlinear beam-column elements with distributed plasticity using fiber discretized cross sections and each element contains three Gauss-Lobatto integration points. The HSS cross sections is discretized into 240 fibers and is modeled with round corners (Tremblay, 2008). The fiber cross section is shown in Fig. 3.11.

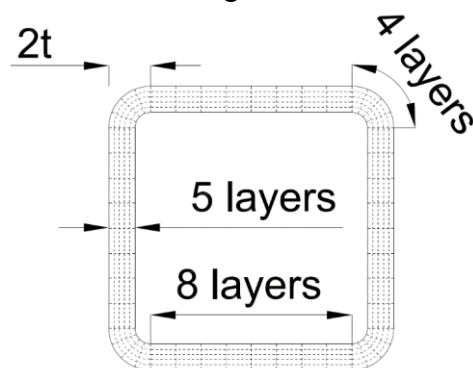


Fig. 3.11 HSS cross section fiber discretization

An initial imperfection of  $L/500$  was assigned to braces in the out-of-plane direction to allow the out-of-plane buckling of braces, where  $L$  is the brace length (Ziemian, 2010). The gusset plate is modeled using springs assigned in the Zerolength element in OpenSees as shown in Fig. 3.12.

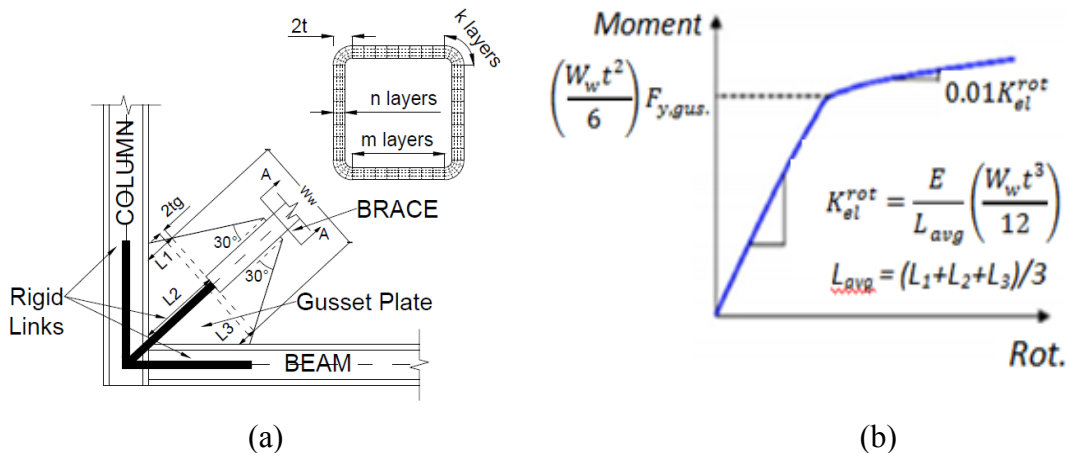


Fig. 3.12 The HSS brace to frame connection model: (a) geometry, (b) nonlinear rotational spring model in the brace buckling plan

In the Zerolength element were assigned two rotational springs and one torsional spring (Uriz and Mahin, 2008). The stiffness of these springs is calculated as discussed in chapter two. The MD-CBF beams and columns are modeled with nonlinear beam column elements with distributed plasticity. The W-shape cross section used for beams and columns is discretized into 120 fibers, whereas each flange and web contain 40 fibers. The fiber discretization of the W-shape cross section is shown in Fig. 3.13.

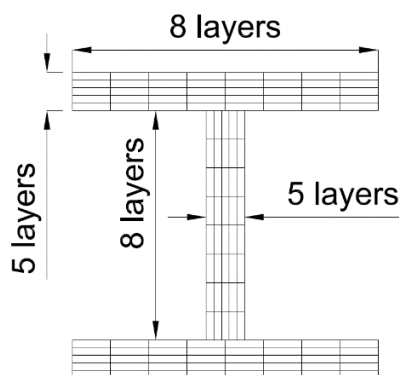


Fig. 3.13 W-shape cross section fiber discretization

Each MD-CBF column is modeled with 8 nonlinear beam column elements with four integration points for each element. The leaning columns are connected to the MD-CBF frame with rigid truss elements to simulate the effect of rigid floor diaphragm. The gravity columns are connected by rigid links and are modeled with elastic beam column elements. A 2% Rayleigh damping was assigned to the 1<sup>st</sup> and 3<sup>rd</sup> vibration mode and only mass proportional damping is considered.

The fundamental period of vibration in the N-S direction is calculated through Eigen value analysis using OpenSees. Vibration periods of buildings are calculated based on elastic stiffness of the structure. Table 3.10 illustrates the periods of first three modes calculated

in N-S direction from OpenSees and also from ETABS for comparison purposes. As resulted the difference between the two software is 1.5%, therefore negligible.

Table 3.10 Vibration periods of MD-CBF building in ETABS and OpenSees (N-S)

Vibration Period	Eigen Value Analysis	
	ETABS	OpenSees
<b>T<sub>1</sub></b>	1.376 s	1.395 s
<b>T<sub>2</sub></b>	0.478 s	0.484 s
<b>T<sub>3</sub></b>	0.263 s	0.267 s

### 3.7.2 Selection of ground motions

Vancouver, B.C., is located in the vicinity of the Juan de Fuca plate and the North America Plate. The Juan de Fuca plate converges under the North America plate in the Cascadia Subduction Zone. In this zone, megathrust earthquakes with a predicted moment magnitude  $M_w$  in the range of 8 to 9 could occur for a return period of about 500 years (Atkinson and Goda, 2011; Tesfamariam and Goda, 2015). Thus, the building stock in Vancouver is exposed to crustal and megathrust subduction inter-plate earthquakes. There are also two seismic sources with an intra-slab subduction mechanism. This type of earthquake was the magnitude 6.8 Nisqually (USA) earthquake in 2001 and the magnitude 6.7 Olympia (USA) earthquake in 1949.

The characteristics of inter-plate subduction ground motions differ from crustal ground motions in terms of amplitude, Trifunac duration, and frequency content (Tirca et al., 2015). To assess the building response caused by the potential megathrust earthquake, records of the main shock Tohoku earthquake in Japan (March 2011) registered on Site Class C that has similar geotechnical profile to Vancouver are employed.

In this light, two suites of 11 ground motions each, one suite of crustal ground motions and one suite of subduction ground motions, are selected and scaled according to NBCC 2015 such that the mean spectrum of each suite is not less than 90% of the design spectrum in the period range of  $0.2T_1$  to  $2.0T_1$ .

The set of crustal ground motions is selected from the Northridge earthquake, Loma Prieta earthquake, and Imperial Valley earthquake. Eleven ground motions corresponding to Site Class C ( $360 \text{ m/s} < V_{s30} < 760 \text{ m/s}$ ) are selected from the PEER-NGA database (<https://ngawest2.berkeley.edu/>). The value of peak ground acceleration,  $PGA$ , peak ground velocity,  $PGV$ , the Trifunac duration,  $t_D$ , the main period of ground motion,  $T_p$ , the average period of ground motion,  $T_m$ , and the shear wave velocity are given in Table 3.11 respectively.

Table 3.11 Seismic characteristics of crustal ground motions selected

ID	NGA	Event	$M_w$	Comp (°)	PGA (g)	PGV (m/s)	PGV /PGA	$t_D$ (s)	$T_p$ (s)	$T_m$ (s)
C1	187	1979, Imperial Valley	6.53	225	0.126	0.204	0.17	18.67	0.16	0.66
C2	779	1989, Loma Prieta	6.93	000	0.525	0.917	0.18	10.15	0.70	0.80
C3	787	1989 Loma Prieta	6.93	360	0.277	0.313	0.12	11.61	0.30	0.69
C4	787	1989, Loma Prieta	6.93	270	0.207	0.314	0.15	12.66	1.00	0.88
C5	802	1989, Loma Prieta	6.93	090	0.321	0.434	0.14	8.02	0.22	0.57
C6	983	1994 Northridge	6.69	022	0.428	0.837	0.20	12.49	0.76	1.32
C7	1013	1994 Northridge	6.69	334	0.333	0.548	0.17	6.62	0.42	0.80
C8	1052	1994 Northridge	6.69	090	0.312	0.340	0.11	10.10	0.32	0.67
C9	1083	1994 Northridge	6.69	170	0.131	0.132	0.10	15.86	0.16	0.59
C10	1085	1994 Northridge	6.69	011	0.963	1.010	0.11	7.09	0.32	0.76
C11	1086	1994 Northridge	6.69	090	0.622	0.647	0.11	6.84	0.52	0.79

The scaled crustal ground motions spectra are shown in Fig. 3.14. The ground motions were scaled such that the mean to much or be above the design spectrum in the period range of  $0.2T_1$  to  $2T_1$ . The design spectrum for site Class C is derived from the Uniform Hazard Spectrum for North Vancouver with a 2% probability of exceedance in 50 years.

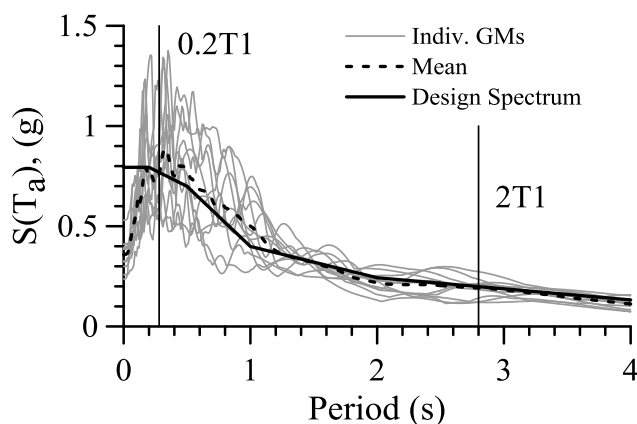


Fig. 3.14 Response spectrum of scaled crustal GMs for 8-storey MD-CBF building. The subduction ground motion set consists of eight  $M_w$ 9 subduction ground motion records from earthquake in Japan Tohoku that match the geotechnical profile for Vancouver site Class C and three intra-plate subduction ground motions. All Tohoku motion records are from K-NET stations and their characteristics are given in Table 3.12. The scaled spectra of subduction ground motion records are shown in Fig. 3.15.

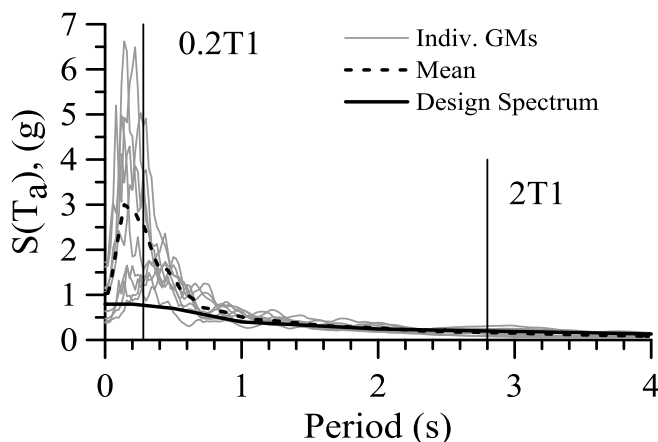


Fig. 3.15 Response spectrum of scaled subduction GMs for 8-storey MD-CBF building

Table 3.12 Seismic characteristics of selected subduction GM records

ID	Station	Event	Comp (°)	PGA (g)	PGV (m/s)	PGV /PGA	$t_D$ (s)	$T_p$ (s)	$T_m$ (s)
*S1	FKS005	2011 Tohoku	EW	0.45	0.35	0.084	92	0.15	0.32
*S2	FKS009	2011 Tohoku	EW	0.86	0.56	0.066	66	0.18	0.27
*S3	FKS010	2011 Tohoku	EW	0.83	0.44	0.054	74	0.20	0.20
*S4	MYG001	2011 Tohoku	EW	0.43	0.23	0.055	83	0.26	0.27
*S5	MYG004	2011 Tohoku	EW	1.22	0.48	0.004	85	0.25	0.26
*S6	IBR004	2011 Tohoku	EW	1.03	0.38	0.038	33	0.15	0.21
*S7	IBR006	2011 Tohoku	EW	0.78	0.30	0.039	36	0.12	0.25
*S8	TCG009	2011 Tohoku	EW	0.15	0.15	0.102	54	0.14	0.52
**S9	Gig Harbor Fire Station	2001 Nisqually	270	0.12	0.12	0.101	27	0.44	0.48
**S10	Hwy Test Lab	1949 Olympia	356	0.27	0.21	0.08	23	0.32	0.47
**S11	Hwy Test Lab	1949 Olympia	86	0.27	0.21	0.08	18	0.32	0.47

\*K-NET database: <http://www.kyoshin.bosai.go.jp/>

\*\*COSMOS database: <https://strongmotioncenter.org/>

Similarly, the spectrum of subduction record is scaled against the design spectrum for Vancouver.

Compared to crustal ground motions, spectra of subduction ground motions show higher pseudo acceleration. Moreover, the Trifunac duration of inter-plate subduction ground motions is in average 80 s versus 12 s of crustal ground motions and the total duration of any Tohoku record is about 300 s. The Trifunac duration of the intra-plate subduction records (S9, S10, and S11) is about 24s. However, the  $T_p$  and  $T_m$  value is around two times greater than those resulted from inter-plate subduction records

### 3.7.3 Seismic response of MD-CBF building subjected to crustal GMs from time history analysis

In addition to the duration of the ground motion record, an additional 10 seconds of zero amplitude was added to account for the free vibration response in the nonlinear analysis. The seismic response of the MD-CBF building is presented in terms of interstorey drift, residual interstorey drift, and floor acceleration. In Fig. 3.16 it is showed the maximum interstorey drift, residual interstorey drift, and floor acceleration resulted for the 8-storey building subjected to crustal ground motions, as well as their mean value and mean+SD, where SD is the standard deviation.

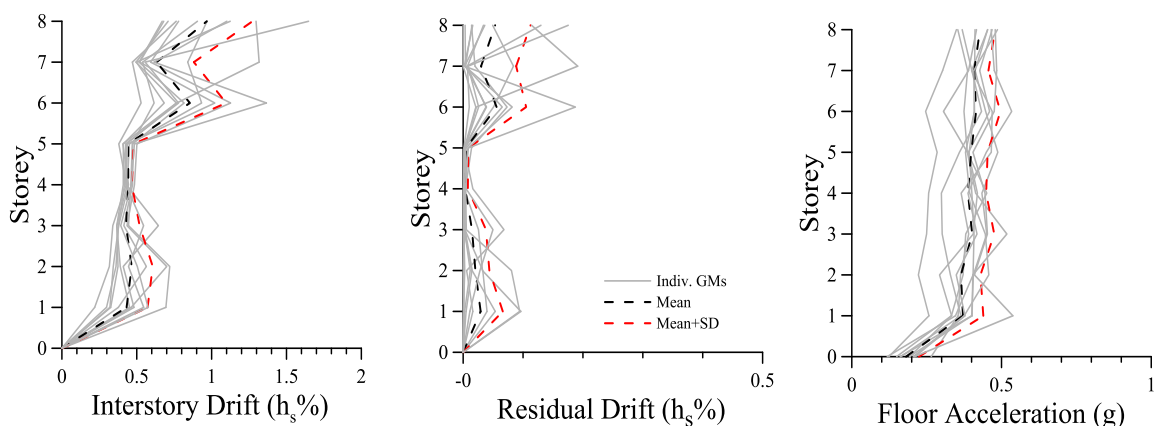


Fig. 3.16 Nonlinear response of 8-storey MD-CBF building subjected to crustal GMs

As resulted from Fig. 3.16, the mean interstorey drift of the building under the 11 crustal ground motions is around 1%; the mean residual interstorey drift is less than 0.1% $h_s$ , and the average floor acceleration is less than 0.5g. The maximum interstorey drift of 1.37%  $h_s$  occurs at the 6<sup>th</sup> floor under ground motion #C8. The maximum roof drift of 1.65%  $h_s$  and occurred under ground motion #C11. Moreover, the peak residual interstorey drift at roof also occurred under ground motion #C11, as well.

The behavior of the 6<sup>th</sup> floor HSS braces subjected to ground motion #C8 is plotted in Fig. 3.17 and that of HSS braces located at the roof level subjected to ground motion #C11 is showed in Fig. 3.18. As depicted in Fig. 3.17b the right HSS brace was the first reaching buckling in compression and at time step  $t_1 = 11.1$  s it reached the peak axial deformation in compression of 34 mm. Meanwhile, at the same time step ( $t_1=11.1$  s) the left brace experienced yielding in tension and the peak axial deformation in tension of about 23 mm. In the following cycle ( $t_2=11.66$ s) the left brace experienced the peak axial deformation in compression about 20mm, while the right brace was in tension below the yielding force.

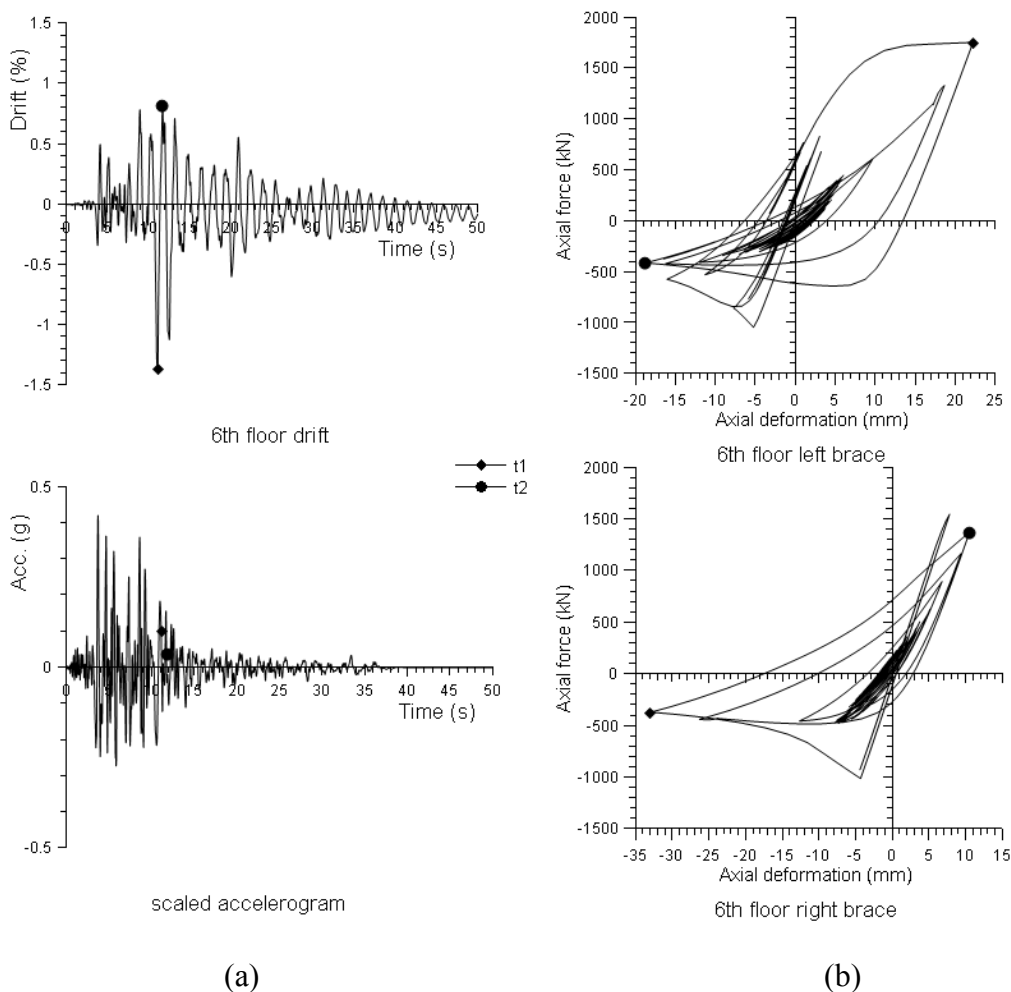


Fig. 3.17 Hysteretic response of 6th floor HSS braces under GM #C8: (a) interstorey drift time history and accelerogram, (b) hysteresis loops of left and right HSS brace

As illustrated in Fig. 3.18 the maximum interstorey drift of 1.7% occurred at  $t_1 = 7.04$  s at roof under #C11. At this time step the right brace experienced yielding in tension while the left brace reached the peak axial deformation in compression (30 mm). In the following cycle ( $t_2 = 7.90$ s) the right brace experienced the peak axial deformation in compression (30 mm) while the left brace exhibited a tensile force below yielding.

In all analyses conducted to study the seismic response under the eleven crustal ground motions no brace fatigue material failure is observed, which means no fracture of brace occurred at design level.

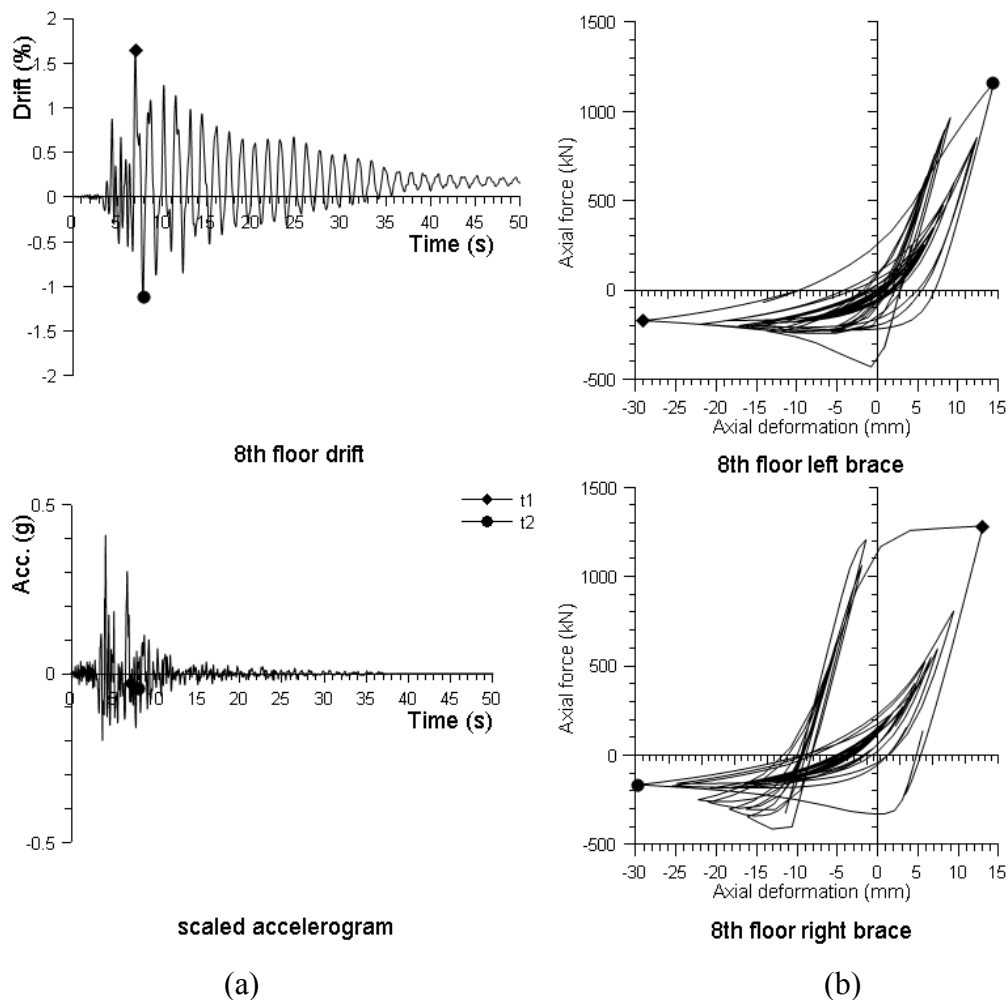


Fig. 3.18 Hysteretic response of 8th floor braces under GM #C11: (a) interstorey drift time history and accelerogram, (b) hysteresis loops of left and right HSS brace

### 3.7.4 Seismic response of MD-CBF building subjected to subduction GMs from time history analysis

Nonlinear time history analysis was performed using the suit of subduction ground motions. The interstorey drift, residual interstorey drift, and floor acceleration are shown in Fig. 3.19. As illustrated, at design level, the maximum of mean interstorey drift is around  $1.5\%h_s$ , the maximum of mean residual drift is around  $0.1\%h_s$  and the peak of mean floor acceleration is around  $1.0g$ . The mean plus standard deviation is also provided in Fig. 3.19.

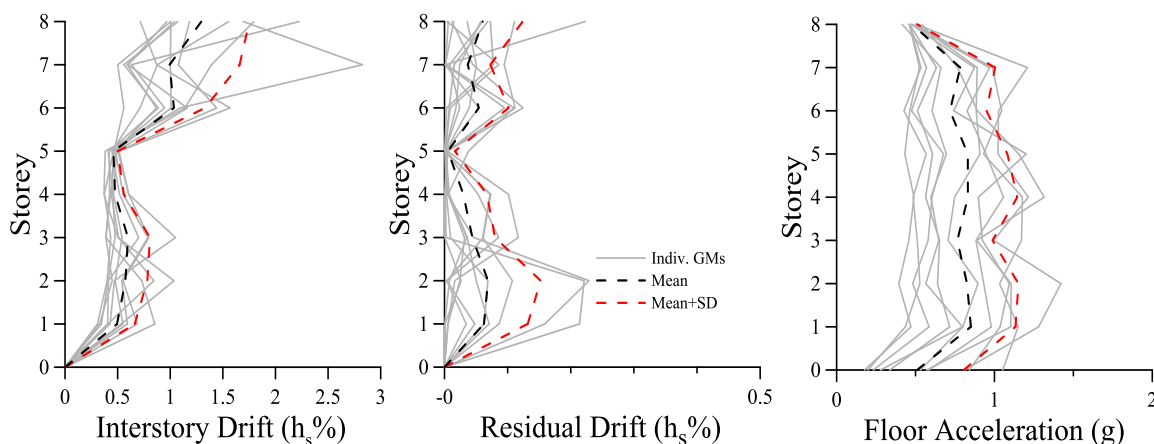


Fig. 3.19 Nonlinear seismic response of MD-CBF building subjected to subduction GMs

However, unlike for crustal ground motions, the HSS brace fracture was observed under #MYG001 record. The fracture occurs on both left and right HSS braces of the 7<sup>th</sup> floor. As depicted in Fig. 3.20, the occurrence of braces fracture leads to large lateral deformation of that floor (7<sup>th</sup> floor) where the peak interstorey drift is  $2.83\%h_s$ . However, after that, the demand was substantially reduced, and the average residual drift is about  $0.1\%h_s$ . The average peak of floor acceleration is about  $0.9g$  which is two times larger than that resulted under crustal records.

In Fig. 3.20 it is showed the hysteretic behavior of the 7<sup>th</sup> floor left and right HSS braces, as well as the time-history series of interstorey drift recorded at the same floor and the ground motion accelerogram. As can be seen from the hysteresis response of braces fracture due to low-cycle fatigue occurred and the brace cannot sustain any force (see the flat line). Since brace fracture occurred at the design level, the seismic response of the building under ground motion #MYG001 is further discussed in the latter section by means of the incremental dynamic analysis, IDA.

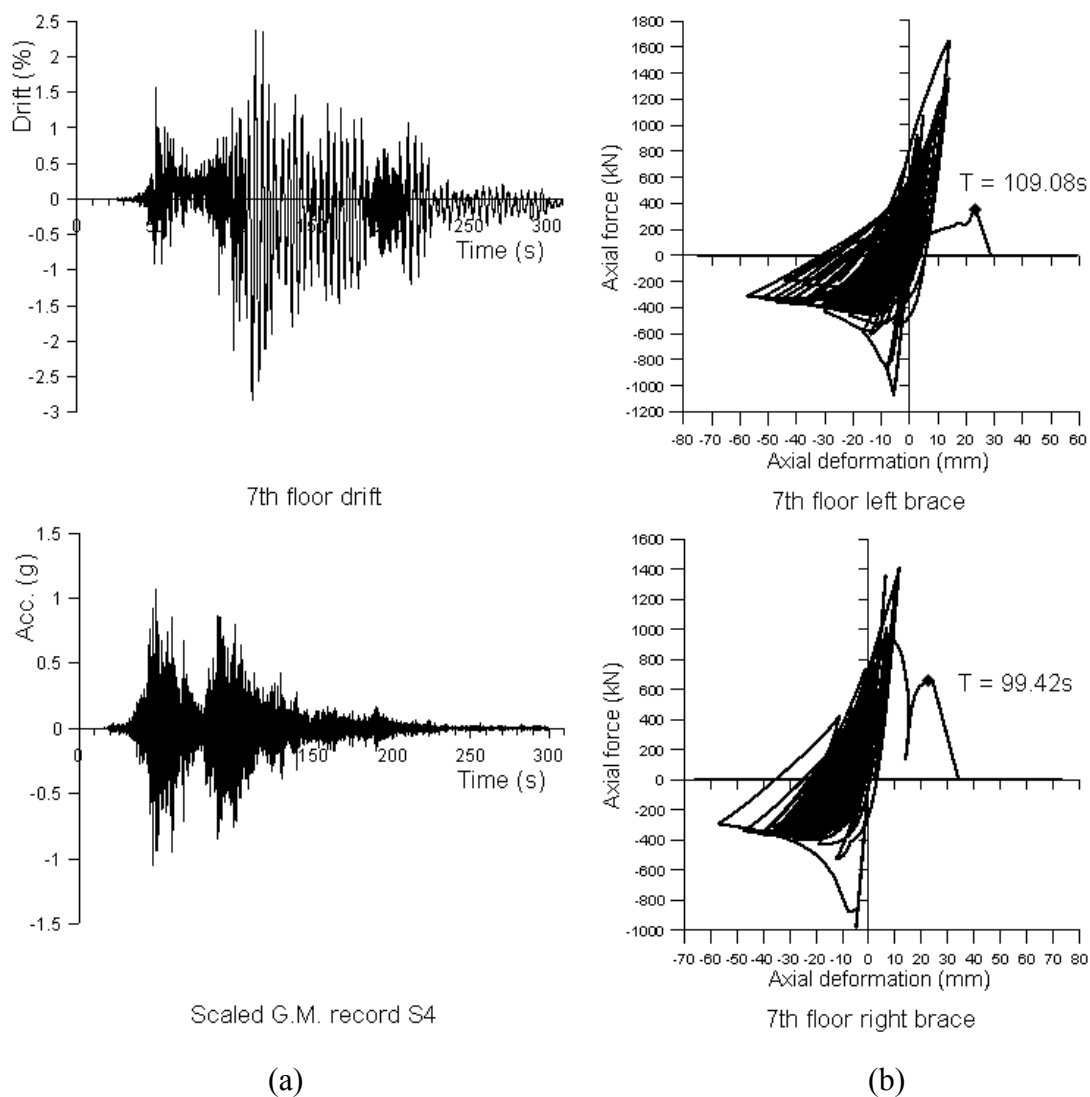


Fig. 3.20 Hysteretic response of 7th floor braces under GM #S4: (a) interstorey drift time history and accelerogram, (b) hysteresis loops of left and right HSS brace

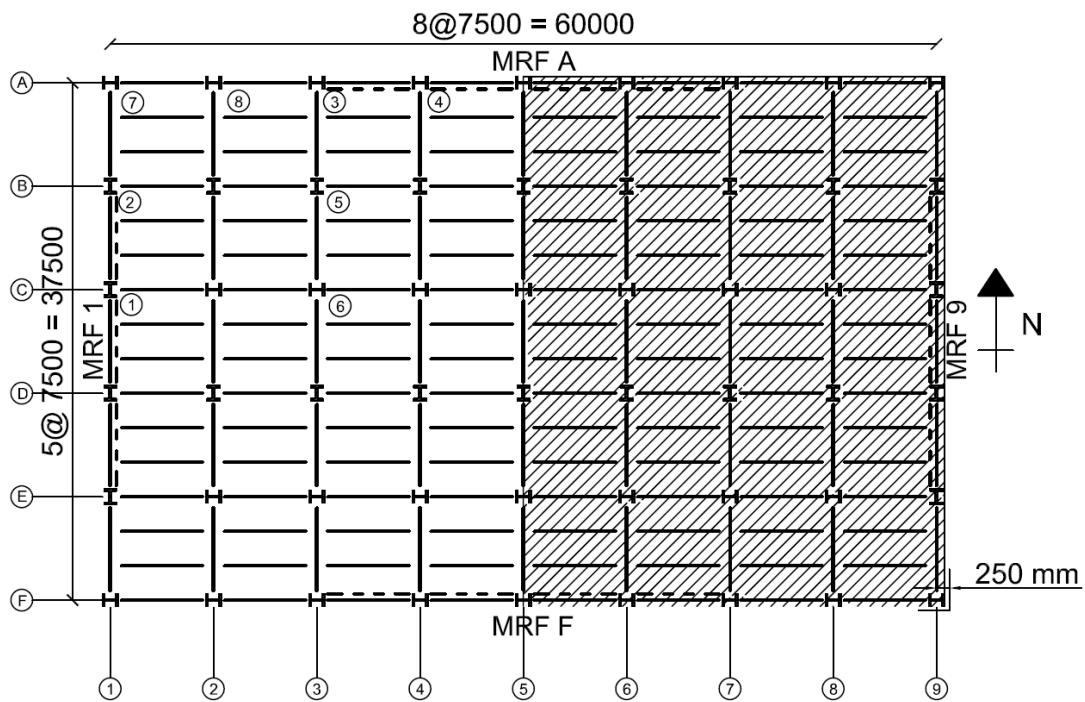
## 3.8 Seismic Response of MD-MRF Building Based on Nonlinear Time-History Analysis

### 3.8.1 Modeling of MD-MRF building using OpenSees

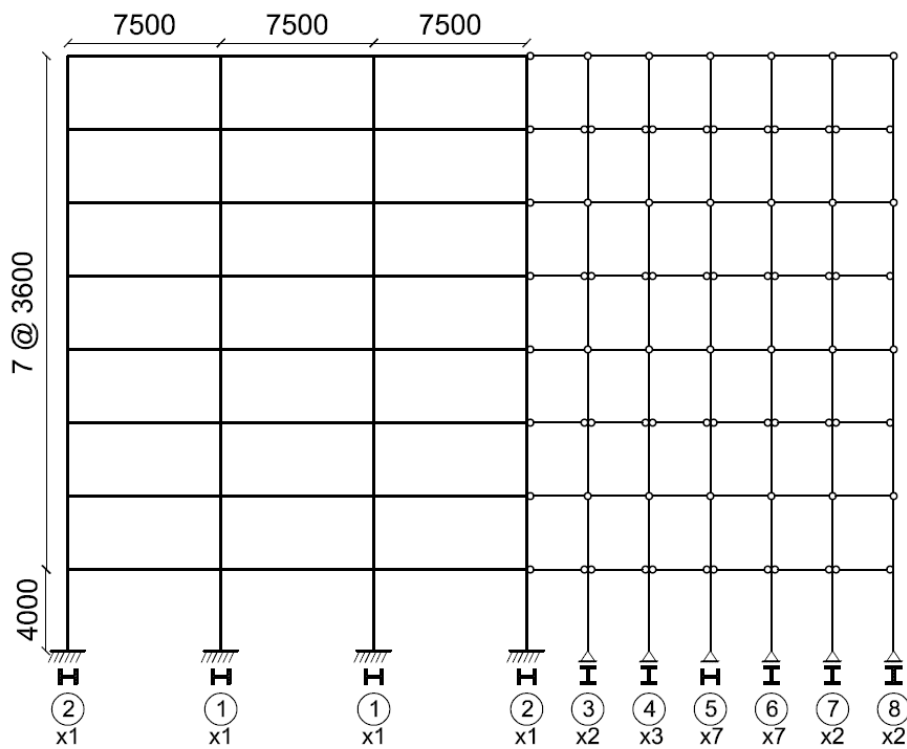
Based on the symmetry feature, only half of the building is simulated using OpenSees as shown in Fig. 3.21a. The numerical model is shown in Fig. 3.21b. It is noted that in this study, only the frame in N-S direction was modeled and analyzed.

The numerical model of MRF beam proposed by Bosco and Tirca (2017) is adapted in this study. To accurately replicate the nonlinear response, the MRF beams are modeled with the “*BeamWithHinges*” element with two-point Gauss-Radau integration scheme developed in OpenSees. Each column is modeled using 8 nonlinear beam-column elements with distributed plasticity using fiber discretized cross sections and each element contains four Gauss-Lobatto integration points. The plastic hinge regions of beam cross sections are discretized into fibers. The *Steel02* material is assigned to beam and column members. The column cross section is discretized into 240 fibers, which is the same as that considered for MD-CBF columns as shown in Fig. 3.13. The beam cross section is discretized into 518 fibers as shown in Fig. 3.22.

Furthermore, in order to account for the deterioration of MRF beam, the low-cycle fatigue material was wrapped to parent *Steel02* material. The low-cycle fatigue material parameters for  $\varepsilon_{0,min}$ ,  $\Delta\varepsilon_0$  and  $m$  are those proposed by Bosco and Tirca (2017) and their equation is presentment in Chapter 2.



(a)



(b)

Fig. 3.21 Opensees model of the MD-MRF building: (a) model plan; (b) model Elevation in N-S direction

As depicted in Fig. 3.22, it was proposed a linear variation between a minimum value provided by  $\varepsilon_{0,min}$  and a maximum value ( $\varepsilon_{0,min} + \Delta\varepsilon_0$ ). From experimental tests it was observed that flanges started to degrade from the far end of cross-section with almost not degradation in vicinity of W-shape web. Thus, the low-cycle fatigue material was assigned only to flanges to show their degradation. During several experimental tests examined, no degradation of the web was identified. All beams and columns are made of W-shape cross-sections with  $F_y = 350$  MPa.

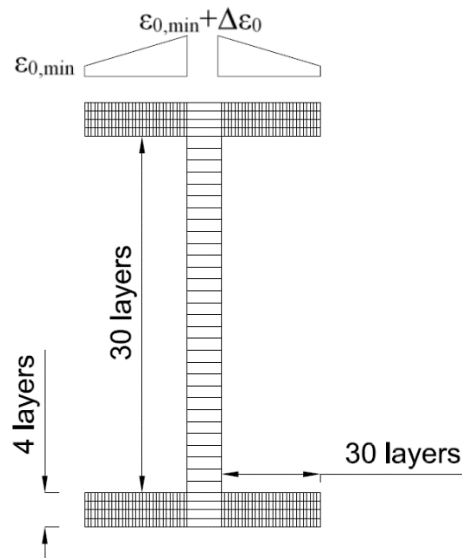


Fig. 3.22 Fiber discretization of MRF beam cross section

The gravity columns are modeled with elastic beam column elements and are connected to the MRF with truss elements to account for rigid floor diaphragm effect. The periods of first three modes are shown in Table 3.13. It is noted that the panel zone is reinforced with a steel plate, the damage is not expected to form in the panel zone, thus, the panel zone is not modeled. In general, to connect the centerline of a beam end to the centerline of a column, in the model, a rigid link could be used. However, in this model, rigid links were not used, since it was found that using rigid links, it would considerably reduce the

interstorey drift. For comparison purpose, the periods of first three vibration modes resulted from OpenSees using a 2D model and from ETABS using a 3D model are given in Table 3.13. As resulted, there is a small difference.

Table 3.13 Vibration periods of MD-MRF 8-st. building in ETABS and OpenSees (N-S)

Vibration Period	Eigen Value Analysis	
	ETABS	OpenSees
$T_1$	2.376 s	2.103 s
$T_2$	0.855 s	0.792 s
$T_3$	0.460 s	0.428 s

### 3.8.2 Selection of ground motions

The same suites of ground motions used for the MD-CBF building are used for analysis of the MD-MRF building and the same scaling method is applied. However, due to the difference in the fundamental period of MD-CBF and MD-MRF buildings, the scaling factor used for each ground motion record is different. The acceleration response spectra of scaled crustal and subduction ground motions are shown in Fig. 3.23 and Fig. 3.24.

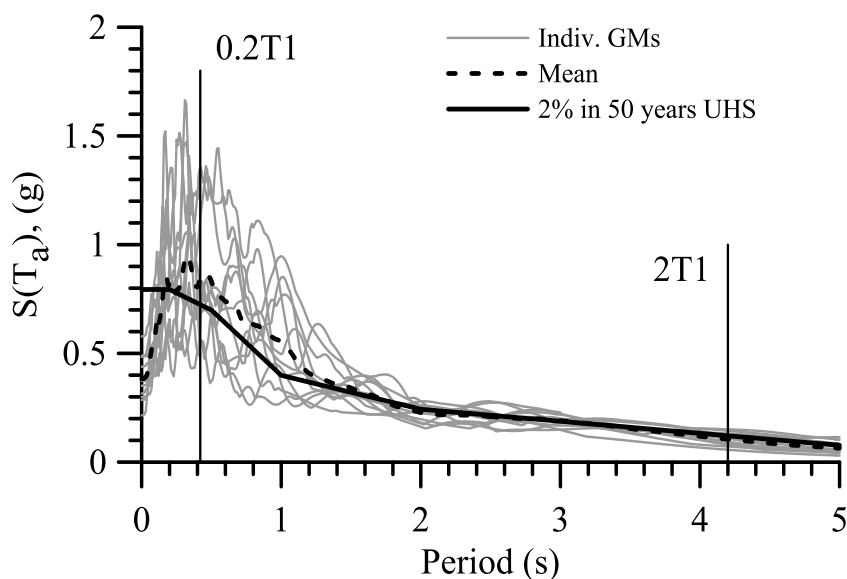


Fig. 3.23 Response spectrum of scaled crustal GMs for 8-storey MD-MRF building

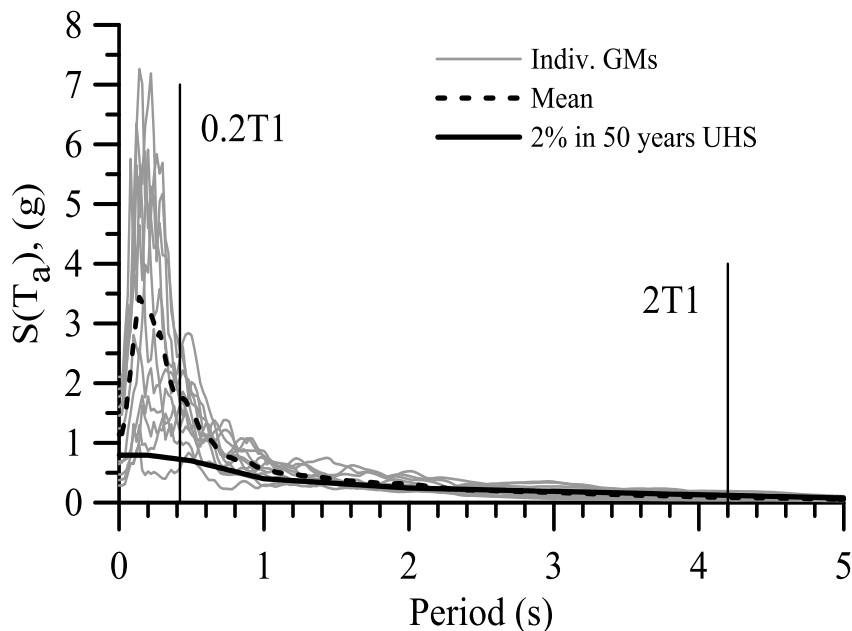


Fig. 3.24 Response spectrum of scaled subduction GMs for MD-MRF building

### ***3.8.3 Seismic response of MD-MRF building under crustal GMs from time history analysis***

The nonlinear response of the MD-MRF building under crustal ground motions is shown in Fig. 3.25. As depicted, the maximum of mean interstorey drift is  $2.4\%h_s$ , which is less than the  $2.5\%h_s$  as limit given in NBCC. However, the interstorey drift is within the code limit because the design was revised and the column sizes of MD-MRFs were increased to reach a demand to capacity ratio around 0.5. The maximum of mean residual drift resulted  $0.3\%h_s$  while the maximum of mean floor acceleration is about  $0.6g$ . All MD-MRF beams experienced yielding within the plastic hinge region.

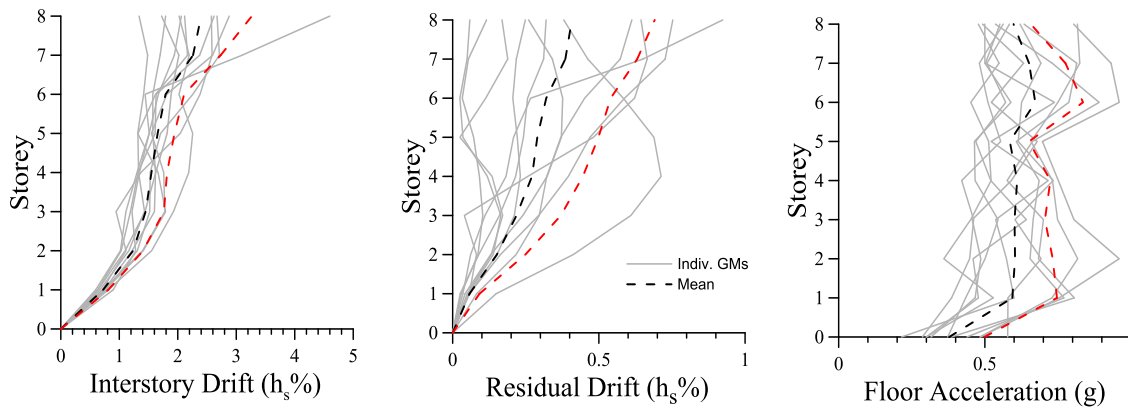


Fig. 3.25 Nonlinear response of 8-storey MD-MRF building subjected to crustal GMs

The building studied showed a maximum interstorey drift when subjected to ground motion #C8. In this case the peak interstorey drift occurred at 7<sup>th</sup> floor and roof level. Strength and stiffness degradation of MRF beam is observed only under ground motion #C8 at the floor where maximum interstorey drift occurred. However, the MD-MRF beam strength did not reduce to 80% of its capping strength. The hysteretic behavior of the left end of beam located at 7<sup>th</sup> floor of the exterior span of MD-MRF and the global damage index are shown in Fig. 3.26. It is noted that the global damage index,  $DI_{80\%}$ , was calculated as the ratio of yielding fibers within the plastic hinge cross-section to the total number of fibers of that cross-section. According to Bosco and Tirca (2017) failure of beam associated to the 20% reduction of flexural strength corresponding to  $DI_{80\%} = 0.375$ .

Fig. 3.26 shows that the probable yielding moments is 1023 KNm for beams at 7<sup>th</sup> floor. The probable moment resistance of MD-MRF beams at the 7<sup>th</sup> floor calculated in the design is 1048 KNm, which is very close to the probable yielding moment obtained from the numerical model. The maximum rotation is 0.037 radians and occurred at time step 6.08s.

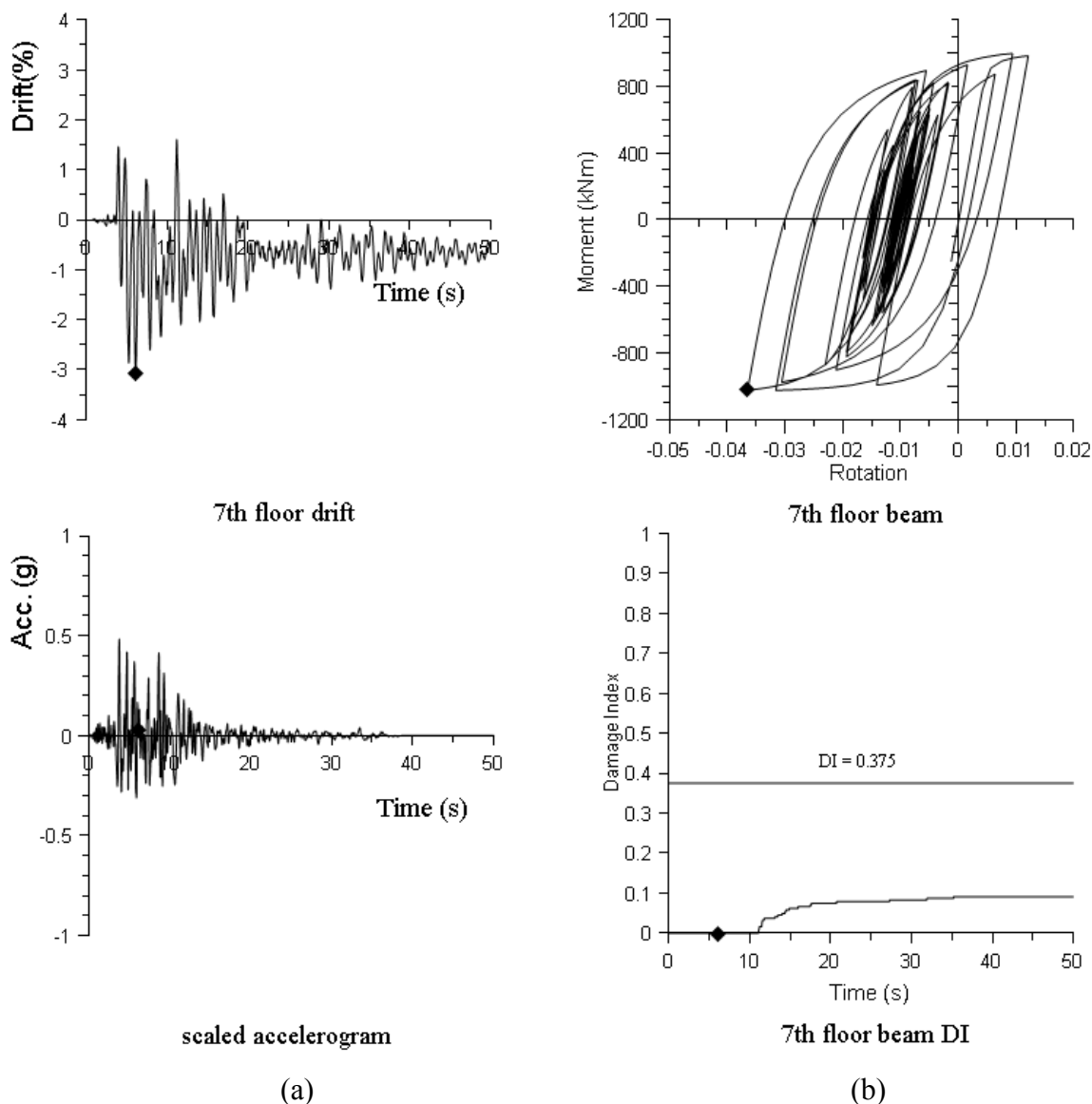


Fig. 3.26 Hysteretic behavior and DI of MD-MRF beam at 7th floor under GM #C8: (a) 7<sup>th</sup> floor drift time history and accelerogram, (b) beam hysteresis loop and damage index

### 3.8.4 Seismic response of MD-MRF building under subduction GMs from time history analysis

The nonlinear response of MD-MRF building under subduction ground motions are shown in terms of interstorey drift, residual interstorey drift and floor acceleration in Fig. 3.27.

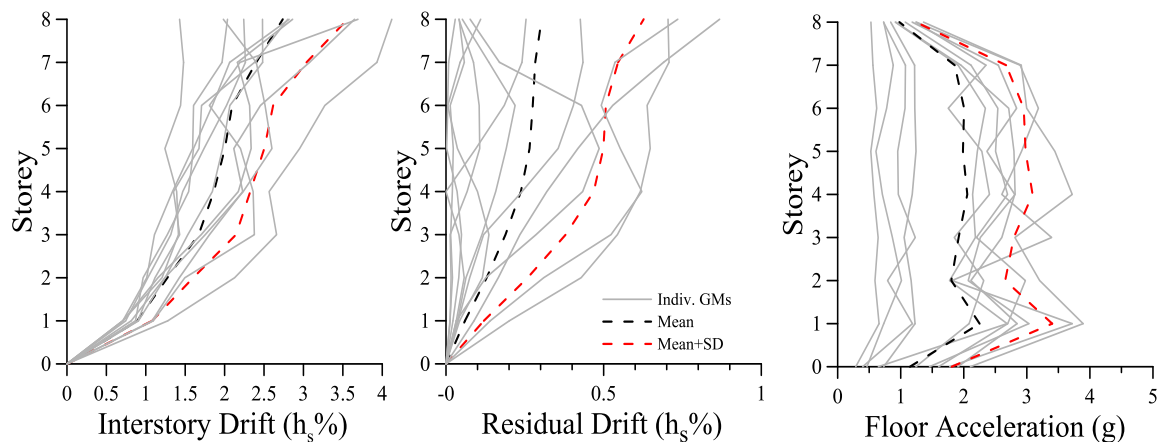


Fig. 3.27 Nonlinear response of MD-MRF building subjected to subduction GMs

The maximum of mean interstorey drift is  $2.8\%h_s$ , and the maximum of mean residual drift is  $0.3\%h_s$ , which occur at the roof level. It is noticed that under ground motion, S2, S3, S4, S5, and S7, failure (20% reduction of flexural strength) of MD-MRF beam is observed in most of cases at the 8<sup>th</sup> floor (roof level). It is always the beams' ends that are adjacent to the MD-MRF side columns that start degrading first and accumulate more damage at the end of ground motions. Furthermore, it is noted that under ground motion #S4 (MYG001), the damage index of the beam reached 1.0, which means the beam lost all its resistance. The hysteretic behavior and damage index are shown in Fig. 3.28.

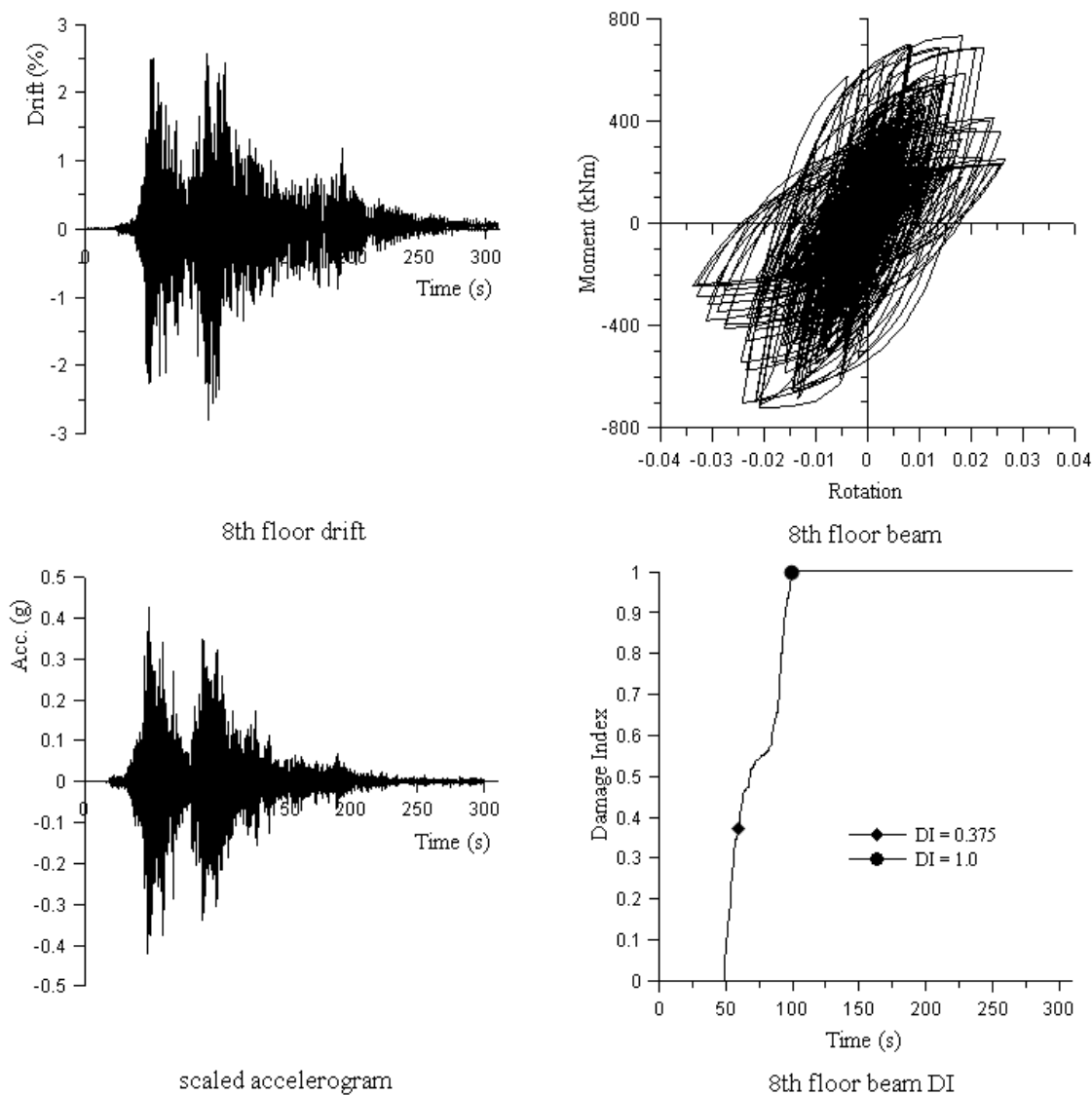


Fig. 3.28 Hysteretic behavior and DI of MD-MRF beam at 8th floor under GM #S4: (a) 8<sup>th</sup> floor drift time history and accelerogram, (b) beam hysteresis loop and damage index

### 3.9 Seismic Assessment of Braced Dual System 8-storey Office Building

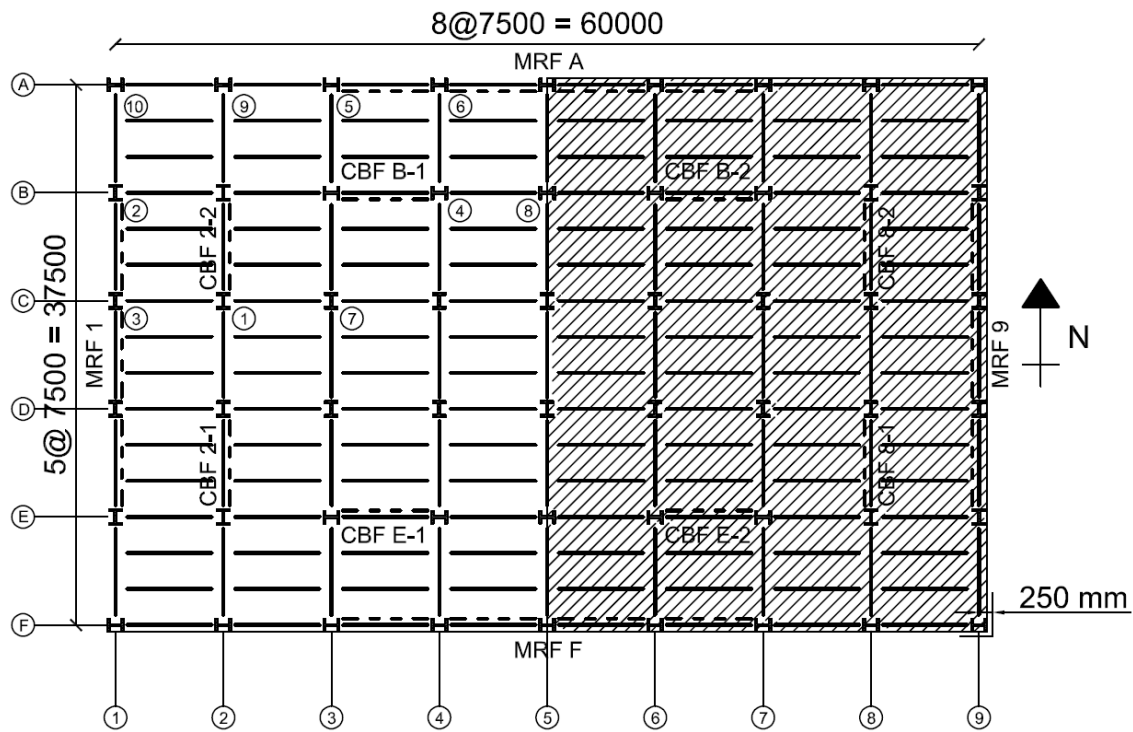
#### Based on Nonlinear Time-History Analysis

To assess the seismic behavior of the office building with Brace Dual System, a comprehensive nonlinear time history analysis is performed using OpenSees.

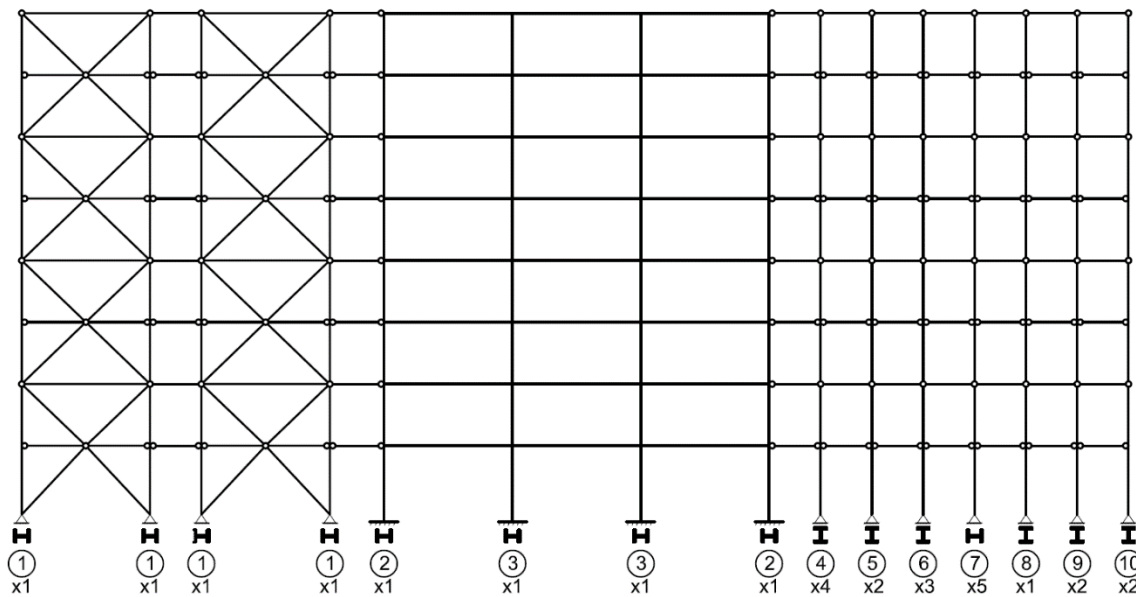
### ***3.9.1 Modeling of Braced Dual System***

Due to the symmetry of the building, only half of the building in N-S direction is simulated as shown in Fig. 3.29a. The OpenSees model is shown in Fig. 3.29b. Since half of the building is modeled, the model includes two identical MD-CBF frames, a three-bay MRF frame and the gravity columns associated to half of the building.

In this model, the MD-CBFs and the 3-bay MRF are modeled as described previously. Thus, the MD-MRF frame was modeled in a 2D system with three degrees of freedom for each node because no out-of-plane deformation was expected. Meanwhile, to allow the out-of-plan buckling of MD-CBF braces, the MD-CBF was modeled in a 3D system with six degrees of freedom for each node. Therefore, the Braced Dual System was modeled in a 3D system. The building is assumed to have a rigid diaphragm. The two MD-CBFs are expected to have similar behavior as presented above. The gravity columns are modeled with elastic beam column elements. All frames are connected to each other with rigid truss elements to account for the rigid diaphragm effect. This building was analysed in ETABS on a 3D model and in OpenSees. For comparison purpose, the 1<sup>st</sup>, 2<sup>nd</sup>, and 3<sup>rd</sup> mode period is given in Table 3.14. As depicted, the period has slightly decrease in comparison to that of MD-CBF (e.g. T1 decreased from 1.395 s to 1.32 s). This is because the backup MRF frame provides very limited stiffness to the system.



(a)



(b)

Fig. 3.29 Opensees model of the Braced Dual System building: (a) model plan; (b) model elevation (N-S direction)

Table 3.14 Vibration periods of building with Braced Dual System (N-S)

Vibration Period	Eigen Value Analysis	
	ETABS	OpenSees
$T_1$	1.343 s	1.320 s
$T_2$	0.464 s	0.459 s
$T_3$	0.255 s	0.255 s

### 3.9.2 Selection of ground motions

The same suites of ground motions used for the MD-CBF building and MD-MRF building are considered and the same scaling method is applied. The acceleration response spectra of scaled crustal and subduction ground motions are shown in Fig. 3.30 and Fig. 3.31.

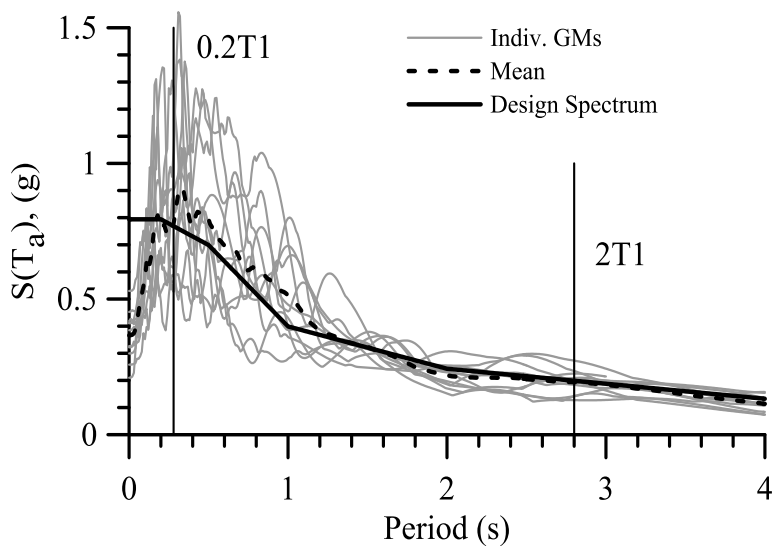


Fig. 3.30 Response spectrum of scaled crustal GMs for 8-storey building with Braced Dual System

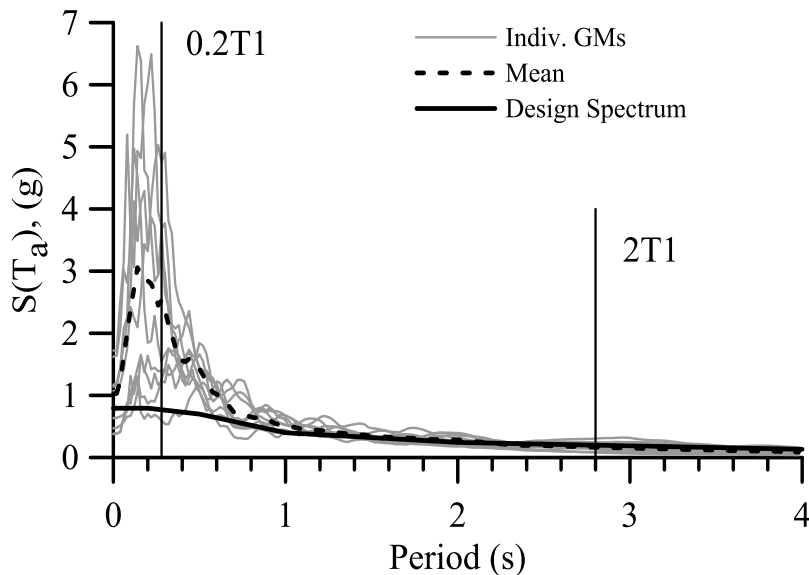


Fig. 3.31 Response spectrum of scaled subduction GMs for 8-storey building with Braced Dual System

### 3.9.3 Seismic response of Braced Dual System building under crustal GMs from time history analysis

The nonlinear response of 8-storey building with Dual system subjected to crustal ground motions is presented in terms of interstorey drift, residual interstorey drift, and floor acceleration in Fig. 3.32.

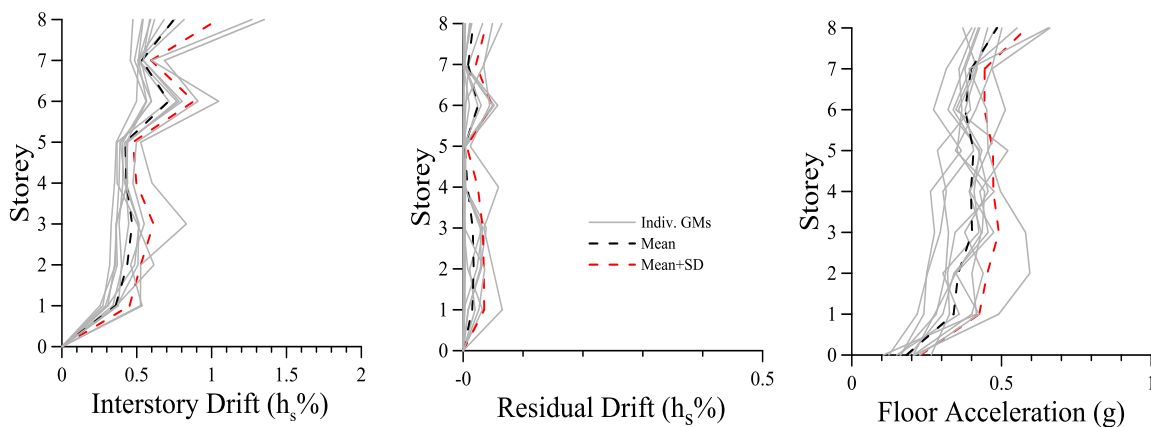


Fig. 3.32 Nonlinear response of 8-st. building with Braced Dual System subjected to crustal GMs

The maximum of mean interstorey drift, residual interstorey drift, and floor acceleration among floors are  $0.75\%h_s$ ,  $0.025\%h_s$ , and  $0.49g$  respectively. Comparing the seismic response with that resulted for the MD-CBF building (Fig. 3.16), the response is slightly reduced. In addition, the peak interstorey drift concentrated at the 6<sup>th</sup> floor is also reduced. Furthermore, there is almost no residual drift. However, the floor accelerations are similar. As illustrated in Fig. 3.32, the maximum interstorey drift occurred at the 6<sup>th</sup> floor and roof level. To understand the response of Braced Dual System subjected to crustal record #C8, the hysteresis loops of MD-CBF1 and MD-CBF2 left and right braces of the 8<sup>th</sup> floor are depicted in Fig. 3.33 and the hysteresis loops of MRF beams of the same floor are plotted in Fig. 3.34.

It can be seen from Fig. 3.33 that the left and right HSS braces of both MD-CBFs exhibited the same behaviour as expected. Braces of both MD-CBFs buckled and yielded at the same time, where  $t_1 = 5.98s$  and  $t_2 = 10.86s$ , respectively. All MRF beams responded in elastic range as depicted in Fig. 3.34. Since the MRF system behaves elastically it acts as a backup self-centering system relaying on the elastic frame action. For this reason, the residual interstorey drift plotted in Fig. 3.32 is almost zero.

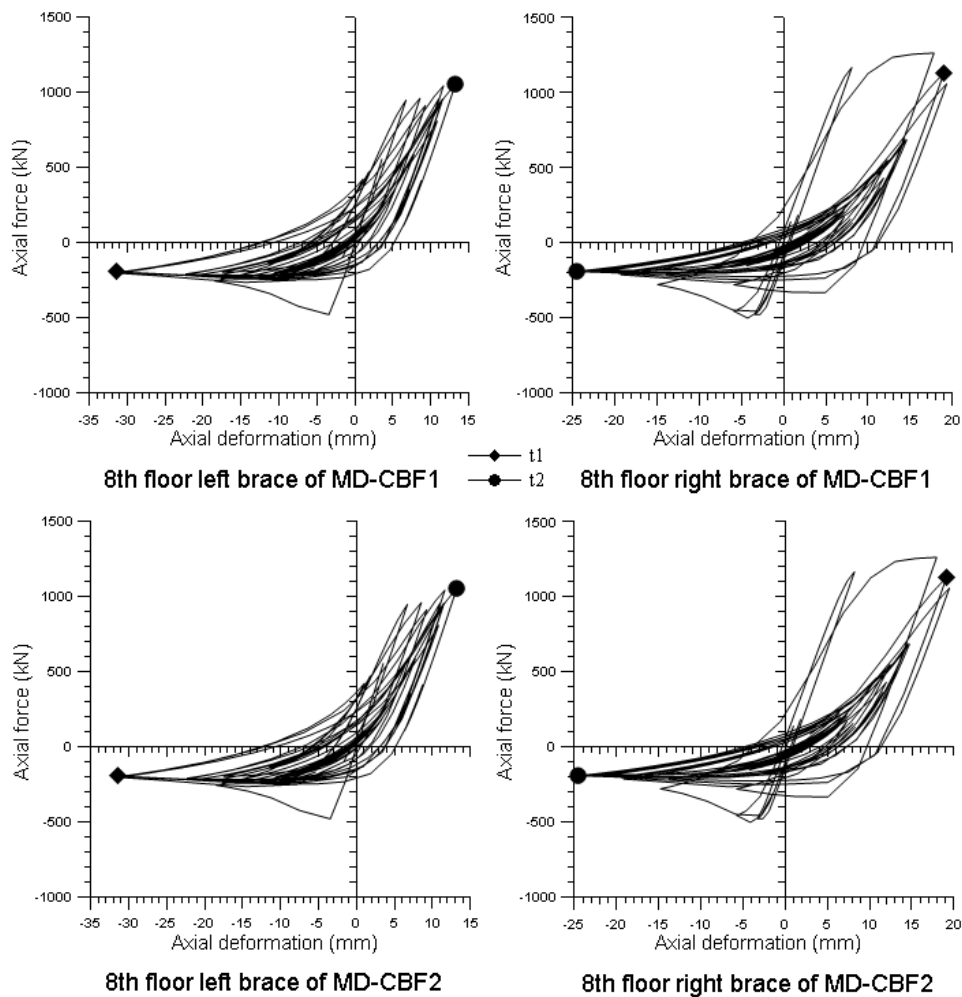


Fig. 3.33 Hysteresis loops of HSS braces of the 8<sup>th</sup> floor of Braced Dual System subjected to #C8

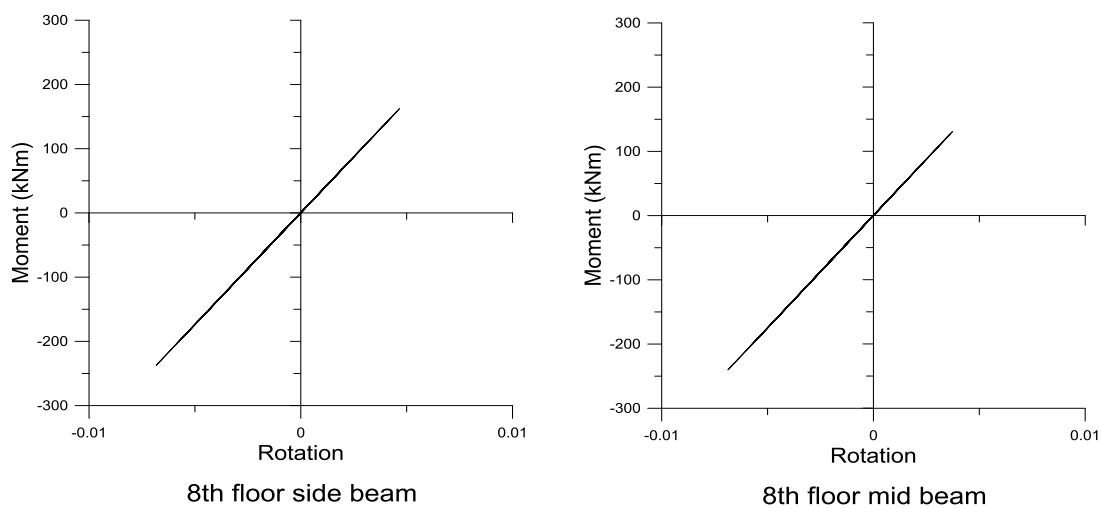


Fig. 3.34 Hysteresis loops of MRF beams of the 8<sup>th</sup> floor of Braced Dual System subjected to #C8

### 3.9.4 Seismic response of Braced Dual System building under subduction GMs from time history analysis

The nonlinear response of Braced Dual System subjected to subduction ground motions is shown in Fig. 3.35 in terms of interstorey drift, residual interstorey drift and floor acceleration.

Fig. 3.35 shows that under subduction ground motions, the maximum of mean interstorey drift, residual drift, and floor acceleration of the building with Braced Dual System are  $1.08\% h_s$ ,  $0.05\% h_s$ ,  $0.88g$ , respectively. Similar to MD-CBF building, the ground motion #MYG001 triggered large strain accumulation in HSS braces of Braced Dual System and fracture of HSS braces caused by low-cycle fatigue was observed at the 7<sup>th</sup> floor. It is noted that fracture occurs on both left and right braces of both MD-CBF frames. However, unlike the MD-CBF building, the interstorey drift of the Braced Dual System shows a uniform distribution along the building height.

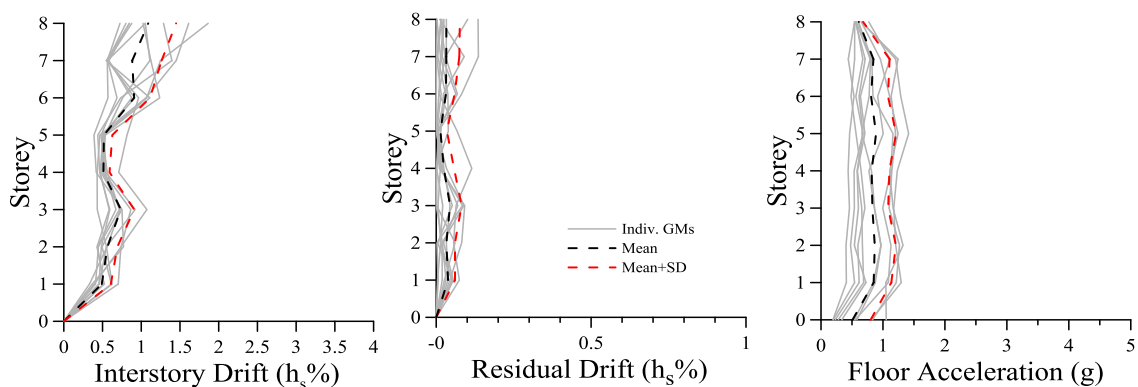


Fig. 3.35 Nonlinear response of building with Braced Dual System subjected to subduction GMs

The hysteretic behaviors of left and right HSS braces of 7<sup>th</sup> floor and the MRF beams of 7<sup>th</sup> floor and 8<sup>th</sup> floors are shown in Fig. 3.36 and Fig. 3.37, respectively. Since the two

MD-CBFs have the same behavior, only the behaviour of HSS braces of MD-CBF1 is shown. As can be seen, both braces at 7<sup>th</sup> floor experienced buckling in compression and yielding in tension. The left brace initiates fracture at  $t = 101.39s$ , the right brace initiates fracture at  $t = 102.09s$ . This means that a fiber in the cross-section was stressed and reached fracture.

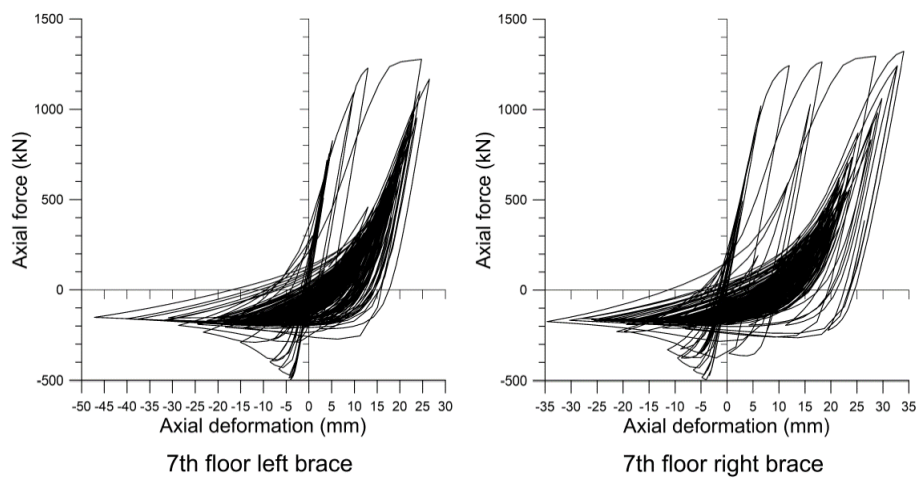


Fig. 3.36 Braced Dual System 7th floor HSS brace hysteretic behavior under #MYG001

From Fig. 3.37 it can be seen that both 7<sup>th</sup> floor and 8<sup>th</sup> floor MRF beam experienced slight yielding which means plastic hinges start initiating. Since the backup MRF frame started dissipating energy, the 7<sup>th</sup> storey didn't experience large interstorey drift after brace fracture of HSS braces was initiated.

Therefore, the benefit of Dual system is to uniform the distribution of damage along the building height and to provide the self-centering action.

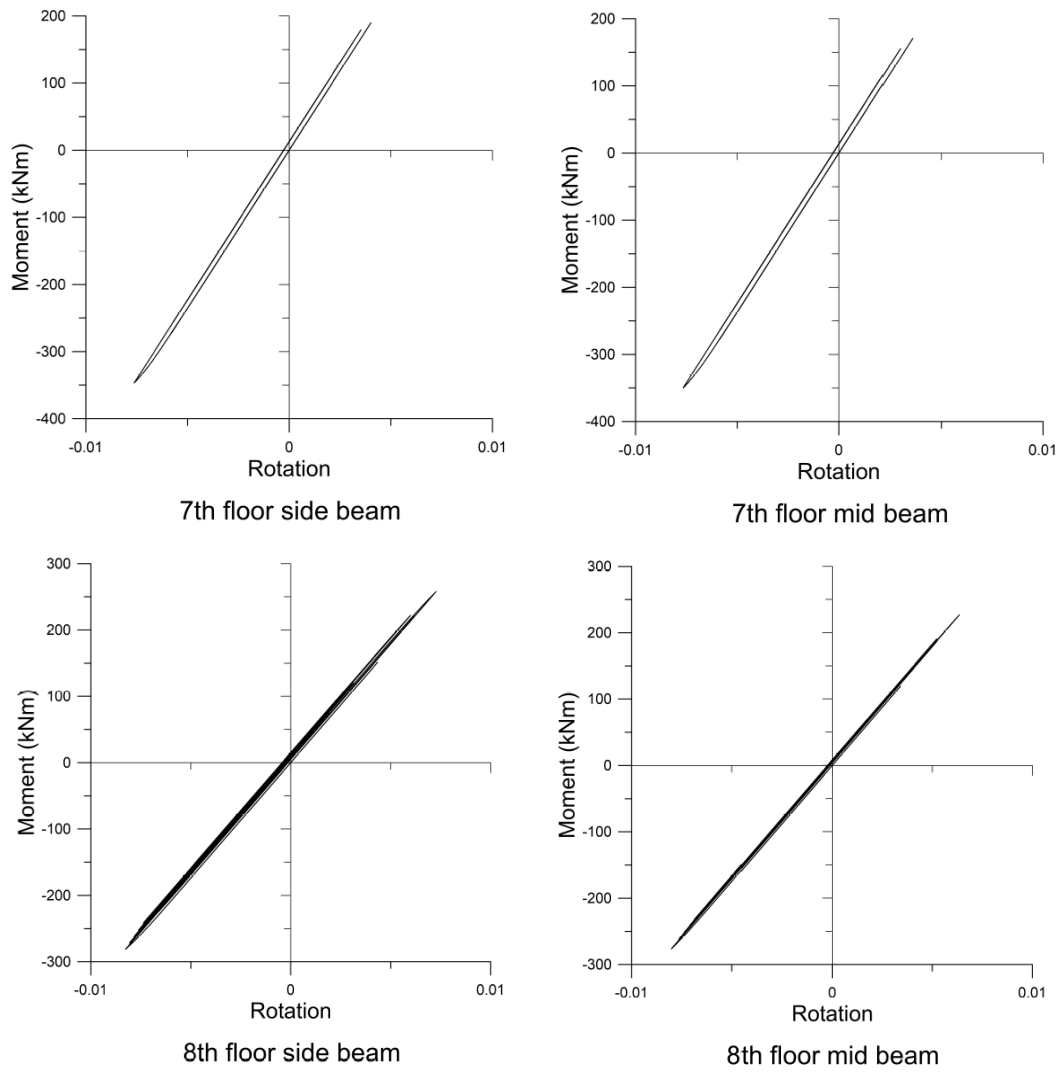


Fig. 3.37 Braced Dual System 8th floor MRF beam hysteretic behavior under #MYG001

# **CHAPTER 4. SEISMIC RESPONSE OF STEEL BUILDINGS USING INCREMENTAL DYNAMIC ANALYSIS**

In this chapter, a study is conducted to analyze the nonlinear seismic behavior from yielding to failure of the 8-storey building with three various earthquake resistant systems such as: MD-CBF system, MD-MRF system, and Braced Dual System. The seismic response is analyzed using the Incremental Dynamic Analysis method.

## **4.1 Incremental Dynamic Analysis of the 8-storey MD-CBF Building**

Regarding the Incremental Dynamic Analysis, one of the challenges is to assess the capacity of the studied earthquake resistant system at the near-collapse limit state. For the MD-CBF system, the near-collapse limit state is defined when the critical brace exhibits fracture. It is noted that when a HSS brace at a critical floor buckles out-of-plane, its inner cross-sectional side is in compression while the outer side is in tension. When a plastic hinge is formed at the brace mid-span, crack always initiates on the compression side of the HSS brace cross section and it opens in the following cycle when it is reloaded in tension. After the critical brace exhibits fracture, a slight increase of intensity measure leads to an adjacent brace to reach failure while the system exhibits large lateral deformations (e.g. interstorey drift, residual interstorey drift). This observation of dynamic instability is strongly correlated to the 20% slope approach proposed by Vamvatsikos and Cornell (2002) for system failure identification on IDA curve.

#### 4.1.1 The IDA response of 8-st. MD-CBF Building under crustal GMs

To assess the seismic performance of the 8-storey MD-CBF building subjected to a set of 11 crustal ground motions the incremental dynamic analysis (IDA) is employed. Nonlinear time history analysis was performed at an interval of about 0.1 g and all 11 IDA curves are shown in Fig. 4.1. The variation among the IDA curves reflects the signature of different ground motions. In Fig. 4.1, the horizontal dashed line marks the design spectral acceleration at the first mode period of the building. For 2% probability of exceedance in 50 years design spectrum, the  $S(T_1)$  is equal to 0.337g. The black solid line shows the average magnitude of spectral acceleration that marks the occurrence of the first brace buckling which is 0.15g.

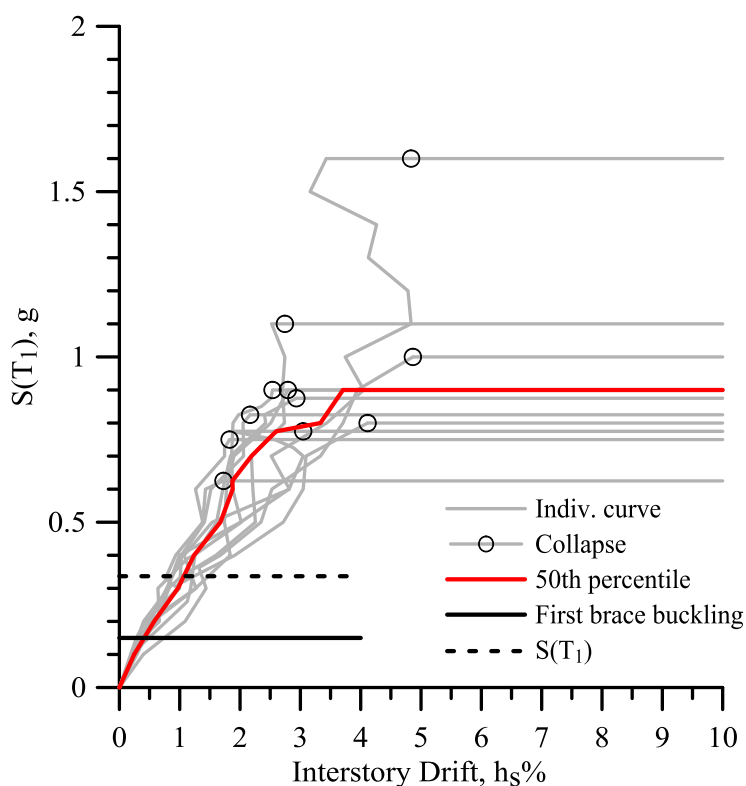


Fig. 4.1 The IDA curves of studied MD-CBF 8-storey building under crustal GMs

The white circles show the response when the structure exhibits its near collapse limit state. The red solid line shows the 50<sup>th</sup> percentile IDA curve which indicates that the building is able to resist a demand of 0.9g while undergoes 3.7% $h_s$  interstorey drift. At near-collapse limit state, the lateral displacement distribution along the building height expressed in terms of interstorey drift and residual interstorey drift, as well as, the floor acceleration are plotted in Fig. 4.2.

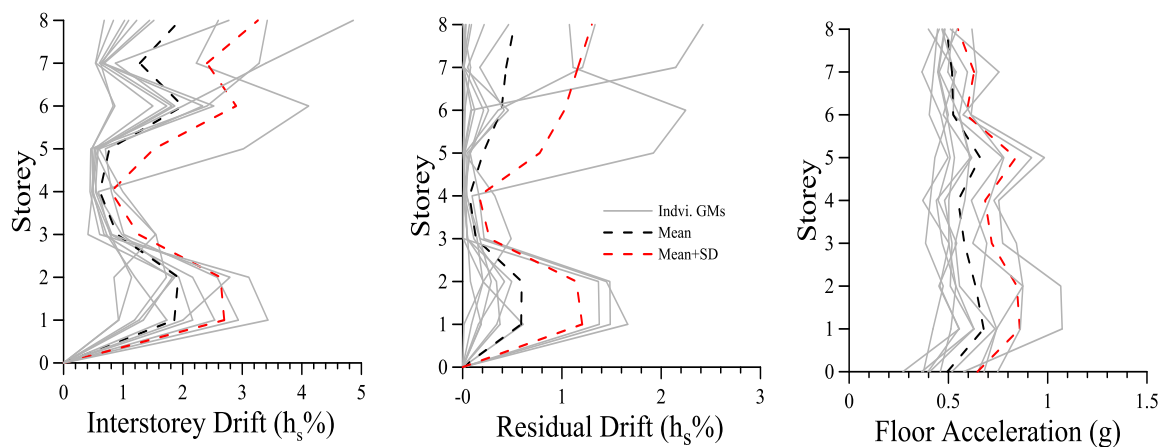


Fig. 4.2 The interstorey drift, residual interstorey drift and floor acceleration associated to the near-collapse limit state of 8-storey MD-CBF building under crustal ground motions

As depicted, the peak of mean interstorey drift is 1.95% $h_s$ , the peak of mean residual interstorey drift is 0.6% $h_s$ , and the peak of mean floor acceleration is 0.7g. It is noticed that damage is mostly concentrated at the 1<sup>st</sup>, 2<sup>nd</sup>, 6<sup>th</sup>, and 8<sup>th</sup> floors. For example, under the ground motion #1083-170, the maximum interstorey drift and maximum residual drift occurs at the roof level. Moreover, even though the maximum interstorey drift/ residual drift and their Mean+SD occur at top floors, the fracture of HSS brace was observed at the bottom floors under the 11 crustal ground motions considered. The hysteresis response of the top floor HSS braces subjected to #1083-170 record is shown in Fig. 4.3. As depicted, the right brace was first loaded in compression while the left brace was loaded in tension.

However, both braces exhibited buckling in compression and yielding in tension. No brace fracture was encountered at the 8<sup>th</sup> floor. The damage index of the critical fiber is shown in Fig. 4.3.

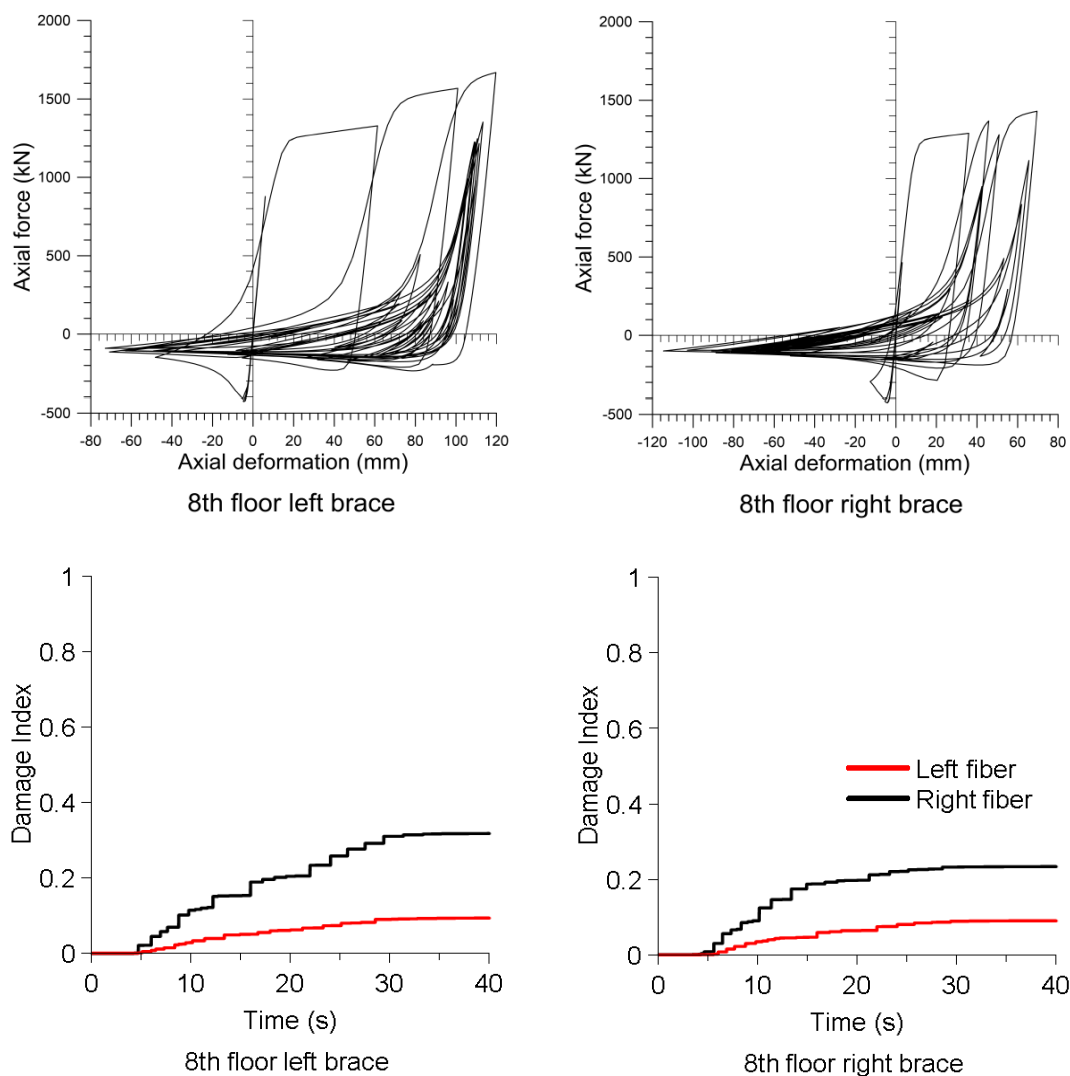


Fig. 4.3 Hysteretic response of 8<sup>th</sup> floor HSS braces of MD-CBF building and their DI of critical fiber of HSS brace cross section under #1083-170 scaled to near-collapse limit state

In Fig. 4.4 is shown the fiber discretization cross section of HSS brace, as well as the location of the outermost fibers investigated.

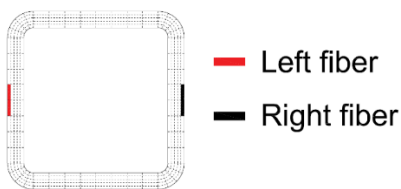


Fig. 4.4 Outermost fibers of HSS brace cross section

The global seismic response at near-collapse limit state is shown in Fig. 4.5. As depicted, the ground floor right brace initiates fracture.

In addition, according to Pillai (1974), a simplified interaction equation for plastic stress distribution of cross section could be used to verify the axial compression and bending capacity of the cross section. The equation has the following expression:

$$M_x \leq M_{px}, \text{ for } 0 \leq C/C_y \leq 0.15 \text{ and,}$$

$$M_x \leq 1.18 \left(1 - \frac{c}{c_y}\right) M_{px}, \text{ for } 0.15 \leq C/C_y \leq 1.0 \quad (4.1)$$

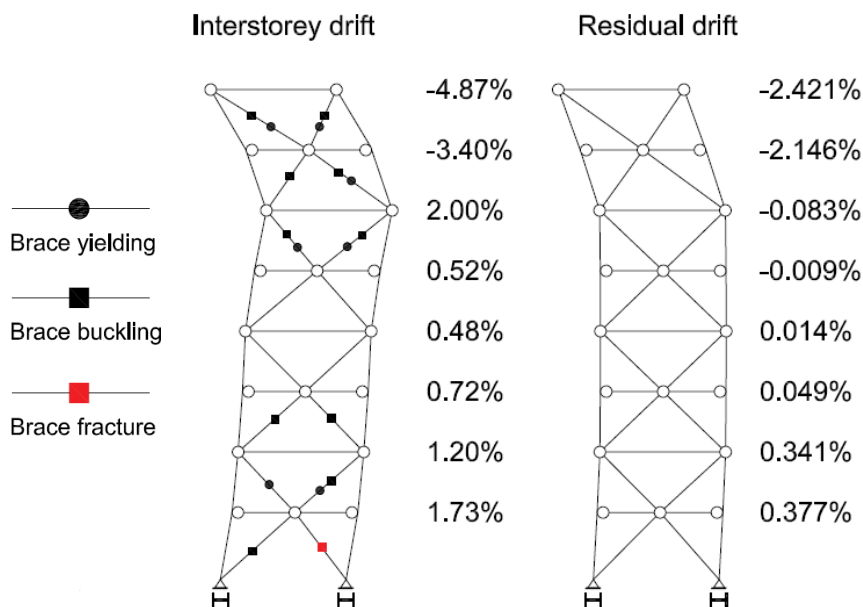


Fig. 4.5 Seismic response of MD-CBF system under #1083-170 scaled to near-collapse limit state

The axial force – bending moment interaction diagram computed for the 1<sup>st</sup> floor MD-CBF beam and adjacent column is shown in Fig. 4.6. As illustrated (Fig. 4.6), the beam and columns of the MD-CBF frame could meet the requirements as described in Eq. (4.1), which means that these elements still behave in the elastic range without forming plastic hinge. Thus, the capacity design procedure provided by CSA/S16-14 for CBF building is sufficient.

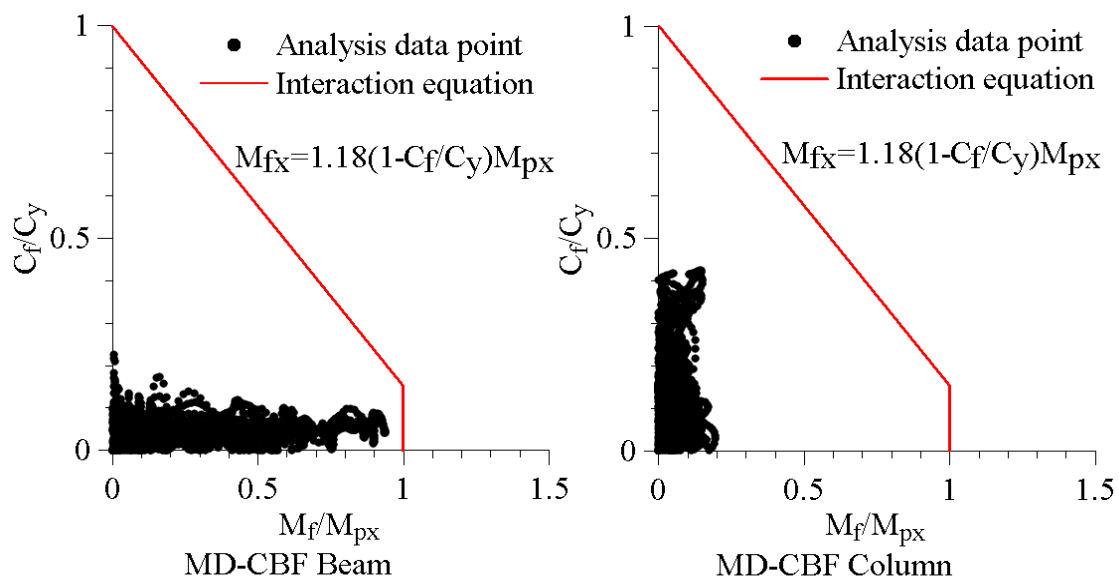


Fig. 4.6 The 1<sup>st</sup> floor axial force-bending moment interaction diagram under #1083-170 scaled to near-collapse limit state

#### 4.1.2 The IDA response of 8-st. MD-CBF building under subduction GMs

Similar to the response of 8-storey MD-CBF building under crustal ground motions, the nonlinear behaviour of the same structural system subjected to subduction ground motions is investigated. The 11 IDA curves of the 8-storey MD-CBF building resulted under subduction ground motions are shown in Fig. 4.7. The IDA curves corresponding to intra-plate subduction records are plotted with blue dashed lines and that corresponding to inter-plate subduction records with grey solid lines. The horizontal dashed line shows the

response of the MD-CBF building when the ground motions are scaled to the design spectrum corresponding to 2% probability of exceedance in 50 years. The horizontal black solid line shows the average demand level of  $S_a(T_1)$  when the critical brace reached buckling, which is 0.083g. Hence, under subduction ground motions, buckling of the first brace occur at almost half of  $S_a(T_1)$  value resulted under crustal ground motions. The occurrence of buckling at this lower magnitude is the effect of total duration and Trifunac duration of subduction ground motions which is up to 10 times greater than in the case of crustal ground motions.

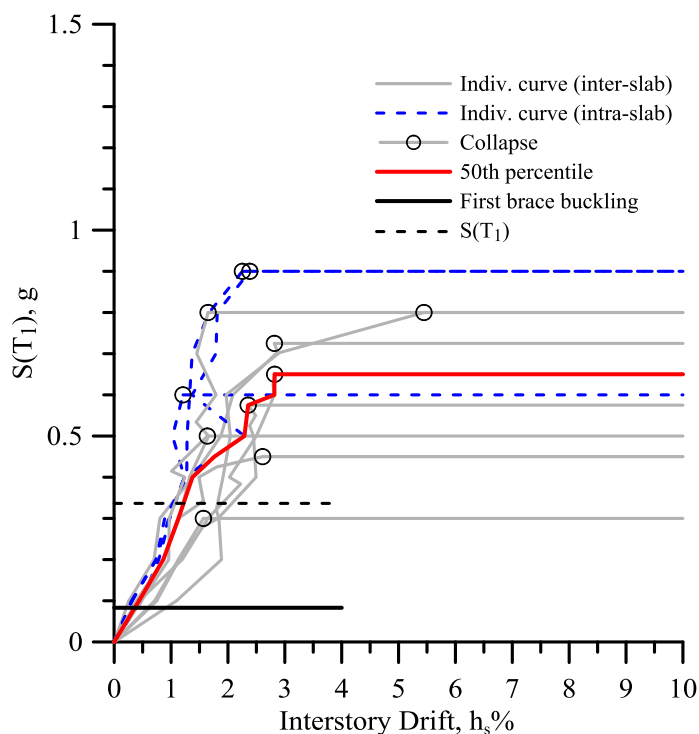


Fig. 4.7 The IDA curves of 8-storey MD-CBF building under subduction GMs

The red solid line shows the 50<sup>th</sup> percentile IDA curve which indicates that the structural system is near collapse when  $S_a(T_1)$  is scaled to 0.65g and the response at this demand is 2.82% $h_s$  interstorey drift. Again, this 50<sup>th</sup> percentile demand is lower than that in the case of crustal ground motions. For example, under ground motion MYG001, the failure of

critical brace occurs when  $S_a(T_1)$  is scaled to 0.3g, which is less than the corresponded design spectrum ordinate,  $S_a(T_1) = 0.337g$ . Due to strain accumulation in HSS braces during several loading/unloading cycles, damage was reached at lower interstorey drift and residual drift values of  $1.57\%h_s$  and  $0.14\%h_s$ , respectively. The seismic response of the MD-CBF building under subduction ground motions expressed in terms of interstorey drift, residual interstorey drift and floor acceleration recorded at the near collapse limit state is shown in Fig. 4.8. The peak of mean interstorey drift, residual interstorey drift, and floor acceleration along the building height are:  $1.87\%h_s$ ,  $0.32\%h_s$  and  $1.19g$ , respectively. The maximum interstorey drift and maximum residual drift occurs at the 7<sup>th</sup> floor under ground motion #TCG009. The brace behavior at this floor is shown in Fig. 4.9.

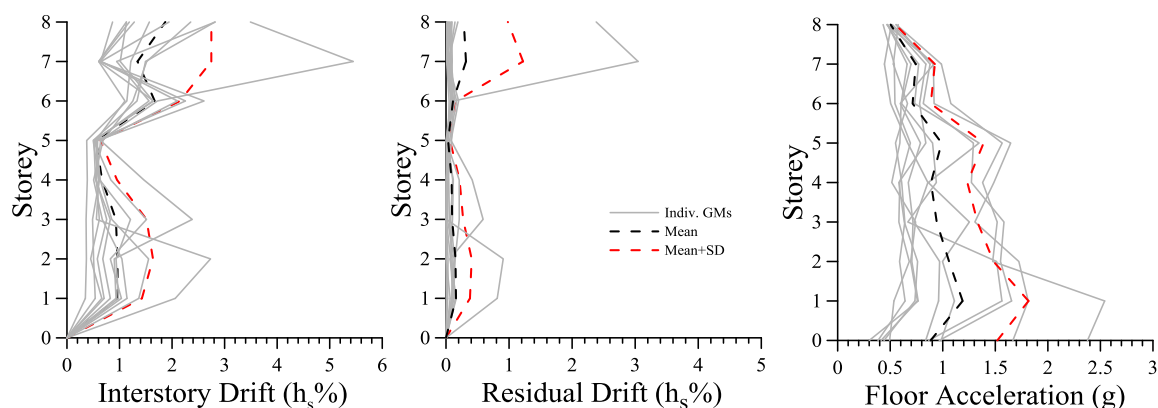


Fig. 4.8 The interstorey drift, residual interstorey drift and floor acceleration associated to the near-collapse limit state of 8-storey MD-CBF building under subduction GMs

As resulted from Fig. 4.9, the left brace reached fracture failure caused by low-cycle fatigue while the right brace that was first loaded in compression is not reached tension yielding. The damage index of critical fiber of HSS brace cross section is showed in Fig. 4.9, as well.

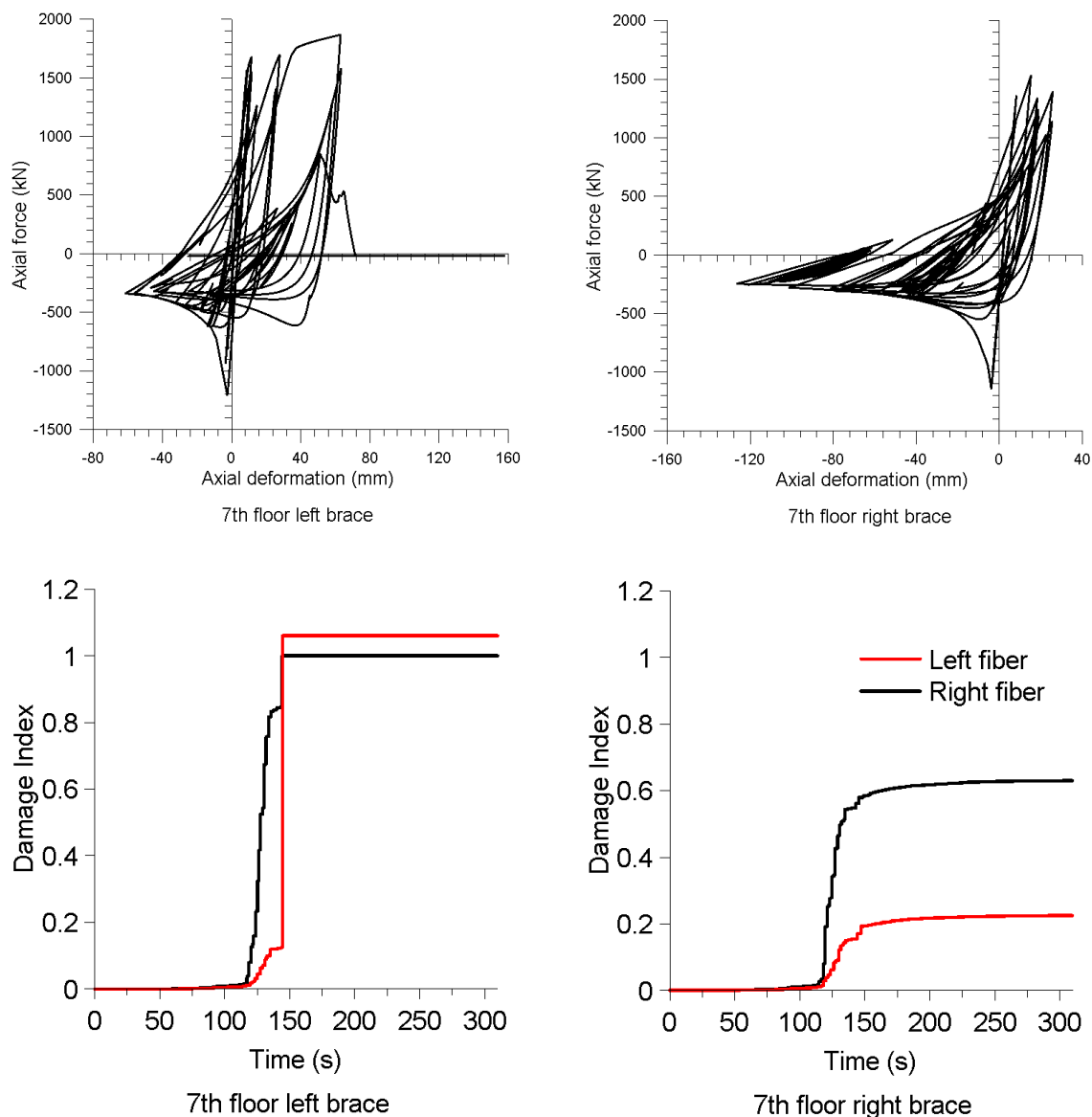


Fig. 4.9 Hysteretic response of 7th floor HSS braces of MD-CBF building under #TCG009 record scaled to near-collapse limit state and the damage index of critical fiber of HSS cross-section

The IDA analysis shows that the MD-CBF building experienced the near-collapse limit state at a lower  $S_a(T_1)$  level when subjected to subduction ground motions compared with crustal ground motions. The peak of mean interstorey drift and residual interstorey drift are similar under both sets of ground motions. However, the floor acceleration under the subduction records is about two times greater than that resulted under crustal records.

As illustrated in Fig. 4.2 and Fig. 4.9, the damage of 8-storey MD-CBF structure always concentrates at some critical floors where HSS braces experienced fracture due to strain cumulating without being able to involve the braces of adjacent floors that might still respond in the elastic range.

## **4.2 Incremental Dynamic Analysis of the 8-storey MD-MRF Building**

To analyze the response of the 8-storey steel MD-MRF building, as well as, to further assess the probability of collapse of the building, the incremental dynamic analysis (IDA) is employed. Nonlinear time history analysis was performed, and the IDA curves were computed using two sets of ground motions scaled with respect to the design spectral acceleration ordinate corresponding to the first mode period of building,  $S_a(T_1)$  in order to obtain the structure response at each 0.1 g multiplier of earthquake demand. However, smaller multipliers were also considered to obtain the first yielding of beam's plastic hinges fibers and the collapse of the system.

According to PEER/ATC (2010), there are four options for modeling of MRF frame. In Option 4, it is specified "if the post-capping portion of a modified backbone curve is not incorporated in the analytical model, the ultimate deformation of a component should be limited to the deformation associated with 80% of the capping strength", which means that the rotation capacity of the plastic hinge is consumed when the beam at the location of plastic hinge cross section loses 20% of its flexural strength. When this occurs the failure of the beam end is considered. However, this is not the 100% physical failure of the beam but is close to it.

According to Bosco and Tirca (2017) who studied the response of several experimental beam tests under cyclic loading, it was found that the MRF beam damage index ( $DI_{80\%}$ ) associated with 80% of capping strength ( $M/M_{max} = 0.8$ ) is in average 0.375 and was recommended as collapse indicator for beams. It was also found that the plastic rotations  $\theta_{pl}$  associated with  $DI_{80\%}$  are in the range of 0.021 rad to 0.040 rad with an average value of 0.028 rad. The DI is calculated as the number of fibers in which the Miner's damage index

is equal to one (i.e. the number of fibers that reach fatigue) over the total number of top and bottom flanges fibers. For  $DI=1.0$ , flanges are not able to sustain the demanded bending moment. Thus, the inelasticity is concentrated in the plastic hinge segments made of Steel02 material and fiber-based cross-sections discretization. In this study, each flange of the I-shape cross-section is divided into two times (30 x 4) fibers with a total number of fibers for both flanges of 480, while the web is discretized into 38 fibers.

For example, in Fig. 4.10 it is illustrated the IDA curve of MD-MRF building subjected to #1052-90 Northridge ground motion. As illustrated, at  $S_a(T_1) = 0.237$  g which is the code demand the peak interstorey drift exceeds the code limit of 2.5% $h_s$ . When the demand exceeds 0.3 g, damage of beam's plastic hinges accumulates at higher rates. Thus, at 0.35g, the plastic hinge developed in the beam at the 8<sup>th</sup> floor reached  $DI_{80\%}$  for a rotation of 0.065 rad., while the interstorey drift at the same floor is 6.8% $h_s$  which is the peak among floors. At  $S_a(T_1) = 0.4$  g the beams of 4<sup>th</sup> floor, 7<sup>th</sup> floor and 8<sup>th</sup> floor reached  $DI_{80\%}$  while the rotation is 0.052 rad., 0.067 rad. and 0.072 rad., respectively. The associated interstorey drift is 5.3% $h_s$ , 7.0% $h_s$  and 8.1% $h_s$ , respectively, while the peak of residual interstorey drift reached 1% $h_s$ . Increasing the demand to 0.6g, it was observed that all beams from the 3<sup>rd</sup>

to 8<sup>th</sup> floors have reached at least  $DI_{80\%}$  and at 0.65g an interstorey drift of  $10\%h_s$  is reached at the top floor, while plastic hinges start developing at the column's base. At 0.7g flexural yielding of columns occurred and the structure encountered excessive lateral deformations. According to Imanpour et al. (2016), the more frequent limit states expected during the nonlinear response of fixed ended column are: *flexural yielding at the base* and *flange local buckling in the base hinge*. Thus, under this ground motion, the global collapse mechanism is obtained, and failure is considered to occur at 0.65g when a peak interstorey drift of  $10\%h_s$  was reached. From 0.65g to 0.7g the lateral deformation increased excessively, and it was decided to consider the collapse point at 0.65g. However, in this study, the IDA curves computed to simulate the response under 11 crustal GMs are stopped when the first MRF beam reaches  $DI_{80\%} = 0.375$ . Because these IDA curves do not show the “real” collapse point, they are labelled truncated IDA curves.

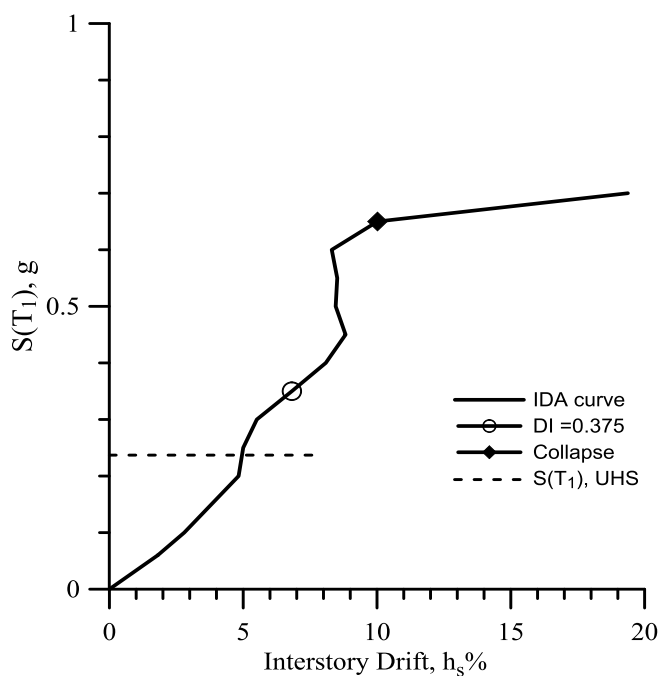


Fig. 4.10 IDA curve of MD-MRF building under #1052-090

#### 4.2.1 The IDA response of 8-st. MD-MRF building under crustal GMs

The truncated IDA curves of the MD-MRF building under crustal ground motions are shown Fig. 4.11. It is noted that the white circle symbolizes the occurrence of  $DI_{80\%}$  in the first beam's plastic hinge among the floor beams and do not symbolize the failure of the structure. For this reason, the IDA curves are labelled truncated IDAs. From analysing the 8-storey MD-MRF building response under the 11 ground motions it resulted that under 9 ground motions the first  $DI_{80\%}$  was reached by beam located on the 4<sup>th</sup> floor, under 1 ground motion (#1052-090) it was reached by the 8<sup>th</sup> floor beam's plastic hinge and under 1 ground motion by the 7<sup>th</sup> and 8<sup>th</sup> floor beams. Therefore, either the 1<sup>st</sup> vibration mode or the 2<sup>nd</sup> vibration mode response was dominant for this building.

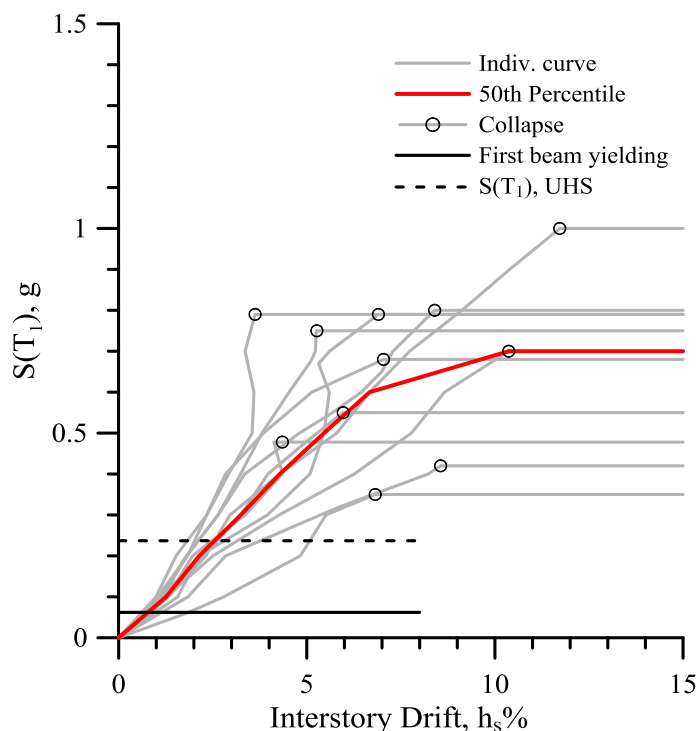


Fig. 4.11 Truncated IDA curves of 8-storey MD-MRF building under crustal GMs  
 In Fig. 4.10, the dashed line shows the demand at the design level (ground motions are scaled to the design acceleration spectrum with 2% probability of exceedance in 50 years),

which in this case is  $S_a(T_1) = 0.237g$ . The black solid line shows the average level of  $S(T_1) = 0.06g$  when the first MRF beam starts to respond in inelastic range. The solid red line shows the 50<sup>th</sup> percentile truncated IDA curve which indicates that the median value of  $S_a(T_1)$  is  $0.7g$  and peak interstorey drift associated to  $DI_{80\%}$  reached by the first beam's plastic hinge is  $10.4\%h_s$ , respectively. The building response at this limit state is shown in Fig. 4.12 in terms of interstorey drift, residual interstorey drift, and floor acceleration.

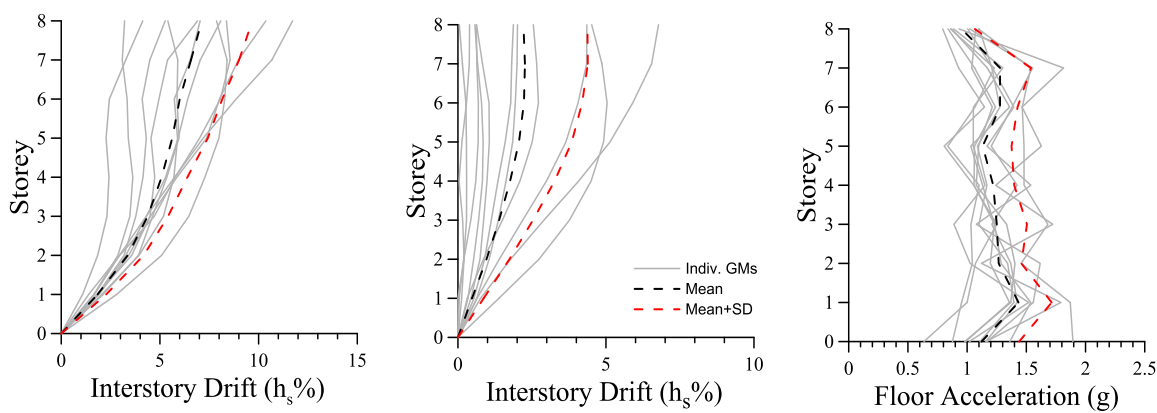


Fig. 4.12 Interstorey drift, residual interstorey drift and floor acceleration of 8-storey MD-MRF building associated to  $DI_{80\%}$  damage limit state under crustal ground motions

As depicted, the average peak interstorey drift is  $7.12\%h_s$ , the average peak residual drift is  $2.26\%h_s$ , and the average peak floor acceleration is  $1.28g$ . With red dashed line is shown the values corresponded to Mean+SD.

When the response to GM #1086-090 is analysed, the maximum interstorey drift and residual drift occur at the 8<sup>th</sup> floor, but it is the 4<sup>th</sup> floor beam's plastic hinge that reaches the  $DI_{80\%} = 0.375$  among floors. This is shown in Fig. 4.13 together with the beam's plastic hinge cross sectional behavior expressed in terms of bending moment vs. rotation.

More in detail, the deflected shape of MD-MRF resulted under this ground motion is given in Fig. 4.14, where the peak interstorey drift and residual drift occur at the top floor. The

hysteresis response of beam's plastic hinge cross sectional behaviour at each floor is showed in Fig. 4.15 in terms of moment vs. rotation. Axial compression force vs. bending moment recorded at the 1<sup>st</sup> floor and 4<sup>th</sup> floor of bottom cross section of columns is showed in Fig. 4.16. As depicted in Fig. 4.15, all beams' plastic hinges behave in the nonlinear range, while the plastic hinge at the base of the column reached the boundary between elastic and plastic nonlinear response (Fig. 4.16).

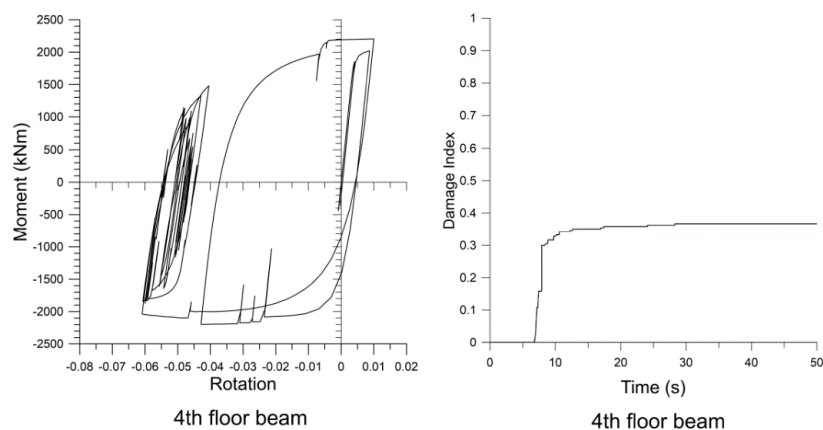


Fig. 4.13 Hysteretic response of 4<sup>th</sup> floor beam of 8-storey MD-MRF building under #1086-090 scaled to reach DI<sub>80%</sub>

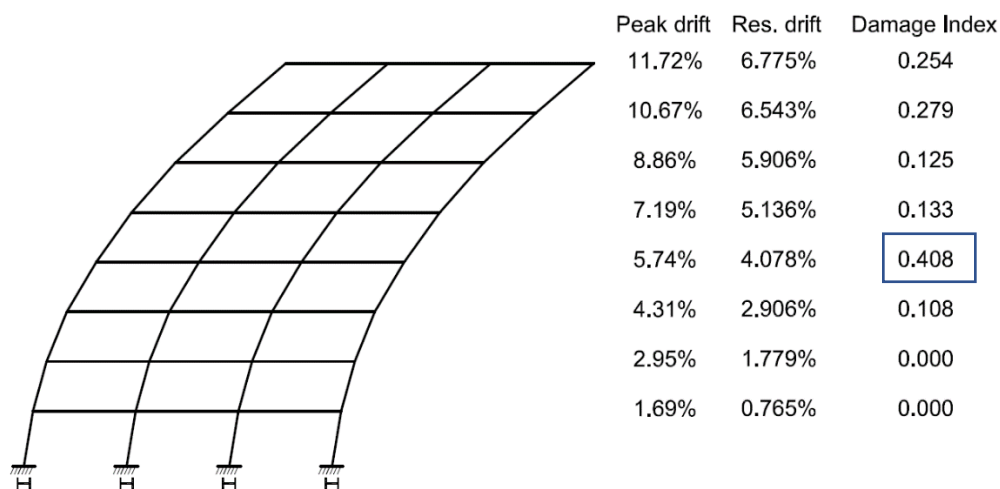


Fig. 4.14 Deflected shape of MD-MRF building under #1086-090 scaled to reach DI<sub>80%</sub> damage state and the maximum damage index at each floor

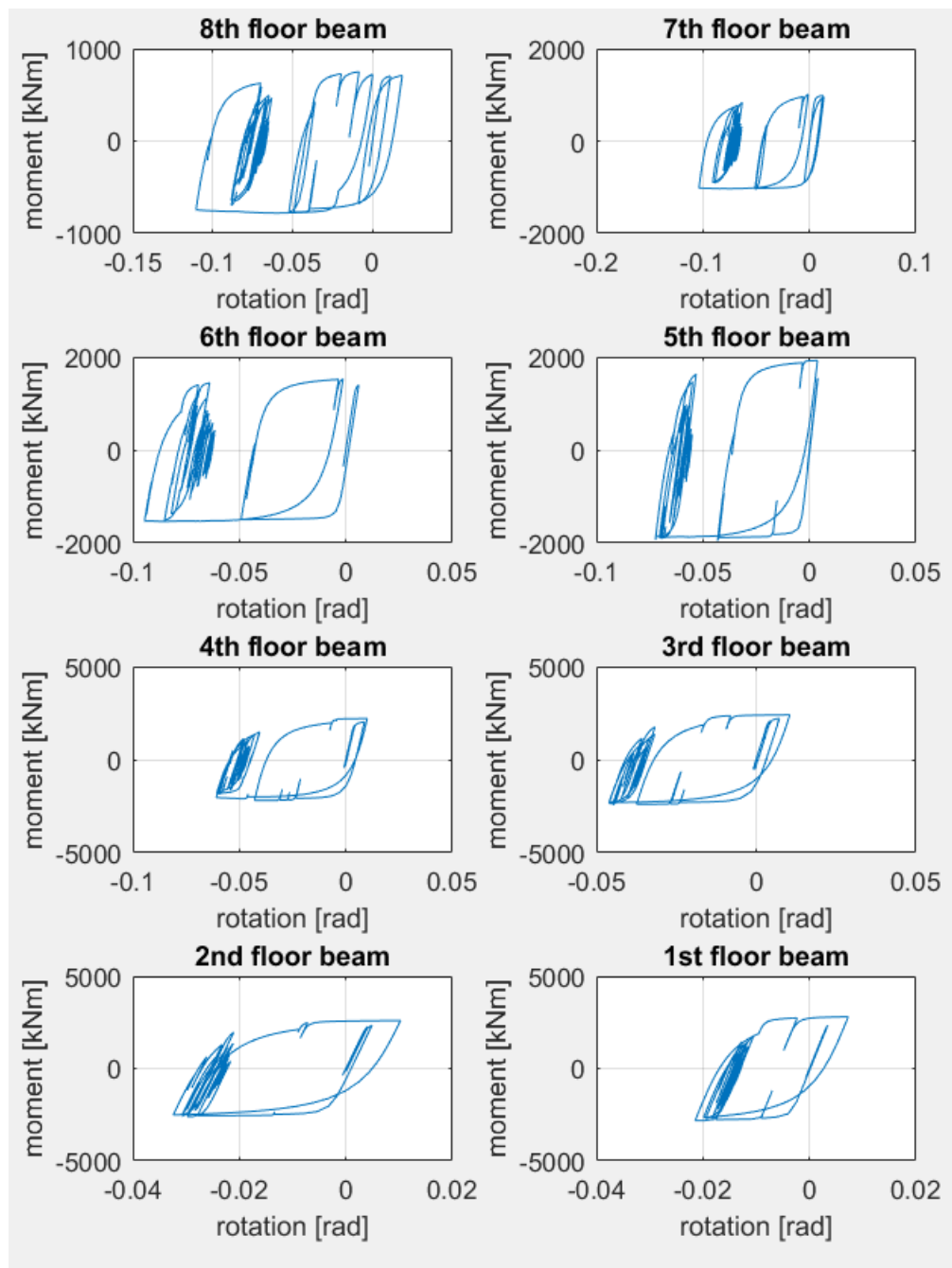


Fig. 4.15 The moment-rotation hysteresis loops of beam's plastic hinge at each floor corresponding to  $DI_{80\%}$  damage state

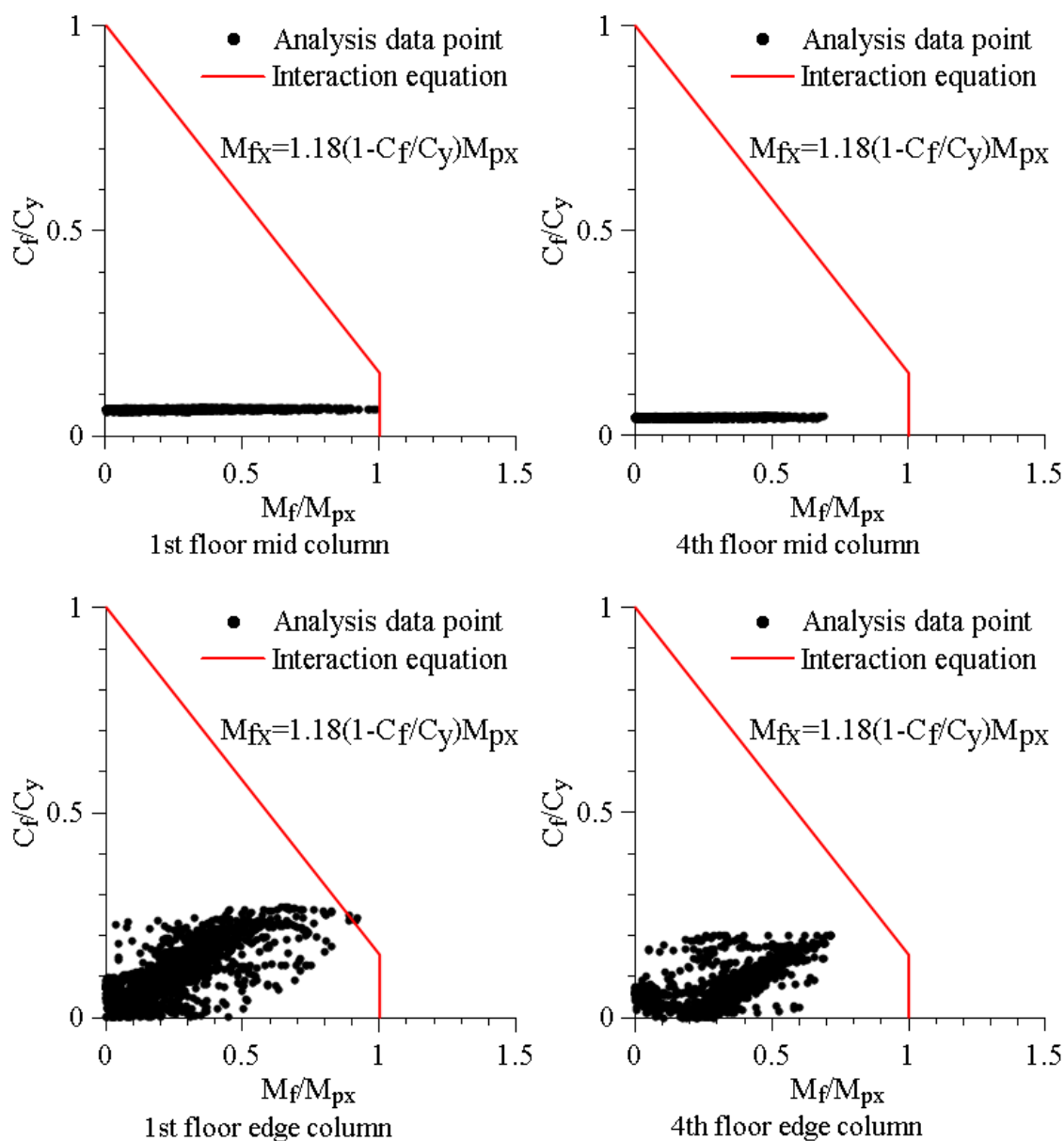


Fig. 4.16 The axial compression force vs. bending moment interaction diagram recorded at the bottom cross section of MD-MRF columns of 1<sup>st</sup> and 4<sup>th</sup> storey under #1086-090 scaled to  $DI_{80\%}$  damage state

#### 4.2.2 The IDA response of 8-st. MD-MRF building under subduction GMs

Similar as above, the 8-storey MD-MRF building is investigated under the suite of 11 subduction ground motions. The truncated IDA curves of the 8-storey MD-MRF building under subduction ground motions are shown in Fig. 4.17. The same symbols as those used in Fig. 4.9 are considered. The  $S(T_1)$  at the design level is 0.237 g.

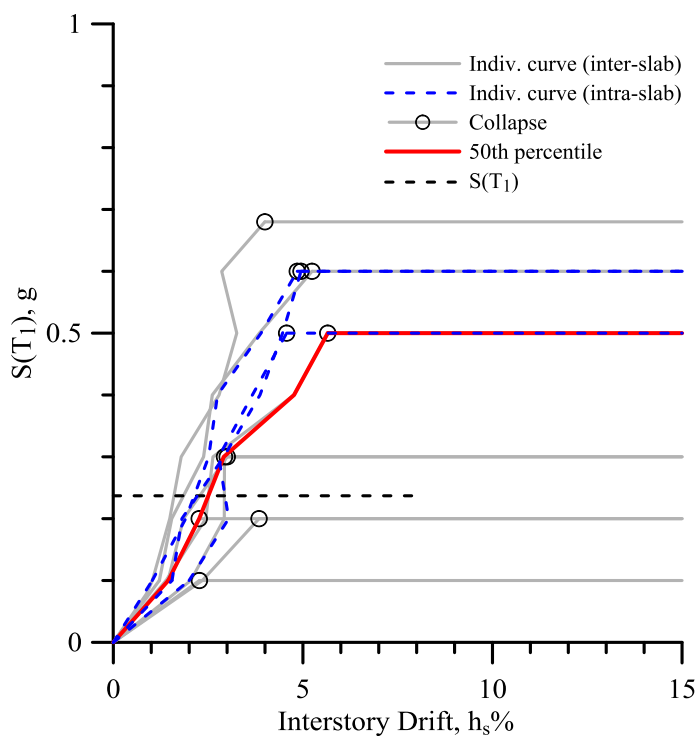


Fig. 4.17 Truncated IDA curves of 8-storey MD-MRF building under subduction GMs

The solid red line plotted is the 50<sup>th</sup> percentile IDA curve, which shows that the median  $DI_{80\%}$  is associated with  $S_a(T_1) = 0.5g$ , and the corresponding interstorey drift is  $5.65\%h_s$ .

It was observed that due to long duration of ground motions ( $\sim 300$  s) and several loading/unloading cycles the critical beam's plastic hinge reached  $DI_{80\%} = 0.375$  at lower demand than  $S_a(T_1) = 0.237$  g which is the design value. For instance, under #MYG001, the beam's plastic hinge of the 8<sup>th</sup> floor reached  $DI_{80\%} = 0.375$  for  $S(T_1) = 0.10$  g. However, in

this case, the interstorey drift is low. It is noted that in this case, the deterioration of beam's plastic hinges was found at the 3<sup>rd</sup>, 6<sup>th</sup>, and 8<sup>th</sup> floor, however, only at the 8<sup>th</sup> floor beam's plastic hinge reached  $DI_{80\%}$  as is showed in Fig. 4.18 and more in detail in Fig. 4.19.

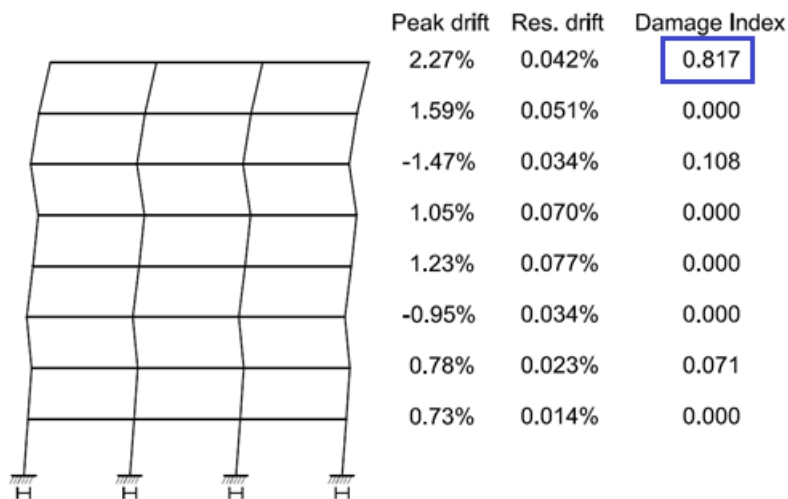


Fig. 4.18 Deflected shape of MD-MRF building under # MYG001 scaled to reach  $DI_{80\%}$  damage state and the maximum damage index at each floor

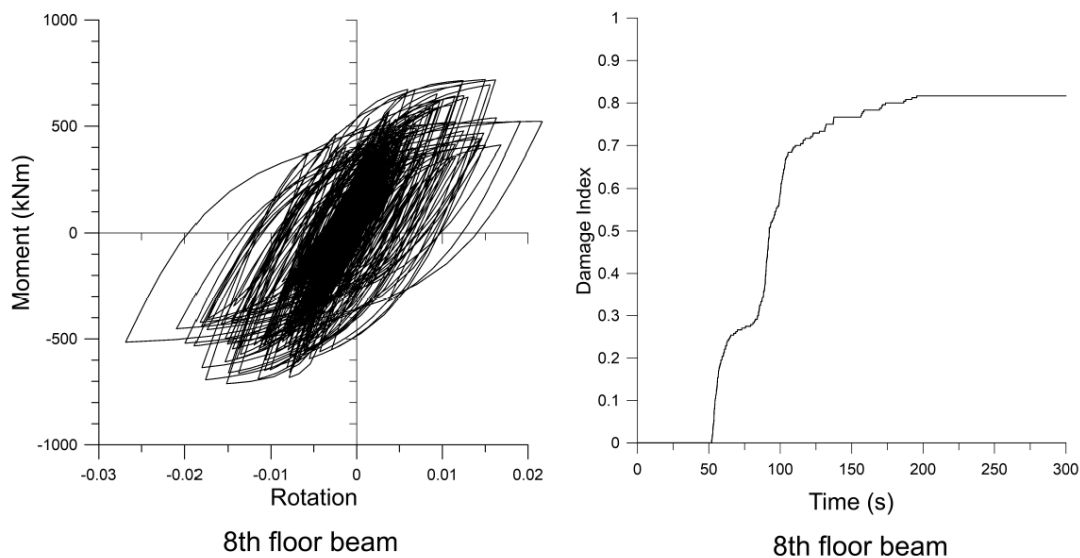


Fig. 4.19 Hysteretic response of 8<sup>th</sup> floor side beam of 8-storey MD-MRF building under #MYG001 scaled to  $DI_{80\%}$  damage state

As depicted, the rotation capacity of the plastic hinge is almost consumed, and the hysteresis response shows strength and stiffness degradation while the maximum bending

moment cannot be sustained. The cause of this substantial damage at lower demand is due to the long-term duration of subduction ground motions characterised by more than 1000 cycles.

The interstorey drift, residual interstorey drift and floor acceleration resulted for the 8-storey MD-MRF building under the set of subduction ground motions scaled up until the first beam's plastic hinge cross section reached  $DI_{80\%}$  are given in Fig. 4.20.

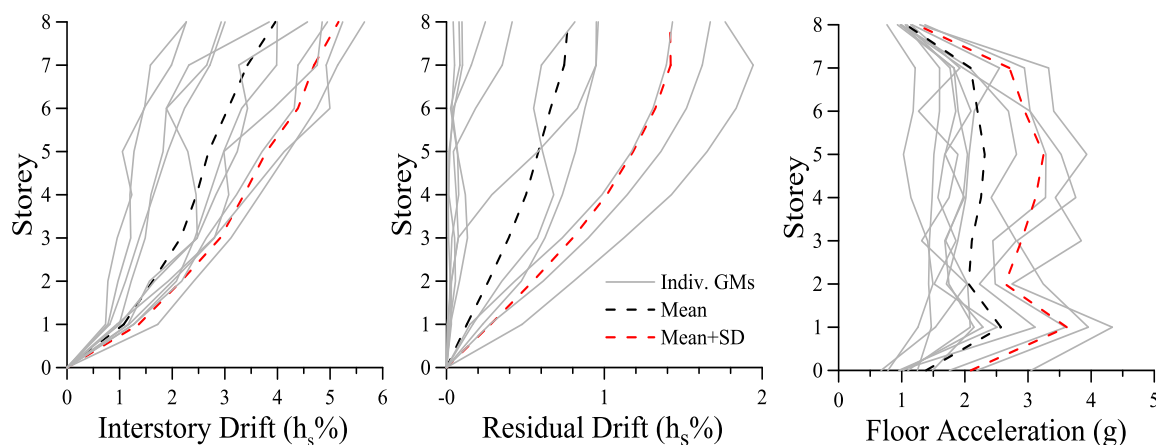


Fig. 4.20 Interstorey drift, residual interstorey drift and floor acceleration of 8-storey MD-MRF building associated to  $DI_{80\%}$  damage state under subduction GMs

As resulted from Fig. 4.20, the peak of mean interstorey drift is  $3.96\%h_s$ , the peak of mean residual drift is  $0.77\%h_s$ , and the peak of mean floor acceleration is  $2.31g$ .

The IDA curve resulted for the 8-storey MD-MRF building subjected to subduction ground motion #MYG001 is shown in Fig. 4.21a and that resulted under the #FKS005 is shown in Fig. 4.21b. It is noted that even after the first beam reaches  $DI_{80\%}$ , the damage still accumulates until the DI reaches 1.0, which means the beam loses all the flange fibers. However, even after the beam of a storey reaches  $DI = 1.0$ , the IDA curve does not show

trend of flattening, and damage still accumulates in beams of other floors, until DI of these beams reaches 1.0, as depicted in Fig. 4.21.

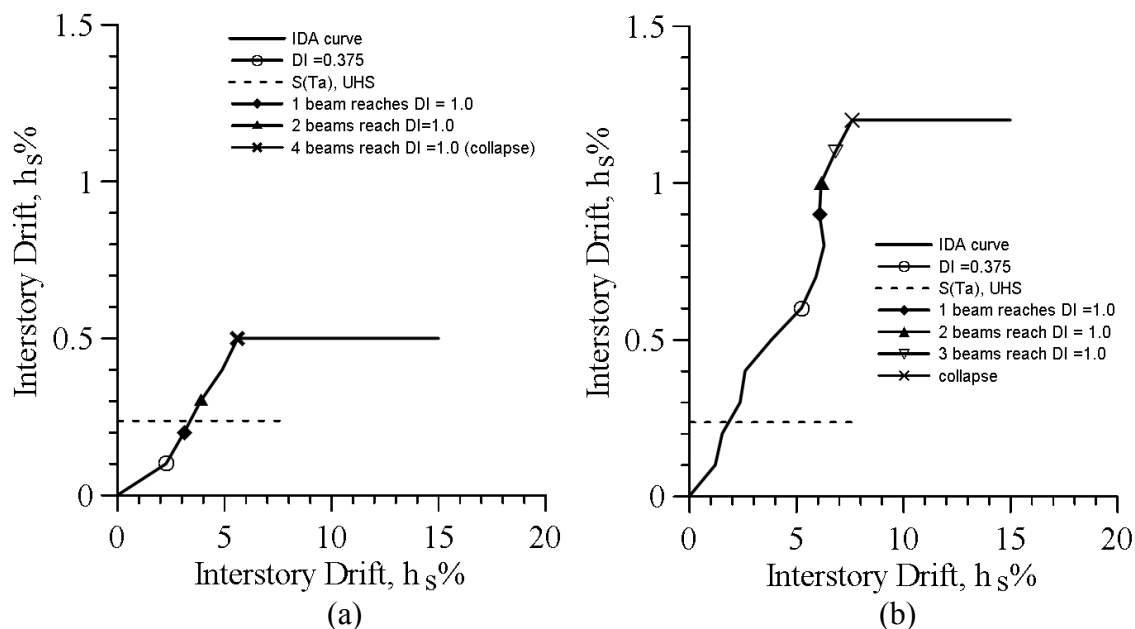


Fig. 4.21 IDA curve of MD-MRF building under GMs: (a) #MYG001 and (b) #FKS005

The deflected shape of 8-storey MD-MRF resulted under #FKS005 scaled to  $DI_{80\%}$  damage state is plotted in Fig. 4.22. As depicted, under  $S(T_1) = 0.6g$  the top floor beam's plastic hinge reached  $DI = 0.4$  which is slightly larger than the proposed  $DI_{80\%} = 0.375$  (Fig. 4.22), while the 4<sup>th</sup> floor beam's plastic hinge almost reached the  $DI_{80\%}$ . The moment-rotation diagram of the 8<sup>th</sup> floor beam's plastic hinge cross section is shown in Fig. 4.23. From Fig. 4.24 results that the bottom floors beams did not exhibit the low-cycle fatigue yet. The axial compression force vs. bending moment interaction diagram plotted for 1<sup>st</sup> and 8<sup>th</sup> floor bottom column cross section of middle and edge column resulted under #FKS005 scaled to  $DI_{80\%}$  damage state is shown in Fig. 4.25.

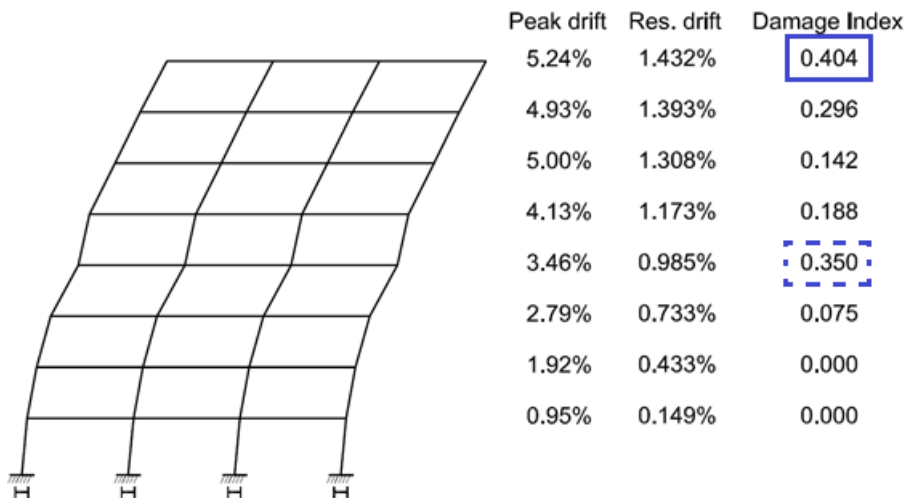


Fig. 4.22 Seismic response of MD-MRF building under #FKS005 scaled to reach DI<sub>80%</sub> damage state

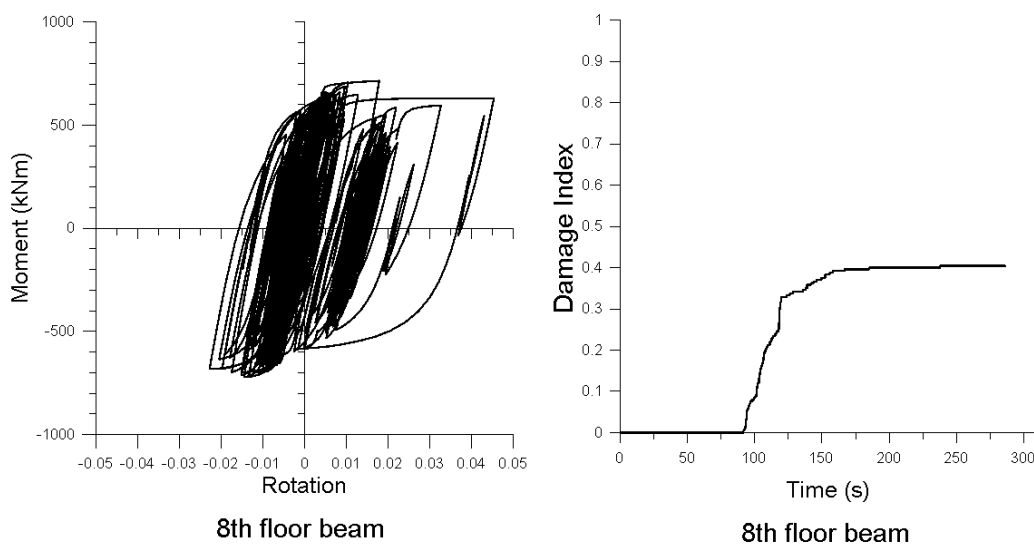


Fig. 4.23 Hysteretic response of 8th floor beam of MD-MRF building under #FKS005 scaled to DI<sub>80%</sub> damage state

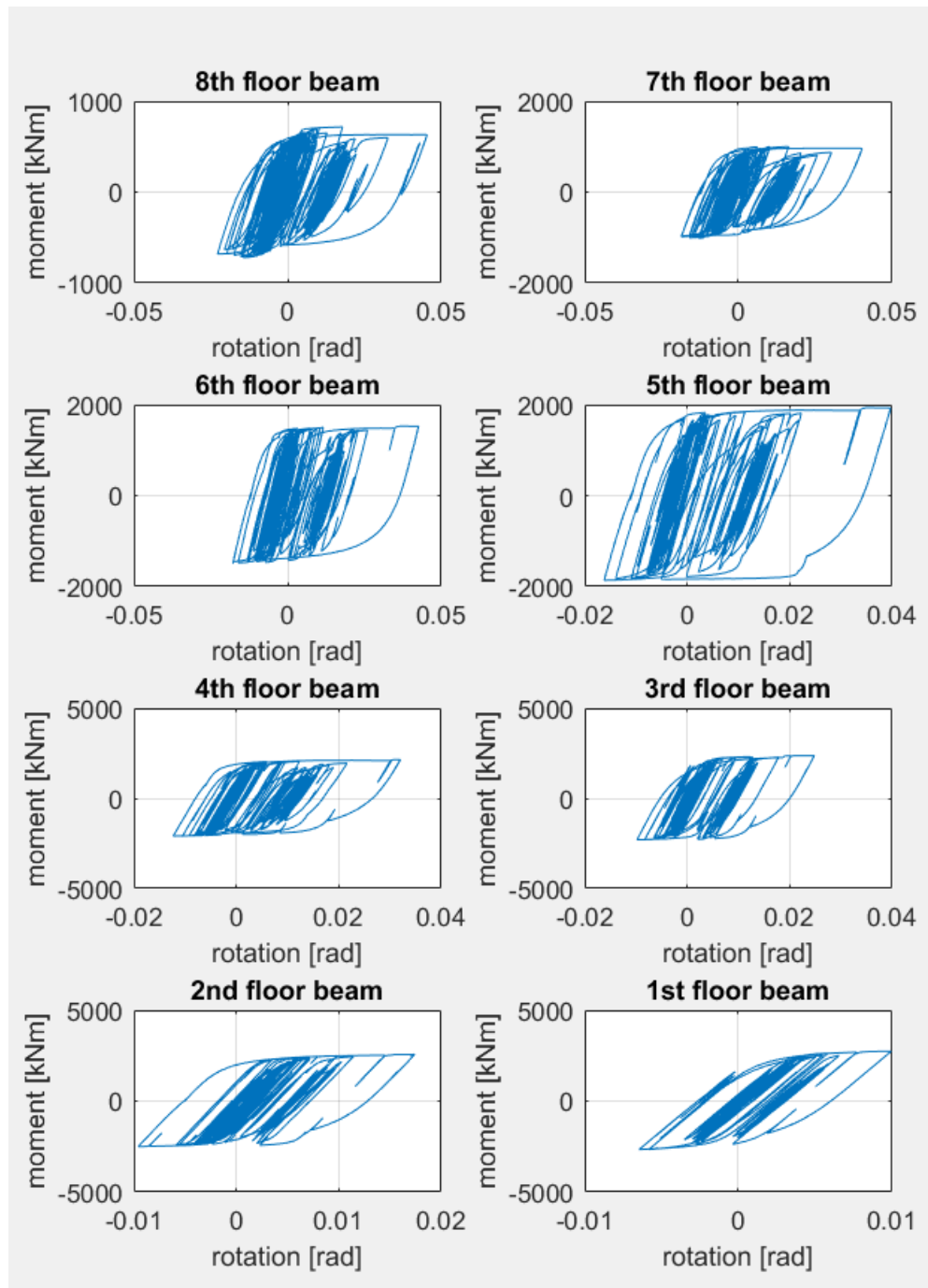


Fig. 4.24 The moment-rotation hysteresis loops of beam's plastic hinges at each floor under #FKS005 corresponding to  $DI_{80\%}$  damage state

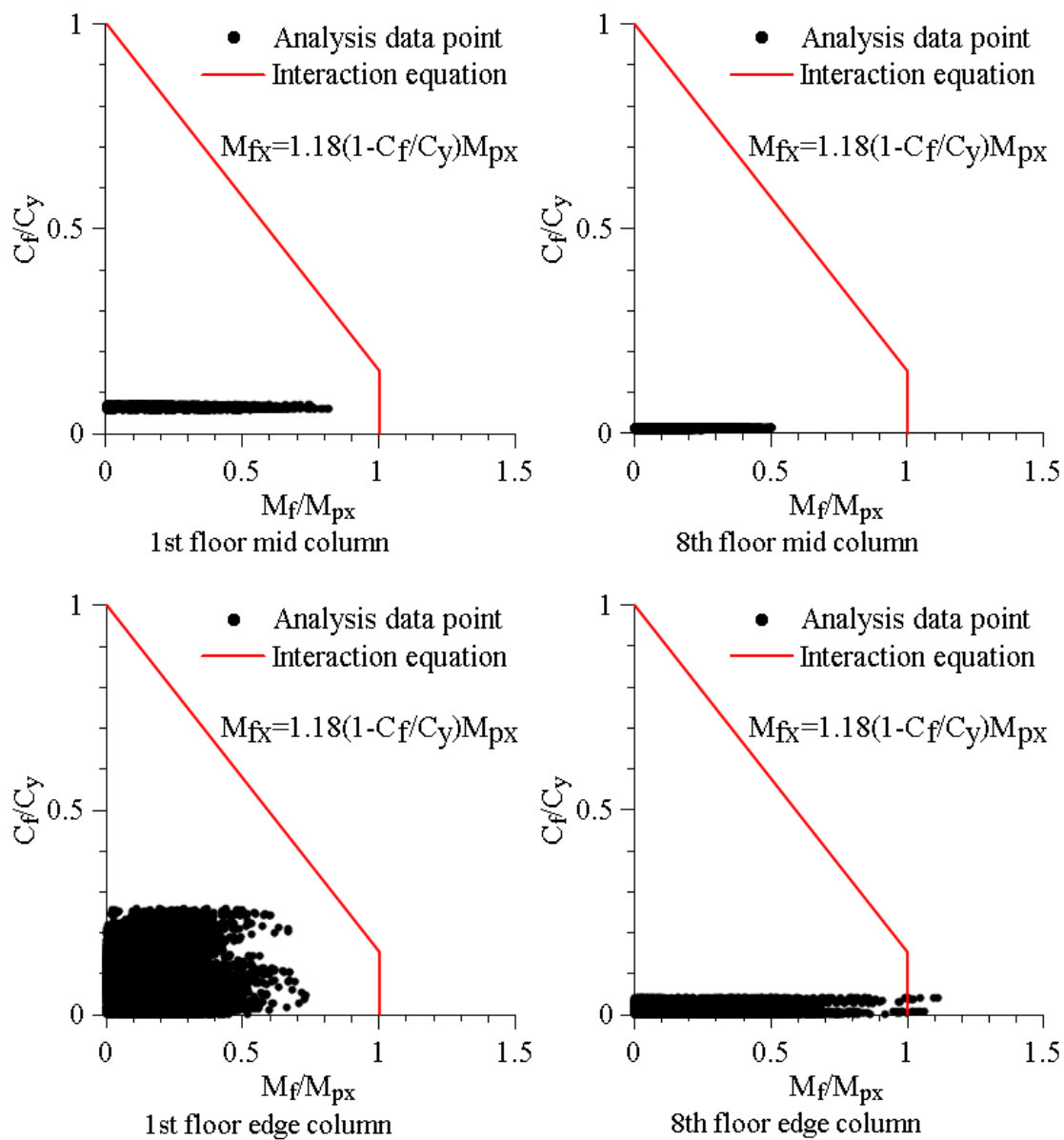


Fig. 4.25 The axial compression force vs. bending moment interaction diagram recorded at bottom column cross section of 1<sup>st</sup> and 8<sup>th</sup> floor under #FKS005 scaled to  $DI_{80\%}$  damage state

### 4.3 Incremental Dynamic Analysis of the 8-storey Building with Braced Dual System

To analyze the seismic response of the building with Braced Dual System, incremental dynamic analysis is performed using the selected two suites of ground motions. It is noted that the MD-CBF was designed to carry 100% design base shear and the MD-MRF was designed to carry an additional 25% base shear and was added to mitigate the weak-storey response of concentrically braced frames.

#### 4.3.1 The IDA Response of 8-st. building with Braced Dual System under crustal GMs

To highlight the response of the 8-storey building with Braced Dual System against the response of the same building braced by MD-CBFs the IDAs curves are built under GMs # 802-90 and #983-022 and are showed in Fig. 4.24.

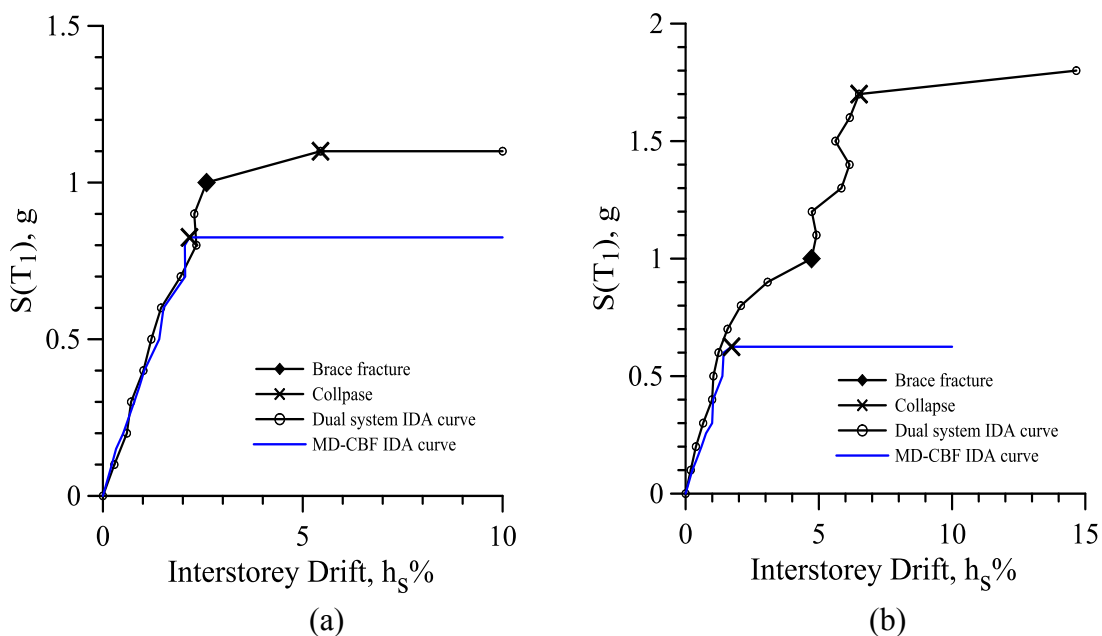


Fig. 4.26 IDA curves of Braced Dual System building vs. CBF building under crustal GMs: (a) #802-90, (b) #983-022

In Fig. 4.26, the diamond symbol shows the occurrence of HSS brace fracture of Braced Dual System and the “X” symbol shows the failure of the system. As resulted from the comparison with the bare MD-CBF system, the response of Braced Dual System is smoother and able to develop larger ductility before encountering the first brace fracture. In Fig. 4.26a, the collapse of Dual system is estimated at  $S(T_1) = 1.1g$ , since the IDA curve becomes unstable after this point. In Fig. 4.26b, the IDA curve of Braced Dual System shows accumulated damage at  $S(T_1) = 1.0g$  follows by greater increase in interstorey drift when the demand increases from  $1.7g$  to  $1.8g$ .

The seismic behavior of MD-CBF system versus the Braced Dual System subjected to ground motion #802-90 scaled to  $S(T_1) = 0.8g$  which signifies the failure of MD-CBF system (see IDA curves in Fig. 4.26a) is explained in Fig. 4.27.

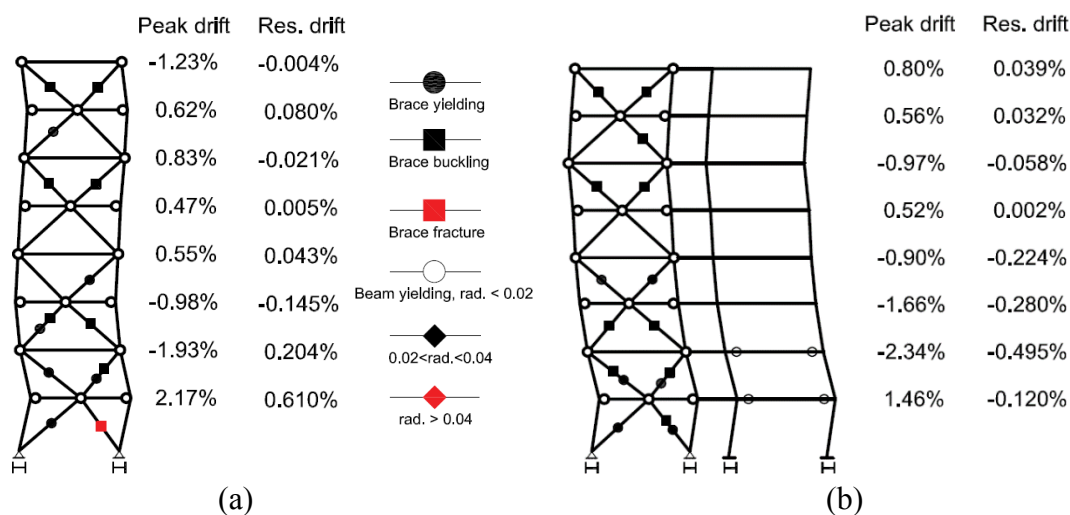


Fig. 4.27 Comparison of seismic response between MD-CBF system and Braced Dual System under #802-90 scaled to  $S(T_1) = 0.8g$ : a) MD-CBF; b) Braced Dual System

As shown in Fig. 4.27, at a demand of  $S(T_1) = 0.8g$ , the Braced Dual System does not experience fracture of brace, while the backup MRF frame shows slight yielding of beams of the 1<sup>st</sup> and 2<sup>nd</sup> floor. Hence, the residual interstorey drift diminishes from  $0.61\%h_s$  at the 1<sup>st</sup> floor of MD-CBF to  $0.495\%h_s$  in the case of Braced Dual System.

When the same ground motion #802-90 is scaled to  $S(T_a) = 1.0g$ , the Braced Dual System response is showed in Fig. 4.28. As depicted, two bottom braces of the same half span marked with red symbol in Fig. 4.28 exhibited initiation of fracture. Under this demand of 1.0g, all braces experienced buckling or/and yielding and four MRF beams experience flexural yielding.

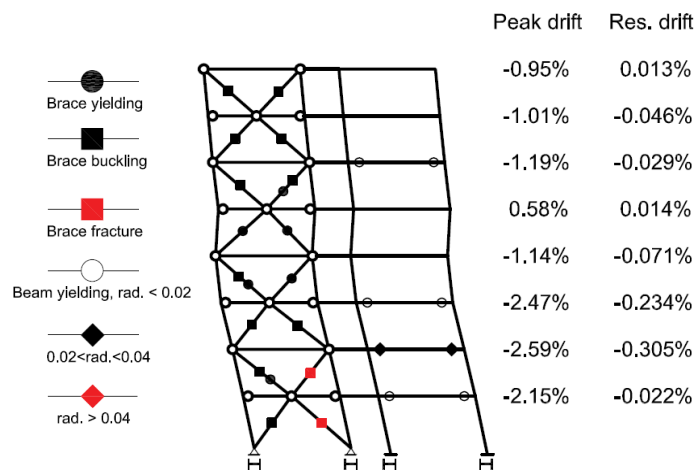
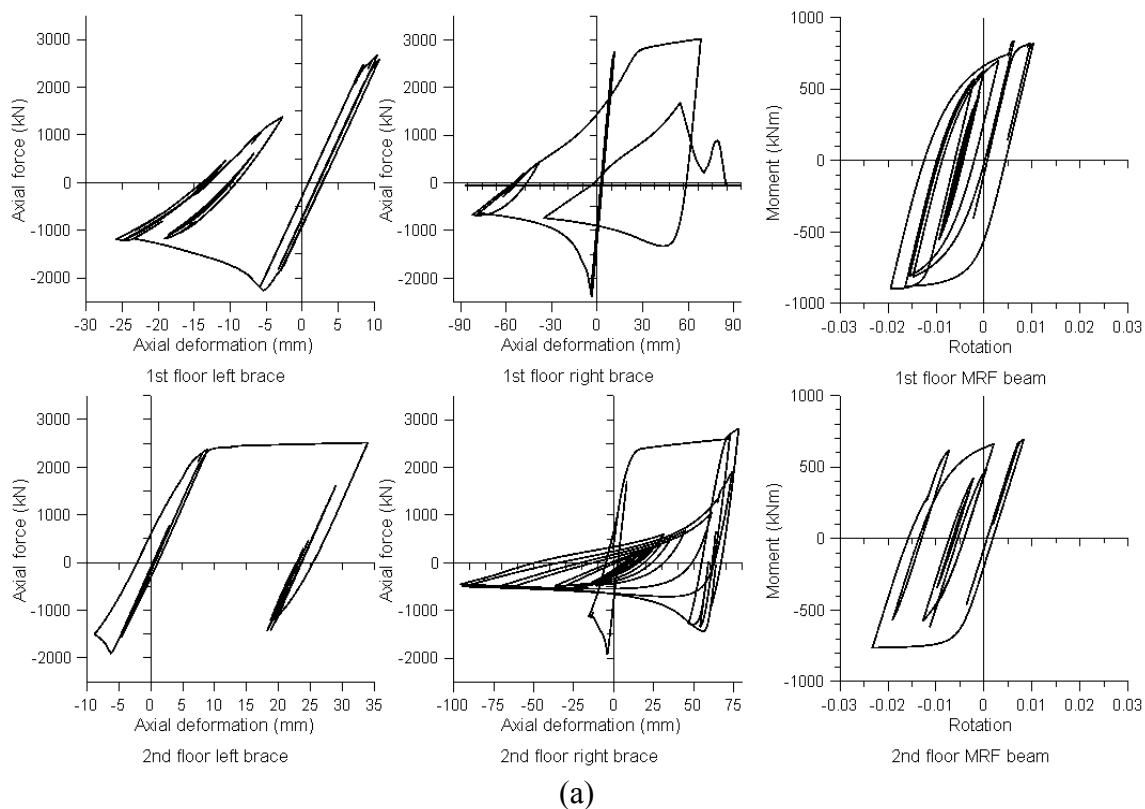
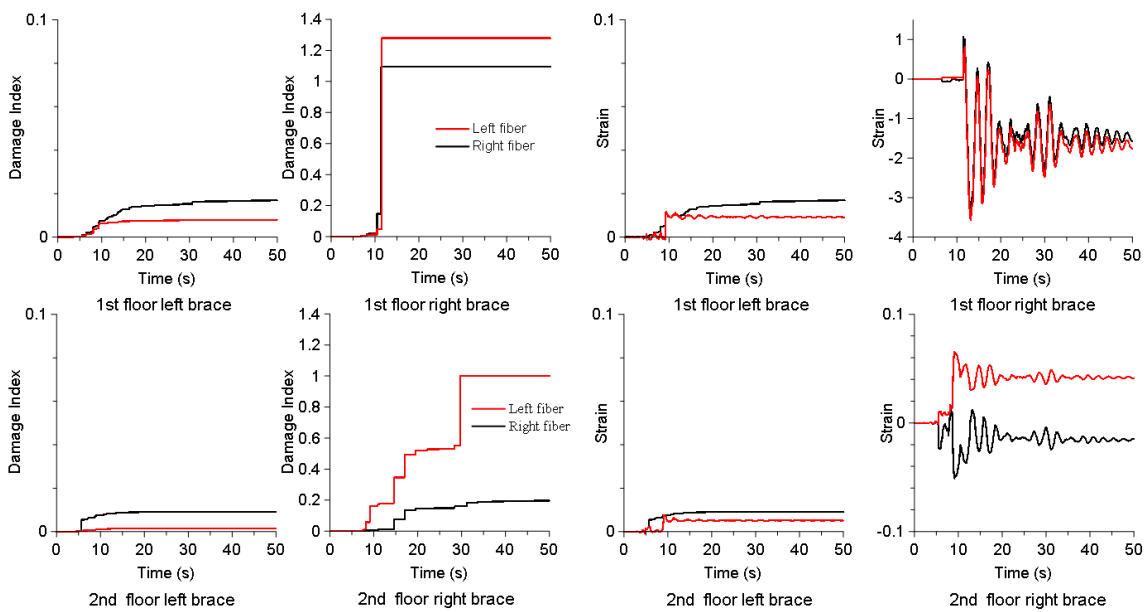


Fig. 4.28 Seismic response of Braced Dual System under #802-90 scaled to  $S(T_1) = 1.0g$

The detail response of left and right braces located at the 1<sup>st</sup> and 2<sup>nd</sup> floor, as well as, the moment-rotation hysteresis loops of the 1<sup>st</sup> and 2<sup>nd</sup> floor beam's plastic hinge cross section are depicted in Fig. 4.29a. Furthermore, since fracture of braces is observed, the strain time history and damage index of the outermost fibers of HSS braces of the 1<sup>st</sup> and 2<sup>nd</sup> floor are illustrated in Fig. 4.29b. It is noted that when the HSS brace buckles, one flange is subjected to tension and the other one to compression.



(a)



(b)

Fig. 4.29 Hysteretic behavior of critical HSS braces, the associated MRF beam and the strain time history and damage of the outermost fibers of HSS brace cross sections of Dual system under #802-90 scaled to  $S(T_1) = 1.0g$ : (a) hysteretic response of HSS brace and MRF beam; (b) strain history and damage of outermost fibers of HSS braces

From the IDA curve of Braced Dual System shown in Fig. 4.26a, the failure occurs under the  $S(T_1) = 1.1g$  demand of GM #802-90. The seismic response of Braced Dual System is shown in Fig. 4.30. It is worth to note that under a small increase in demand from 1.0g to 1.1g the peak interstorey drift at bottom floors increases from  $2.59\%h_s$  to  $5.44\%h_s$  and the peak residual drift increases from  $0.3\%h_s$  to  $0.683\%h_s$ . In addition, the 1<sup>st</sup> floor beam of braced frame experienced flexural yielding due to the redistribution of brace forces after the two bottom floors braces exhibited fracture.

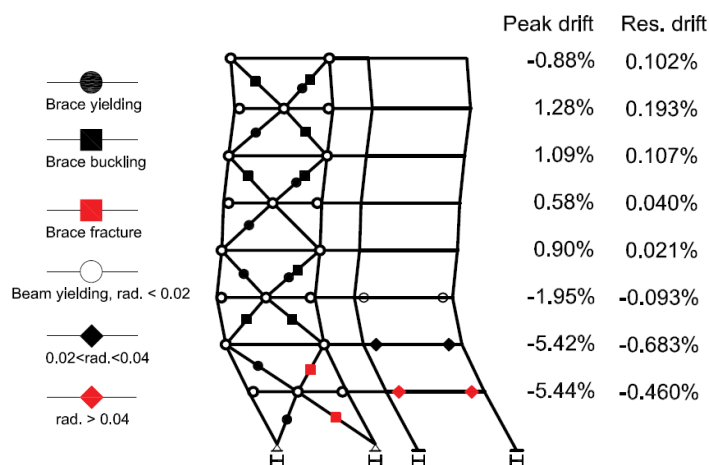


Fig. 4.30 Seismic response of Braced Dual System under #802-90 scaled to near-collapse limit state ( $S(T_1) = 1.1g$ )

As illustrated in Fig. 4.30, all braces excepting the 5<sup>th</sup> floor right brace experienced buckling or/and yielding, and the first 3 storey MRF beam experienced yielding. The damage of the structure is concentrated at the 1<sup>st</sup> and 2<sup>nd</sup> floor, the right brace of both floors shows fracture, the beam of braces attached experienced yielding and the 1<sup>st</sup> floor MRF beam shows rotation more than 0.04 radian.

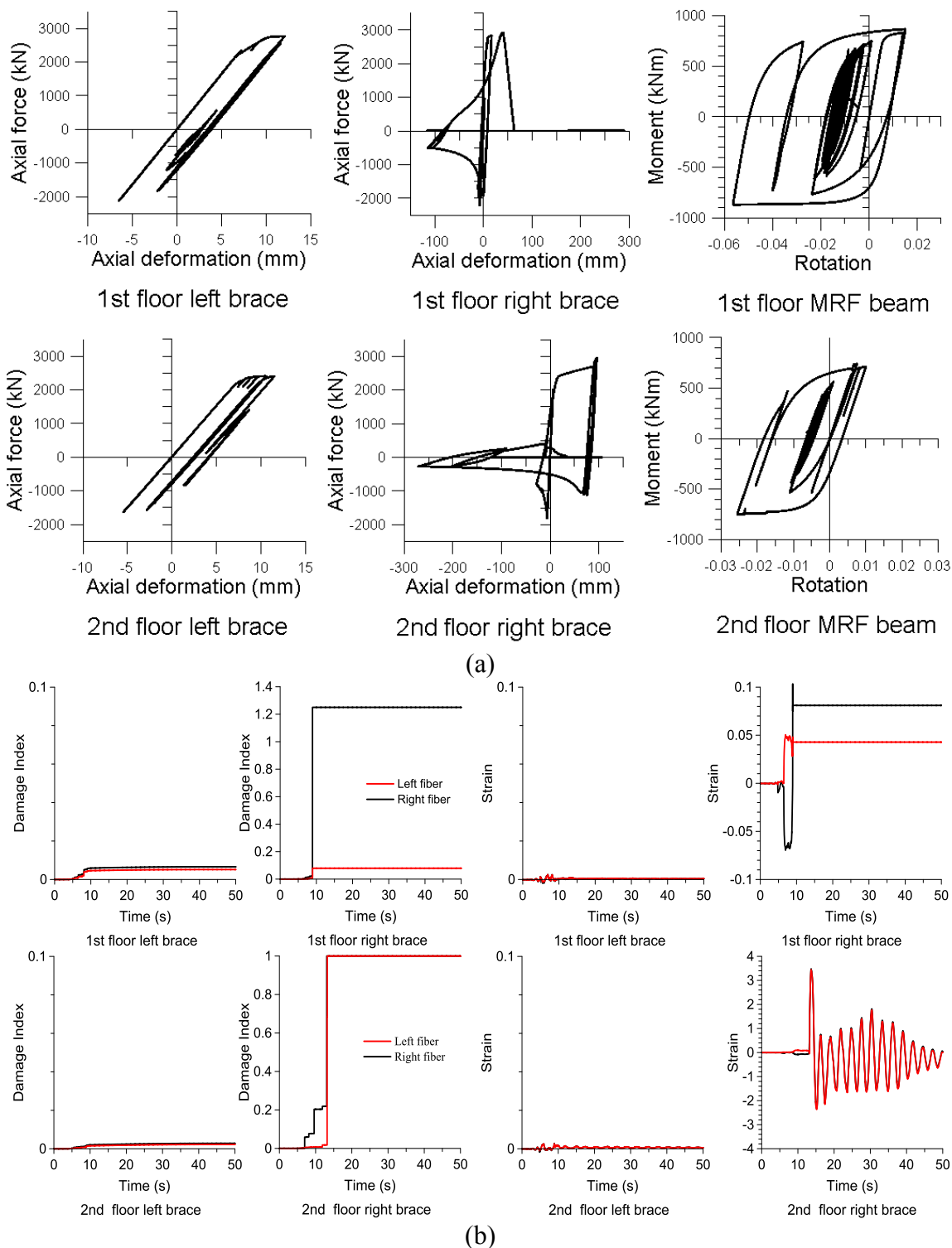


Fig. 4.31 Hysteretic behavior of critical HSS braces, the associated MRF beam and the strain time history and damage of the outermost fibers of HSS brace cross sections of Dual system under #802-90 scaled to  $S(T_1) = 1.1g$ : (a) hysteretic response of HSS brace and MRF beam; (b) strain history and damage of outermost fibers of HSS braces

The hysteresis loops of 1<sup>st</sup> and 2<sup>nd</sup> floor right and left HSS braces and that of MRF beams of 1<sup>st</sup> and 2<sup>nd</sup> floor are shown in Fig. 4.31a. As depicted, both 1<sup>st</sup> floor and 2<sup>nd</sup> floor right HSS braces reached fracture caused by low-cycle fatigue, while the 1<sup>st</sup> floor MRF beam reached a rotation of 0.06 rad but no strength and stiffness degradation was observed. In Fig. 4.31b, the damage index and strain time history of the outermost fibers of 1<sup>st</sup> and 2<sup>nd</sup> floor HSS braces are presented.

In addition, the simplified interaction diagram for plastic stress distribution within the cross section due to axial compression and bending given in Eq.(4.1) is applied.

As shown in Fig. 4.32, the 1<sup>st</sup> floor beam of braced bay and 1<sup>st</sup> floor MRF column show formation of plastic hinges. However, in the numerical model, it was not introduced a Min-max material to show beam failure under compression and bending after the attached braces reached failure. Since the MRF columns are fixed at the base, the formation of plastic hinges cannot be avoided. No failure is observed in the case of MD-CBF columns.

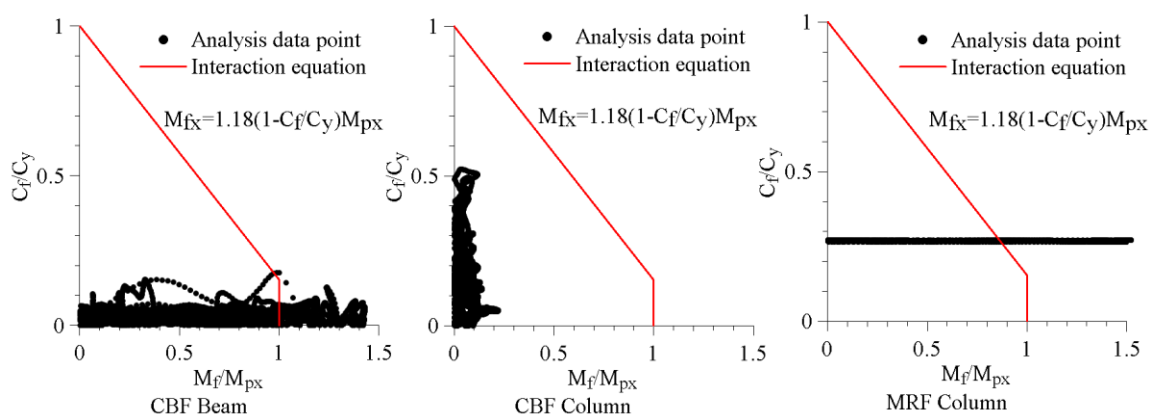


Fig. 4.32 The 1<sup>st</sup> floor axial compression force-bending moment interaction diagram under #802-90 scaled to 1.1g (near-collapse limit state)

The time-history response of fractured braces, the bending developed in the 1<sup>st</sup> floor MD-CBF beam and the axial force developed in the MD-CBF column and flexural moment in the MRF column are shown in Fig. 4.33.

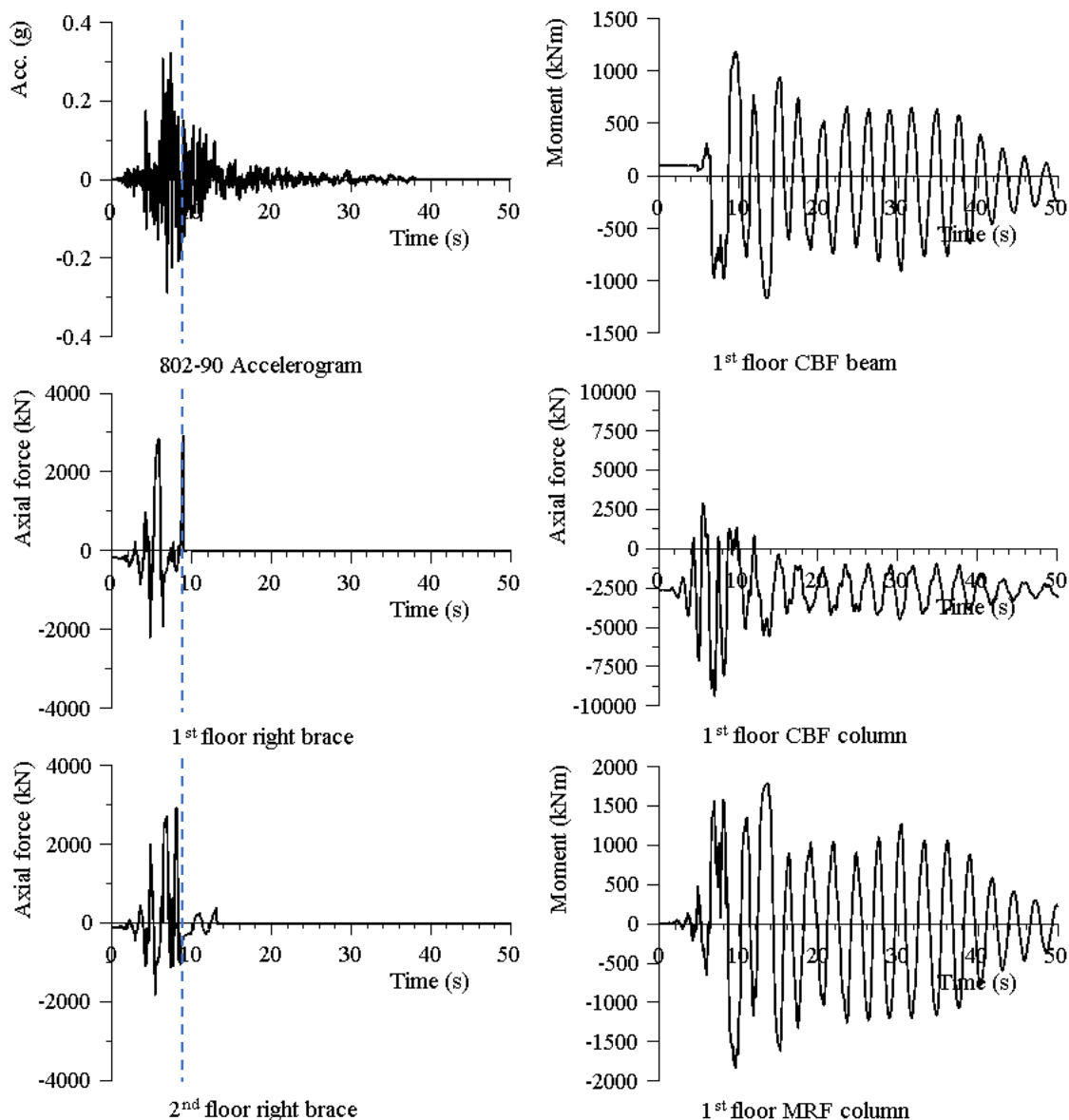


Fig. 4.33 Time-history response of Braced Dual System members under #802-90 scaled to 1.1g (near-collapse limit state)

As depicted, after the peak of accelerogram occurred at  $t=9.575$  s the 1<sup>st</sup> floor right brace fractured at  $t=9.585$  followed by the 2<sup>nd</sup> floor brace ( $t = 13.27$ s). Meanwhile, the attached beam of fractured braces experienced larger bending moment at the same time sequence.

As resulted, this failure mechanism is labelled two-floor mechanism and is typical for split “X” brace system.

The second type of failure mechanism is observed under ground motion # 787-270, where failure of braces occurs only at the bottom floors. The comparison of IDA curves is shown in Fig. 4.34. Similarly, the failure mechanism is explained hereafter.

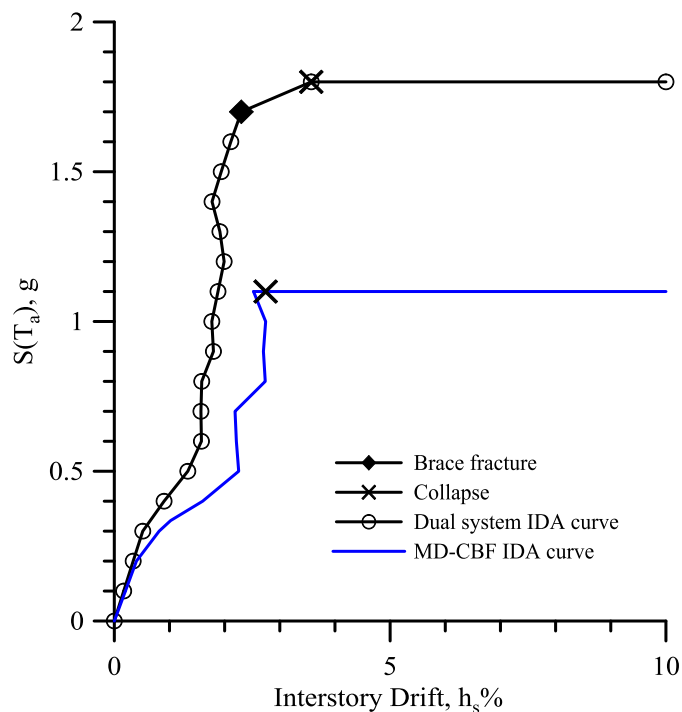


Fig. 4.34 IDA curve of Braced Dual System vs. MD-CBF system of 8-storey building under #787-270

From Fig. 4.35, it is observed that under GM #787-270 scaled to  $S(T_a) = 1.1g$ , the bare MD-CBF building experienced failure caused by 5 HSS braces fracture marked with red square in Fig. 4.35a. Under this demand intensity the Braced Dual System experienced buckling and/or yielding of braces but no fracture as depicted in Fig. 4.35b.

The IDA of Braced Dual System is in the “weaving” type until  $S(T_1) = 1.7g$  is reached. At this demand level, it shows the initiation of failure as depicted in Fig. 4.36.

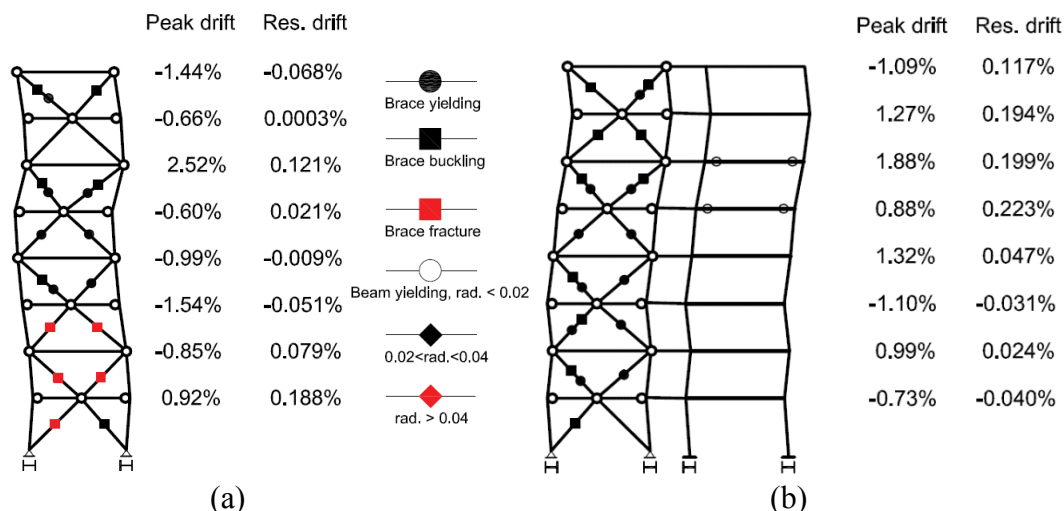


Fig. 4.35 Comparison of seismic response between MD-CBF system and Braced Dual System under #787-270 scaled to  $S(T_1) = 1.1g$ : (a) MD-CBF; (b) Braced Dual System

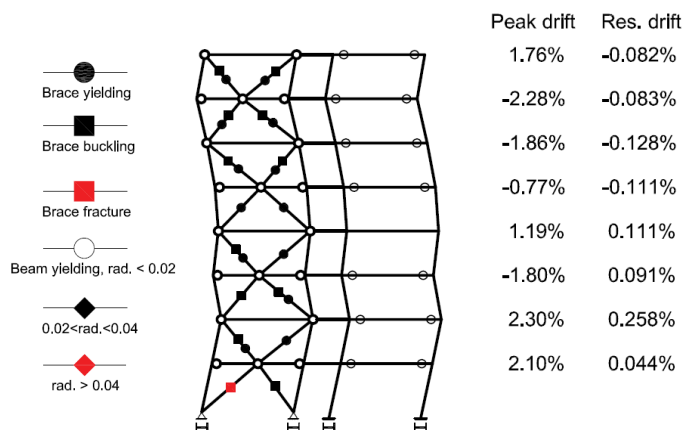


Fig. 4.36 Seismic response of Braced Dual System under #787-270 scaled to 1.7g. As illustrated in Fig. 4.36, under GM #787-270, all HSS braces experienced buckling or/and yielding; all the MRF beams but that of the 4<sup>th</sup> floor experienced flexural yielding while exhibiting a rotation less than 0.02 radian. However, only the ground floor left brace shows fracture caused by low-cycle fatigue. The hysteresis loops of HSS braces and MRF beams of the 1<sup>st</sup> and 2<sup>nd</sup> floor are shown in Fig. 4.37a, the damage index and strain time history of the outermost fibers of HSS braces are shown in Fig. 4.37b. It results that the 2<sup>nd</sup> floor left brace is closed to fracture.

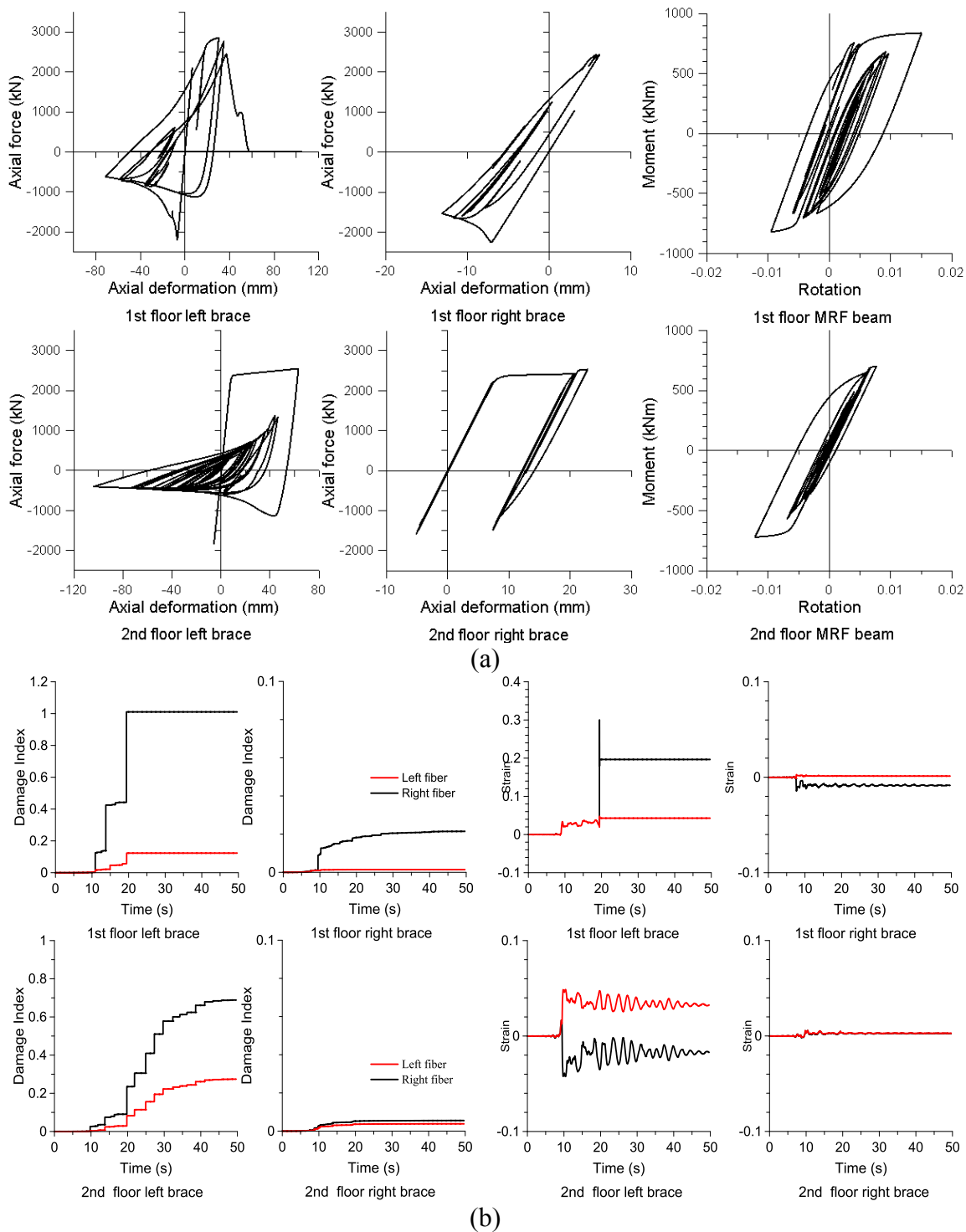


Fig. 4.37 Hysteretic behavior of critical HSS braces, the associated MRF beam and the strain time history and damage of the outermost fibers of HSS brace cross sections of Dual system under #787-270 scaled to  $S(T_1) = 1.7g$ : (a) hysteretic response of HSS brace and MRF beam; (b) strain history and damage of outermost fibers of HSS braces

When the GM #787-270 is scaled to  $S(T_a) = 1.8g$ , the Braced Dual System response is shown in Fig. 4.38. At the 2<sup>nd</sup> floor the peak interstorey drift is 3.57% $h_s$  and the residual interstorey drift is 0.9% $h_s$ .

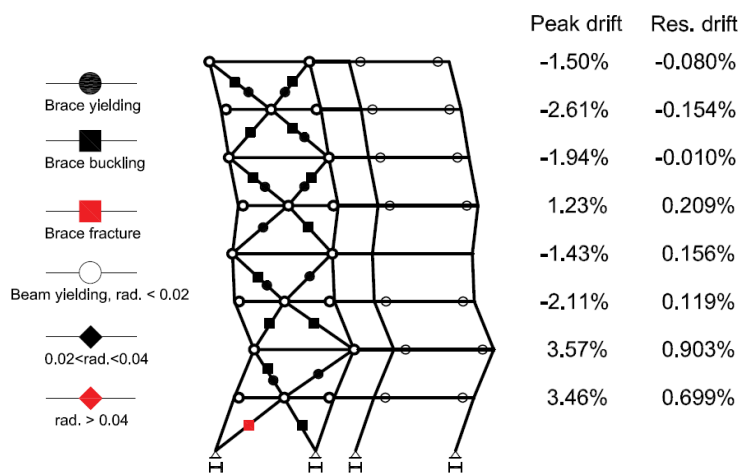


Fig. 4.38 Seismic response of Braced Dual System under #787-270 scaled to 1.8g (near-collapse limit state)

The hysteresis loops of HSS braces and MRF beams of the 1<sup>st</sup> and 2<sup>nd</sup> floor are shown in Fig. 4.39a, the damage index and strain time history of the brace outermost fibers are shown in Fig. 4.39b. It is noticed from Fig. 4.39b that even though only the 1<sup>st</sup> floor left brace shows fracture, the 2<sup>nd</sup> floor left brace shows a damage index around 0.6.

Similar to previous case, the beam of the attached fracture brace is examined and the axial compression and bending developed are plotted in Fig. 4.40 as depicted for the 1<sup>st</sup> floor braced bay beam. Results of for the 1<sup>st</sup> floor braced bay column and MRF column are also shown in Fig. 4.40.

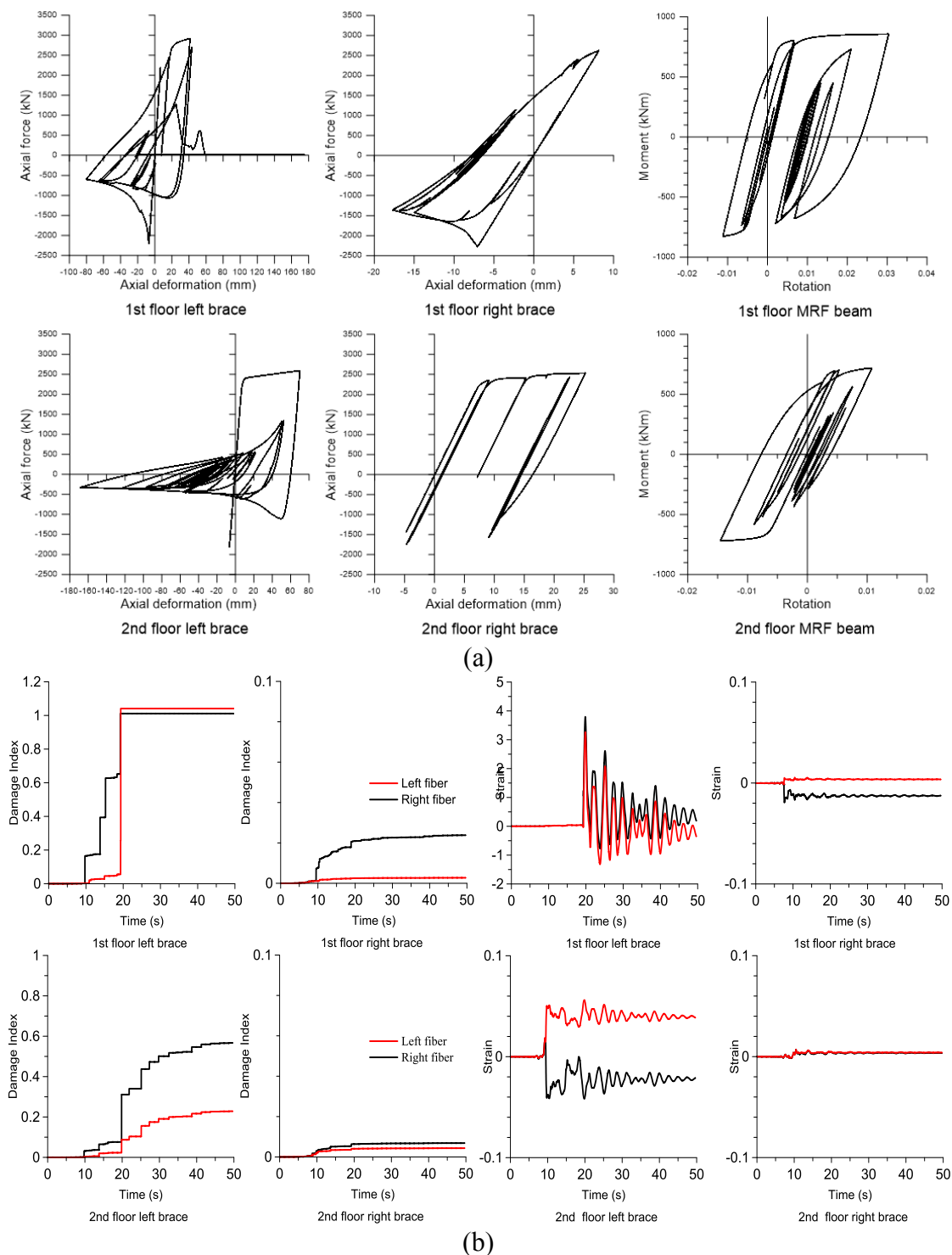


Fig. 4.39 Hysteretic behavior of critical HSS braces, the associated MRF beam and the strain time history and damage of the outermost fibers of HSS brace cross sections of Dual system under #787-270 scaled to  $S(T_1) = 1.8g$ : (a) hysteretic response of HSS brace and MRF beam; (b) strain history and damage of outermost fibers of HSS braces

As depicted, the 1<sup>st</sup> floor MD-CBF beam and MRF column show nonlinear behavior, while the MD-CBF columns are still safe in elastic range. This finding is similar with the response of Braced Dual System subjected to GM #802-90.

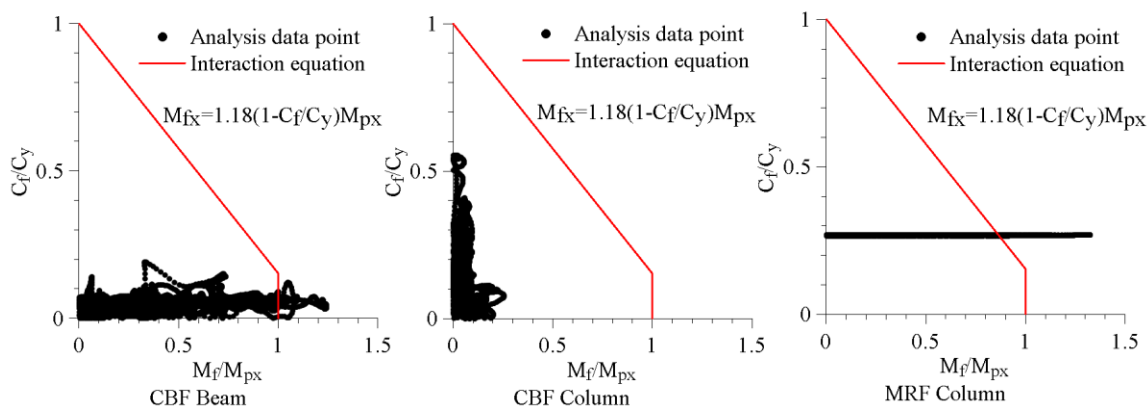


Fig. 4.40 The 1<sup>st</sup> floor axial force-bending moment interaction diagram under #787-270 scaled to 1.8g (near-collapse limit state)

The eleven IDA curves resulted for the 8-storey building with Braced Dual System subjected to crustal ground motions are summarized in Fig. 4.41. The 50 percentile IDA curve is plotted with a red solid line and shows that the collapse of the building occurs at  $S(T_1)$  of 1.5g which corresponds to interstorey drift of  $5.04\%h_s$ . The solid black line shows the medium intensity of 0.2g required to load braces until the first reaches buckling. At this level of loading the MD-CBF pass from the elastic to plastic range. The solid blue line shows the medium intensity of 0.7g when first MRF beam passes the elastic response and the flexural yielding is initiated.

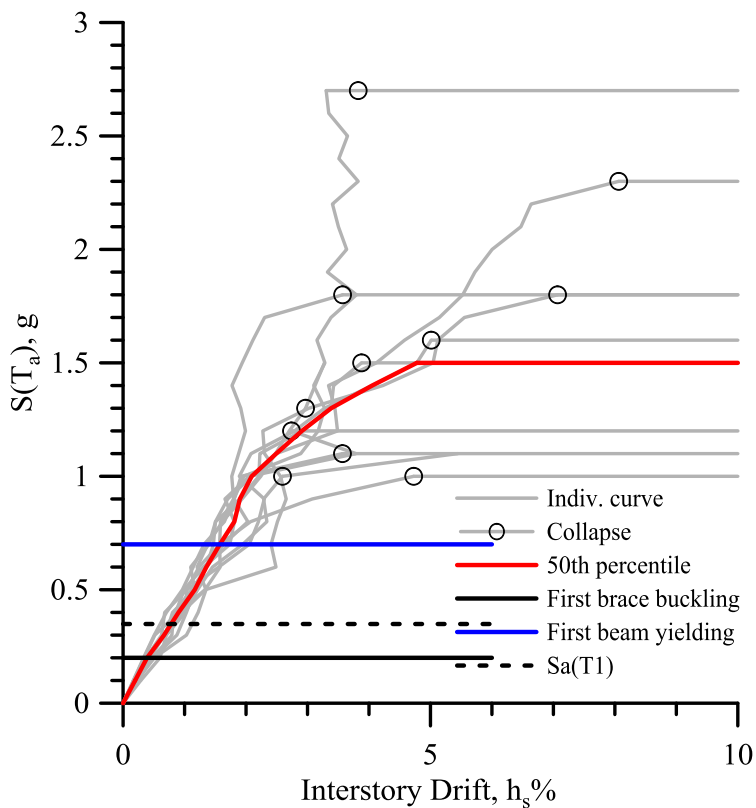


Fig. 4.41 IDA curves of studied 8-storey building with Braced Dual System under 11 crustal GMs

The building response at the near collapse limit state is shown in Fig. 4.42 in terms of interstorey drift, residual interstorey drift, and floor acceleration. It is concluded that the peak of mean interstorey drift occur at bottom two floors and is  $3.58\%h_s$ , while the peak of mean residual drift is  $0.82\%h_s$ . The peak of mean floor acceleration is  $0.91g$  and seems uniformly distributed along the building height. From interstorey drift distribution it is showed the tendency of forming the weak two-storey mechanism at the bottom floors. The (Mean+SD) is showed with red dashed line.

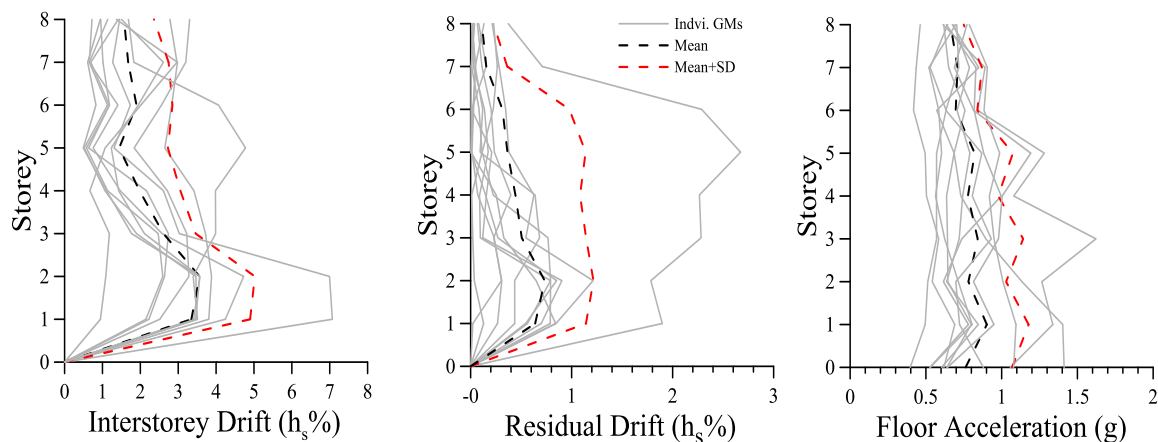


Fig. 4.42 Near collapse response of building with Braced Dual System under crustal GMs

There are two different failure mechanisms observed to occur under the 11 crustal ground motions. For 10 ground motions but one the building structure fails when both two bottom floors braces fractures, as well as the beam to which these braces are attached fails due to axial compressing and bending interaction. In one case, only one brace reached fracture while the second is closed to fracture, but the attached beam failed.

#### ***4.3.2 The IDA response of 8-st. building with Braced Dual System under subduction***

##### ***GMs***

Similarly, the failure mechanisms of building with Braced Dual System under subduction ground motions are investigated. There were identified three failure mechanisms presented hereafter.

The failure mechanism observed under Tohoku GMs #FKS005, #FKS009, #IBR006 and #MYG001 are similar between them and different than that identified in the case of crustal GMs. The single IDA curves of MD-CBF and Braced Dual System subjected to GM #IBR006 is shown in Fig. 4.43.

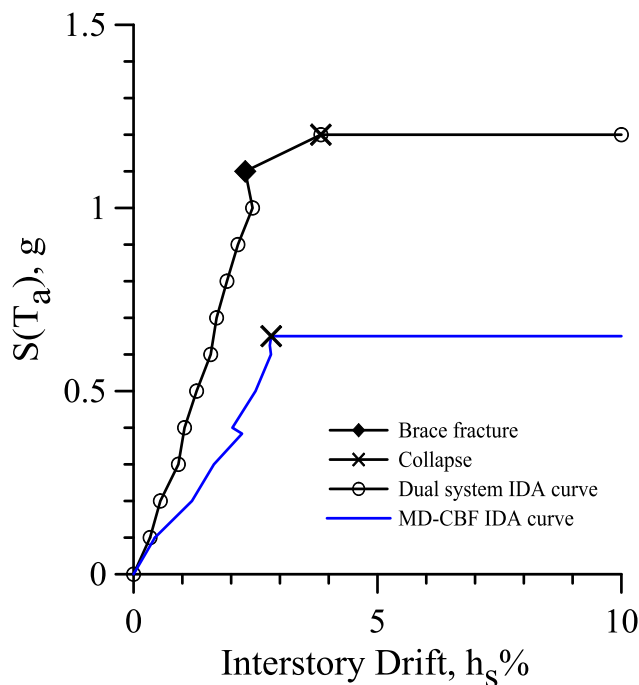


Fig. 4.43 IDA curve of 8-storey building with Braced Dual System vs. MD-CBF system under #IBR006

The seismic behavior of MD-CBF system versus Braced Dual System under ground motion #IBR006 scaled to  $S(T_1) = 0.7g$  is plotted in Fig. 4.44. It is shown that failure of MD-CBF system is reached when both left and right braces on 6<sup>th</sup> floor initiates fracture followed by beam failure. At this demand level no damage was observed for Braced Dual System. However, there are braces buckled and top floors beams of MRF that initiated flexural yielding.

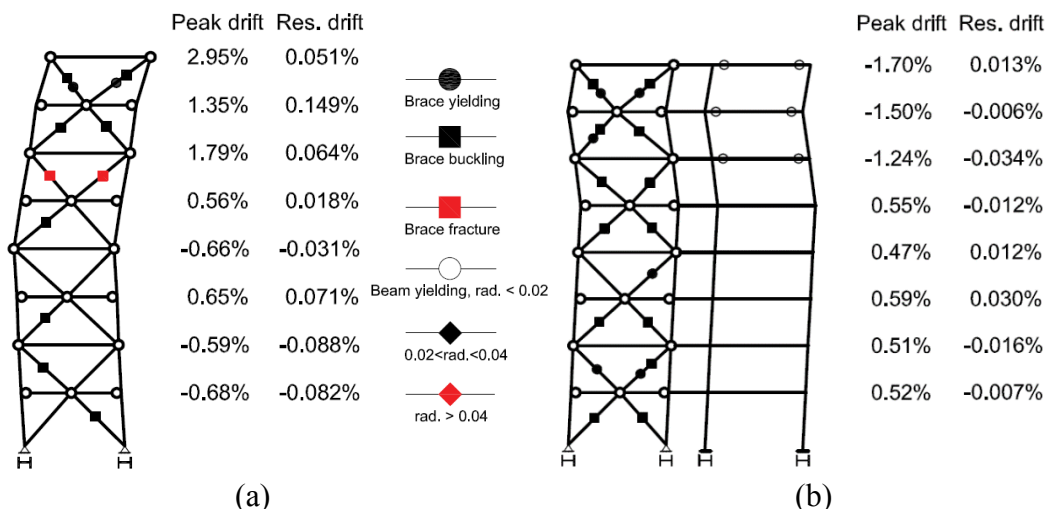


Fig. 4.44 Comparison of seismic response between MD-CBF system and Braced Dual System under #IBR006 scaled to  $S(T_1) = 0.7g$ : (a) MD-CBF; (b) Braced Dual System

When GM #IBR006 is scaled to  $S(T_1) = 1.1g$ , the Braced Dual System shows initiation of failure. The seismic response is depicted in Fig. 4.45. It is shown that the peak interstorey drift is  $2.29\%h_s$ , peak residual drift is  $0.11\%h_s$ , and occurred at the top floor. From analysing the braces response, it was identified that the 1<sup>st</sup> floor left brace and the 7<sup>th</sup> floor right brace are in the verge of fracture. The hysteresis response of these braces and DI computed for their outermost tension/compression fibers are plotted in Fig. 4.46. It resulted  $DI = 0.8$  which is close to fiber failure at  $DI = 1.0$ .

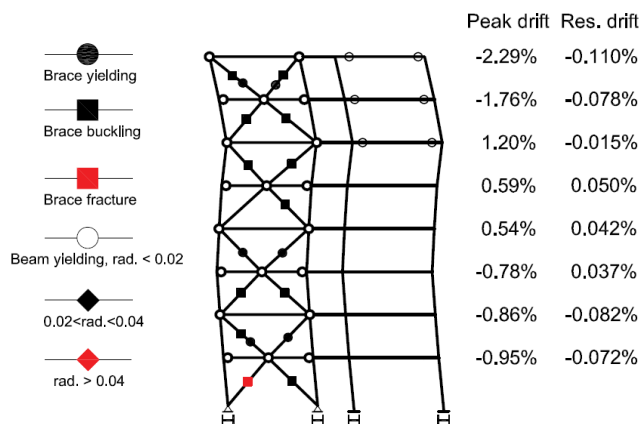
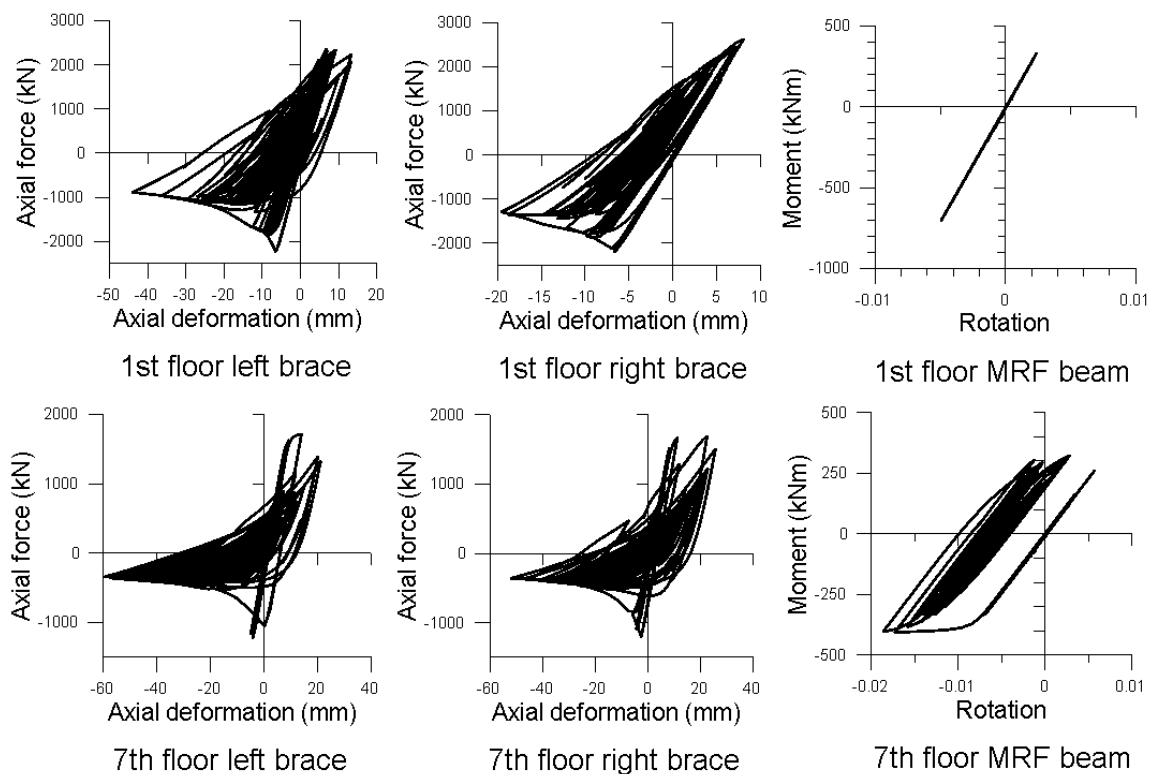
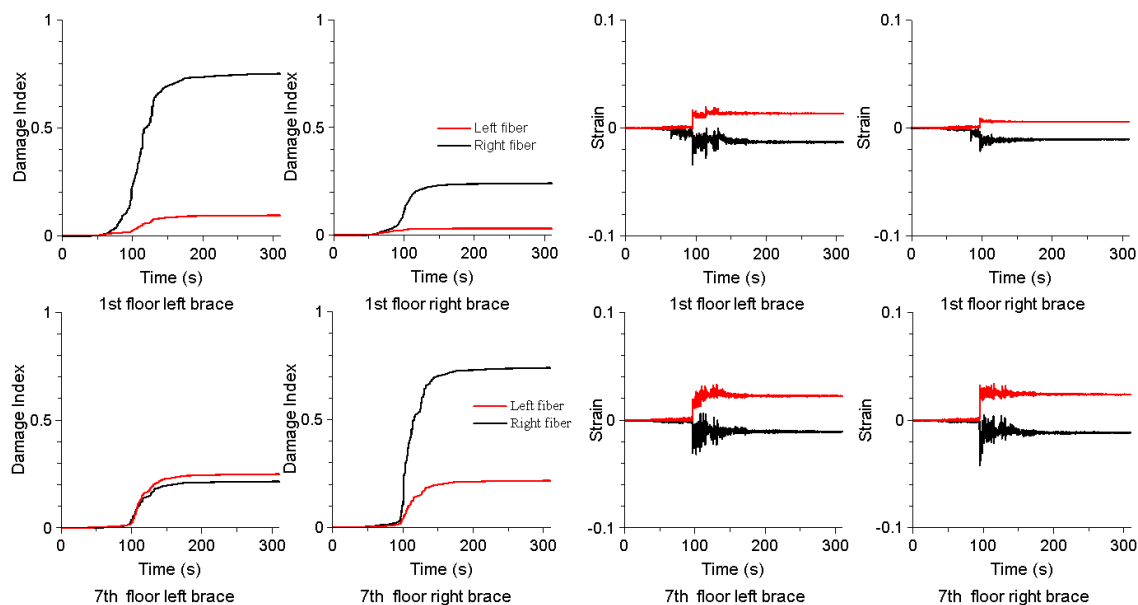


Fig. 4.45 Seismic response of 8-st. Braced Dual System under #IBR006 scaled to 1.1g



(a)



(b)

Fig. 4.46 Hysteretic behavior of critical HSS braces, the associated MRF beam and the time history of strain and damage of the outermost fibers of HSS brace cross sections of Braced Dual System under #IBR006 scaled to  $S(T_1) = 1.1g$ : (a) hysteretic response of HSS brace and MRF beam; (b) strain history and damage of outermost fibers of HSS braces

When GM #IBR006 is scaled to  $S(T_a) = 1.2g$ , the IDA curve shows substantial increase of interstorey drift and residual interstorey drift at the 7<sup>th</sup> floor which are  $3.84\%h_s$  and  $0.458\%h_s$ , respectively. The deflected shape of Braced Dual System is depicted in Fig. 4.47.

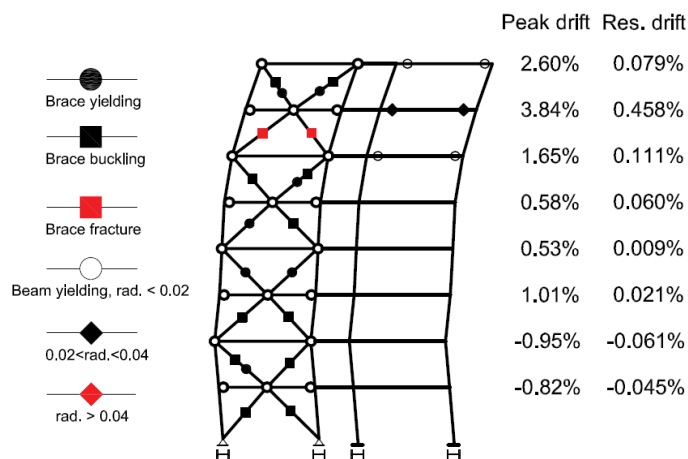


Fig. 4.47 Seismic response of Braced Dual System under #IBR006 scaled to near-collapse limit state

It is observed that all HSS braces of the Braced Dual System experienced buckling or/and yielding. Fracture of left and right braces are observed at 7<sup>th</sup> floor. However, only the 6<sup>th</sup>, 7<sup>th</sup>, and 8<sup>th</sup> floor MRF beams of MRF system experienced yielding.

The hysteretic behavior of HSS brace members and MRF beam of 1<sup>st</sup> and 7<sup>th</sup> floor is illustrated in Fig. 4.48a. The damage index and strain time history of outermost fibers of critical brace cross section is shown in Fig. 4.48b. It is noted that the ground floor left brace also reached a damage index of 0.6.

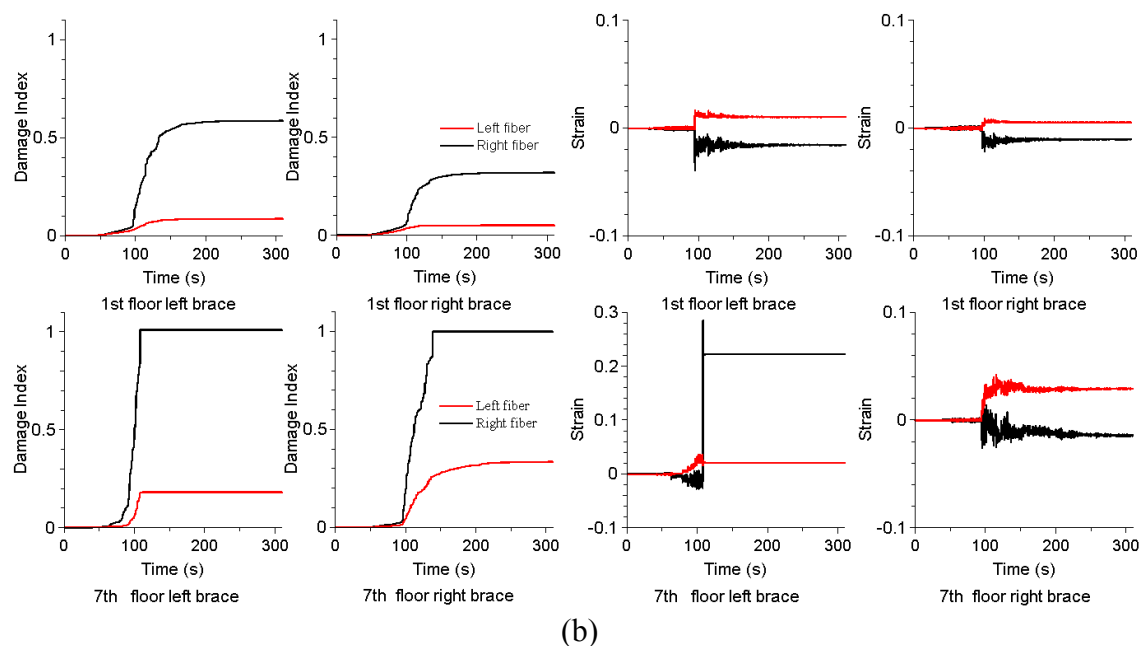
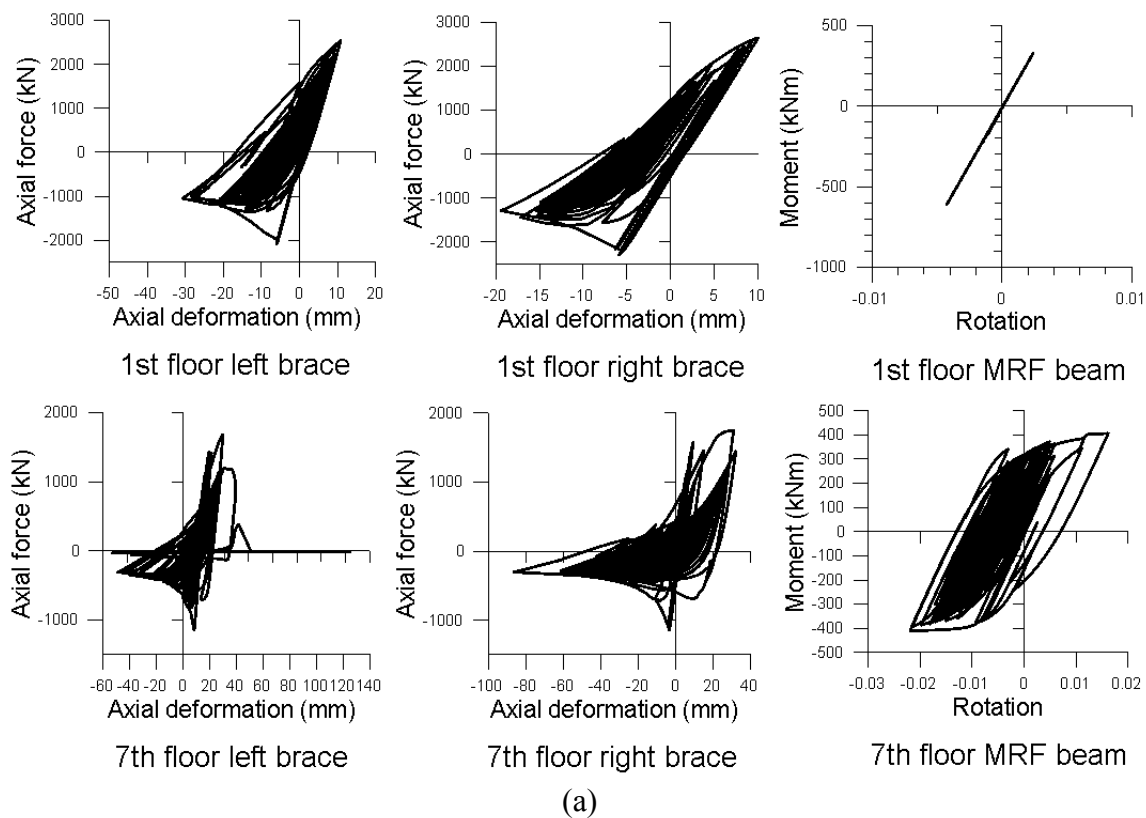


Fig. 4.48 Hysteretic behavior of critical HSS braces, the associated MRF beam and the strain time history and damage of the outermost fibers of HSS brace cross sections of Braced Dual System under #IBR006 scaled to  $S(T_1) = 1.2g$ : (a) hysteretic response of HSS brace and MRF beam; (b) strain history and damage of outermost fibers of HSS braces

To investigate the response of 7<sup>th</sup> floor beam to which braces initiated fracture are attached, as well as the behaviour of columns, the axial force – bending moment diagrams of these members located at the 1<sup>st</sup> floor and 7<sup>th</sup> floor are shown in Fig. 4.49 and Fig. 4.50. From these figures, it is shown that the 7<sup>th</sup> floor MD-CBF beam and MRF column responding in the plastic range.

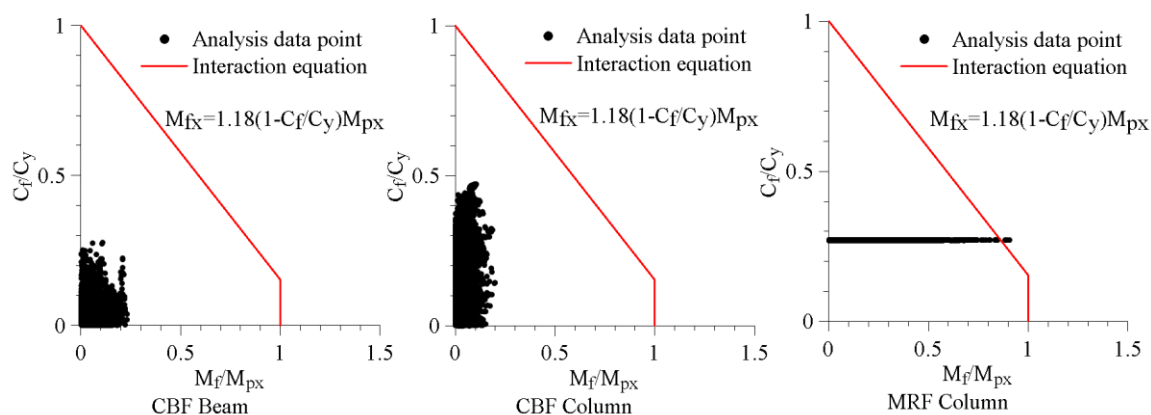


Fig. 4.49 The 1<sup>st</sup> floor axial force-bending moment interaction diagram under #IBR006 scaled to 1.2g (near-collapse limit state)

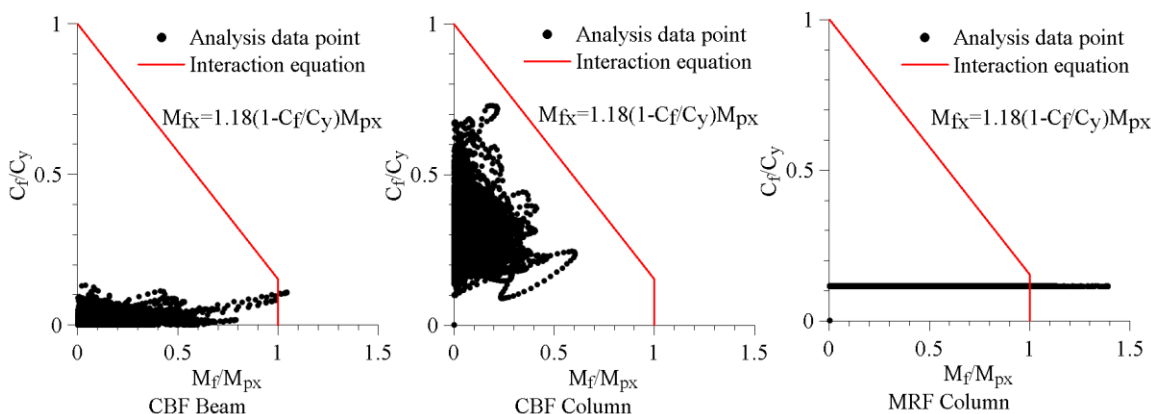


Fig. 4.50 The 7<sup>th</sup> floor axial force-bending moment interaction diagram under #IBR006 scaled to 1.2g (near-collapse limit state)

This type of failure mechanism is different than that observed under crustal records. Under #IBR006 record the failure mechanism occurs at the 7<sup>th</sup> floor and is within a floor.

The second type of failure mechanism is observed under GMs #0725a\_a, #103156ol\_y0b, #TCG009, and #MYG004. The failure occurs due to fracture initiates in the first and second floor left brace or right brace and is similar to that resulted under crustal ground motions. The single IDA curve under #MYG004 is shown in Fig. 4.51 for both systems: MD-CBF and Braced Dual System for comparison purposes. The seismic response of 8-storey building with both structural systems subjected to #MYG004 scaled to 0.5g is showed in Fig. 4.52.

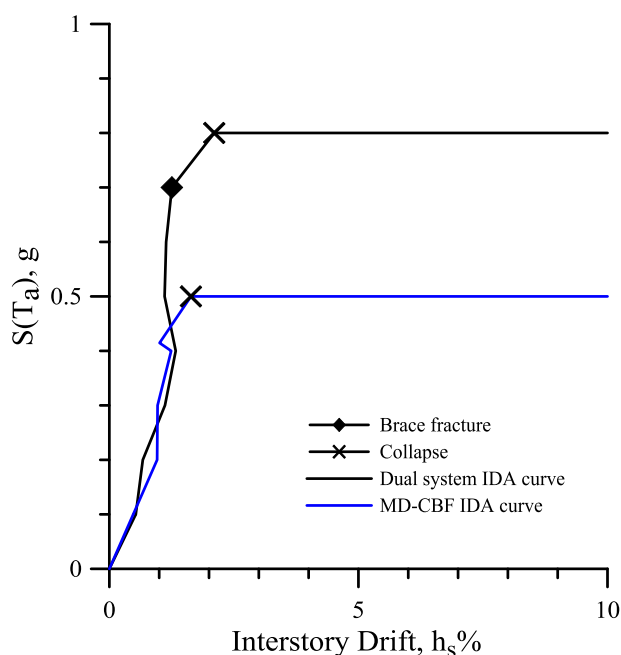


Fig. 4.51 IDA curve of 8-storey building with Braced Dual System vs. MD-CBF system under #MYG004

Fig. 4.52 shows that the MD-CBF system exhibits failure of left brace at the 1<sup>st</sup> floor under  $S(T_1) = 0.5g$ , however, the right brace of the 2<sup>nd</sup> floor and left brace of the 5<sup>th</sup> floor still behave in elastic range. At small increases in demand the MD-CBF system reached failure when the left brace of 2<sup>nd</sup> floor reached failure. For the Braced Dual System, no failure of structural members is observed at this demand level. However, all HSS braces experienced buckling or/and yielding, and only the MRF beam of the 7<sup>th</sup> floor experienced yielding.

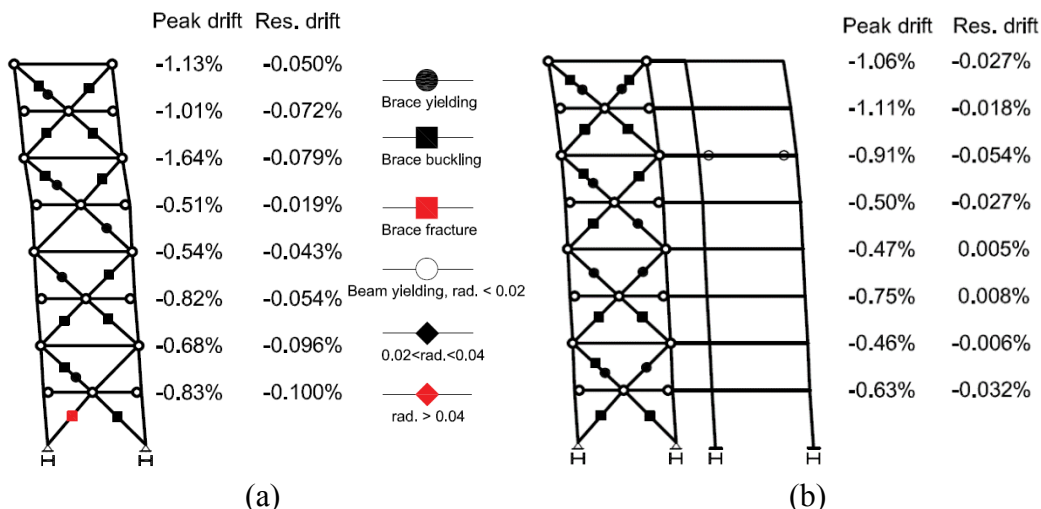


Fig. 4.52 Comparison of seismic response between MD-CBF system and Braced Dual System under #MYG004 scaled to  $S(T_1) = 0.5g$ : (a) MD-CBF; (b) Braced Dual System

When #MYG004 is scaled to  $S(T_1) = 0.7g$ , the Braced Dual System still does not show any sign of failure; the seismic response of the structure is illustrated in Fig. 4.53.

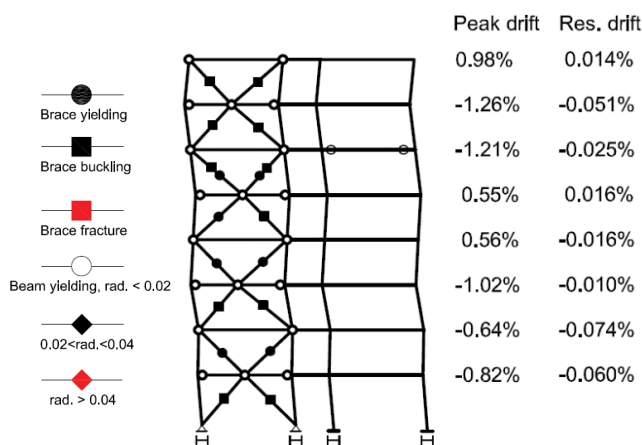


Fig. 4.53 Seismic response of 8-st. Braced Dual System under #MYG004 scaled to  $0.7g$

Comparing Fig. 4.52b with Fig. 4.53, there is no significant difference observed in terms of peak storey drift and peak residual drift. The hysteretic behavior of members located at the 1<sup>st</sup> and 7<sup>th</sup> floor are illustrated in Fig. 4.54a, the damage index and strain time history of the outermost fibers of critical HSS brace cross section is shown in Fig. 4.54b. It is noted that both HSS braces of the first floor reached a damage index greater than 0.6.

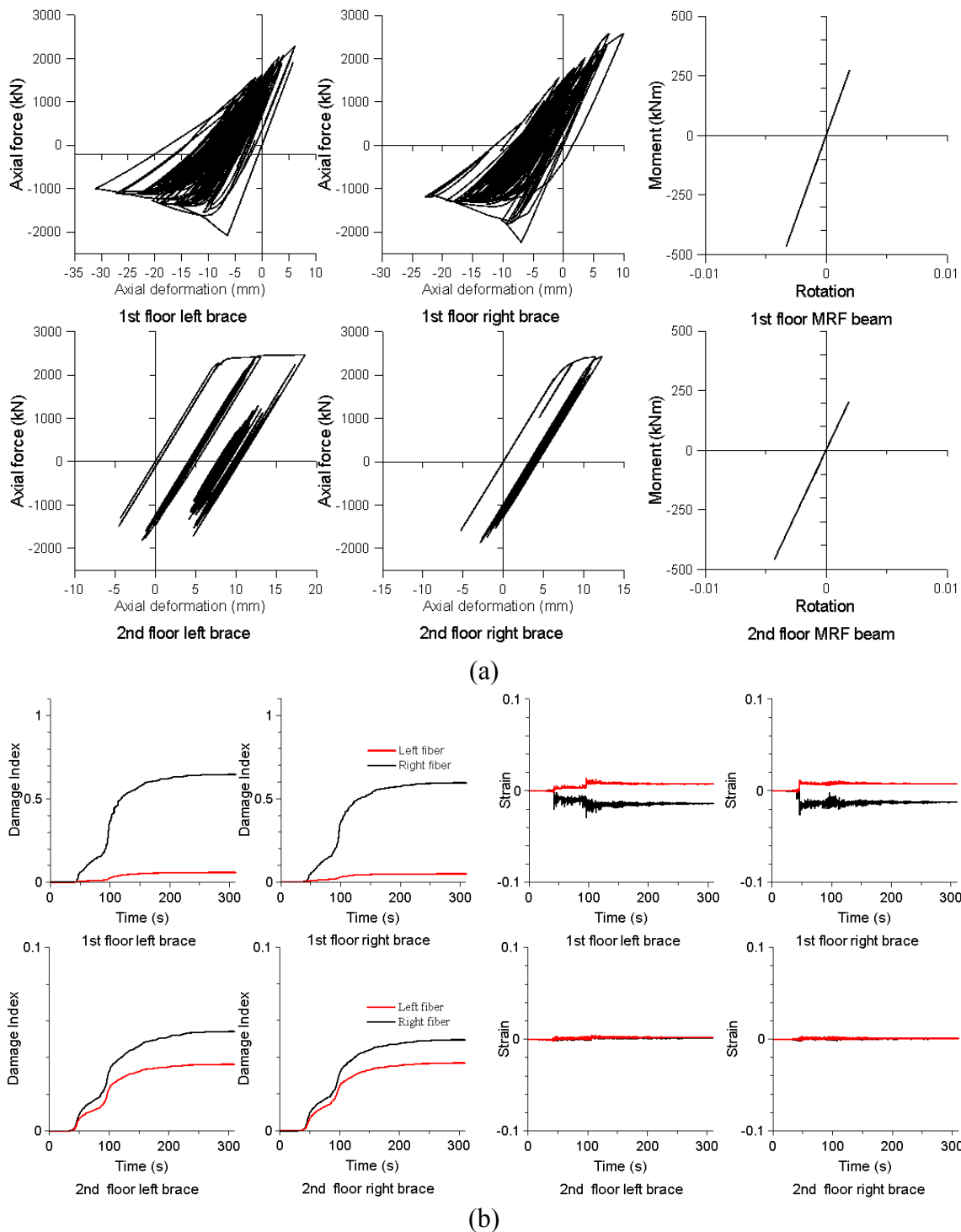


Fig. 4.54 Hysteretic behavior of critical HSS braces, the associated MRF beam and the strain time history and damage of the outermost fibers of HSS brace cross sections of Braced Dual System under #MYG004 scaled to  $S(T_1) = 0.7g$ : (a) hysteretic response of HSS brace and MRF beam; (b) strain history and damage of outermost fibers of HSS braces

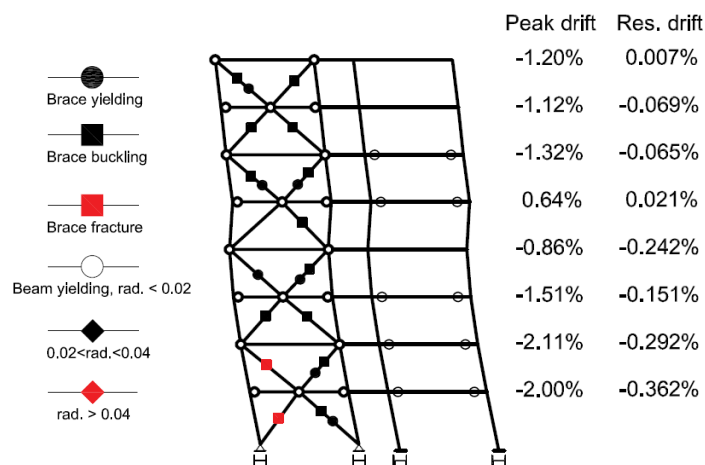
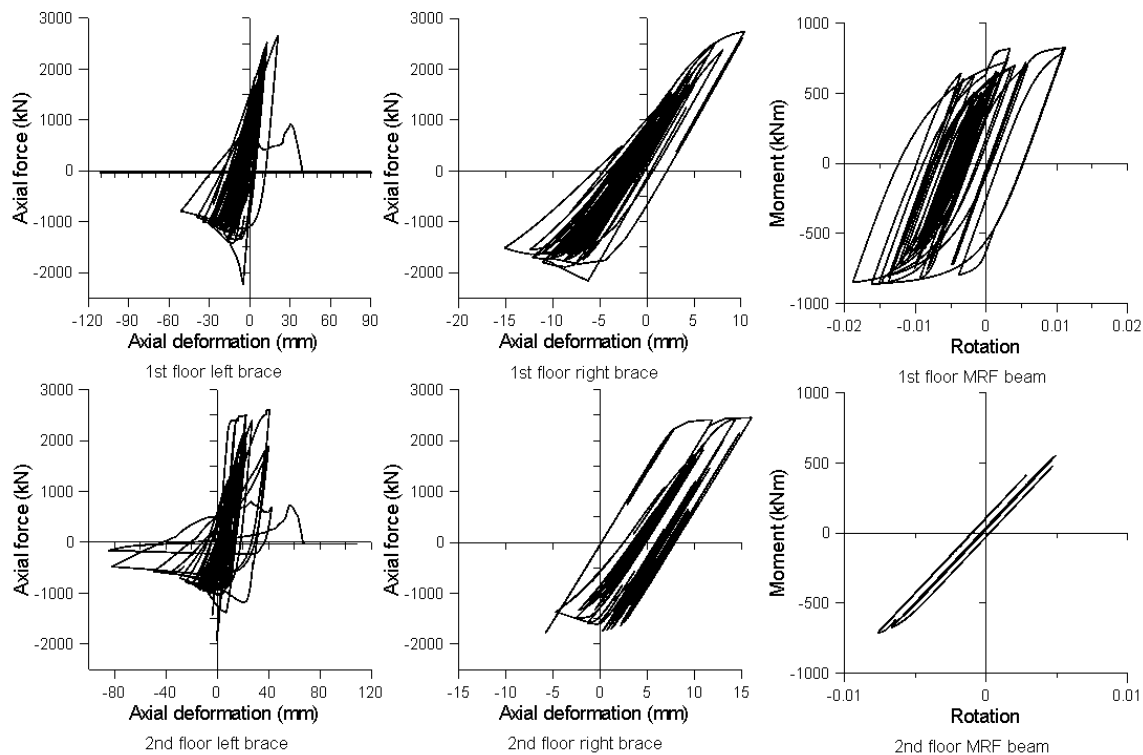


Fig. 4.55 Seismic response of 8-storey Dual system under #MYG004 scaled to 0.8g (near-collapse limit state)

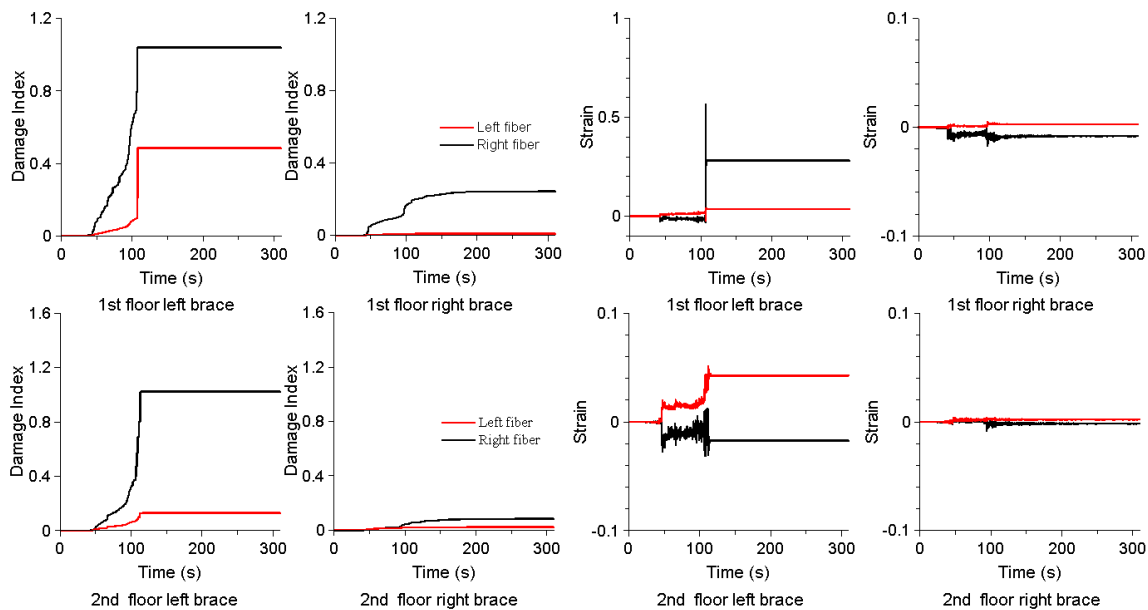
When the same record #MYG004 is scaled to  $S(T_1) = 0.8g$ , the system shows failure and the seismic response of the structure is illustrated in Fig. 4.55.

It is noted that in this case, fracture of HSS braces caused by low cycle fatigue is observed at the 1<sup>st</sup> and 2<sup>nd</sup> floor left braces. The left brace of the 5<sup>th</sup> floor shows an elastic behavior, while yielding of MRF beams is observed at the 1<sup>st</sup>, 2<sup>nd</sup>, 3<sup>rd</sup>, 5<sup>th</sup> and 6<sup>th</sup> floor. However, all yielded MRF beams have a rotation less than 0.02 radian.

The hysteretic behavior of HSS braces and MRF beam members of 1<sup>st</sup> and 2<sup>nd</sup> floor are illustrated in Fig. 4.56a, while the damage index and strain time history of outermost critical fibers of HSS brace cross sections is shown in Fig. 4.56b.



(a)



(b)

Fig. 4.56 Hysteretic behavior of critical HSS braces, the associated MRF beam and the strain time history and damage of the outermost fibers of brace cross sections of Braced Dual System under #MYG004 scaled to  $S(T_1) = 0.8g$ : (a) hysteretic response of HSS brace and MRF beam; (b) strain history and damage of outermost fibers of HSS braces

The axial force-bending moment interaction diagram of 1<sup>st</sup> floor MD-CBF beam to which the fractured braces are attached, the 1<sup>st</sup> floor MD-CBF column and MRF column is shown in Fig. 4.57. As depicted the MD-CBF beam is on the failure verge, behaving in the nonlinear range. Similar response is exhibited by the 1<sup>st</sup> floor MRF column at its base.

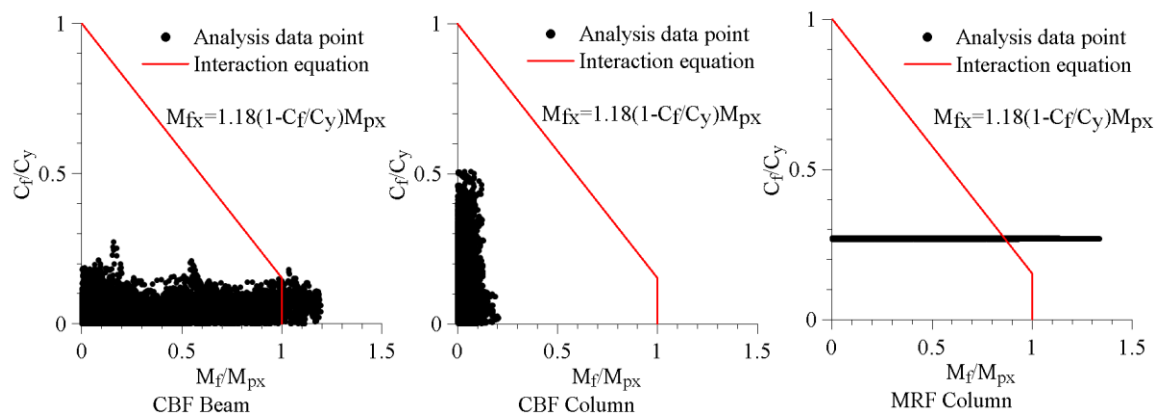


Fig. 4.57 The 1<sup>st</sup> floor axial load-bending moment interaction diagram under #MYG004 scaled to 0.8g (near-collapse limit state)

The third type of failure mechanism is observed under GMs #FKS010, #103156ol\_y0a and #IBR004. The failure occurs due to fracture initiates in the first, second, and third floor left or right braces. The single IDA curve is shown for both 8-storey MD-CBF system and Braced Dual System under #IBR004 in Fig. 4.58.

The seismic response of both structural systems subjected to GM #IBR004 scaled to  $S(T_a) = 0.6g$  is depicted in Fig. 4.59 from where is showed that the MD-CBF system exhibited the first brace fracture caused by low-cycle fatigue at the 1<sup>st</sup> floor, while the Braced Dual System shows only buckling and/or yielding of HSS braces.

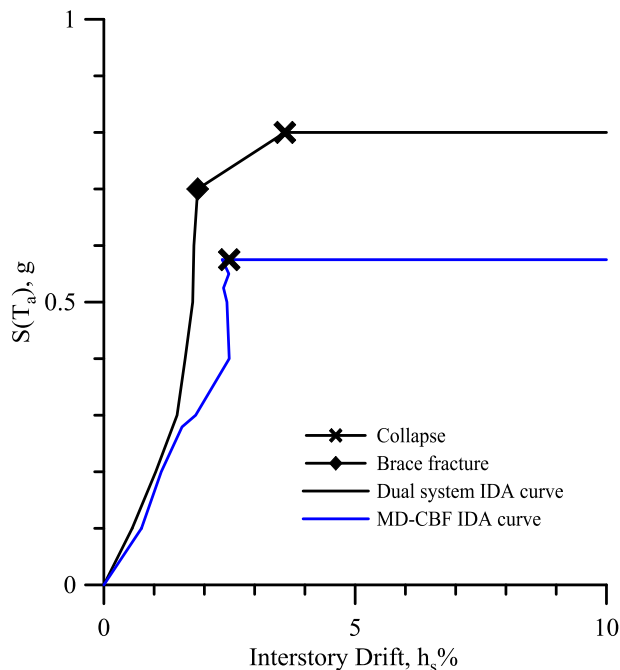


Fig. 4.58 IDA curve of 8-storey building with Braced Dual System vs. MD-CBF system under #IBR004

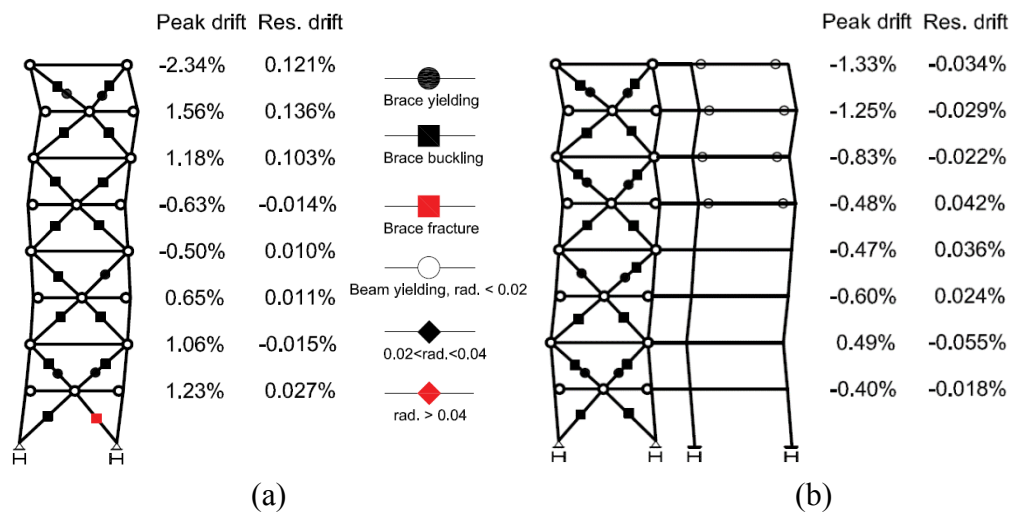


Fig. 4.59 Comparison of seismic response between MD-CBF system and Dual system under #IBR004 scaled to  $S(T_a) = 0.6g$ : (a) MD-CBF; (b) Braced Dual System

When GM #IBR004 is scaled to  $S(T_a) = 0.7g$ , the Braced Dual System response depicted in Fig. 4.60 shows the initiation of first HSS brace fracture caused by low-cycle fatigue (e.g. the 1<sup>st</sup> floor right brace as depicted in Fig. 4.61).

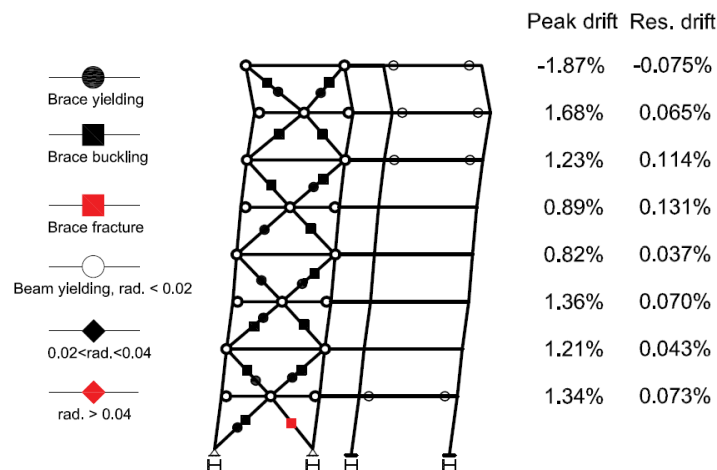


Fig. 4.60 Seismic response of 8-st. Braced Dual System under #IBR004 scaled to 0.7g

Comparing Fig. 4.59b with Fig. 4.60 it results that the 5<sup>th</sup> floor MRF beam does not yield while the 1<sup>st</sup> floor MRF beam yields.

The hysteretic behavior of braces and MRF beam members of 1<sup>st</sup> floor are illustrated in Fig. 4.61a and the damage index and strain time history of the outermost critical fibers of HSS braces is shown in Fig. 4.61b. As depicted in Fig. 4.61a, the 1<sup>st</sup> floor left brace reached buckling in compression and yielding in tension, while the 1<sup>st</sup> floor right brace was first loaded in compression and exhibited strain damage including the failure of critical fiber (DI=1.0, Fig. 4.61). The 1<sup>st</sup> floor MRF beam behaves at the border line between the elastic and plastic range.

The seismic response of 8-storey Braced Dual System under GM #IBR004 scaled to 0.8g is depicted in Fig. 4.62. Under this increase demand, the 8-storey Braced Dual System experienced the near collapse limit state described hereafter.

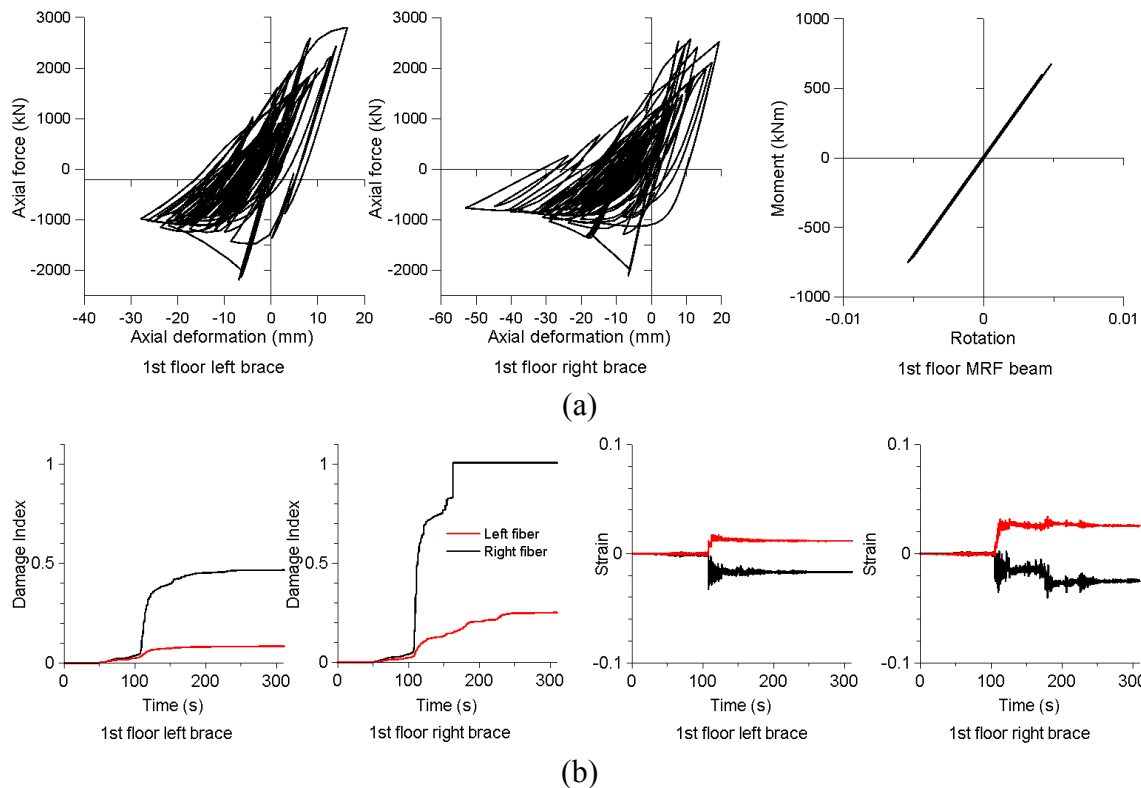


Fig. 4.61 Hysteretic behavior of critical HSS braces, the associated MRF beam and the strain time history and damage of the outermost fibers of brace cross sections of Braced Dual System under #IBR004 scaled to  $S(T_1) = 0.7g$ : (a) hysteretic response of HSS brace and MRF beam; (b) strain history and damage of outermost fibers of HSS braces

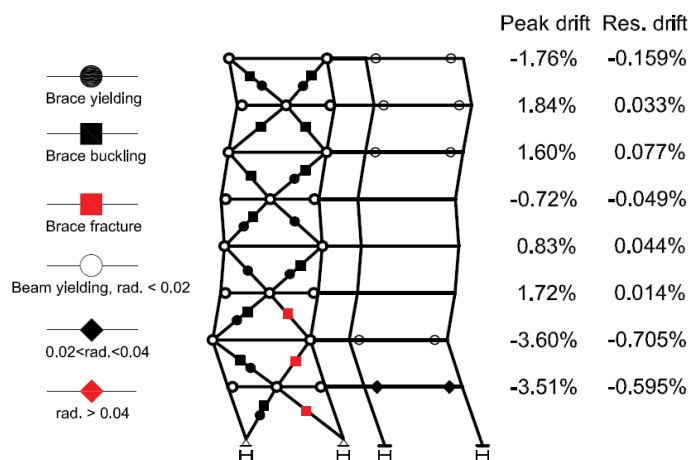
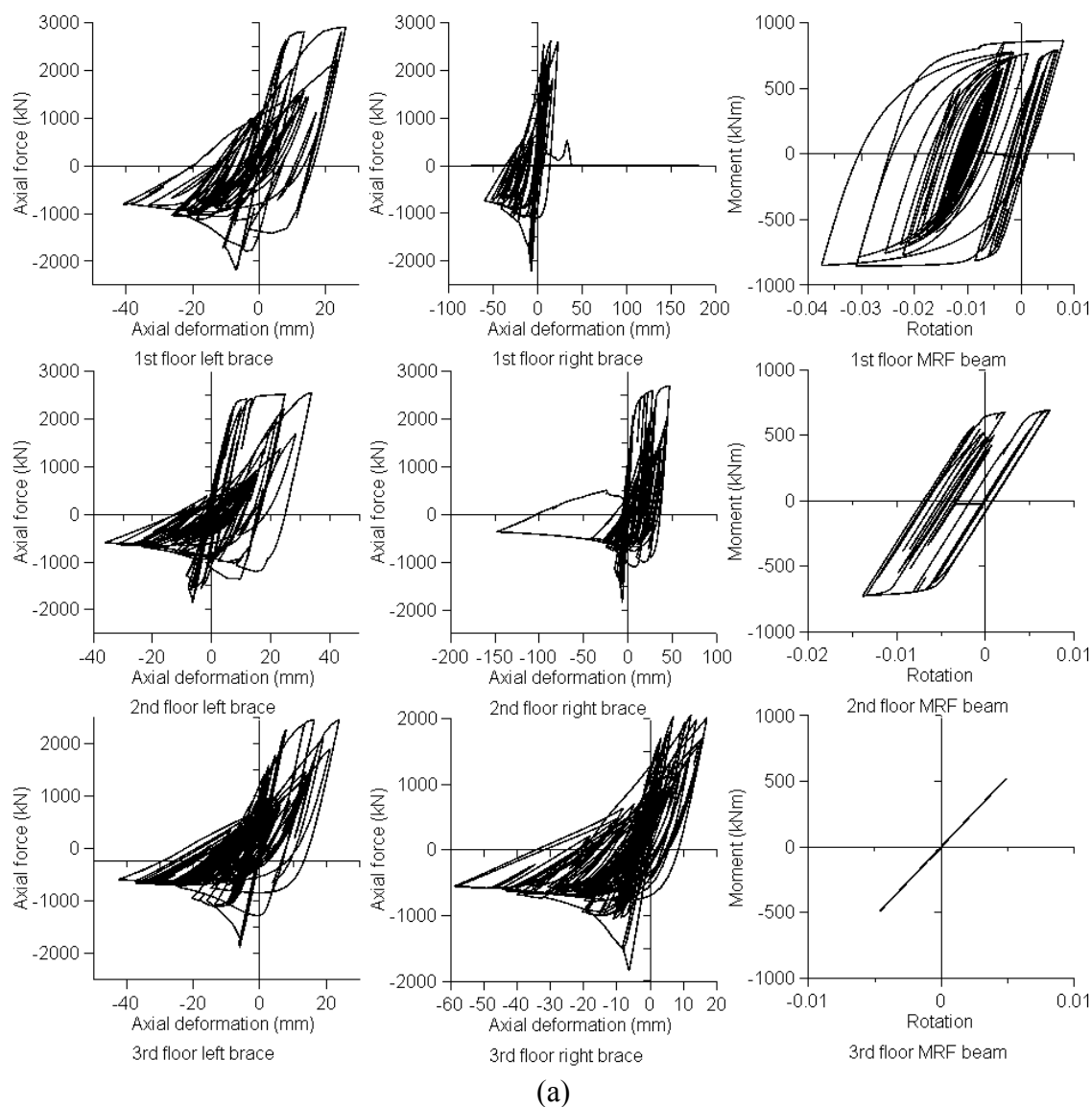


Fig. 4.62 Seismic response of 8-storey Braced Dual System under #IBR004 scaled to 0.8g (near-collapse limit state)

The hysteresis response of HSS braces located at the 1<sup>st</sup>, 2<sup>nd</sup>, and 3<sup>rd</sup> floor, as well as the hysteresis response of MRF beams located at these floors are depicted in Fig. 4.63a. The first floor MRF beam undergoes 0.04 rad. rotation and the 2<sup>nd</sup> floor MRF beam 0.02 rad. rotation. The damage index and strain time history of outermost critical fibers of HSS braces is presented in Fig. 4.63b where is showed that the 1<sup>st</sup> and 2<sup>nd</sup> floor right braces reached fracture caused by low-cycle fatigue, while the 3<sup>rd</sup> floor right brace is close to fracture initiation.



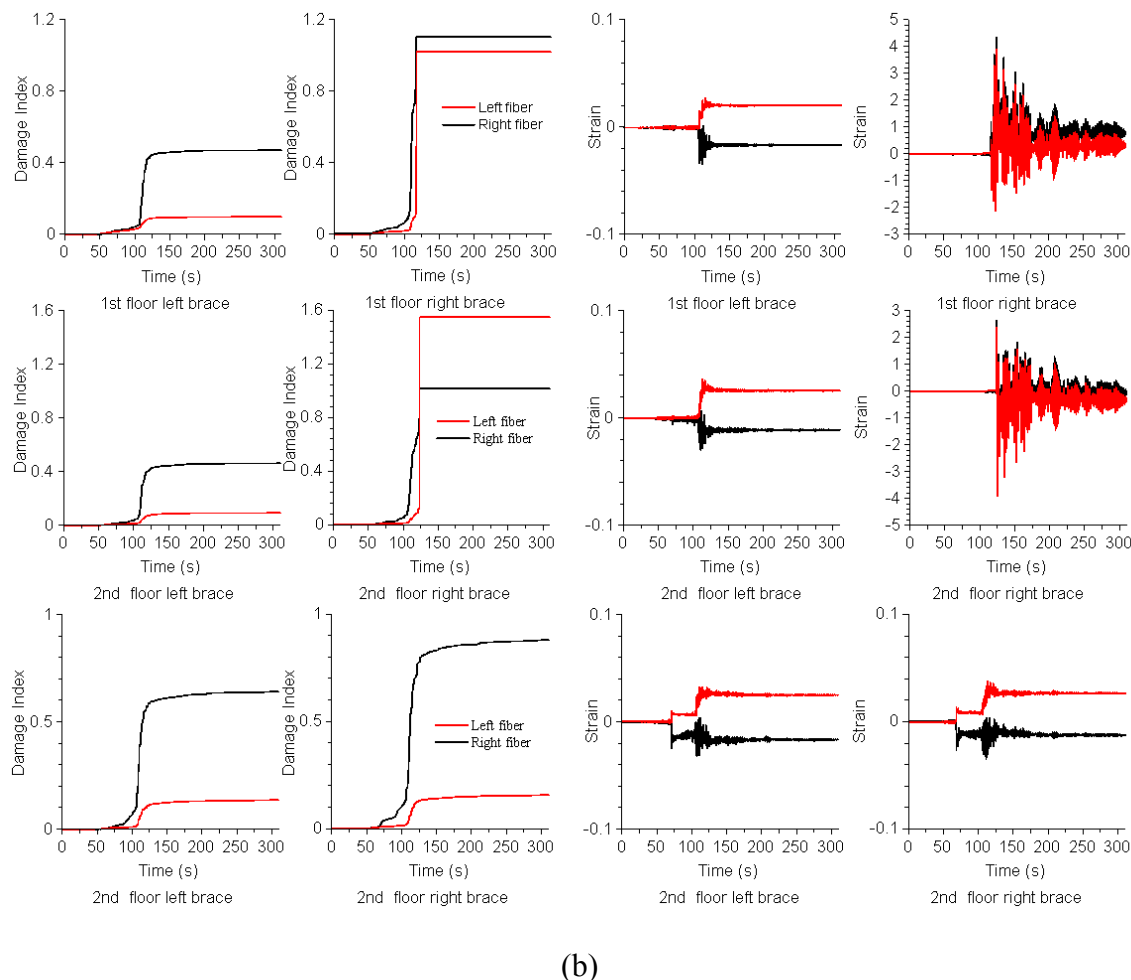


Fig. 4.63 Hysteretic behavior of critical HSS braces, the associated MRF beam and the strain time history and damage of the outermost fibers of brace cross sections of Braced Dual System under #IBR004 scaled to  $S(T_1) = 0.8g$ : (a) hysteretic response of HSS brace and MRF beam; (b) strain history and damage of outermost fibers of HSS braces

The axial force-bending moment interaction diagram of 1<sup>st</sup> floor MD-CBF beam to which the fractured braces are attached, the 1<sup>st</sup> floor MD-CBF column and MRF column is shown in Fig. 4.64. Nonlinear response and possible is observed in the case of 1<sup>st</sup> floor MD-CBF beam and MRF column. It seems that the cross section of MRF columns should be further investigated before recommended the increase of cross sectional size. It is noted that no fatigue material was assigned to MRF columns. This research is on-going based on recent experimental tests conducted on steel MRF columns.

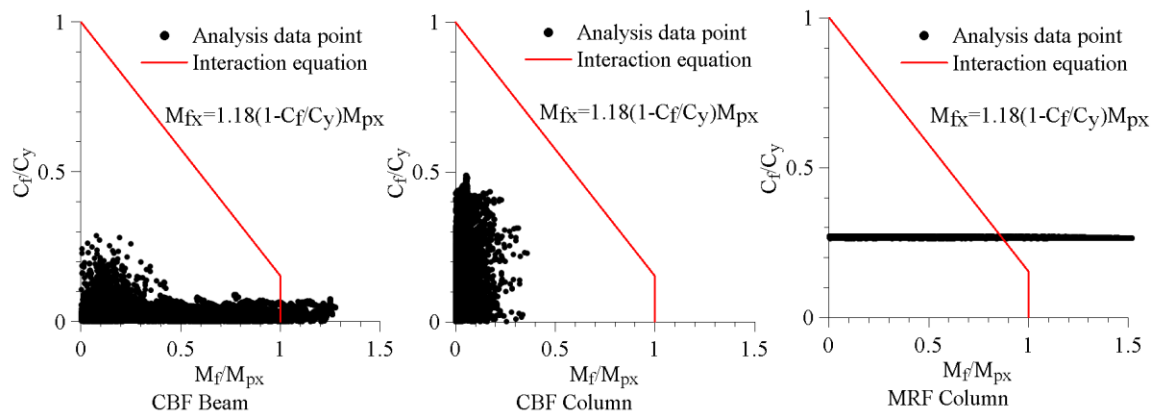


Fig. 4.64 The 1<sup>st</sup> floor axial force-bending moment interaction diagram under #IBR004 scaled to 0.8g (near-collapse limit state)

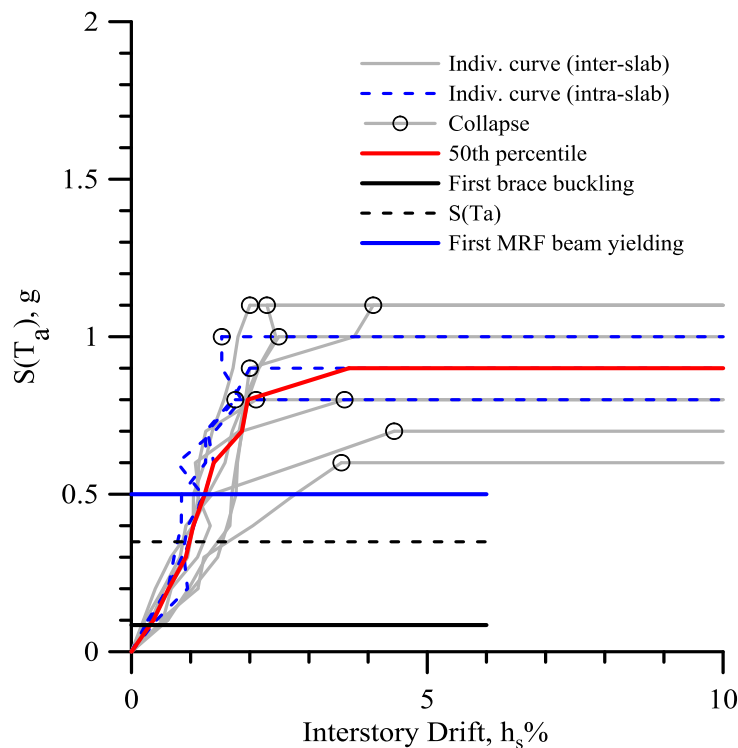


Fig. 4.65 IDA curves of 8-storey Braced Dual System building under subduction GMs

The eleven IDA curves resulted for the 8-storey building with Braced Dual System subjected to subduction ground motions are summarized in Fig. 4.65. The 50 percentile IDA curve is shown with red line and indicates that collapse of 8-storey Braced Dual System occurs at  $S_a(T_1)$  of 0.9g with a corresponding interstorey drift of  $3.67\%h_s$ . The

solid black line shows the average intensity of occurrence of first brace buckling, the solid blue line shows the average intensity when the first MRF beam starts yielding. The average value of IM when braces start buckling and the MRF beams flexural yielding are 0.085g and 0.5g, respectively.

The building response in terms of interstorey drift, residual interstorey drift and floor acceleration recorded under subduction ground motions at near collapse limit state are shown in Fig. 4.66. The maximum average interstorey drift is  $1.98\%h_s$ , the maximum average residual drift is  $0.297\%h_s$ , the maximum average floor acceleration is 1.32g. All these peak values occur at the 1<sup>st</sup> floor. The distribution of interstorey drift among floors show a pronounced peak at the 1<sup>st</sup> and 2<sup>nd</sup> floor even 3<sup>rd</sup> floor and a less pronounced one at the 7<sup>th</sup> floor. The Mean+SD is showed with dashed red line.

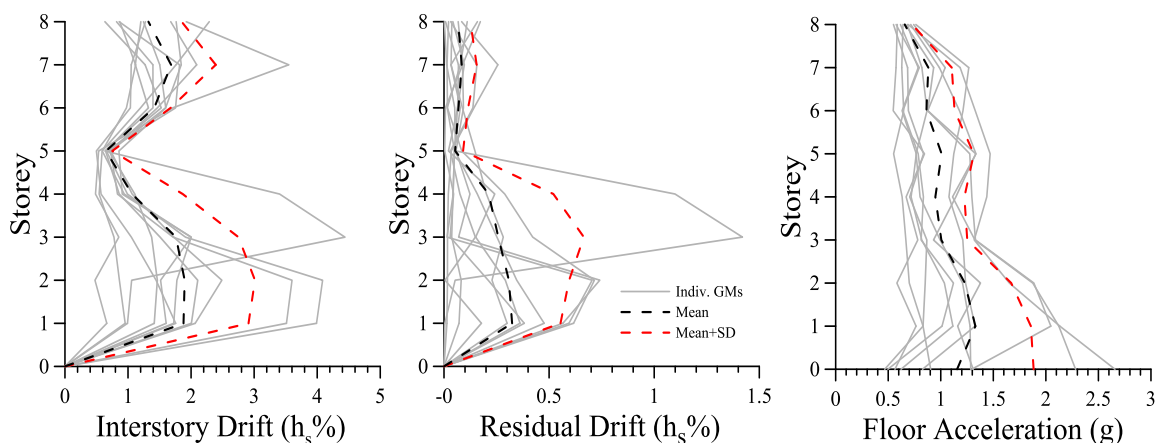


Fig. 4.66 Seismic response of 8-storey building with Braced Dual System under subduction GMs at near-collapse limit state

## 4.4 Discussion

### *4.4.1 Comparison of seismic responses between the MD-CBF and Braced Dual System*

From incremental dynamic analyses presented above, in general, there are two types of failure mechanisms for both MD-CBF and Braced Dual System.

In the case of 8-storey MD-CBF with split “X” braces configuration failure concentrates in general of the 1<sup>st</sup> floor and 2<sup>nd</sup> floor where HSS braces located of the same half span reached brace fracture caused by low-cycle fatigue and the attached beam exhibited failure. This lead to a weak two-storey mechanism. In two or three cases out of 22 this type of mechanism involves the top two floors instead of bottom floors. The other failure mechanism type that was observed under three or four ground motions consists of failure of both braces located at the same floor followed by failure of the beam to which the fractured braces are attached.

In the case of Braced Dual System, the general failure mechanism is the weak two-storey mechanism involving the bottom two floors, the attached beam, and the yielding of MRF beam located at the same floor. However, the degradation is slight, and the MRF beam is far from losing 20% of its flexural strength. The second type of failure mechanism of Braced Dual System occurs when both braces at the same floor reached fracture caused by low-cycle fatigue, the attached braced frame beam is on the verge of failure due to flexural bending and axial force interaction, while the MRF beam at the same floor presents flexural yielding up to 0.04 rad. rotation. When the MRF column located at the same critical floor was investigated, dynamic instability due to flexure and axial compression was observed. It is noted that no low-cycle fatigue material was assign to plastic hinge cross section of

W-shape MRF column because this research is ongoing and valid experimental tests of MRF columns were recently conducted. Both braced frame columns have enough reserve capacity.

Since the MRF frame of Braced Dual System is a backup system, the stiffness of the structure is mainly provided by the MD-CBF frame; hence both structural systems have similar vibration periods. The effect of adding the backup MRF to Braced Dual System is discussed by comparing the seismic performance of MD-CBF building with the Braced Dual System building when the ground motions are scaled to near-collapse limit state. The comparison expressed in terms of interstorey drift, residual drift, and floor acceleration obtained under 11 crustal ground motions is showed for the 8-storey MD-CBF and 8-storey Braced Dual System in Fig. 4.67. Similarly, the seismic response under 11 subduction ground motions is showed in Fig. 4.68.

As resulted from Fig. 4.67, the Braced Dual System provides larger ductility than the MD-CBF system. Thus, the peak of mean interstorey drift is about  $3.5\%h_s$  for Braced Dual System vs.  $2.0\%h_s$  for MD-CBF system. In case of Braced Dual System, the peak demand is at the bottom floors, while the distribution of interstorey drift along the height is more uniform. It is noted that at near failure limit state the Braced Dual System is able to respond to greater intensity measure than the MD-CBF system (Fig. 4.69a).

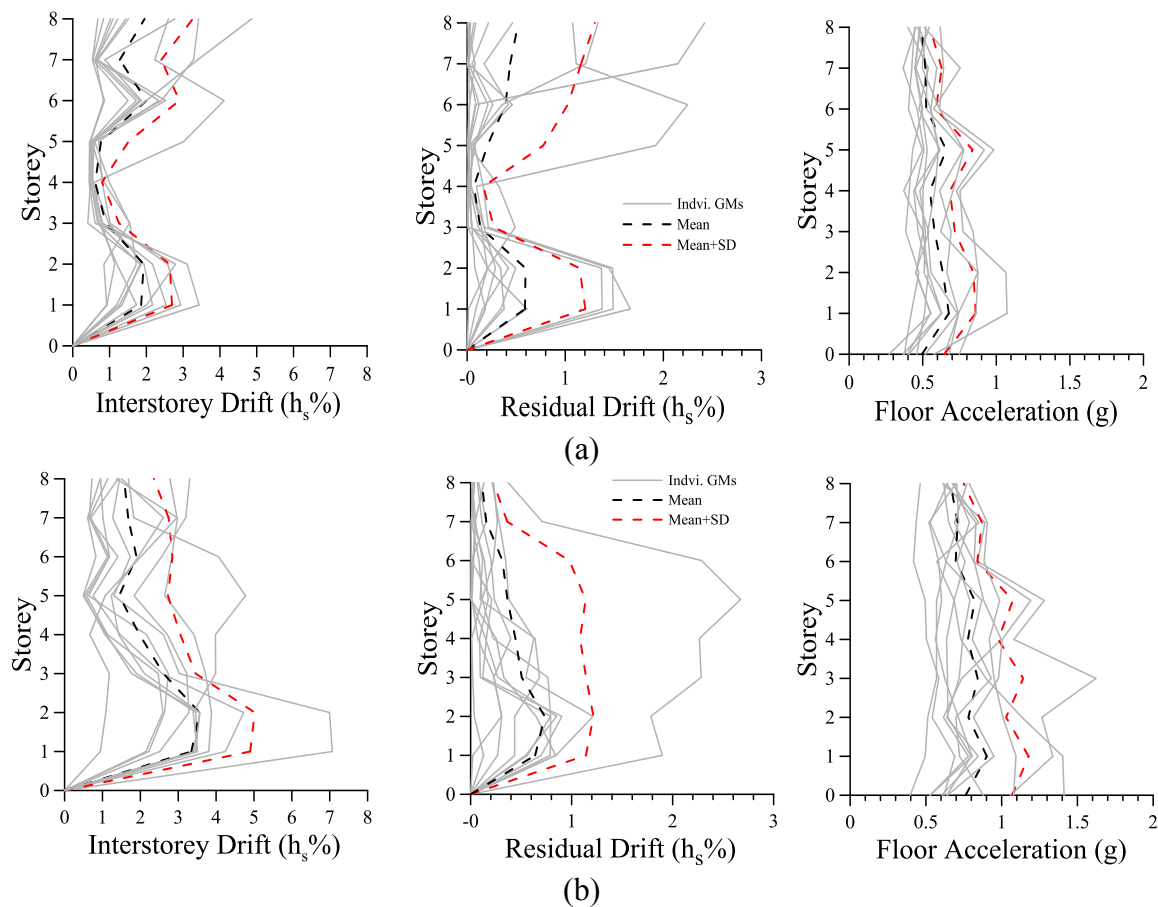


Fig. 4.67 Comparison of seismic responses of 8-storey MD-CBF vs. 8-storey Braced Dual System under 11 crustal GMs scaled to near-collapse limit state: (a) MD-CBF building; (b) Braced Dual System building

In consequence, the Braced Dual System experienced greater peak interstorey drift, peak residual interstorey drift and peak floor acceleration than the MD-CBF system. Thus, the peak of mean residual interstorey drift increases from 0.4%h<sub>s</sub> for MD-CBF system to 0.9%h<sub>s</sub> for Braced Dual System, while the peak of mean floor acceleration increases from 0.7g to 0.9g.

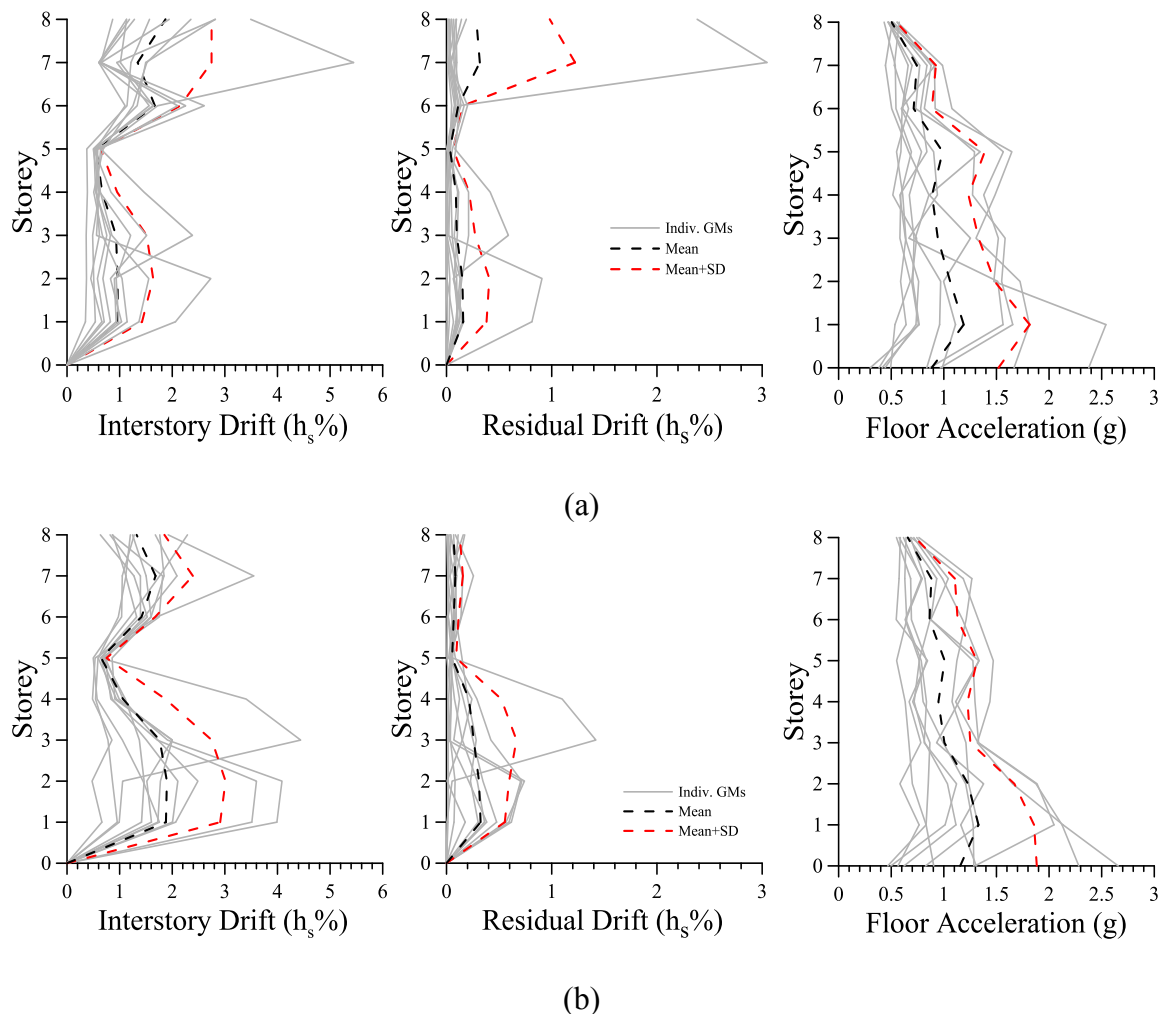


Fig. 4.68 Comparison of seismic responses of 8-storey MD-CBF vs. 8-storey Braced Dual System under 11 subduction GMs scaled to near-collapse limit state: (a) MD-CBF building; (b) Braced Dual System building

When long duration subduction ground motions are considered both MD-CBF system and Braced Dual System fail at lower demand intensity than in the case of crustal ground motions. Especially, the Braced Dual System subjected to subduction GMs resist to half of the demand intensity than in the case of crustal ground motions (Fig. 4.69b). In consequence, the peak of mean interstorey drift and residual drift are reduced when compare with the responses resulted under crustal GMs. Conversely, in case of subduction ground motions the peak of floor acceleration increases. However, it seems that the 8-storey building with Braced Dual System shows a more uniform distribution of interstorey

drift compared to 8-storey MD-CBF building. Moreover, the building with Braced Dual System is more likely to avoid the weak-storey mechanism at an intensity measure required to pass the collapse safety criteria explained in Chapter 5. However, the residual drifts and floor accelerations are slightly bigger, which is because larger scaling factors are needed for Braced Dual System building to reach failure.

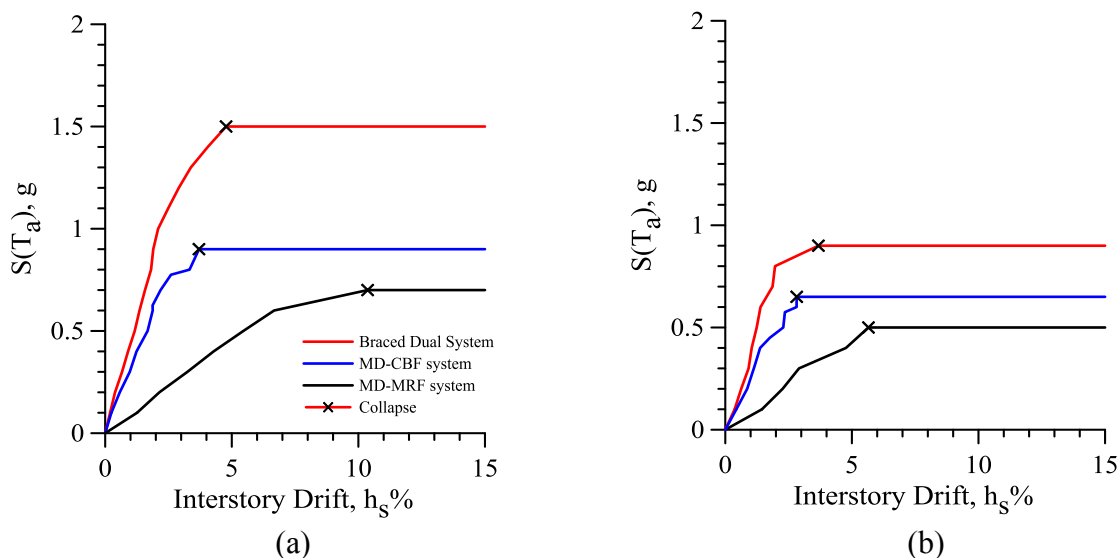


Fig. 4.69 Comparison of 50<sup>th</sup> percentile IDA curve among studied buildings subjected to: (a) crustal ground motions, (b) subduction ground motions

Nevertheless, the comparison 50<sup>th</sup> percentile of IDA curves among the three prototype buildings subjected to crustal and subduction GMs is shown in Fig. 4.69.

It is noted that for the MD-CBF system, even that the ground motions are scaled to near collapse limit state, there may be few braces that behave in elastic range. However, for the Braced Dual System, when ground motions are scaled to near collapse limit state, all braces experience buckling or/and yielding, which means the Braced Dual System is more efficient in dissipating energy. It is worth to note that caution should be given when subduction ground motions apply to a structural system because the demand is higher than in the case of crustal ground motions.

#### ***4.4.2 Issues on reaching convergence during nonlinear time history analysis***

Model convergence problem is always a concern for nonlinear time history analysis. In this study, no convergence problem was observed for the MRF model even when structural members fail. For the MD-CBF model, convergence issue is observed after fracture of braces when the IDA curve always becomes flat.

For Dual frame model composed of a MD-CBF model and an MRF model, convergence problem is sometimes observed after fracture of braces initiates. However, there is no sign of building failure from the IDA curve. Due to the existence of backup MRF frame, the building could still sustain large lateral loads.

Few solutions are illustrated to solve the convergence problem. It was found that the *NewtonLineSearch* algorithm in OpenSees has the best chance of convergence for transient analysis, while using other algorithms does not help with the convergence. Furthermore, by reducing the time steps could help with the convergence problem.

Finer mesh of HSS cross section and W section were used to try to solve convergence problem, however, it is found it does not help with the convergence problem when increasing the fiber discretization of HSS cross section from 240 to 480 and for W-shape cross section when increasing the number of fibers from 120 to 240.

In regards of modeling, since, the model is a 2D frame but built with 6 degrees of freedom as a 3D system in order to allow HSS braces to buckle out of plan, for most of springs in the model, the degree-of-freedom in direction 3, 4, 5 is needed to be constrained. Better convergence is obtained by using *equalDOF* command to constrain the nodes for *Zerolength* elements rather than using a very stiff material in those three directions.

Moreover, convergence problem could still be found when ground motions are scaled to a certain intensity. It is found that when the ground motions are scaled to a high intensity, by slightly increasing or decreasing the scale factor, convergence could be reached.

## CHAPTER 5. COLLAPSE ASSESSMENT AND FRAGILITY ANALYSIS

In this Chapter, the seismic performance of the three prototype buildings is assessed using the methodology provided in FEMA P695. Moreover, fragility analysis is performed using results from IDA curves. It is assumed that non-structural components are not interacting with the structure during earthquake. Only the fragility of structural components is investigated.

### 5.1 Collapse Margin Ratio

Collapse Margin Ratio (CMR) is an important parameter to characterize collapse safety of a structure. According to FEMA P695 procedure (FEMA, 2009), the median collapse capacity,  $\hat{S}_{CT}$ , is defined as the intensity of ground motion at which half of the records in the selected suite of ground motion cause collapse of the structure. The CMR is defined as the ratio between  $\hat{S}_{CT}$  and the maximum design ground motion intensity,  $S_{MT}$ .

Table 5.1 Collapse margin ratio (CMR) derived from IDA curves

		$\hat{S}_{CT}$ , (g)	$S_{MT}$ , (g)	CMR
MD-CBF	Crustal GMs	0.90	0.337	2.67
	Subduction GMs	0.65	0.337	1.93
MD-MRF	Crustal GMs	0.70	0.237	2.95
	Subduction GMs	0.50	0.237	2.10
Braced Dual System	Crustal GMs	1.50	0.349	4.30
	Subduction GMs	0.90	0.349	2.58

The collapse margin ratios derived from IDA curves for the studied prototype buildings are presented in Table 5.1.

According to FEMA P695 (FEMA, 2009), the collapse safety is evaluated based on the adjusted collapse margin ratio,  $ACMR$ , which is calculated using the following equation:

$$ACMR = CMR \times SSF \quad (5.1)$$

where  $SSF$  is the spectral shape factor dependent on the fundamental period of building and period -based ductility,  $\mu_T$ . It is noted that  $\mu_T$  is recommended to be calculated from a pushover curve as the ratio of ultimate roof displacement,  $\delta_u$  to the equivalent yield roof displacement,  $\delta_{y,eff}$ , whereas  $\delta_u$  is defined as the displacement at 80% of the capping strength in the descending branch of the pushover curve. The  $SSF$  is given in Table 7-1 of FEMA P695 for different values of  $T_1$  and  $\mu_T$  ranging from 1.0 to  $\geq 8.0$ . For  $T_1 = 1.4$  corresponded to the studied MD-CBF system, the proposed  $SSF$  as function of  $\mu_T$  is given in Table 5.2. However,  $\mu_T$  cannot be less than  $R_d$ . Herein, a conservative value for  $\mu_T = R_d$  was considered. The  $SSF$  of the three prototype buildings presented in this study are shown in Table 5.3.

Table 5.2 Selection of  $SSF$  according to FEMA P695

Period-based ductility	1.0	1.1	1.5	2.0	3.0	4.0	6.0	$\geq 8.0$
$SSF$ for $T_1 = 1.4$ s	1.00	1.08	1.16	1.22	1.31	1.38	1.49	1.58

Table 5.3 Spectral shape factor ( $SSF$ ) for studied buildings

Building ID	$T$ (s)	$R_d$	$SSF$
MD-CBF	1.40	3.0	1.31
MD-MRF	2.10	3.5	1.36
Braced Dual System	1.32	3.0	1.29

To pass the collapse safety criteria, the  $ACMR$  for each performance group should be larger than a denoted  $ACMR$  value, which is  $ACMR_{10\%}$ , which representing 10% of acceptable collapse probability.

To get the value of  $ACMR_{10\%}$ , uncertainties are involved. The total uncertainty,  $\beta_{TOT}$ , incorporates four sources of uncertainty: Record-to-Record Uncertainty ( $\beta_{RTR}$ ), Design Requirements Uncertainty ( $\beta_{DR}$ ), Test Data Uncertainty ( $\beta_{TR}$ ), and Modeling Uncertainty ( $\beta_{MDL}$ ). The total uncertainty,  $\beta_{TOT}$ , is derived using the following equation:

$$\beta_{TOT} = \sqrt{\beta_{RTR}^2 + \beta_{DR}^2 + \beta_{TR}^2 + \beta_{MDL}^2} \quad (5.2)$$

In this study, the following assumptions are made in order to quantify  $\beta_{TOT}$ : (1) the quality of design requirements were considered as “(A) Superior” with corresponding  $\beta_{DR} = 0.1$ ; (2) the quality of test data was considered as “(B) Good” with corresponding  $\beta_{TR} = 0.2$ ; (3) the model quality was considered as “(B) Good” with corresponding  $\beta_{MDL} = 0.2$ .

Thus, the  $\beta_{TOT}$  value is calculated as 0.5. It is noted that the  $\beta_{TOT}$  value could be obtained from Table 7-2 of FEMA P695 based on these assumptions. Herein, the value of  $ACMR_{10\%}$  is obtained based on  $\beta_{TOT}$  using Table 7-3 of FEMA P695. Considering  $\beta_{TOT} = 0.5$  the resulted  $ACMR_{10\%}$  value for all three studied buildings is 1.90. These parameters used to assess the collapse safety of the prototype buildings are presented in Table 5.4. It is concluded that the 8-storey buildings with three different earthquake resistant systems pass the collapse safety criteria. The braced dual frame considered shows about 150% and 130% larger safety capacity under crustal GMs and subduction GMs, respectively than the MD-CBF system. It results that slightly larger ductility factor can be assigned to Braced Dual System. Comparing the ratio  $ACMR/ACMR_{10\%}$  resulted under the subduction GMs effect

versus the crustal GMs effects the collapse safety is reduced by 30% to 40%. Thus, when buildings with  $T_1 > 1.0$  s are designed in B.C., the subduction earthquake effect is more likely to govern the design. The effect of long duration subduction earthquake on the collapse safety of steel braced frame buildings was previously reported by Tirca et al. (2015).

Table 5.4 Evaluation of collapse safety according to FEMA P695 methodology

Parameters	MD-CBF		MD-MRF		Braced Dual System	
	Crustal GMs	Sub. GMs	Crustal GMs	Sub. GMs	Crustal GMs	Sub. GMs
$\hat{S}_{CT}$	0.90	0.65	0.70	0.50	1.50	0.90
CMR	2.67	1.93	2.95	2.10	4.30	2.58
ACMR	3.50	2.53	4.01	2.86	5.55	3.32
ACMR <sub>10%</sub>	1.90	1.90	1.90	1.90	1.90	1.90
ACMR/ ACMR <sub>10%</sub>	1.84	1.33	2.10	1.50	2.89	1.74
Pass/Fail	Pass	Pass	Pass	Pass	Pass	Pass

## 5.2 Fragility Analysis

Fragility is an important reference for seismic performance assessment as well as risk assessment for structures. Fragility describes the probability of the structure to reach a certain performance. Moreover, it can be used to determine probabilistic safety margins for decision making (Wen et al, 2004).

### 5.2.1 Performance limit states and damage levels

The performance limit states describe the level of damage that a structure may experience during an earthquake event. In general, there are three performance limit states defined in ASCE/SEI 41-13 which are: Immediate Occupancy (IO), Life Safety (LS), and Collapse

Prevention (CP). For each limit state, ASCE/SEI 41-13 gives description of damage observation, and quantitative approaches based on interstorey drift and residual interstorey drift.

For CBF structures, the performance levels could be summarized as described in Fig. 5.1 by Tirca et al (2014).

Performance Levels	Operational	Immediate Occupancy	Life Safety	Collapse Prevention	
Performance Ranges	No structural damage	Damage Control range	Limited Safety range	Collapse	
Degree of Damage	None	Very Light Damage	Light Damage	Moderate Damage	Complete Damage
Damage Levels	Very Light	Light	Moderate	Severe	
Suggested $\delta_{max}$		0.5% $h_s$	1.5% $h_s$	2.0% $h_s$	
Suggested $\delta_{max.res.}$		-	0.5% $h_s$	2.0% $h_s$	

Fig. 5.1 Mapping damage control against building performance levels according to ASCE/SEI 41 (Tirca et al., 2014)

In this study, for the CBF structure, the IO level corresponds to the point on the IDA curve that marks the first brace buckling, the CP level correlates to the near-collapse point when failure mechanism formed. However, according to Wen et al (2004), the LS level is hard to define. Thus, the quantitative approach is applied. The LS performance level is defined as “Many braces yield or buckle but do not totally fail” (ASCE). Base on the quantitative approach, it is suggested that LS occurs when peak residual drift is around 0.5% $h_s$ . From Tirca et al. (2014), it was shown that this residual drift of 0.5% $h_s$  is somehow associated with 1.5% $h_s$  storey drift. Herein, the LS performance level is considered when one of the two drift conditions is satisfied.

On the other hand, Gomez (2014) summarized the performance levels according to ASCE/SEI 41 for MRF structures as illustrated in Fig. 5.2. The IO level corresponds to the

point on the IDA curve when the first beam yields, the CP level correlates to the point that failure mechanism formed. The LS level is considered when the maximum interstorey drift reaches  $2.5\%h_s$  or maximum residual drift reaches  $1.0\%h_s$ , whichever occurs first.

Performance Levels	Operational		Immediate Occupancy	Life Safety		Collapse Prevention
Performance Ranges	No Structural Damage		Damage Control Range		Limited Safety Range	Collapse
Degree of Damage	None	Very Light Damage	Light Damage		Moderate Damage	Complete Damage
Damage Levels	Very Light		Light	Moderate		Severe
Suggested $\delta_{max}$			0.7%	2.5%		5%
Suggested $\delta_{res}$				1.0%		5%

Fig. 5.2 Structural performance levels and damage for steel MRF as per ASCE/SEI 41

As of Braced Dual System, there is no standard provided. However, since the MRF of the Dual frame is considered as a backup frame, the Dual frame has similar vibration characteristics as the CBF frame, the IO level could be considered the same as for CBF, which is the point when the first brace buckles, and the CP level is the point when failure mechanism occurs. As for the LS level, it is observed that when many braces buckle, the backup MRF beam starts yielding, however, no failure mechanism occurs.

### 5.2.2 Calculation of fragility

The fragility curve of structural system correlated to each performance level is derived from IDA curves using Eq. 2.16. The fragility curve follows a lognormal cumulative distribution defined by a median and standard deviation of  $\ln(IM)$ . However, the inherent randomness in ground motions and assumptions made in the analysis bring uncertainty to the response of structures. In this study, the aleatoric uncertainty and the epistemic uncertainty (Ellingwood et al., 2007) are considered. By replacing  $\beta_R$  in Eq. 2.17 with Eq.

2.18, the aleatoric and epistemic uncertainty can be taken into consideration. According to Ellingwood et al. (2007), the epistemic uncertainty  $\beta_{RU}$  is taken as 0.2,  $\beta_{RR}$  is calculated using Eq. 2.19. As illustrated in Eq. 2.19,  $\beta_{RR}$  is dependent on  $\beta_C$  and  $\beta_{D|S_a}$ . The  $\beta_C$  value is considered 0.25 as suggested by Ellingwood et al. (2007) and  $\beta_{D|S_a}$  value is assessed through a nonlinear regression analysis using Eq. 2.20. By employing a lognormal transformation, Eq. 2.20 could be transformed to a linear form as shown in Eq. 2.21, where  $a$  and  $b$  are constants and could be determined by a simple linear regression analysis.

### ***5.2.3 Fragility of 8-storey MD-CBF building***

Following the steps described before, constants  $a$  and  $b$  for the CBF building under crustal ground motions are calculated as 3.11 and 1.07 respectively, the record to record uncertainty  $\beta_{D|S_a} = 0.268$ . The value for the aleatoric uncertainty is calculated as  $\beta_{RR} = 0.37$ , the total uncertainty  $\beta_R$  is 0.418. Considering three damage levels, Light Damage (LD), Moderated Damage (MD), and Severe Damage (SD), which are defined based on Fig. 5.1, the seismic demand for selected performance levels and fragility curves are shown in Fig. 5.3. It is noted that in Fig. 5.3, three targeted damage levels corresponding to the LD, MD, and SD damage states are presented. These targeted levels are considered as the average intensity that the set of ground motions reaching the correlated damage states. At the code design level (labelled DS), the probability of reaching LD is 100%, the probability of reaching MD is below 10%, and the probability of reaching SD is 0%.

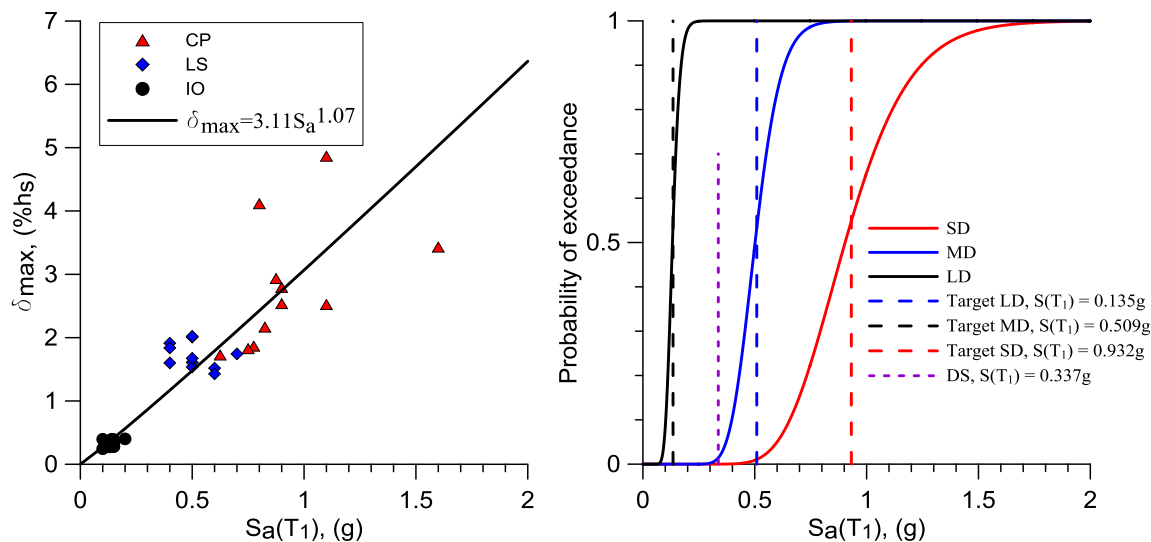


Fig. 5.3 Seismic demand for selected damage levels and fragility curves of 8-Storey MD-CBF building under Crustal GMs

Similarly, constants  $a$  and  $b$  for the MD-CBF building under subduction ground motions are calculated as 2.69 and 0.74 respectively, the record to record uncertainty is  $\beta_{D|S_a} = 0.346$ . The value for the aleatoric uncertainty is calculated as  $\beta_{RR} = 0.43$ , the total uncertainty,  $\beta_R$ , is 0.472. The seismic demand and fragility curves are shown in Fig. 5.4. Note that for 2% in 50 years hazard level (see DS in Fig. 5.4), the associated spectral acceleration value is  $S_a = 0.337g$ . At the code design level, the probability of reaching LD is 100%, the probability of reaching MD is around 35%, and the probability of reaching SD is less than 10%.

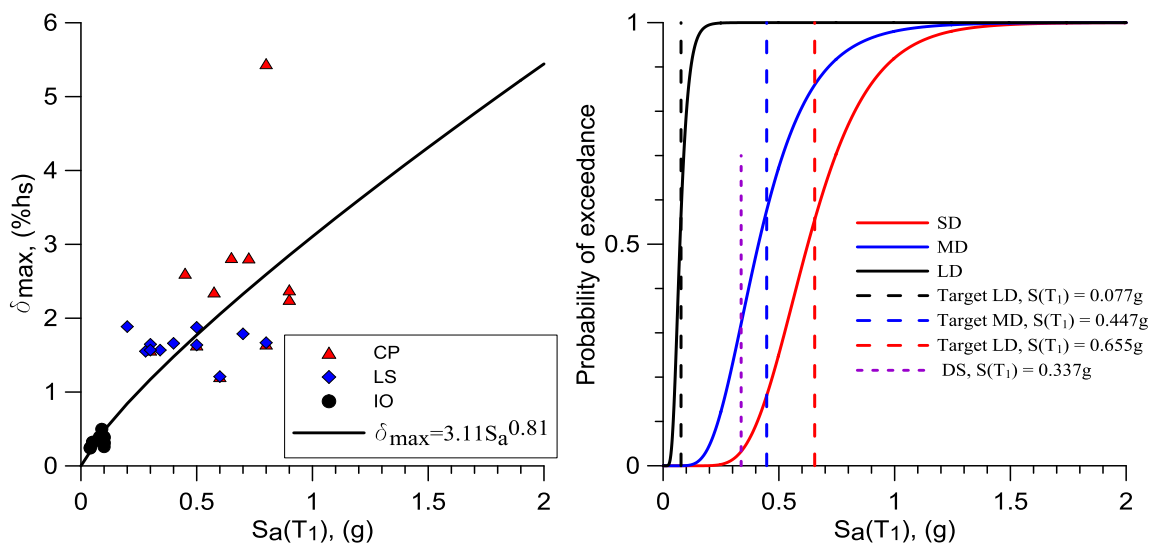


Fig. 5.4 Seismic demand for selected damage levels and fragility curves of 8-Storey MD-CBF building under subduction GMs

#### 5.2.4 Fragility of 8-storey MD-MRF building

Repeating the same steps, constants  $a$  and  $b$  for the 8-storey MD-MRF building under crustal ground motions are calculated as 8.57 and 0.78 respectively, the record to record uncertainty is  $\beta_{D|S_a} = 0.346$ . The value for the aleatoric uncertainty is calculated as  $\beta_{RR} = 0.43$  and the total uncertainty is  $\beta_R = 0.472$ . Considering three damage levels, Light Damage (LD), Moderated Damage (MD), and Severe Damage (SD), which are defined based on Fig. 5.2, the seismic demand and fragility curves are shown in Fig. 5.5. At the code design level (DS), the probability of reaching LD is 100%, the probability of reaching MD is around 30%, and the probability of reaching SD is 0%. The target  $S_a(T_1)$  of each damage state is shown in Fig. 5.5. It is noted that the fragility curve resulted at SD state is obtained from the truncated IDA curves, where the resulted collapse point resulted when the first beam of MD-MRF reached  $DI=0.375$  which mean that 20% of flexural strength capacity of the beam was consumed.

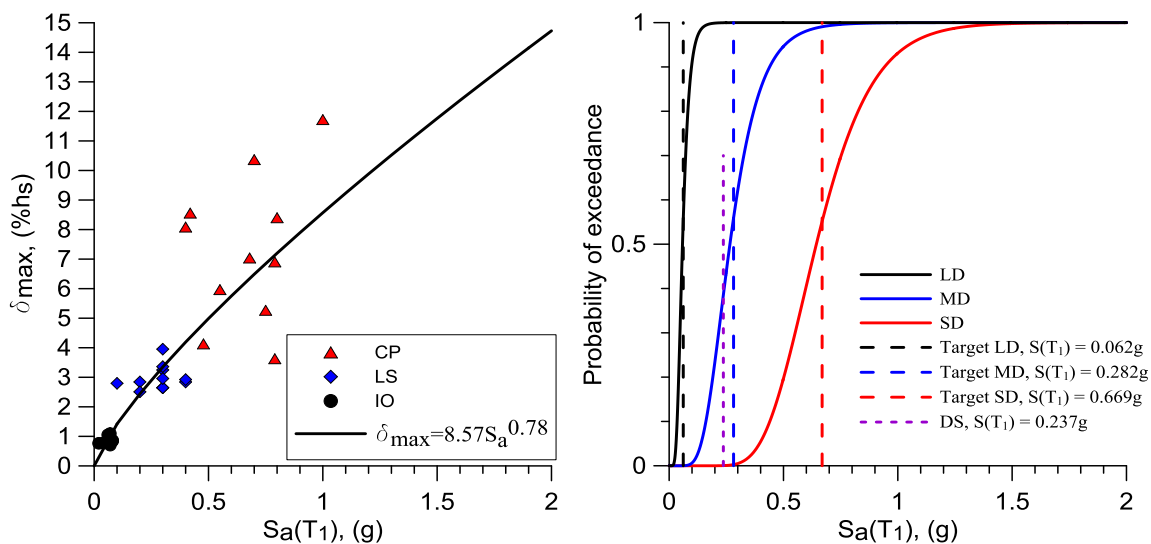


Fig. 5.5 Seismic demand for selected damage levels and fragility curves of 8-Storey MD-MRF building under crustal GMs

Similarly, constants  $a$  and  $b$  for the MD-MRF building under subduction ground motions are calculated as 6.81 and 0.65 respectively, the record to record uncertainty is  $\beta_{D|S_a} = 0.355$ . The value for the aleatoric uncertainty is calculated as  $\beta_{RR} = 0.43$ , the total uncertainty  $\beta_R$  is 0.478. The seismic demand and fragility curves are shown in Fig. 5.6. For 2% in 50 years hazard level, the associated spectral acceleration value is  $S_a = 0.237g$ . At the code design level (DS), the probability of reaching LD is 100%, the probability of reaching MD is around 65%, and the probability of reaching SD is around 30%. The target  $S_a(T_1)$  of each damage state is shown in Fig. 5.6. It is noted that the fragility curve resulted at SD state is obtained from the truncated IDA curves.

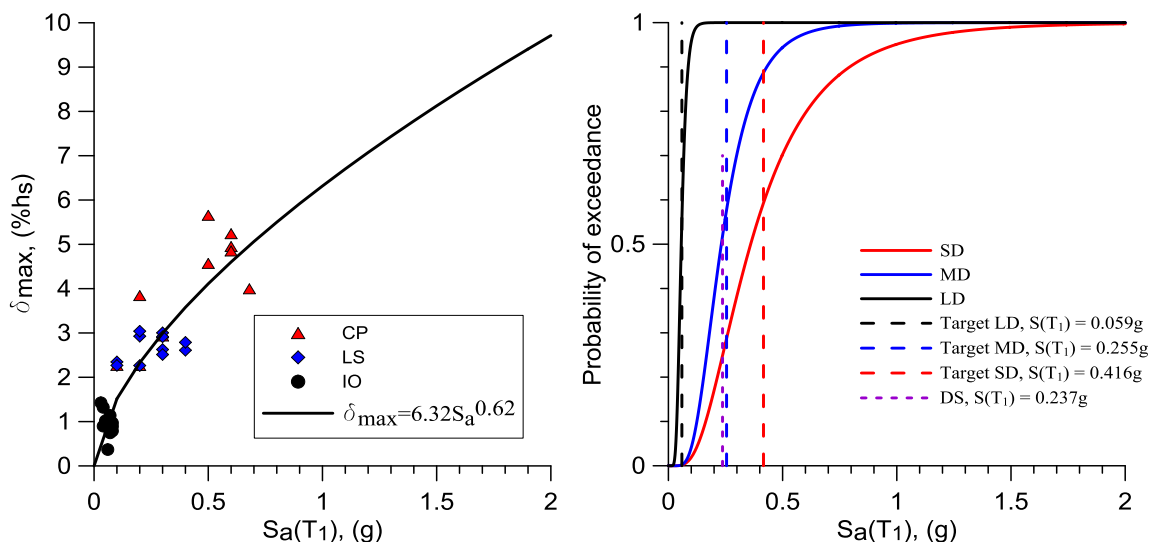


Fig. 5.6 Seismic demand for selected damage levels and fragility curves of 8-Storey MD-CBF building under subduction GMs

### 5.2.5 Fragility of 8-storey building with Braced Dual System

Repeating the same steps, constants  $a$  and  $b$  for the 8-storey building with Dual system under crustal ground motions are calculated as 2.41 and 1.07 respectively, the record to record uncertainty is  $\beta_{D|S_a} = 0.252$ . The value for the aleatoric uncertainty is calculated as  $\beta_{RR} = 0.35$ , the total uncertainty  $\beta_R$  is 0.407. Considering three damage levels, Light Damage (LD), Moderated Damage (MD), and Severe Damage (SD), which are defined based on Fig. 5.1, the seismic demand at selected performance levels and fragility curves are shown in Fig. 5.7. At the code design level, the probability of reaching LD is 100%, while the probability of reaching MD and SD is 0%. Similarly, the target  $S_a(T_1)$  of each damage state is shown.

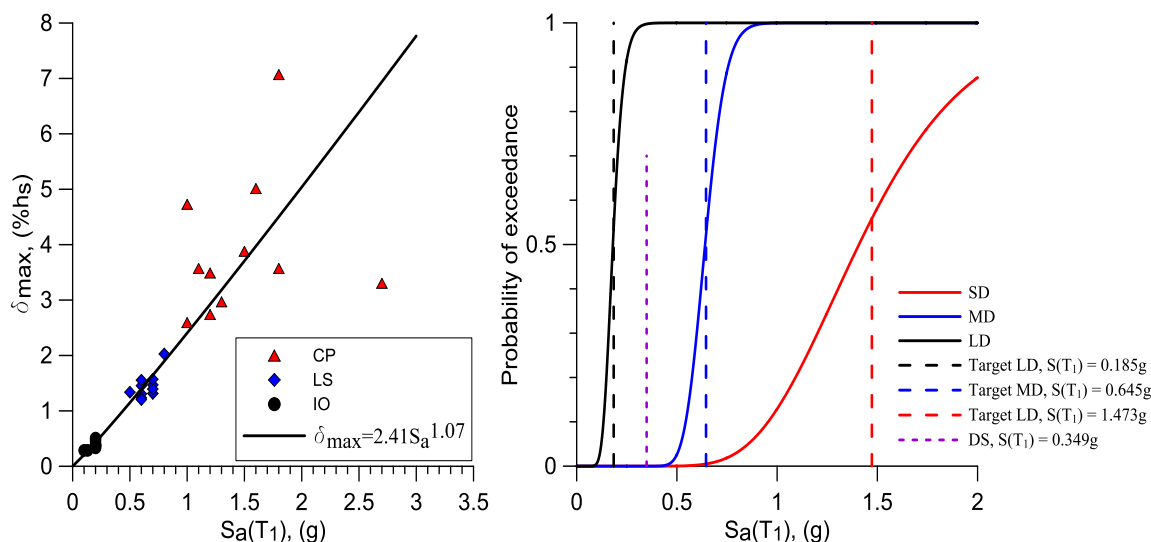


Fig. 5.7 Seismic demand for selected damage levels and fragility curves of 8-Storey building with Braced Dual System under crustal GMs

Constants  $a$  and  $b$  for the 8-storey building with Braced Dual System under subduction ground motions are calculated as 2.35 and 0.80 respectively, and the record to record uncertainty  $\beta_{D|S_a} = 0.344$ . The value for the aleatoric uncertainty is calculated as  $\beta_{RR} = 0.43$ , and the total uncertainty is  $\beta_R = 0.470$ . The seismic demand at selected performance levels and fragility curves are shown in Fig. 5.8. For 2% in 50 years hazard level, the associated spectral acceleration value is  $S_a = 0.349g$ . At the code design level (DS), the probability of reaching LD is 100%, the probability of reaching MD is around 15%, and the probability of reaching SD is 0%. Similarly, the target  $S_a(T_1)$  of each damage state is shown in Fig. 5.8.

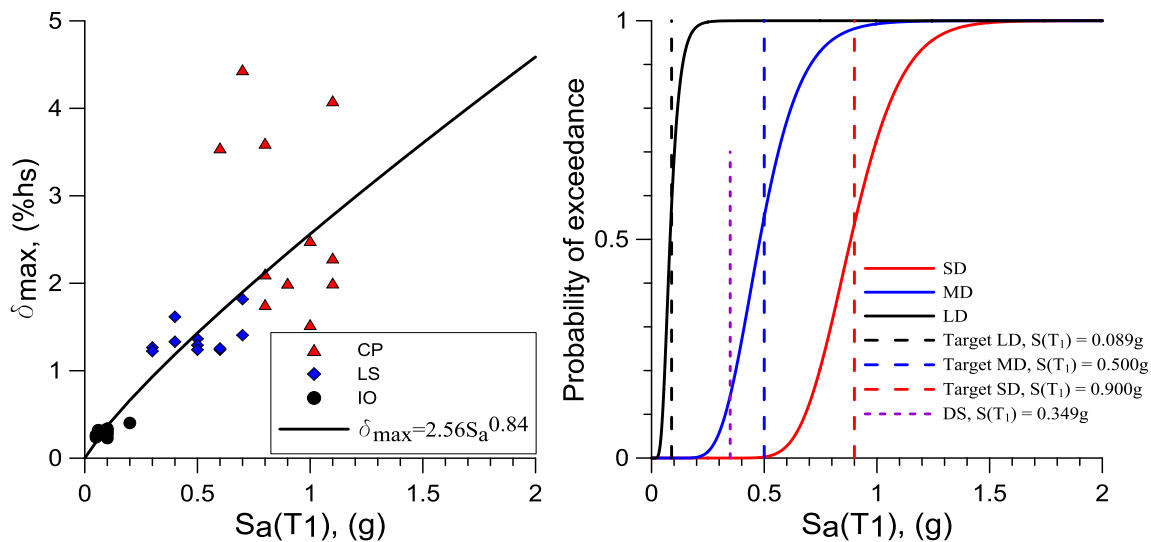


Fig. 5.8 Seismic demand for selected damage levels and fragility curves of 8-Storey building with Braced Dual System under subduction GMs

### 5.3 Comparison of Fragility Curves

The fragility curves at collapse prevention (CP) level computed for the three prototype buildings under crustal and subduction ground motions are illustrated in Fig. 5.9.

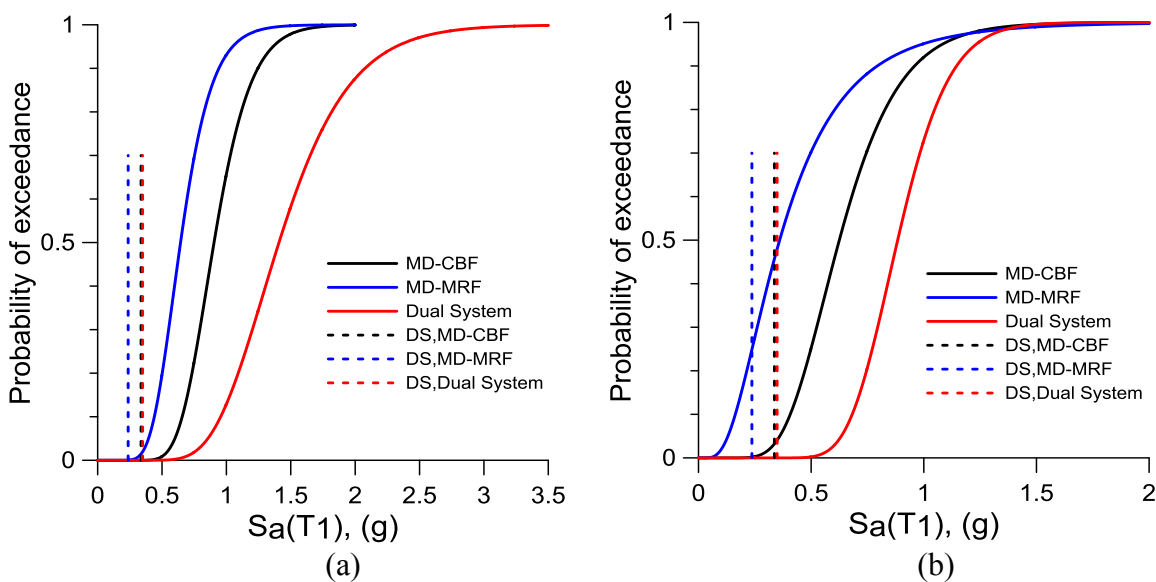


Fig. 5.9 Comparison of fragility curves of 8-storey building with different SFRSs at SD state under: (a) crustal GMs; (b) subduction GMs

As shown in Fig. 5.9 (a), the 8-storey building with Braced Dual System has a much less probability to collapse compared to the 8-storey building with MD-CBF and MD-MRF system when ground motions are scaled to the same intensity. Moreover, it is noted that the building with Braced Dual System has a similar fundamental period as the building with MD-CBF system, which means the seismic demand of the two buildings is similar. However, at CP limit state resulted under crustal ground motions, the Braced Dual System experiences 100% probability of exceedance for  $S_a(T_1) = 3.0g$ , while both MD-CBF and MD-MRF system experiences 100% probability of exceedance for  $S_a(T_1) = 1.5g$ , which means that the lateral resistant capacity of Braced Dual System is much higher than that of MD-CBF or MD-MRF system. However, in the case of MD-MRF, truncated IDA curves were used to identify the collapse point associated to each ground motion.

Analysing the CP limit state under subduction ground motions, Braced Dual System experiences 100% probability of exceedance for  $S_a(T_1) = 1.8g$  which is close to that resulted for both MD-CBF system and MD-MRF system.

## CHAPTER 6. CONCLUSIONS AND FUTURE

### WORK

#### 6.1 Conclusions

This study was conducted to assess the seismic performance of middle-rise steel buildings with traditional earthquake resistant systems such as MD-CBF, and MD-MRF. Using the dual concept, the same middle-rise steel building equipped with Braces Dual System was also investigated. The three 8-storey office buildings that share the same floor plan were located on firm soil in Vancouver, B.C. and were designed according to NBCC 2015 and CSA/S16-14 standard provisions. The seismic performance of these buildings was assessed from nonlinear time history analysis using two suites of seismic records: short-duration crustal ground motions and long-duration subduction ground motions. The incremental dynamic analysis was performed to identify the failure mechanisms of these three prototype buildings. Fragility curves were derived from the computed IDA curves and collapse margin safety was assessed for the three prototype buildings subjected independently to both suites of ground motions. In this study, the following findings are reported:

- The design requirements for steel moment resisting frames presented in CSA/S16 standard are sufficient for ultimate limit state design but could not satisfy the serviceability limit specified in NBCC 2015 for buildings with office occupancy type. From analysis, it was found that the serviceability limit requirements could be fulfilled when the column sizes of MD-MRFs are increased such that the demand to capacity ratio to be around 0.5.

- The MD-MRF system is vulnerable to subduction ground motions. At the design level, partial collapse of MD-MRF beams is observed at upper floors under 5 out of 11 subduction ground motions. Furthermore, when the MD-MRF columns are designed with a demand to capacity ratio around 0.5, the structure is more stable and the MD-MRF columns initially designed with rigid connection at the base reach the boundary of forming plastic hinges at their base, while the columns at all floors behave elastically. This is not the case when the 8-storey MD-MRF building is subjected to crustal ground motions, because the demand is lower.
- The MD-CBF building designed according to current code provisions is able to sustain both crustal and subduction earthquakes. At the design level, fracture of HSS braces is observed under 1 out of 11 subduction ground motions. Even though the failure happens, the beams and columns of CBF still show elastic behavior, which means the current capacity design approach is sufficient. However, the CBF system often shows damage concentration at some specific floors. By adding 25% of MRF as a backup frame to MD-CBF system, the damage concentration is significantly reduced. Moreover, the maximum interstorey drift and maximum residual drift are reduced.
- The finite element model developed for concentrically braced frames with HSS braces is capable of simulating buckling, yielding, and fracture caused by low-cycle fatigue of HSS braces. In the model the HSS brace are able to deflect either out-of-plane or in plane, as well as flexural hinging of braced bay beams and columns was simulated. The gusset plate brace to frame connections are simulated by two rotational and one torsional spring. Thus, the MD-CBF model is able to simulate

the seismic response from the initiation of buckling up to system failure. However, after the first HSS brace experienced fracture failure, convergence problems are encountered, and a few recommendations to avoid convergence problem are provided

- The MRF model developed in OpenSees is able to account for beam degradation caused by low-cycle fatigue. The columns of MRFs made of W-shape cross sections are simulated by using the *nonlinear beam column element* and the combination of compression and flexure was accounted for during the time history response series.
- The Braced dual numerical model incorporated all features of braced frame and moment resisting frame models. It is noted that the accuracy of these models is justified by the calibration of dissipative members against several experimental tests.
- The IDA methodology was applied to all three prototype buildings using OpenSees. The collapse margin ratios and types of failure mechanisms of each structural system are computed and discussed. For Braced dual frame buildings two types of failure mechanisms were identified under both suites of ground motions: the first failure mechanism happens when all braces in the same storey fracture; the second failure mechanism was observed when two braces which are on the same side but on adjoined floors fracture. It is found that in general, Braced Dual System experienced collapse localized at the bottom two floors. Beam deterioration of the backup MRF is found only under one subduction ground motion, however, no significant strength loss of MRF beam is observed (damage index of beams is very

small). Moreover, plastic hinges were observed in the MD-CBF beams to which the fractured braces are attached. However, columns of braced frame system have sufficient reserve capacity even when the structure is at near collapse.

- Methodology proposed in FEMA P695 was applied to assess the seismic performance of all three prototype buildings. It is concluded that all three prototype buildings could fulfill the collapse safety criterion of  $ACMR > ACMR_{10\%}$ . It is also found that the adjusted collapse margin ratio is around 1.5 times larger under the crustal ground motion set than the subduction ground motion set for all structural systems.
- Fragility analysis was performed incorporating aleatoric and epistemic uncertainties using data collected from IDA curves, three damage levels of structure are defined based on performance limit states specified in ASCE/SEI 41-13. It is concluded that all three 8-storey buildings have a greater probability to collapse when subjected to subduction ground motions compared to crustal ground motions. Furthermore, the probability of collapse at design level for the 8-storey building with dual system is 0% under all cases. Comparing to the MD-CBF building, the building with Braced Dual System has significantly reduced probability to collapse under both sets of ground motions.

## 6.2 Future Work

In this study, assumptions have been made and some issues require further clarifications.

The following recommendations are made for further research regarding this topic:

- Building with increased heights should be considered, and other brace configurations (chevron, X-brace, etc.) could be investigated to check if the same conclusions are obtained.
- The appraisal of building with Braced Dual System and earthquake-induced economic loss should be studied in order to assess their seismic resilience. For loss estimation the methodology described by Hwang and Lignos (2017) could be applied.
- The ductility-related force modification factor,  $R_d$ , of Braced Dual System could be slightly increase. From this study, it resulted that the middle-rise Braced Dual System possesses larger ductility than that associated to  $R_d = 3.0$ . A value of  $R_d = 3.5$  could be appropriate.
- Seismic behavior of other Dual system types (e.g. friction damper with backup MRF) could be studied.
- The MRF model cannot capture the low-cycle fatigue failure of MRF columns when plastic hinges are formed. This research is on-going based on the recent experimental studies conducted to investigate the failure of MRF columns. Further research is required to predict the low-cycle fatigue model assigned to column's plastic hinges fibers of MRF structural system.
- For the Braced Dual System, it is found that when one brace fails, the braced frame beam is likely to form plastic hinge at the location of attached braces. Thus, a more conservative way of capacity design applied to braced frame beams considering various brace failure scenarios could be applied and investigated.

## ***REFERENCES***

- Aguero, A., Izvernari, C., Tremblay, R. (2006). “Modelling of the Seismic Response of Concentrically Braced Steel Frames Using the OpenSees Analysis Environment”. *International Journal of Advanced Steel Construction*, Vol. 2-3, pp. 242-274.
- Archambault, M.H. (1995). “Etude du Comportement Seismique des Contreventements Ductile en X avec Profiles Tubulaires en Acier”. *Ecole Polytechnique*, Montreal, Canada, Report no. EPM/GCS-1995-09.
- ASCE. (2010). “Minimum design loads for buildings and other structures”. ASCE/Structural Engineering Institute (SEI) 7-10, Reston, VA.
- ASCE. (2013). “Seismic rehabilitation of existing buildings.” ASCE/Structural Engineering Institute (SEI) 41-13, Reston, VA.
- Atkinson, G., Goda, K. (2011). “Effects of seismicity models and new ground-motion prediction equations on seismic hazard assessment for four Canadian cities”. *Bull. Seismol. Soc. Am.* 101 (2011) 176–189.
- Baker, J. W. (2015). “Efficient analytical fragility function fitting using dynamic structural analysis”. *Earthquake Spectra*: February 2015, Vol. 31, No. 1, pp. 579-599.
- Baker, J. W., and Cornell, C. A. (2005). “A vector-valued ground motion intensity measure consisting of spectral acceleration and epsilon”. *Earthquake Engineering & Structural Dynamics*, 34(10), 1193–1217.

- Bosco, M., Marino, E.M. and Rossi, P.P. (2012). "Behavior Factor of Dual Concentrically Braced Systems Designed by Eurocode 8". *The 15th World Conference on Earthquake Engineering*, 2012, Lisbon.
- Bosco M., Tirca L. (2017). "Numerical simulation of steel I-shaped beam using a fiber-based damage accumulation model". *Journal of Constructional Steel Research*, Volume 133, June 2017, Pages 241-255.
- Canadian Standards Association (CSA). (2014). "Design of Steel Structures". *S16.1-14 Standard*, CSA, Mississauga, ON.
- Chopra A. K., McKenna F. (2016). "Modeling viscous damping in nonlinear response history analysis of buildings for earthquake excitation". *Earthquake Engineering & Structural Dynamics*, 45:193–211.
- Coffin L. (1954). "A study of the effect of cyclic thermal stress on a ductile metal". *Trans ASME*, 76: 931-950.
- CSI, *ETABS Software, Computer and Structures Inc., Berkeley, California, 2009.*
- D'Aniello M., Landolfo R., Piluso V., Rizzano G. (2012). "Ultimate behaviour of steel beams under non-uniform bending". *Journal of Constructional Steel Research*, 78: 144-158.
- Dicleli, M. and Mehta, A. (2007). "Simulation of Inelastic Cyclic Buckling Behaviour of Steel Box Sections". *Computer and Structures Journal*, pp. 446-457.
- Ellingwood, B., Celik, O.C., Kinali, K. (2007). "Fragility assessment of building structural systems in Mid-America". *Earthquake Engineering & Structural Dynamics*, 36, 1935-1952.

- Engelhardt M.D., Sabol T.A. (1994). "Testing of welded steel moment connections in response to the Northridge Earthquake". Progress report to the AISC advisory subcommittee on special moment resisting frame research.
- Federal Emergency Management Agency (FEMA). (2000). "Recommended seismic design criteria for new steel moment-frame buildings". *FEMA 350*, prepared by the SAC Joint Venture, Washington, D. C.
- Federal Emergency Management Agency (FEMA). (2006). "Designing for Earthquakes: A Manual for Architects". *FEMA 454*, Washington, DC.
- Federal Emergency Management Agency (FEMA). (2009). "Quantification of building seismic performance factors". FEMA P695, Washington, DC.
- Giugliano, M.T., Longo, A., Montuori, R., Piluso, V. (2010). "Failure Mode and Drift Control of MRF-CBF Dual Systems". *The Open Construction and Building Technology Journal*, 2010, 4, 121-133.
- Gómez, L.V.D. (2014). "Seismic Fragility Analysis of Steel Moment-Resisting Frames (MRF) Designed in Canada in the 1960s, 1980s, and 2010". Master thesis, University of Toronto.
- Hsiao, P.C., Leham, D., Roeder, C. (2013). "A Model to Simulate Special Concentrically Braced Frames Beyond Brace Fracture". *Journal of Earthquake Engineering and Structural Dynamics*, Vol. 42, pp. 182-200.
- Hsiao, P.C., Lehman, D., Roeder, C. (2012). "Improved Analytical Model for Special Concentrically Braced Frames". *Journal of Constructional Steel Research*, Vol. 73, pp.80-94.

- Hwang, S., and Lignos, D.G. (2017). “Effect of Modeling Assumptions on the Earthquake-Induced Losses and Collapse Risk of Steel-Frame Buildings with Special Concentrically Braced Frames”. *Journal of Structural Engineering*, 143(9), 04017116-1, DOI:10.1061/(ASCE)ST.1943-541X.0001851.
- Ibarra, L., Medina, R., and Krawinkler, H. (2002). “Collapse assessment of deteriorating SDOF systems.” *Conf. Proc., 12th European Conference on Earthquake Engineering*, London, Elsevier Science Ltd, paper no. 665.
- Imanpour, A., Lignos, D., Clifton, C., Tremblay, R. (2016). “Comparison of Seismic Design Requirements for Steel Moment Resisting Frames with Emphasis on Stability of Columns in North America, New Zealand, And Europe”. 11<sup>th</sup> Pacific Structural Steel Conference, Shanghai, Oct. 26- 28, 2016.
- Jain, A.K., Redwood, R.G. and Lu, F. (1993). “Seismic response of concentrically braced dual steel”. *Canadian Journal of Civil Engineering* 20, 672-687.
- Khatib I.F., Mahin S.A., and Pister K.S. (1988). “Seismic behaviour of concentrically braced steel frames”. Earthquake Engineering Research Center, Report No. UCB/EERC-88/01. University of California.
- Kiggins, S. and Uang, C. (2006). “Reducing residual drift of buckling-restrained braced frames as a dual system”. *Engineering Structures*, 28 (2006) 1525–1532.
- Kim T., Whittaker AS, Gilani ASJ, Bertero VV, Takhirov SH. (2000). “Cover-Plate and Flange-Plate Reinforced Steel Moment resisting connections”. PEER report 2000/07. Pacific Earthquake Engineering Research Center, University of California, Berkeley.

- Lamarche, C.P., and Tremblay, R. (2008). “Accounting for residual stresses in the seismic stability of nonlinear beam-column elements with cross-section fiber discretization”. *Annual Stability Conference*, 59-78.
- Lay M.G. (1965). “Flange Local Buckling in Wide-Flange Shapes”. *Journal of the Structural Division*, ASCE, 91(6):95-115.
- Lignos D.G, Krawinkler H. (2011). “Deterioration modelling of steel components in support of collapse prediction of steel moment frames under earthquake loading”. *Journal of Structural Engineering*, 137 (11): 1291-1302.
- Lignos, D. and Karamanci, E. (2013). “Predictive Equations for Modelling Cyclic Buckling and Fracture of Steel Braces”. *10th International Conference on Urban Earthquake Engineering*, Tokyo Institute of Technology, Tokyo, Japan.
- Longo, A., Montuori R., Piluso, V. (2014). “Theory of plastic mechanism control for MRF–CBF dual systems and its validation”. *Bull Earthquake Eng* (2014) 12:2745–2775. DOI 10.1007/s10518-014-9612-2.
- Longo, A., Montuori R., Piluso, V. (2016). “Moment frames – concentrically braced frames dual systems: analysis of different design criteria”. *Structure and Infrastructure Engineering*, 12:1, 122-141, DOI: 10.1080/15732479.2014.996164.
- Nastri, E., Montuori, R. & Piluso, V. (2015). “Seismic Design of MRF-EBF Dual Systems with Vertical Links: EC8 vs Plastic Design”. *Journal of Earthquake Engineering*, 19:3, 480-504, DOI: 10.1080/13632469.2014.978917.

- Manolache, L., Wang, Y., Tirca, L., Bagchi, A. (2017). “Vibration Characteristics of an Existing High-Rise Building in Montreal and the Effects of Retrofit”. EUROSTEEL Conference 2017, Copenhagen, Denmark.
- Manson, S. (1965). “Fatigue: A complex subject – some simple approximations”. *Experimental Mechanics* 5 (7): 193-226.
- Mazzolani, F.M., & Piluso, V. (1996). “Theory and design of seismic resistant steel frames”. London: E&FN Spon, an Inprint of Chapman&Hall.
- Mazzolani, F.M., & Piluso, V. (1997). “Plastic design of seismic resistant steel frames”. *Earthquake Engineering and Structural Dynamics*, 26, 167–191.
- Mazzoni, S., McKenna, F., Scott, M., Fenves, G.L. et al., (2013). “Open system for earthquake engineering simulation”. OpenSees software, Pacific Earthquake Engineering Research Center (PEER), University of California, Berkeley.
- McKenna, F., and Fenves, G. L. (2004). “Open system for earthquake engineering simulation (OpenSees)”. (<http://www.opensees.berkeley.edu/index.html>) (Mar. 5, 2015).
- Montuori, R., Nastri, E. & Piluso, V. (2016). “Theory of Plastic Mechanism Control for MRF–EBF dual systems: Closed form solution”. *Engineering Structures*, Volume 118, 1 July 2016, Pages 287-306.
- National Research Council of Canada (NRCC). (2015). “National Building Code of Canada. Associate Committee on the National Building Code”. NRCC, Ottawa, ON.

- OpenSees version 2.4.6 [Computer software]. Berkeley, CA, Pacific Earthquake Engineering Research Center.
- PEER/ATC. (2010). “Modeling and acceptance criteria for seismic design and analysis of tall buildings”. Rep. No. 72-1, ATC—Applied Technology Council, Redwood City, CA.
- Pillai, S. (1974). “Beam-columns of hollow structural sections”. *Can. J. Civ. Eng.*, 1(2), 194-198.
- Ribeiro F.L., Barbosa A.R., Scott M.H., Neves L.C. (2015). “Deterioration modeling of steel Moment-resisting frames using finite-length plastic hinge force-based beam columns elements”. *J. of Struct. Eng.*, 141(2), doi: 10.1061/(ASCE)ST.1943-541X.0001052.
- Salawdeh, S. and Goggins, J. (2013). “Numerical Simulation for Steel Brace Members Incorporating a Fatigue Model”. *Engineering Structures*, Vol. 46, pp. 332-349.
- Santagati, S., Bolognini, D., Nascimbene, R. (2012). “Strain Life Analysis at Low-cycle Fatigue on Concentrically Braced Steel Structures with RHS Shape Braces”. *J. Earthquake Eng.*, Vol.16 (S1), pp. 107-137.
- Tesfamariam, S., Goda. K. (2015). “Loss estimation for non-ductile reinforced concrete building in Victoria, British Columbia, Canada: effects of mega-thrust  $M_w$ 9-class subduction earthquakes and aftershocks”. *Earthq. Eng. Struct. Dyn.*, 44: 2303–2320. doi: 10.1002/eqe.2585.

- Tirca, L., Chen, L. (2014). “Numerical simulation of inelastic cyclic response of HSS braces upon fracture”, *J. Adv. Steel Constr.* 10 (4) 442–462.
- Tirca, L., Chen, L., Tremblay, R. (2015). “Assessing collapse safety of CBF buildings subjected to crustal and subduction earthquakes”. *Journal of Constructional Steel Research*, Volume 115, December 2015, Pages 47-61.
- Tirca, L., Serban, O., Lin L., Wang, M.Z., Lin, N., (2016). “Improving the seismic resilience of existing braced-frames office buildings”. Published in the Special Issue: Resilience-based analysis and design of structures and infrastructures. *Journal of Structural Engineering (ASCE)*, Vol. 142, No. 8, 2016.
- Tremblay, R. (2008). “Influence of Brace Slenderness on the Fracture Life of Rectangular Tubular Steel Bracing Members Subjected to Seismic Inelastic Loading”. Proc. 2008 ASCE Structures Congress, Vancouver, BC.
- Tremblay, R., Archambault, M.H., Filiatrault, A. (2003). “Seismic Response of Concentrically Braced Steel Frames Made with Rectangular Hollow Bracing Members”. *Journal of Structural Eng.*, ASCE, Vol. 129, No. 12, pp.1626-1636.2012.
- Tsai, K.C., Popov, E.P. (1988). “Steel beam-column joints in seismic moment resisting frames”. Report no. UCB/EERC-88/19. Earthquake Engineering Research Center, Berkeley.
- Uang, C.M., Latham C. (1995). “Cyclic test of full scale MNH-SMRFTH dual strong axis moment connections”. Report No. TR-"95/01, University of California, San Diego, USA.

- Uriz, P. (2005). "Towards Earthquake Resistant Design of Concentrically Braced Steel Buildings". *Ph.D. Dissertation*, University of California, Berkeley.
- Uriz, P. and Mahin, S. (2008). "Toward Earthquake Resistant Design of Concentrically Braced Steel Frame Structures". *PEER Report*.
- Uriz, P., Filippou, F.C., Mahin, S. (2008). "Model for Cyclic Inelastic Buckling of Steel Braces". *Journal of Structural Engineering*, ASCE, pp. 619-628.
- Uriz, P., Mahin, S. (2008). "Toward Earthquake-Resistant Design of Concentrically Brace Steel-Frame Structures". Pacific Earthquake Engineering Research Center (PEER) report, University of California, Berkeley.
- Vamvatskos, D., Cornell, C.A. (2002). "Incremental Dynamic Analysis". *Earthquake Engng Struct. Dyn.* 2002; 31:491–514 (DOI: 10.1002/eqe.141).
- Vamvatskos, D., Cornell, C.A. (2004). "Applied Incremental Dynamic Analysis". *Earthquake Spectra*: May 2004, Vol. 20, No. 2, pp. 523-553.
- Wang, Y., Nistri, E., Tirca, L., Montuori, R., Piluso, V. (2018). "Comparative Response of Earthquake Resistant CBF Buildings Designed According to Canadian and European Code provisions". *Key Engineering Materials*, Vol. 763, pp 1155-1163, Trans Tech Publications, Switzerland.
- Wen, Y.K., Ellingwood, B., and Bracci, J. (2004). "Vulnerability function framework for consequence-based engineering". *MAE Center Project DS-4 Report*.
- Whitmore, R.E. (1952). "Experimental investigation of stresses in gusset plates." *Bulletin No.16, Engineering Experiment Station*, University of Tennessee.

- Xie, Q. (2008). "Dual System Design of Steel Frames Incorporating Buckling-Restrained Braces". *The 14th World Conference on Earthquake Engineering*, October 12-17, 2008, Beijing, China.
- Yang, T.Y. and Mahin, S. (2005). "Limiting Net Section Fracture in Slotted Tube Braces". *Steel Tips*, Structural Steel Education Council, Orinda, Ca.
- Ziemian, R. (2010). "Guide to Stability Design Criteria for Metal Structures". J. Wiley & Sons, 2010.